TECHNISCHE UNIVERSITÄT MÜNCHEN

Ingenieurfakultät Bau Geo Umwelt

Lehrstuhl für Metallbau

Fire resistance of hot-dip galvanized steel structures

Christian Wolfgang Gaigl

Vollständiger Abdruck der von der Ingenieurfakultät Bau Geo Umwelt der Technischen Universität München zur Erlangung des akademischen Grades eines

Doktor-Ingenieurs (Dr.-Ing.)

genehmigten Dissertation.

Vorsitzender:	Prof. Dr.-Ing. Oliver Fischer
Prüfer der Dissertation:	1. Prof. Dr.-Ing. Martin Mensinger
	2. Prof. Dr. Markus Knobloch
	3. Prof. Dr.-Ing. František Wald

Die Dissertation wurde am 06.03.2019 bei der Technischen Universität München eingereicht und durch die Ingenieurfakultät Bau Geo Umwelt am 25.07.2019 angenommen.

For me

Acknowledgement

First of all, a special thanks goes to Prof. Dr.-Ing. Dipl. Wirt.-Ing. (NDS) Martin Mensinger for giving me the opportunity, the trust and the support to write this thesis at the Chair of Metal Structures at the Technical University of Munich.

A special thanks goes to Univ.-Prof. Dr. Markus Knobloch and Prof. Ing. František Wald, CSc. for joining the examination board of my doctoral thesis. In addition, I want to thank Prof. Ing. František Wald, CSc. for his warming hospitality at my stay in Prague. Additionally I have to thank Dr. Christian Mühlbauer for being my mentor during my thesis.

Furthermore, I am very grateful for the outstanding expertise and help of Dr. Horst Fark, Dr. Ernest Berghofer, Hans Birg, Stefan Sommer and Markus Uemminghaus in the fire laboratory of the Technical University of Munich.

Of course, I have to thank the whole team at our Chair of Metal Structures for the funny moments in the middle of all the work and the real good atmosphere. Especially, I would like to thank Samuel Pfenning for the constructive discussions – professional and the private ones. Special thanks goes to all my bachelor and master students, working on thesis under my supervision, as well as to my working students Malik Ltaief and Johannes Diller for helping me at the experiments.

Again, I have to thank Martin Mensinger for our bets during my time at your chair and for keeping my winning odds always at 100 % – it was a pleasure.

The greatest thanks of all goes to my friends and my family. Always believing in me and supporting me not only in times of the thesis, but also for my whole life. A special thanks goes, therefore, to my parents Frieda and Wolfgang, as well as to my sister Verena. You're the best! Finally, I want to thank my fiancée Dorothee for being always on my side, helping me in every possible way to enrich my life – Thank you!

Christian Wolfgang Gaigl

Preface

The research, for this thesis, was done during my time at the Chair of Metal Structures at the Technical University of Munich. Parts of this research were accompanied by the IGF project 18887 N of the Forschungsvereinigung Gemeinschaftsausschuss Verzinken e.V. – GAV, which was funded by the AiF within the Industrial Collective Research ("Industrielle Gemeinschaftsforschung", IGF) of the Federal Ministry for Economic Affairs and Energy. Some of those findings have been already presented or published during this time. My previous thanks also, of course, goes to all those who have helped to realise this project.

Abstract

Since the beginning of mankind, fire has been a constant threat. Today's building structures have to deal with it and have to resist for a certain time in the accidental situation of a fire. If fire resistance is required for load-bearing structures, it must be proven that the load-bearing behaviour fulfils the static requirements in the event of fire. The state of the art for protecting steel structures from excessively high temperatures in the accidental design situation of fire is passive fire protection. European standardizations also offer mathematical verification procedures to verify the fire-resistant requirements. For example, the steel component temperature must be determined and the load-bearing capacity verification must be carried out in accordance with EN 1993-1-2, taking into account the reduction of the material characteristic properties at higher temperatures. For this purpose, positive effects of hot-dip galvanizing on the temperature development of structural steel members under the influence of fire are investigated. The aim is to enable hot-dip galvanized steel structures to resist a fire at least for a 30-minute requirement, without any additional aids.

For this purpose, a test stand was developed within the framework of this research, which enabled a detailed investigation of the heat absorption behaviour. In addition, two full-scale fire tests were carried out, confirming the results of the small-scale tests. The responsible factor contributing to this behaviour was determined and quantified.

The results show much better behaviour of certain hot-dip galvanized samples in case of fire due to different emissivity levels, which are in contrast to the normative, globally-applied value of EN 1993-1-2. In addition, the research result holds strong economic potential. Due to this positive effect, a significant proportion of fire protection measures for *R30* requirements can be omitted by considering hot-dip galvanizing.

Kurzfassung

Seit Beginn der Menschheit ist Feuer eine ständige Bedrohung. Heutige Gebäudestrukturen müssen sich damit auseinandersetzen und einer gewissen Zeit für den außergewöhnlichen Fall eines Brandes widerstehen. Wird für Tragwerke eine Feuerwiderstandsfähigkeit gefordert, so ist nachzuweisen, dass das Tragverhalten im Brandfall die statischen Anforderungen erfüllt. Stand der Technik zum Schutz von Stahlkonstruktionen vor zu hohen Temperaturen im Brandfall ist ein passiver Brandschutz. Europäische Normen bieten auch mathematische Nachweisverfahren zur Überprüfung der Brandschutzanforderungen an. So ist beispielsweise die Stahlbauteiltemperatur zu ermitteln und der Tragfähigkeitsnachweis nach EN 1993-1-2, unter Berücksichtigung der Reduzierung der Materialkennwerte, bei höheren Temperaturen durchzuführen. Zu diesem Zweck wurden positive Auswirkungen der Feuerverzinkung auf die Temperaturentwicklung von Stahlbauteilen unter Brandeinfluss untersucht. Ziel war es, dass feuerverzinkte Stahlkonstruktionen ohne zusätzliche Hilfsmittel einem Brand mindestens 30 Minuten lang standhalten können.

Zu diesem Zweck wurde im Rahmen dieser Forschung ein Versuchsstand entwickelt, der eine detaillierte Untersuchung des Wärmeaufnahmeverhaltens ermöglicht. Darüber hinaus wurden zwei vollständige Brandversuche durchgeführt, die die Ergebnisse der Kleinversuche bestätigten. Der verantwortliche Faktor, der zu diesem Verhalten beiträgt, wurde ermittelt und quantifiziert.

Die Ergebnisse zeigen ein wesentlich besseres Verhalten bestimmter feuerverzinkter Stahlbauteile im Brandfall, aufgrund unterschiedlicher Emissionsgrade, die im Gegensatz zum normativen, global angewandten Wert der EN 1993-1-2 stehen. Darüber hinaus hat das Forschungsergebnis ein großes wirtschaftliches Potenzial. Aufgrund dieses positiven Effekts kann ein erheblicher Teil der passiven Brandschutzmaßnahmen, unter Zuhilfenahme einer Feuerverzinkung, für *R30* Brandschutzanforderungen entfallen.

Content

List of symbols

In the course of the thesis, only the relevant parameters will be mentioned in the direct content of the text. Information for all parameters and constants can be found in the following list of symbols. Typical units have been indicated, while other quantities that are non-dimensional are designated by [-].

Abbreviations

EP-T	Emissivity Performance – Test
HDG	Hot-dip galvanizing
3MH1	Infrared sensor from Optris GmbH measuring at a wavelength range of 2.3 µm
LT	Infrared sensor from Optris GmbH measuring at a wavelength range of 8-14 µm

Latin letters

c_a	specific heat of steel $[J/(kgK)]$
$\dot{h}_{net}$	net heat flux $[W/m^2]$
$\dot{h}_{net,c}$	net convective heat flux component $[W/m^2]$
$\dot{h}_{net,r}$	net radiative heat flux component $[W/m^2]$
k	absorption coefficient [-]
$k_{y,\theta}$	effective yield strength, relative to yield strength at 20 °C [-]
$k_{p,\theta}$	proportional limit, relative to yield strength at 20 °C [-]
$k_{E,\theta}$	slope of linear elastic range, relative to slope at 20 °C [-]
k_{sh}	correction factor of the shadowing effect [-]
l	length $[m]$
n	refractive index [-]
r	radius $[m]$
r_e	electrical resistance $[\Omega]$
Δt	time interval $[sec]$

A	area $[m^2]$
A_m/V	section factor for unprotected steel members $[1/m]$

A_m	surface area of the member $[m^2/m]$
E	emissive power $[W/m^2]$
$E_\lambda(\lambda, T)$	spectral specific emissive power $[W/(m^2 \mu m)]$
E_d	design value of loads
$E_{fi,d,t}$	design value in the fire situation at the time t
G_k	characteristic value of the permanent action
G_d	design value of the permanent action
I	radiative intensity $[W/m^2 sr]$
I_λ	spectral intensity $[W/(m^2 \mu m\ sr)]$
$Q_{k,1}$	characteristic value of the leading variable action *1*
Q_d	design value of a variable action
$R_{fi,d,t}$	design value of the resistance of the member in the fire situation at time *t*
R	electrical resistance $[\Omega]$
T	temperature $[°C]$ or $[K]$
T_{ges}	total-temperature $[°C]$ or $[K]$
V	volume of the member $[m^3/m]$
$\Delta T_{y \rightarrow x}$	temperature change in component X due to component Y $[°C]$ or $[K]$

Greek letters

α_c	coefficient of heat transfer by convection $[W/(m^2 K)]$
$\gamma_{Q,1}$	partial factor for variable action 1 [-]
ε_m	surface emissivity of the member [-]
ε_f	emissivity of the fire [-]
η_{fi}	reduction factor in fire [-]
ϑ	polar angle [°]
λ	wavelength $[\mu m]$
ρ_a	the unit mass of steel $[kg/m^3]$
ρ	specific electrical resistance $[(\Omega\ mm^2)/m]$
σ	Stefan-Boltzmann constant (= 5.67×10^{-8} $[W/(m^2 K^4)]$)
φ	azimuth angle [°]
$d\omega$	solid angle element

$\theta_{a,cr}$	critical steel temperature $[°C]$ or $[K]$
θ_a	steel temperature $[°C]$ or $[K]$
θ_g	gas temperature in the fire compartment $[°C]$ or $[K]$
θ_m	surface temperature of the member $[°C]$ or $[K]$
ϕ	configuration factor [-]
$\Delta\theta_{a,t}$	Temperaturanstieg des Stahlbauteils zum Zeitpunkt t $[°C]$ or $[K]$
$d\Phi$	radiative power $[W]$

Indices

a	steel
b	black body
d	design value
fi	fire
g	gas
k	characteristic value
m	member
λ	spectral

1 State of research

1.1 Galvanizing / Hot-dip galvanizing (HDG)

Galvanizing processes are the state of the art in the field of corrosion protection, having been successfully used for many decades across the world. Due to evolving technologies, multiple new galvanizing methods where developed, which differ in terms of their processes as well as regarding the application or layer formation. An overview of various galvanizing processes is shown in Table 1.

Table 1: Galvanizing methods and their characteristics

Galvanizing method	Thickness of the coating [µm]	Structure / composition of the coating
Electro-galvanization		
Discontinuous	5 – 25	Coating comprises of pure zinc layers
Continuous	2.5 – 5	
Thermal zinc spraying	80 – 150	Coating of zinc drops including an oxide skin. No alloying
Zinc-rich paint (zinc dust)		
Sheradising	15 – 25	Iron-zinc-alloy layers
Mechanical plating	10 – 20	Homogenous zinc coating
Hot-dip galvanizing		
Batch hot-dip galvanizing	50 – 220	Pronounced iron-zinc alloy layer. Partly with an additional overlying pure zinc coating
Continuous sheet galvanizing	7 – 25	Slight iron-zinc alloy layer with an pure zinc coating on top

In this research, the hot-dip galvanizing was used, since this process plays a leading role in the construction industry and corresponds to the current state of the art to protect larger structures from corrosion.

In order to fathom the outcomes of the underlying tests, it is necessary to understand the exact procedure of this galvanizing method. Therefore, the hot-dip galvanizing process with its related iron-zinc alloy layers will be first discussed in detail.

According to DIN EN ISO 1461 [1], hot-dip galvanizing (HDG) is a discontinuous application of a zinc coating to steel by immersing the prefabricated and pre-treated steel elements in molten zinc.

The quality of the zinc coating strongly depends on the surface quality of the delivered workpieces. An upstream surface preparation is necessary. Therefore, an HDG process includes the following procedural steps after the incoming inspection:

Degreasing – Rinsing – Pickling – Rinsing – Fluxing – Drying – Galvanizing – Cooling.

Subsequently, a post treatment like a passivation will be added in some cases. An inspection has to be conducted to assure the quality and the minimum requirements of the zinc coating. These include inter alia the thickness control of the samples according to the DIN EN ISO 1461 [1].

Indispensable for the quality of the zinc coating is the knowledge of the requirements and the corrosion protection design regarding the application of zinc coatings. The background knowledge for this is provided in Germany by the DASt-Richtlinie 022 [2]. Not every component or construction can be submerged in the zinc basin without further processing. In addition, and particularly relevant for this research, it is important to have knowledge of the properties of the base materials used.

In the following Chapter 1.2, a more detailed view of the HDG process regarding the fundamental concern of this thesis is examined, namely the fire resistance of galvanized constructions. Among other things, the technology of HDG as well as the elementary details of the processes taking place in the formation of the layering process are discussed in further detail.

1.2 Properties of important materials for a HDG coating

The layer growth arises in strong dependence of the interacting base material used. In this case, this is the steel composition of the structural steel members, although it also depends on the molten zinc and the temperature of the zinc bath. All factors have a decisive influence on the respective microstructure, which in turn has a major influence on the fire resistance, as shown in the main chapters of the thesis. The iron-zinc reaction that takes place during the immersion process forms intermetallic phases of the two metals. This reaction also determines the properties in terms of layer thickness, appearance, adhesion and corrosion resistance.

The reactive initial material of galvanized steel is iron. In turn, iron (*Fe*) is a metal from the 8th sub-group of the periodic table and probably the most common and one of the most important heavy metals. Pure iron is a good conductor of electricity, relatively soft and paramagnetic below 770 °C. However, due to its reactivity it corrodes easily in the presence of water and oxygen [3]. According to DIN EN 10020 [4], the term ‘steel’ is understood as a material whose percentage by weight of iron is greater than that of any other accompanying element. In addition, the carbon content of the material must generally be less than 2 %. Besides that, steel is classified according to the chemical composition. In order to improve its physical and chemical properties, a number of alloying elements are added to the steel. These can also be contained in steel due to the raw materials or production used. Regardless of their origin, they change the structural constitution and the respective characteristic properties. More information can be taken from literature such as *Läpple* [5].

For hot-dip galvanizing, two chemical elements hold prior interest, namely the silicon and the phosphorous content. For the most important content of the galvanizing process – the silicon content – a very high maximum of 0.60 % is declared by norms. However, there are no statements about the important phosphorous content. While silicon is used as a deoxidizing agent in steel production, it is also important for galvanizing, since no contaminant-poor boundary layer of α-iron is formed, which holds strong importance for the formation of the δ_1-phase in the coating (see Chapter 1.4.2). The influence of both chemicals on the galvanizing process is discussed in detail below. Due to mechanical and welding requirements, today's steels are rather low in phosphorus, whereby the focus is more on the silicon concentration.

In contrast to iron, zinc (*Zn*) is an element of the 2nd sub-group of the periodic table. As a material, zinc is very valuable in its metallic form. For example, it is used in the construction industry, the automotive industry as well as mechanical engineering. The most important application is the corrosion protection of steel. In Germany, according to *Schulz et al.* [3], about 40 % of the total processed zinc is used in the area of galvanizing.

The following Table 2 from [3] summarizes some important properties of iron and steel for galvanizing. Comparing the elements iron and zinc, it can be noticed that some properties are similar, such as density, whereas others are different, such as the melting temperature.

Table 2: Properties of iron, steel and zinc according to [3,5]

	Iron (Fe)	**Steel**	**Zinc (Zn)**
Relative atomic mass	55.9	like iron	65.4
Densitiy [kg*m^3]	$7.87 \cdot 10^3$		$7.14 \cdot 10^3$
Melting point [°C]	1536		419.5
lattice constant (a/c) [m]	$a = c = 2.867 \cdot 10^{-10}$ (α-iron)	-	$a = 2.665 \cdot 10^{-10}$; $c = 4.947 \cdot 10^{-10}$

Each material can be described by its texture and its structure. The latter is the geometrical arrangement of the chemical components, like atoms, ions and molecules in a given space grid. Texture in turn describes the arrangement of larger units, which are composed of the structures – such as crystalline areas – in the space itself. The texture is divided by grain boundaries into individual structural areas.

Intermolecular forces characterize a metallic bond, as is the case with metallic solids such as iron. This results in many of the respective properties of the metal. In order to reach a metallic state, the metal atoms release their outer valence electrons, creating an ionic state. These floating electrons produce an electron gas. Consequently, metals are – inter alia – electrically and thermally conductive and well reflective. Every material tries to achieve a stable energetic state, which is also the lowest in energy. In the case of a metal, this is the crystalline state. The smallest unit of spatial unity is the elementary cell. It contains all of the regularities of the atomic arrangement of a crystal. An elementary cell is characterized by its atomic distances and the angles between the crystal axes. The geometric parameters a (distance in the plane) and c (distance over the height) – as the centre distances of the atoms – are called lattice parameters or lattice constants. These parameters for iron and zinc are given in Table 2.

In practice, particularly lattices of increased symmetry are common, in which several elementary cells are intricate. Thus, α-iron crystallises in a body-centred cubic lattice (*bcc*). In contrast, zinc crystallises in another arrangement, the hexagonal close-packing (*hcp*). Schematically, both unit cells are shown in Figure 1.

In the *bcc* arrangement, the metal atoms are oriented in the corners as well as the middle of a cube. The packing density – which represents the number of atoms per unit volume as an index – is 68 % in this case [5]. A number of metals are polymorphic, which is the reason why they occur in different lattice structures. Depending on the temperature, this also includes iron. Greek letters have been introduced to indicate their modification. For example, for steel temperatures lower than 900 °C, α-iron has this structure, which can be described as a *bcc* packing of spheres. Given that 900 °C is higher than the upper limit of steel temperatures reached in this research, this packing is the only important for the course of the thesis.

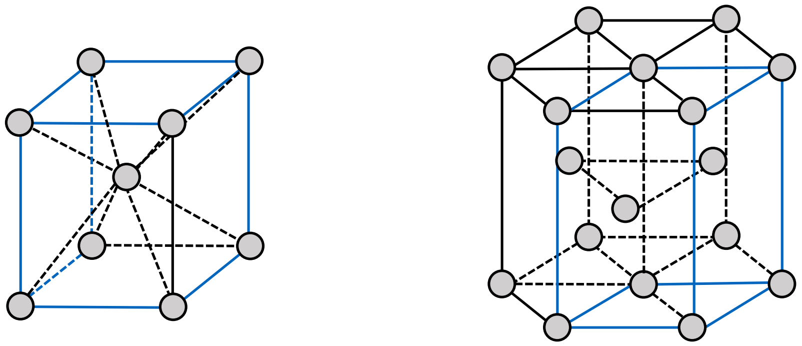

Figure 1: Left: body-centred cubic lattice (bcc) of α-iron; Right: hexagonal close-packing (hcp) of zinc

Zinc crystallises in another lattice type, namely the hexagonal closest packing, where atoms are arranged in a hexagonal column, with an additional atomic layer between the upper plane surface and the lower plane surface. The packing density, according to [5], is 74 %, which is higher than in the *bcc* lattice.

Both metals differ in essential properties, whereby a simple epitaxial growth of the zinc coating on a steel component is thus not possible. Metal structures change due to the effect that not only inherent metal atoms are in the lattice, but also foreign atoms of the alloying partner. However, these usually do not fit perfectly into the structure of the dominant material. The reasons for this are either the different atomic sizes or – as in this case – even different lattice types with varying lattice constants.

Intermetallic phases have different concentration ranges. Each of them has its own stable system with varying crystal structures, depending on the element concentrations. They typically comprise of sub-grids that interpenetrate each other. These processes are covered by the generic term ‘diffusion’. The consequence of such diffusion processes in metals are recrystallization, grain growth and segregation. The predominant type of bond in intermetallic phases is the metal bond, although portions of a covalent or ionic bond are also present.

To specify planes or corresponding parallel planes of atoms in a crystal lattice, the *Miller indices* [6] were introduced. In a cubic crystal system three numbers *h*, *k* and *l*, with the notation (*hkl*), can describe such a lattice plane. The hexagonal system represents a special case, as it is common to describe the planes with four indices (*hkil*) – the *Miller-Bravais indices* [6]. Whereas *h*, *k* and *l* are the same as in cubic systems, *i* can be calculated as $i = -(h + k)$ out of them. The third index *i* helps to identify planes of a family. Although, this is not explicit necessary to describe a plane; therefore, it is common in literature to omit the third index and replace it by a dot, i.e. (*hkil*) = (*hk.l*). Further details can be found in *Graf and McHenry* [6].

1.3 Zinc bath compositions

A brief look at the zinc bath will be given in the following, since the additives have an effect on the coating formation. This consequently has an influence on the surface condition with respect to a varying heating behaviour. By heating up solid metals, two key temperatures have to be kept in mind, one of them is the melting point at which the solid material melts. As shown in Table 2, for zinc this occurs at 419.5 °C. The other important temperature is the boiling point at which the melted metal passes into gas. For zinc, this occurs at around 907 °C.

In molten metals, the above-indicated metal lattice order is rescinded by an increase in the temperature accompanied by an increased induced particle energy. A near-order emerges, obeying rather loose rules. The more closely that the temperature of the molten metal equals the melting point, the greater the near-order. Zinc bathes are generally slightly above the melting point of zinc. Consequently, diffusion processes take place slowly.

Over the years, the zinc melts used in practice have changed due to ongoing research and progresses. Not only has environmentally-harmful lead been removed, but also other disadvantages that resulted from certain additions have been replaced or limited in their concentration. Today's requirements – such as the chemical composition of the zinc bath – can be found in DIN EN ISO 1461 [1] and DASt-Richtlinie 022 [2]. For example, the chemical elements tin, bismuth and lead must be limited due to their influence on the risk of cracking. The following Table 3 gives a composition of a standard zinc melt for different bath classifications.

Table 3: Zinc bath composition from DASt 022 [2]

Zinc bath classification	**Ratio in the zinc melt [*wt.-%]***				
	Sn	**Pb+10Bi**	**Ni**	**Al**	**Sum of other elements (without Zn + Fe)**
1	≤ 0.1	≤ 1.5	< 0.1	< 0.1	< 0.1
2	0.1 – 0.3	≤ 1.5	< 0.1	< 0.1	< 0.1
3	> 0.3	≤ 1.3	< 0.1	< 0.1	< 0.1

Originating from a conventional zinc bath composition, various zinc coatings can be achieved. They can differ in terms of layer thickness, growth, microstructure and the appearance of the Fe - Zn alloy layer, due to the dependencies of influencing factors, such as galvanizing temperature and time, the steel composition and surface finish. The silicon and phosphorus contained in the steel is significantly involved in this, being responsible for reactivity differences with the molten zinc. For HDG, this has important consequences, since many properties of the coatings are associated with it.

1.4 Layer growth in conventional zinc melt

If a steel component is hot-dip galvanized, it requires a long immersion time. This is in contrast to the continuous process, where the component is immersed shortly, and in which the alloy layer has to be kept very thin to enable the transformation into the final shape. For a discontinuously hot-dip galvanized steel member it is possible to produce alloy layers, which are much thicker. A thicker alloy layer is sometimes desired to provide a longer lifetime of the final product, with respect to corrosion protection.

Even more important for an alloy formation is the fact that the submerged object has to align itself to the bath temperature. Immersing a relatively cold, thick-walled, large profile results in a thin skin of molten zinc solidifying on the profile's surface. In order for the coating to be metallurgically bonded to the steel, the profile must reach the zinc bath temperature to remelt the solidified zinc. Thereafter, additional time is needed to develop an iron-zinc alloy formation by diffusion processes.

1.4.1 Steel composition

During immersion process in HDG, as a result of mutual diffusion of the liquid zinc melt with the iron of the steel sample, a coating of multiple different composed iron-zinc alloy layers is formed. Depending on the zinc coating, these layers are more or less pronounced. From outside to inside the η-, ζ-, δ_1- and Γ-phases are generated. They differ from each other, as shown in Table 4, not only in their iron or zinc concentration, but also in their different characteristics. A detailed overview is given in *Schulz et al. [3]* and *Horstmann et al* [7] also assembled the well-known iron-zinc state diagram, depending on the chemical composition and the temperature.

As described above, the dominant factor is the silicon content of the steel. Furthermore, the phosphor contained in the structural steel is at least partially attributable to a significant effect. According to studies by *Schubert et al.* [8] and *Katzung et al.* [9], a significant layer thickness-increasing influence of phosphorus is present, especially at low-silicon contents (below 0.03 %). As the silicon content increases, this influence of the phosphor on the zinc coatings decreases. Below 0.02 % phosphorus, the influence of phosphorus can be neglected in principle.

Table 4: Phases of an iron-zinc alloy layer

Phase	**Composition**	**Iron content [%]**	**Thermal resistant level [°C]**	**Crystal structure [°C]**	**Space group**
Eta (η)	Zn	0.08	419	Hexagonal (hcp)	$P6_3mc$
Zeta (ζ)	$FeZn_{13}$	6 – 6.2	530	Monoclinic	C2/m
Delta$_1$ (δ_1)	$FeZn_7$ / $FeZn_{10}$ / $Fe_{13}Zn_{126}$	7 – 11.5	620 – 630	Hexagonal (hcp)	$P6_3mc$
Gamma (Γ)	Fe_5Zn_{21}	21 – 28	670 – 700	Cubic (fcc / bcc)	F43m / I43m
Steel	Fe	100	1536	Cubic (bcc)	Im3m

The four steel categories, which are classified according to their silicon content, are described in further detail in the following Table 5.

Table 5: Classification of steel following DIN EN ISO 14713-2 [10]

Category	**Si- & P-content**	**Alloy formation**	**Typical Layer properties**
A **Low-silicon content steel ("killed" steel)**	Si ≤ 0.04 % and P < 0.02 % or Si + 2.5 P ≤ 0.09 %	Normal iron-zinc reaction. Low layer thickness.	Shiny appearance with a fine texture. The coating structure usually contains a pure zinc coating on top. Good resistance to mechanical damage.
B **Sebisty steel**	0.14 % < Si < 0.25 %	The Fe-Zn alloy can extend to the surface of the coating. The coating thickness increases with increasing silicon content.	
C **Sandelin steel**	0.04 % < Si ≤ 0.14 %	High reactivity. Very thick coatings can be generated.	Appearance can be dark or dull with a coarse texture. The coating structure is dominated by iron-zinc alloy layers, which often reach the surface.
D **High-silicon content steel**	Si > 0.25 %	The coating thickness increases with increasing silicon content. High alloy coating thickness.	

1.4.2 Structure and texture of Fe-Zn alloy layers

Normal zinc bath temperatures vary between 435 °C and 460 °C. In this research, the samples have been hot-dip galvanized in this range, at around 450 °C. Therefore, only the structure in this temperature range will be discussed in further detail below. Nevertheless, even in this small temperature range, the layer thickness of a coating is already very variable as shown in Figure 2. The phosphorus and especially silicon dependence, as it is noticeable for the microstructure, can be found again in the growing of zinc coating.

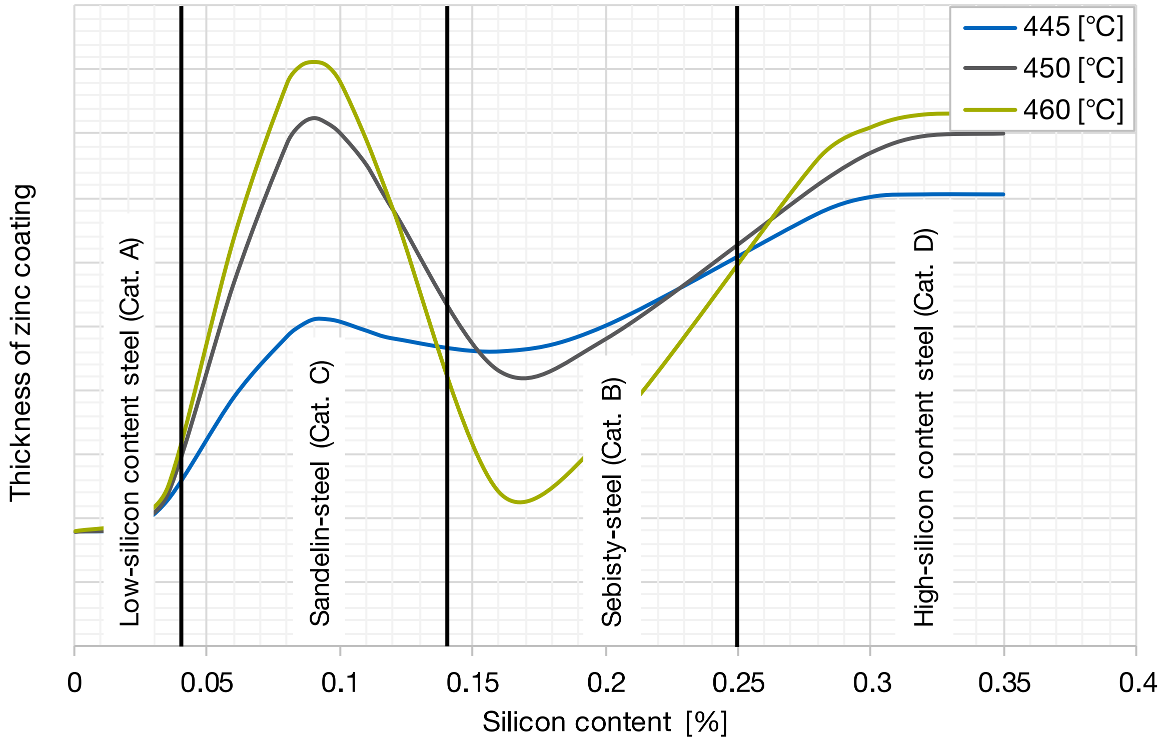

Figure 2: Schematic zinc coating thickness in dependence of the temperature and the silicon content of steel

1.4.2.1 Category A – Low-silicon content steel (< 0.04% Si)

On low-silicon steel – also known as 'killed' or 'rimmed' steel – a typical structure of a zinc coating forms. From the inside to the outside, a dense and relatively uniform δ_1-phase develops on the steel surface, consisting of a compact (δ_{1K}) and a palisades-shaped (δ_{1P}) layer. This phase is often separated from the steel substrate by a thin gap. It is followed by the ζ-phase, with its visible crystals and a narrow two-phase region to the outer pure zinc top-coating. This $\zeta + \eta$ two-phase region is characterized by floating ζ-crystals embedded in the pure zinc layer. The latter is the η-phase, generated by extracting the sample out of the zinc bath. An often shown Γ-phase, which is directly on the steel, forms distinctly after a longer galvanizing time and is therefore not visible on many micrographs *[3]*.

The self-developing fissure formation, between the steel substrate and the δ_1-phase, leads to the consequences that the atoms can no longer perfectly diffuse into each other and that the reaction rate drops sharply. As a result, the rate of growth collapses and it evolves a thin layer of pure zinc (η-phase) on the low-silicon steel.

1.4.2.2 Category C – Sandelin-steel (0.04 % to 0.14 % Si)

The alloy coating is much thicker compared to the low-silicon steel ('Sandelin effect'). By soothing with silicon, the steel substrate has a lack of a low-gas boundary layer of α-iron. Therefore, the compact δ_1-phase and the fissure cannot be developed at the beginning of the galvanizing process. The zinc layer structure consists almost exclusively of the ζ-phase. Only a very thin δ_1-phase with a thickness of 1 - 2 µm, in the immediate vicinity of the steel surface, is generated. The ζ-phase has tightly packed hard zinc crystals of a size of about 1 - 10 µm, which are embedded in solidified molten zinc and therefore shows a fine-crystalline, homogeneous structure.

1.4.2.3 Category B – Sebisty-steel (0.14 % to 0.25 % Si)

The sebisty-range has an exceptional position. It's high temperature-dependency does not allow to describe the layer growth only by the silicon content of the steel. The layer formation below and above 450 °C takes place according to different time laws or different mechanisms.

For galvanizing temperatures below 450 °C, a thick, fully alloyed zinc coating is formed with layer thicknesses above 200 µm. If present, the δ_1-phase is, with a range of about 5 – 10 µm, very thin. It is followed by the ζ-phase in which large, up to 100 µm long, palisaded crystals are present. These are oriented perpendicular to the steel surface and embedded in an approximately 1 % iron-containing zinc melt. Often, inter alia depending on the thickness of the immersed sample, a thin η-pure zinc coating forms on the outer layer.

At higher temperatures, above 450 °C until 470 - 480 °C, the growth rate of the alloy coating on the sebisty-steel is strongly reduced. The '*Sebisty-effect'* is described in more detail in *[3]*. The reduced growth rate leads to a compact δ_1-phase, which is approximately 25 µm thick, and thus to an external η-pure zinc layer. The in between ζ-phase then reveals densely packed ζ-crystals. The zinc coating on a steel in the sebisty-range thus assumes a similar structure, as it is known from low-silicon steel.

1.4.2.4 Category D – High-silicon content steel (> 0.25 % Si)

On steel samples with a high-silicon content, the reactions are fast and strong. Such coatings are characterized by the fact that they consist almost exclusively of the ζ-phase. Therefore, thicker coatings are formed. Adjacent on a 5 - 7 µm thick δ_1-phase, a thicker ζ-layer of hard zinc crystals embedded in an intergranular phase extends. The influence of the increase in temperature of the zinc bath from 445 °C to 460 °C manifests itself in contrast to the Sebisty steel in a continuous increase of the growth rate and, consequently, with an increasing layer thickness.

1.4.2.5 Texture of the Fe-Zn phases

The microstructure depends, as already mentioned, strongly on different variables. On the one hand, zinc coatings have a bright, slightly reflective, surface due to the presence of very smooth and reflective zinc flowers, but on the other hand they may have a dull appearance due to a high percentage of rough, poorly reflective zinc flowers. This affects not only the visual appearance, but also the surface reactivity (see *Seré et al.* [11]). Such a difference in reactivity suggests that bright and dull areas of the alloys coating also have different surface compositions and thus have a different heating behaviour. There is evidence in the literature that dull zinc spangles [12] contain more lead and aluminium than this is the case for bright zinc spangles.

The preferred crystallographic orientation depends mainly on external factors such as the cooling rate gradient, the surface state of the steel substrate during the coating solidification process, and as written above, the chemical composition of the bath [13]. Regarding the corrosion resistance of the zinc coatings, in particular a dependence on the chemical composition of the zinc coating could be found. The latter is additionally influenced by the crystallographic orientation.

Chang et al. [13] described that the crystallographic orientation (see Chapter 1.2) is related to the appearance of the zinc surface. Bright crystals are based on a basal texture. Therefore, planes, like (00.2), are parallel to the surface. Whereas matt appearing crystals have a crystallographic preference orientation of pyramidal (10.2) (10.3), (11.2), or prismatic planes (10.0) parallel to the surface. Consequently, the matte pyramidal crystal structure, in contrast to bright basal structures, leads to fewer reflections and thus appears darker. However, this not only deteriorates the appearance of the surface but also the corrosion resistance. In *Seré et al.* [11], a salt spray cabinet test of different specimens, with dull or bright crystals, was performed. While many corrosion products have formed on the matt crystal surface samples, with their (10.3) plane parallel to the surface, only a few residues appeared on the bright sample, with their (00.2) plane parallel to the surface.

It was therefore necessary in the course of the research to investigate the heating and thermal behaviour of the different surfaces and ascertain whether there is a dependence of the emissivity on the level of the texture.

1.5 Fire scenario and heat transfer

Once a fire ignites, a fire development with different phases occurs. A typical progress can be seen in Figure 3. The vertical axis represents the temperature, whereas the horizontal axis shows different phases of a complete fire. It begins with an ignition phase, passes into the smouldering phase and develops into a fully evolved fire. The transition is accompanied by a sudden ‘flash over’, which means that at this moment the room temperatures increase abruptly. After a certain development, accompanied by a continuous increase of temperature, a fire cools down. These phases vary in their characteristics in dependence of the fire. The intensity and duration of each phase is therefore influenced by several factors, for example: the fire load type, the fire load mass, and their distribution in the fire area.

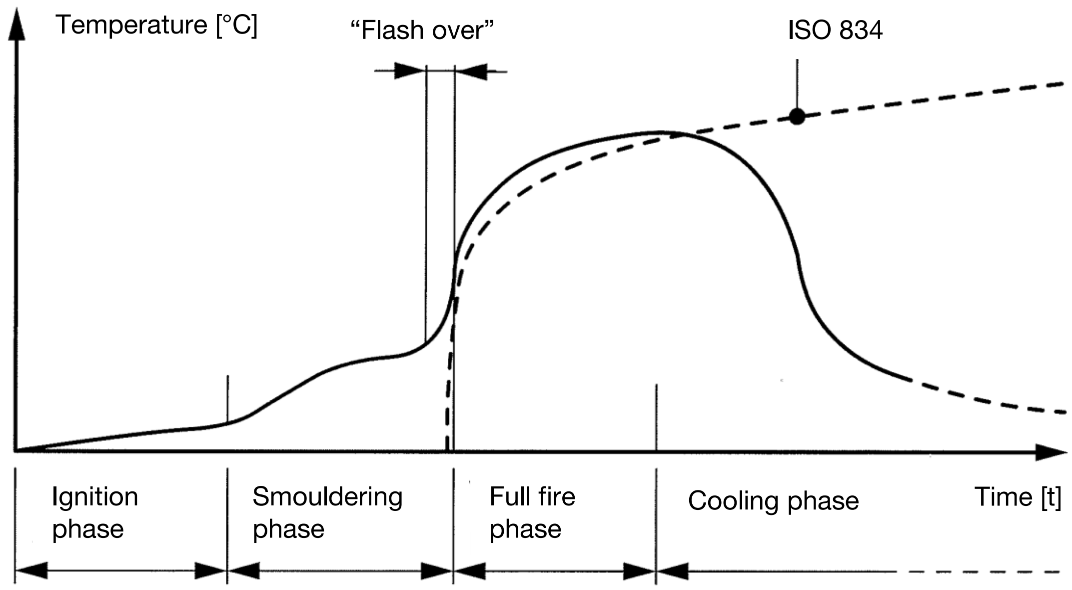

Figure 3: Fire development and standard temperature-time curve (ISO 834)

In order to create a uniform fire scenario for fire tests of building materials or components as a basis for fire investigations and structural fire design, different nominal temperature-time curves have been introduced as international standards. Theses curves corresponds to different types of fire scenarios. Besides other scenarios, there are two temperature-time curves, which can be used for structural fire design according to DIN EN 1991-1-2 [14]. The standard temperature-time curve (ISO 834), in accordance with DIN EN 1363-1 [15] and ISO 834-1 [16], represents such a normative fire. It begins shortly before the full fire phase and therefore rises rapidly in temperature (Figure 3). For example, after 30 minutes the chamber temperature rises up to 842 °C.

In addition, natural parametric temperature-time curves of natural fire models may be used, in dependence of national regulations, for structural fire design. Some parameters have to be known to calculate the fire development. For this purpose, for example, the ventilation, the fire load and the fire duration are taken into account. Due to national regulations, the ISO 834 is mainly used in Germany and is therefore the basis of the underlying thesis.

The exchange of heat energy between different objects depends on the actual objects' temperatures as well as the material properties of objects and the surrounding medium. During a fire, heat energy is distributed in three different ways: heat conduction, convection and heat radiation. Heat conduction distributes heat in the form of thermal energy through objects from higher temperature regions to lower temperature regions. Heat conduction therefore depends on the movement at molecular level and is a heat flow without additional macroscopic material flow. The second mechanism is convection. For this mechanism, heat energy is transported in the form of a material flow, for example a hot air stream. The last and most important mechanism for this research is the electromagnetic heat radiation. It will be discussed in further detail in Chapter 2. Both effects – heat conduction and convection – are part of the normative calculation in structural fire design according to DIN EN 1993-1-2 [17] and DIN EN 1994-1-2 [18]. This design procedure is shown in the next chapter.

1.6 Fire resistance of materials and buildings

1.6.1 Materials in fire

Building materials are assessed based on their influence during a fire, their composition and thus their flammability. Steel and concrete are non-flammable materials. However, even if they do not burn, their material properties change significantly with increasing temperature. From around 100 °C, for example, the modulus of elasticity of the steel begins to decrease and after around 400 °C the yield point decreases as well.

The following graphs in Figure 4 show the reduction factors for the stress-strain relationship of steel under the influence of elevated temperatures. The reduction factors are defined as follows according to DIN EN 1993-1-2 [17]:

- effective yield strength, relative to yield strength at 20 °C: $k_{y,\theta} = f_{y,\theta}/f_y$
- proportional limit, relative to yield strength at 20 °C: $k_{p,\theta} = f_{p,\theta}/f_y$
- slope of linear elastic range, relative to slope at 20 °C: $k_{E,\theta} = E_{a,\theta}/E_a$

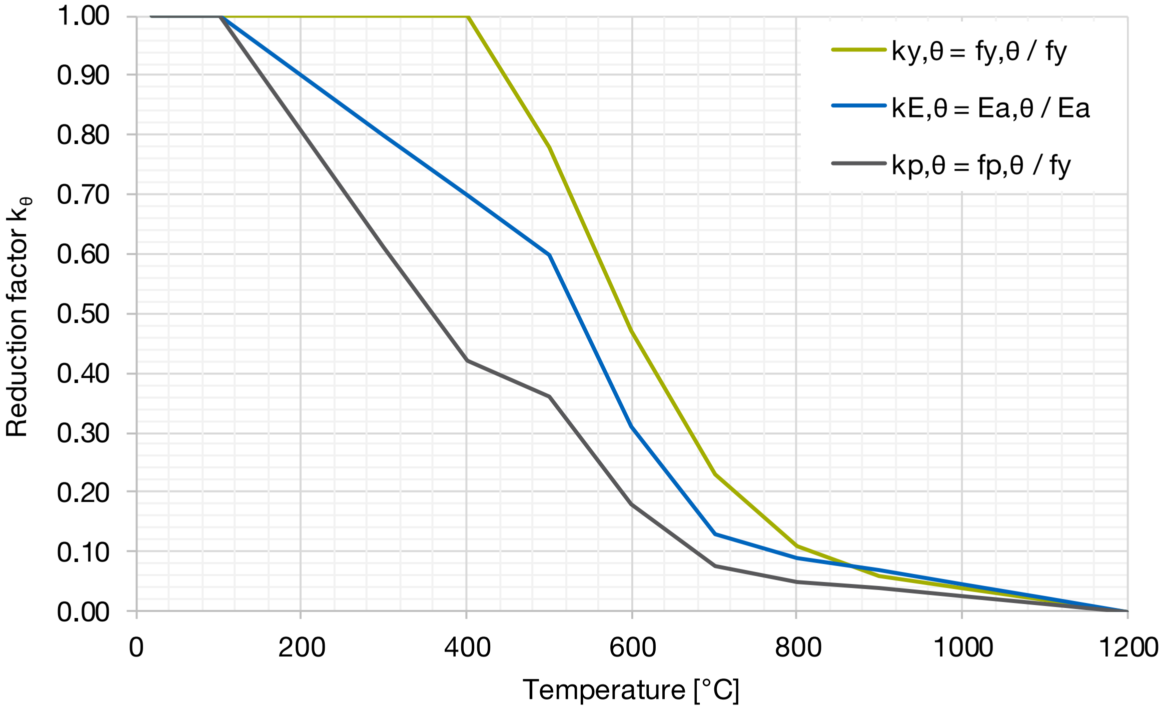

Figure 4: Reduction factors kθ for the stress-strain relationship for steel at elevated temperatures

In the event of a fire, components or supporting structures must retain certain functions over a specified fire duration. Some of these criteria can be found in DIN 13501-2 [19]. For load-bearing components, the following three criteria are of interest in the European classification system:

- R – Load-bearing capacity
- E – Integrity
- I – Insulation

1.6.2 **Fire resistance classification**

DIN EN 13501 [19] defines various fire resistance classes. In order to classify the fire resistance requirements, a distinction is made between *R30* / *R60* / *R90* and higher classes. These classifications are regulated in the different state building codes and the special construction regulations. These classes are defined depending, among other things, on the building class, the usage and the implemented fire protection measures, such as fire alarm systems, fire extinguishing systems or heat extraction systems. The respective fire resistance classes determine how long a building has to remain stable. Many office buildings in Germany, for example, can be classified in category *R30*. This corresponds to a requirement for the load-bearing capacity in the event of a fire of at least 30 minutes of a fire duration. Such proof can then be provided either by a mathematical verification or by certain tested building products.

1.7 **Structural fire design – DIN EN 1993-1-2**

Information about thermal actions and structural fire resistance are given in all parts ending with "-1-2" of the Eurocodes. They additionally contain design methods that allow a wider range of structural fire design for individual parts as well as for complete structures. For determination of fire resistance, the following analysis methods are permitted:

- simplified calculation models
- advanced calculation models
- fire tests

The simple calculation models are methods used for the fire design of individual members. They are based on some conservative assumptions. More accurate and economical evidence can be obtained by the advanced calculation models. The latter are therefore of more complex nature and can be applied for both – individual components as well as for partial structures. As they have an ease of use character, the simplified calculation models are the state of the art for civil engineering companies for analysis in structural fire design of individual components. In addition, in accordance with DIN EN 1993-1-2 [17], this method offers two analyse options for the dimensioning of steel components in case of fire:

- Verification of the design resistance $E_{fi,d,t} < R_{fi,d,t}$

The analysis is comparable to the standard procedure of the Eurocodes at ambient temperatures. The load-bearing behaviour of a steel member in the accidental load case of a fire should maintain a certain time period t. Therefore, it has to be proven that the design value of actions $E_{fi,d,t}$ for the fire design situation is at any time t not greater than the corresponding design resistance $R_{fi,d,t}$ of the steel member. The design effect of actions can be calculated as

$$E_{fi,d,t} = E_{fi,d} = \eta_{fi} \cdot E_d, \tag{1-1}$$

where E_d is the design value of loads, calculated according to DIN EN 1990 [20] and η_{fi} is a reduction factor. The latter can be calculated for design load in fire, according to [20], as follows and is shown in Figure 5 for some load categories.

$$\eta_{fi} = \frac{G_k + \psi_{fi} \cdot Q_{k,1}}{\gamma_G \cdot G_K + \gamma_{Q,1} \cdot Q_{k,1}}, \tag{1-2}$$

where

G_k is the characteristic value of the permanent action,

$Q_{k,1}$ is the characteristic value of the leading variable action 1,

ψ_{fi} is the combination factor of a variable action (in case of fire)

and

$\gamma_{Q,1}$ is the partial factor for variable action 1.

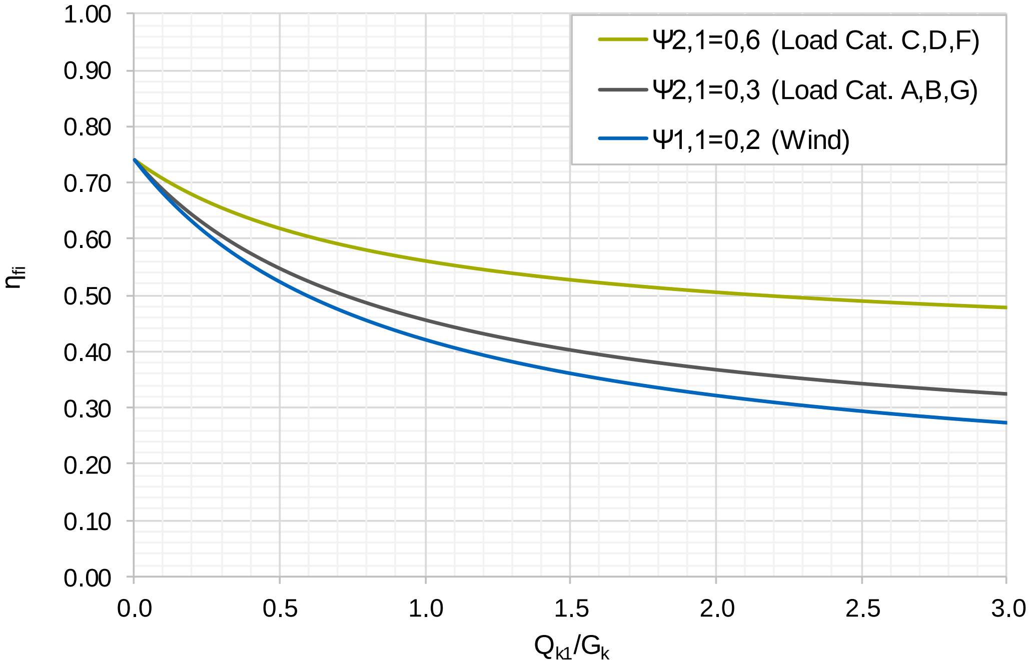

Figure 5: Reduction factor η_{fi} in dependence of the load ratio $Q_{k,1}/G_k$

- Verification of the critical temperature $\theta_{a,d} < \theta_{a,cr,d}$

In contrast to the first method, the verification can be carried out by the dedicated temperature of the member. At the appropriate time t, the temperature of the cross section $\theta_{a,d}$ has to be lower than the critical temperature $\theta_{a,cr,d}$. The latter is the temperature where, for example, the strength of carbon steel falls below the strength at which the limit state of the load capacity is undershot.

1.7.1 **Temperature development in the steel section**

The temperature increase $\Delta\theta_{a,t}$ in an unprotected steel cross section during a fire for the time interval Δt can be calculated according to DIN EN 1993-1-2 [17] with the following equation.

$$\Delta\theta_{a,t} = k_{sh} \frac{A_m/V}{c_a \rho_a} \dot{h}_{net}\, \Delta t \tag{1-3}$$

where

k_{sh}	is the correction factor for the shadow effect,
A_m/V	is the section factor for unprotected steel members [1/m],
A_m	is the surface area of the member [m²/m],
V	is the volume of the member [m³/m],
ρ_a	is the unit mass of steel [kg/m³],
c_a	is the specific heat of steel [J/kgK],
$\dot{h}_{net}$	is the design value of the net heat flux per unit area [W/m²]

and

Δt	is the time interval [sec].

1.7.2 **Net heat flux according to DIN EN 1993-1-2**

On the one hand, the heating behaviour of the cross section is strongly influenced by its geometrical parameters, for example by the section and on the other hand its mainly influenced by the net heat flux $\dot{h}_{net}$. In space, heat energy is transported, as described in Chapter 1.5, by convection and radiation. By combination, they provide the net heat flux in structural fire design:

$$\dot{h}_{net} = \dot{h}_{net,c} + \dot{h}_{net,r} \tag{1-4}$$

with

$$\dot{h}_{net,c} = \alpha_c(\theta_g - \theta_m) \tag{1-5}$$

and

$$\dot{h}_{net,r} = \phi \cdot \varepsilon_m \cdot \varepsilon_f \cdot \sigma \cdot \left[(\theta_g + 273)^4 - (\theta_m + 273)^4\right]. \tag{1-6}$$

where

$\dot{h}_{net}$	is the net heat flux,
$\dot{h}_{net,c}$	is the net convective heat flux component,
$\dot{h}_{net,r}$	is the net radiative heat flux component,
α_c	is the coefficient of heat transfer by convection [W/m²K],
θ_g	is the gas temperature in the fire compartment [°C],
θ_m	is the surface temperature of the member [°C],
ϕ	is the configuration factor,
ε_m	is the surface emissivity of the member,
ε_f	is the emissivity of the fire

and

σ	is the Stefan-Boltzmann constant (= 5.67×10^{-8} [W/(m²K⁴)])

A closer analysis (see Figure 6) of the two last equations (1-5) and (1-6) shows that the heating behaviour of a steel component is mainly influenced by the radiative part of the net heat flux. Equation (1-6) is in turn, inter alia, influenced by two emissivity values – ε_f and ε_m. This is the emissivity of the fire in the vicinity of the component, as well as the emissivity of the members' surface. Both factors have a major influence on the energy transfer by radiation. It thus holds strong interest if a smaller emissivity of galvanized steel has such a large influence that an *R30* fire protection requirement can be met without additional measures.

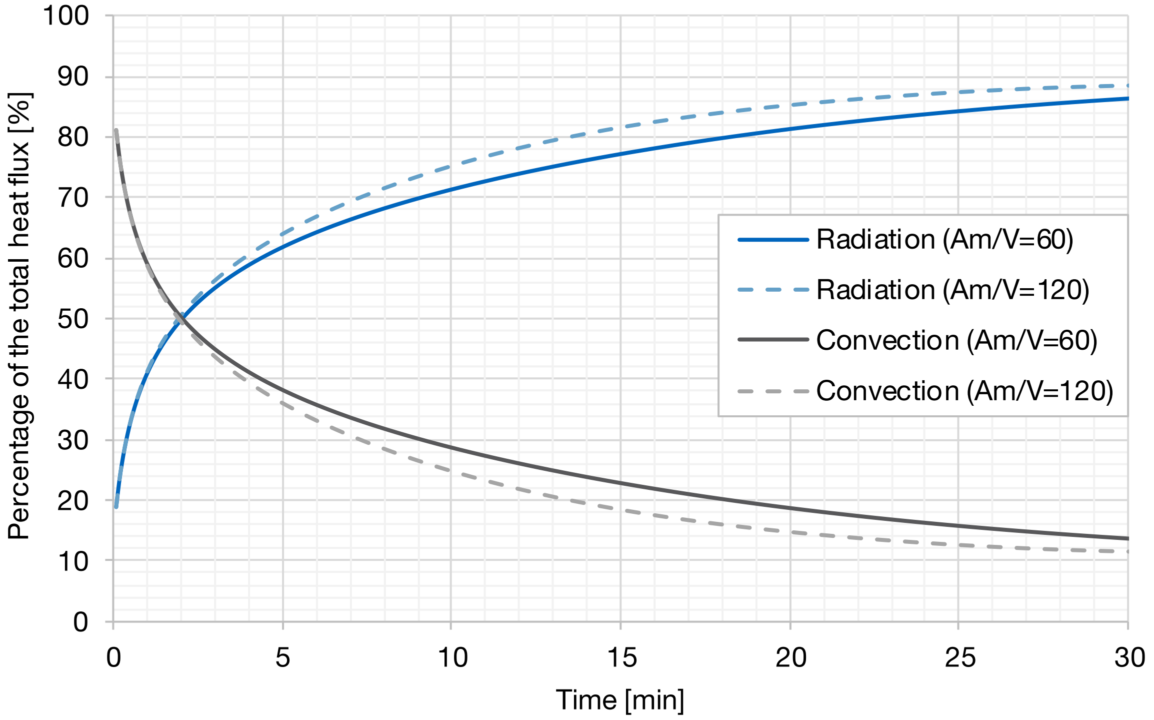

Figure 6: Ratio of radiation and convection of the total net heat flux

2 Heat transfer by radiation

The following chapter provides the basis for the analysis of heat radiation mechanisms and describes the different behaviour of objects for thermal impact by radiation. A special focus lies on metal bodies, respectively metal surfaces. The provided subsequent formulas will be used in Chapters 5, 6, 7 and 8 of this thesis.

2.1 Heat radiation

Thermal radiation is different from heat transfer by conduction and convection due to its basic physical laws. As already described in Chapter 1.5, the heat transfer by radiation is not bound to matter. Therefore, the emitted energy, which is transmitted by electromagnetic waves, can be spread out through vacuum. For materials with a temperature above absolute zero ($T = -273$ °C), an internal material energy results in a continuous emission of electromagnetic radiation.

In case of fire, one reason for the importance of temperature radiation is based in the dependence of the emitted radiation on the temperature itself. In contrast to the other two types of heat transfer – convection and conduction – in which the energy transfer between two points depends usually from the 1st power of each temperature, the energy exchange by electromagnetic radiation depends on the 4th power of the individual absolute temperatures between two bodies. The influence due to this fact can be seen in Figure 6. As shown for different section factors, radiation contributes the most energy in case of heat exchange.

While energy in heat transfer by conduction or convection is transported in physical mediums it is only dependent on the prevailing temperature gradient and the physical properties in the immediate vicinity of the interacting elements. The energy radiated by an object is of a more complex nature, since it is distributed differently among various parts of the electromagnetic spectrum. This wavelength dependence of the radiation has to be considered as well as its distribution in the different directions of space. In case of an energy exchange by radiation, the mathematically necessary equations become more complicated, although the required information is more varied and often not sufficiently available. These include, for example, the physical properties of the substance, the roughness of a surface, the purity of material, the thickness of coatings, the wavelength of radiation and the radiation angle.

The following section discusses these fundamental physical quantities needed to formulate the laws of thermal radiation and, based on this, to define the physical properties of real radiators that are important in this dissertation.

2.1.1 Radiation spectrum

Heat or thermal radiation depends on the material properties and on the temperature of the object. For a theoretical description of radiant energy, as well as its emission, transmission and absorption, two physical approaches are available: the classical theory of electromagnetic waves and the quantum theory. In the following, it is often referred to the wave theory, as it is widely spread in engineering, as well as in fire design of buildings (see *Siegel et al.* [21]).

Electromagnetic waves are transverse waves that oscillate biaxial perpendicular to the propagation direction. They expand in a straight line and reach the speed of light $c_0 = 299792458\,\mathrm{m/s}$ in a vacuum. Their velocity c in other mediums is accordingly slightly lower than c_0 while the associated frequency ν remains unchanged. The wavelength λ is related to the frequency ν by the following equation:

$$\lambda \cdot \nu = c \tag{2-1}$$

The electromagnetic spectrum covers a wide range of wavelengths, which, for example, includes light, x-rays as well as heat radiation (see Figure 7). They only differ in their wavelength. Thus, light is propagated in an electromagnetic wavelength spectrum of 0.35 to 0.75 µm, whereas heat is emitted in the wavelength range of about 0.01 to 1000 µm and therefore in the infrared range.

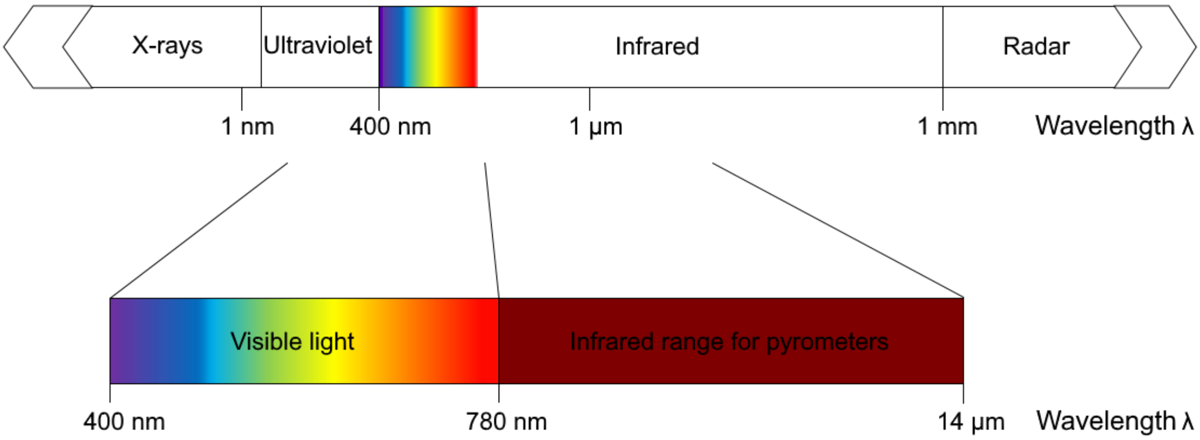

Figure 7: Electromagnetic spectrum

The infrared spectral range, which is used to measure the temperature, occupies only a very narrow section in the spectrum of electromagnetic wavelength. Due to *Wien's law* most infrared sensors work in the spectrum of 0.78 to 14 µm.

2.1.2 **Physical quantities of radiation**

However, temperature radiation depends not only on its wavelength, as described above, but also on the distribution respectively on the directions in space, especially for radiation exchange between different bodies. This multiple dependence leads to difficult quantitative description of thermal radiation, which cannot be described by only one parameter. Therefore, several types of physical radiation quantities – which differ in their depth of details – are needed:

- Directed spectral quantities: The directional and wavelength distribution of radiant energy can be described in a detailed manner. They are of a more complex nature and therefore more difficult to determine experimentally and theoretically, but are of fundamental importance to physical processes.

It is therefore desirable to use radiation quantities that capture only one effect, either the dependence on the wavelength or the directional dependence, such as:

- Hemispheric spectral quantities, which combine the radiation energy of all directions of the hemisphere over a surface element. They depend only on the wavelength.
- Directed overall quantities: The radiation energy of all wavelengths is summarized and describes only the dependence on the directions of the half space.
- Hemispheric total quantities: The radiation of all wavelengths and all directions is combined in one value. They do not convey any information about the spectral distribution and the directionality of the radiation. In most cases, this value is suitable and sufficiently accurately in science to describe heat transfer by radiation.

These four physical quantities and their combinations are treated for the specific cases of emissive power and the dedicated emissivity in radiation, which are needed to measure and calculate the heating behaviour of metal surfaces. For other physical parameters, like absorption or reflection, the exact definitions and equations are omitted. Detailed information can be found, inter alia, in *Baehr et al.* [22].

2.2 Black body

By introducing an ideal radiator, a so-called black body, the interaction of the impinging radiant energy with a surface can be explained in further detail and delivers the basis for further considerations. However, this interaction is not only a result of individual surface properties, but also of the material's property beneath the considered surface.

In reality, if radiation impinge on a homogeneous body, one part will be reflected and another part will penetrate the surface and consequently enter the object. Radiation can then be completely or only partially absorbed – depending on the property of the material. If it has a strong absorbing effect, which is for example provided by metals, like the underlying specimens, the impinged radiation energy is absorbed in a very thin layer underneath the surface. A good absorber must have a low reflectance on its surface and a high degree of absorption inside the body. By contrast, in low-absorbing materials, the unreflected radiation can penetrate the body almost unhindered. Non-metals can have an exactly opposite tendency.

In contrast, a black body is defined as a body in which all incident radiation can penetrate the surface, no energy is reflected, and all of the impinging radiation is completely absorbed inside. Consequently, no energy is transmitted through the object. This applies to radiation of all wavelengths and angles of incidence. The black body is therefore an ideal absorber. Physically, such a body does not exist and cannot be produced. However, such a construct can be approximated. Nonetheless, the idea of a black body serves as a basis for the processes of radiation and the associated energy exchange. Since it is considered to be the ideal absorber with a maximum degree of absorption, real surfaces can be compared to the black body. In reality, only a few surfaces come close to these regions of ideal absorption, such as soot, platinum black or 3M-black [21]. As an approximation, some holes with specific properties fulfil the same characteristics (see Chapter 5.1).

In addition, a black body has not only the property to absorb the maximum possible impinging energy, it also emits the maximum possible radiation at each wavelength and each direction.

2.3 Relationship between emissivity, absorption and reflectivity

Since in reality there is no ideal black body and thus no pure absorption, part of the incident radiation is reflected and a part is also transmitted. Consequently, when a radiation reaches a real body, reflection, absorption and transmission always take place together:

$$\alpha + \rho + \tau = 1, \tag{2-2}$$

where

α is the degree of absorption,

ρ is the degree of reflection

and

τ is the degree of transmission.

A body absorbs and emits at the same time. Between the absorption and emissivity of a body exist thermodynamic relationships. *Kirchhoff's law* [23] states that for a given wavelength interval a body, in thermal equilibrium, emits as much radiation power as it absorbs from radiation of a black body. As a simplification, it follows:

A good absorber is also a good emitter.

According to *Kirchhoff*, emissivity can be assigned to absorptivity:

$$\alpha = \varepsilon \tag{2-3}$$

Furthermore, for opaque bodies, as they are the basis of this work, the transmittance τ can be set to zero, since no transmission takes place in thicker metal specimens. Equation (2-2) can thus be simplified to:

$$\varepsilon + \rho = 1 \tag{2-4}$$

2.4 Emittance

Thermal radiation is based on internal energy. This internal energy transforms into heat energy or heat radiation and is emitted by a body, as described above, through electromagnetic waves. Based on quantum theory, the energy is dissipated by photons that emerge on the surface of the emitting body. In such processes, molecules or atoms shift from a higher energy state to a lower energy state.

Any kind of matter, regardless of its state of aggregation, emits heat radiation. In solids as they are the basis of this work, radiation that is emitted by inner atoms and molecules is usually strongly absorbed by its neighbouring molecules. In this case they cannot reach the surface of the body and can therefore not emit the energy into the environment. Consequently, the thermal radiation generally only originates from the molecules in a very thin outer layer, directly below the surface. The thickness given in literature of this layer, depending on the material, is only about one micron to a few microns (see [22]). Due to this minimal thickness, the emission can be assigned to the surface.

Regarding processes in fire tests or ‘free’ fires, it should be noted that for gases the radiation emanating from a finite volume is the summary of local emissions within the considered volume.

2.4.1 **Emissive power**

For an area $dA,$ of an emitting object, the corresponding heat or energy flow $d\Phi$ can be assigned. This energy flow is the radiative power, emitted into the half space (hemisphere) from the area dA. Hence, taking both parameters into relation, the (hemispherical) emissive power E, with its temperature dependency, can be described as:

$$E = E(T) = \frac{d\Phi}{dA}\left[\frac{W}{m^2}\right]. \tag{2-5}$$

2.4.2 **Spectral intensity**

To investigate the detailed distribution of the radiative power $d\Phi$ over the wavelength spectrum, as well as over the direction in the half space, the spectral intensity I_λ was introduced in science. A certain direction in the hemisphere is defined by two angle coordinates ϑ and φ. In this case, as it can be seen in the following Figure 8, φ is the azimuth angle and ϑ is the zenith or polar angle measured from the surface normal.

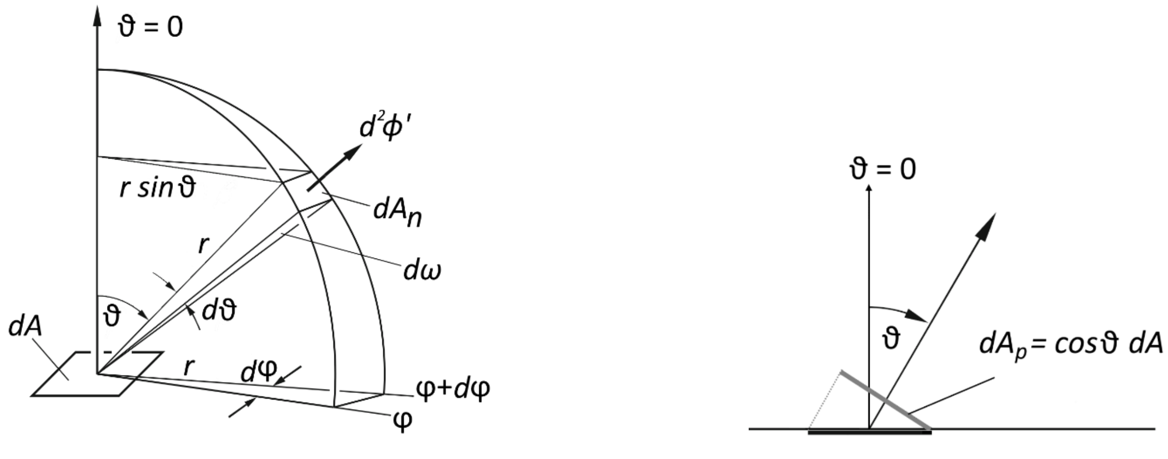

Figure 8: Radiative flux $d^2\Phi'$ in to a solid angle element (left); lateral view of dA_p, corresponding to the surface element dA, perpendicular to the radiation direction (right)

With respect to Figure 8, the solid angle element $d\omega$, which characterizes the content of a conical spatial section, is closely connected to the area dA_n and the two angles ϑ and φ. Therefore, the following mathematical relationship is obtained for the solid angle element:

$$d\omega = \frac{dA_n}{r^2} = \frac{r\, d\vartheta \cdot r\, sin\vartheta\, d\varphi}{r^2} = sin\vartheta\, d\vartheta\, d\varphi \tag{2-6}$$

A radiative flux which an area dA emits into a solid angle, and which contains only the part of the radiative flux which is emitted in a defined wavelength range or an explicit wavelength λ, is referred to as $d^3\Phi$. This radiated energy is directional- and wavelength-dependent. Linked to the spectral intensity I_λ, it is defined by the following equation:

$$d^3\Phi = I_\lambda(\lambda, \vartheta, \varphi, T) \cos\vartheta\, d\omega\ \ d\lambda\, dA \tag{2-7}$$

Furthermore, there is a temperature dependence of the spectral intensity, as it is indicated by the arguments of $I_\lambda(\lambda, \vartheta, \varphi, T)$. Thus, the temperature of the body as well as its material or surface properties are included. In contrast to the emissive power $E(T)$, the spectral radiance is not related to the size dA of the surface element, but, as it can be seen in Figure 8, to its projection $dA_p\ =\ \cos\vartheta\, dA$ perpendicular to the radiation direction. As a consequence, the radiation is set to zero for an angle of $\vartheta = \pm\pi/2$ and reaches its maximum for an angle of ϑ = 0 and, therefore, at the surface normal.

2.4.3 **Hemispherical spectral emissive power and radiant intensity**

It is a difficult task, to determine the different parameters of $I_\lambda(\lambda, \vartheta, \varphi, T)$ theoretically and experimentally for all materials. In the field of engineering, as well as for other purposes, it is widely common that this detailed approach, with its directionality and wavelength dependence, is not used. As shown in Chapter 2.2, quantities that summarize the emission, for example, across all directions in half space or over all wavelengths are mostly taken into account. Such an approach is done in the following for the spectral specific emissive power E_λ and the radiative intensity I.

By integrating the spectral radiance $d^3\Phi$, from Equation (2-7), over all solid angles of the hemisphere one obtains the spectral specific emissive power $E_\lambda(\lambda, T)$ of an object. This is associated with the radiant flux $d^2\Phi$, which is send out by the area element dA in the wavelength interval $d\lambda$ into the hemisphere.

$$d^2\Phi = E_\lambda(\lambda, T)\, d\lambda\, dA \tag{2-8}$$

with

$$E_\lambda(\lambda, T) = \int_{\frown} I_\lambda(\lambda, \vartheta, \varphi, T) \cos\vartheta \, d\omega. \tag{2-9}$$

The integration over all solid angles of the entire hemisphere is done by a double integration over the two angles ϑ and φ. By implementing Equation (2-6) one obtains

$$E_\lambda(\lambda, T) = \int_{\varphi=0}^{2\pi} \int_{\vartheta=0}^{\pi/2} I_\lambda(\lambda, \vartheta, \varphi, T) \cos\vartheta \sin\vartheta \, d\vartheta \, d\varphi \,, \tag{2-10}$$

which can be more simplified, due to the fact that the spectral radiative intensity I_λ depends generally not on the azimuth angle φ but only on the polar angle ϑ (see [21,24]):

$$E_\lambda(\lambda, T) = \int_0^{\pi/2} I_\lambda(\lambda, \vartheta, T) \cos\vartheta \sin\vartheta \, d\vartheta. \tag{2-11}$$

From this hemispheric spectral variable $E_\lambda(\lambda, T)$, with the SI unit $[W/m^2\mu m]$, the wavelength distribution of the specific emissive power can be identified. By an additional integration of the radiant flux $d^2\Phi$ over all wavelengths, $d\phi$ can be assigned as

$$d\Phi = \int_0^\infty E_\lambda(\lambda, T) \, d\lambda \, dA, \tag{2-12}$$

and with Equation (2-5) therefore the emissive power can be described as

$$E(T) = \int_0^\infty E_\lambda(\lambda, T) d\lambda. \tag{2-13}$$

By contrast, the directional distribution of the radiative intensity integrated over all wavelengths, is described by the spectral intensity $I_\lambda(\vartheta, \varphi, T)$. By integrating Equation (2-4) over the wavelength λ this gives the radiative flux $d^2\Phi'$, which the surface element emits in the direction of the solid angle element $d\omega$:

$$d^2\Phi' = I(\vartheta, \varphi, T) \cos\vartheta \, d\omega \, dA, \tag{2-14}$$

with

$$I(\vartheta, \varphi, T) = \int_0^\infty I_\lambda(\lambda, \vartheta, \varphi, T) d\lambda. \tag{2-15}$$

If one integrates $d^2\Phi'$ over all angles of the hemisphere, one obtains the radiation flux $d\Phi$, which a corresponding surface element dA emits into the complete hemisphere. This can be seen in following equation:

$$d\Phi = \int_{\frown} I(\vartheta, \varphi, T) \cos\vartheta \, d\omega \, dA. \tag{2-16}$$

Applying Equation (2-5) one can calculate the emissive power $E(T)$ from the total intensity $I(\vartheta, \varphi, T)$:

$$E(T) = \int_{\frown} I(\vartheta, \varphi, T) \cos\vartheta \, d\omega. \tag{2-17}$$

2.4.4 **Summarize – radiative quantities**

The following paragraph gives a short overview of the derived equations to set each physical quantity into relation, as these connections between the physical quantities are important for the underlying analysis. As described at the beginning of this chapter, a radiation emitted from a surface element can be evolved in further detail by four, mutually dependent, radiation quantities:

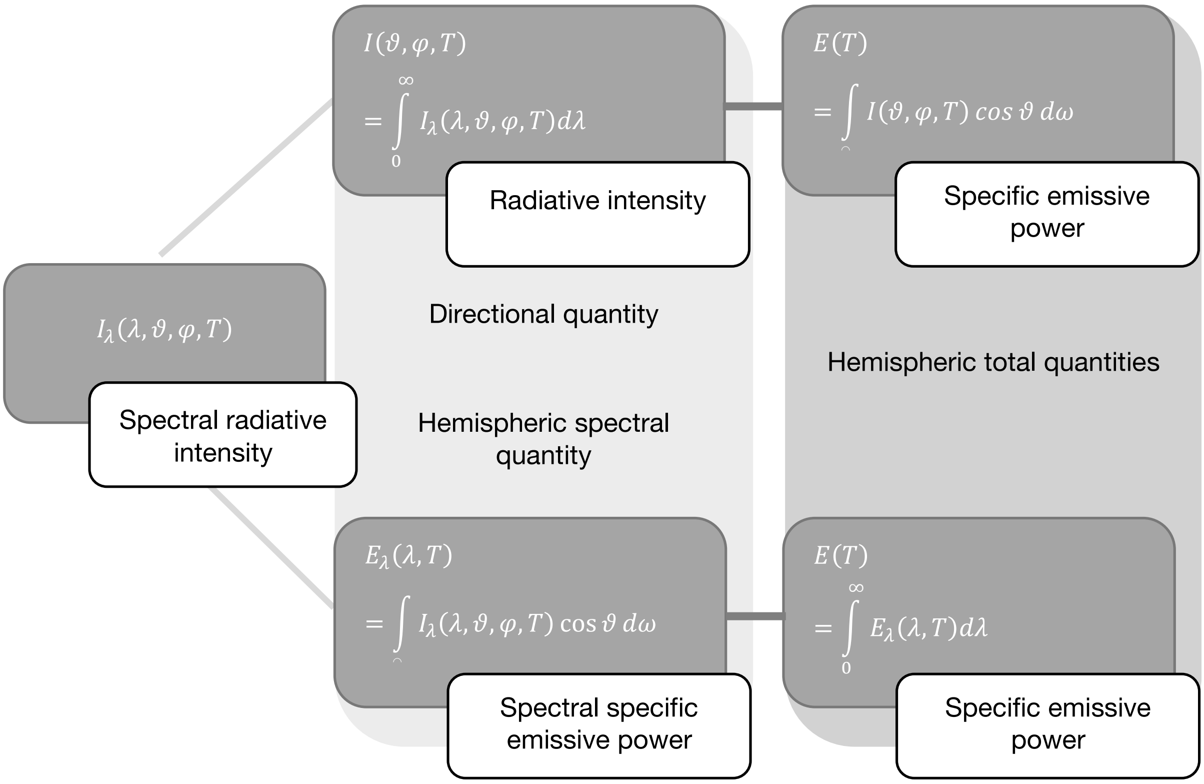

Figure 9: Overview of radiation quantities

The physical output quantity is the directional spectral quantity and thus the spectral radiative intensity $I_\lambda(\lambda, \vartheta, \varphi, T)$. It describes the distribution of the emitted radiative flux on the spectrum of the wavelengths and the solid angles of the hemisphere. In addition, all other radiation parameters originate of this. By integration over the solid angles of the hemisphere one obtains the spectral specific emissive power $E_\lambda(\lambda, T)$. This includes the wavelength dependence of the energy radiated into the whole half space. After re-integration over all wavelengths, one obtains the specific emissive power $E(T)$, which includes the emitted radiation flux over all wavelengths and in the entire hemisphere.

Integrating the spectral radiative intensity $I_\lambda(\lambda, \vartheta, \varphi, T)$ over all wavelengths leads to the radiative intensity $I(\vartheta, \varphi, T)$, a directed total size describing the emitted energy distribution to the solid angles of the hemisphere at all wavelengths. By an additional integration over the entire solid angles, the result is again the specific emissive power $E(T)$.

2.5 **Radiating bodies**

2.5.1 **Diffuse radiator – Lambert's cosine law**

A real body with a wavelength-independent, spectral radiative intensity I_λ does not exist. In contrast, the assumption that the spectral radiance I_λ does not depend on the solid angles ϑ and φ leads in many cases to good approximations. The spectral radiance is then considered to be directional independent intensity $I_\lambda = I_\lambda(\lambda, T)$. Such a body is called a diffuse radiator. According to (2-10) the spectral specific emissive power follows as

$$E_\lambda(\lambda, T) = I_\lambda(\lambda, T) \int_{\varphi=0}^{2\pi} \int_{\vartheta=0}^{\pi/2} \cos\vartheta \sin\vartheta \, d\vartheta \, d\varphi, \tag{2-18}$$

leading, after the double integration, to the subsequent relation between the spectral emissive power and the spectral intensity

$$E_\lambda(\lambda, T) = \pi \, I_\lambda(\lambda, T). \tag{2-19}$$

Considering also the independence of radiative intensity I of both solid angles one obtains from (2-14).

$$d^2\Phi' = I(T) \cos\vartheta \, d\omega \, dA \tag{2-20}$$

and consequently

$$E(T) = I(T) \int_{\frown} \cos\vartheta \, d\omega = \pi \, I(T). \tag{2-21}$$

This relationship is referred to as *Lambert's cosine law*, which can be seen in Figure 10. Where the distribution of the intensity is independent of the angle ϑ and the directional emissive power decreases (in dependence of $\cos\vartheta$) with an increasing angle of ϑ.

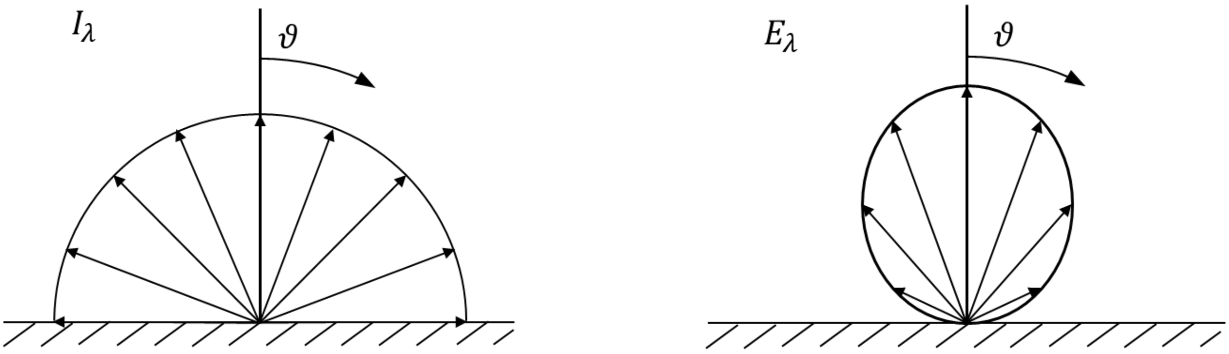

Figure 10: Angular distribution of intensity I_λ (independent of ϑ) and directional emissive power E_λ (dependent on ϑ)

2.5.2 **Black body radiator**

A black body absorbs any incident radiation. No radiation is reflected or penetrates it. As can be seen by the spectral radiance $I_{\lambda b}(\lambda, T)$ of the black radiator, it is independent of the direction and can thus be regarded as a diffuse radiator (see Chapter 2.5.1), depending on the wavelength and the temperature. Based on Equation (2-17), its spectral specific emissive power $E_{\lambda b}(\lambda, T)$ is related to the spectral intensity $I_{\lambda b}(\lambda, T)$ by the following equation

$$E_{\lambda b}(\lambda, T) = \pi \, I_{\lambda b}(\lambda, T). \qquad \text{(2-22)}$$

In 1900 *Planck* describes, by various assumptions, the law of spectral radiance of a black body. The spectral specific emissive power of a black body follows this equation, which is known as *Planck's law*:

$$E_{\lambda b}(\lambda, T) = \pi \, I_{\lambda b}(\lambda, T) = \frac{c_1}{\lambda^5 e^{(c_2/\lambda T - 1)}}, \qquad \text{(2-23)}$$

with

$$c_1 = 2\pi h c_0^2 = (3.74177107 \pm 0.00000029) \cdot 10^{-16} \, [W m^2] \qquad \text{(2-24)}$$

and

$$c_2 = \frac{h c_0}{k} = (14387.752 \pm 0.024) \, [\mu m \, K]. \qquad \text{(2-25)}$$

Equation (2-23) is based on two radiation constants c_1 and c_2, which in turn follow fundamental natural constants: the speed of light c_0 in vacuum, the Planck constant h, and the Boltzmann constant k.

Planck's *law* is shown for some isotherms in Figure 11. The curves of the different isotherms are similar, but do not intersect each other (except at λ = 0). All have a very low radiation at wavelengths $\lambda \approx 0$, but increase rapidly with increasing wavelength λ and fall off after reaching their maximum. For wavelengths $\lambda \to \infty$, the limit value of the spectral emissive power approaches the asymptote of $E_{\lambda,b} = 0$.

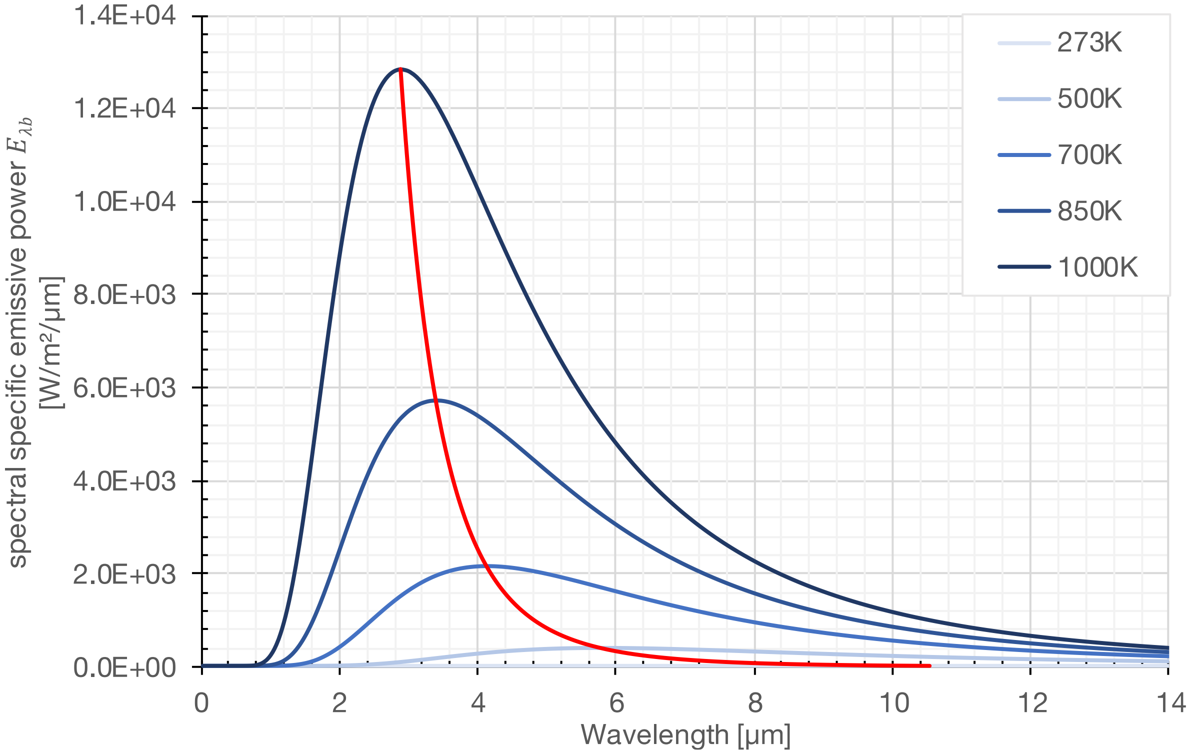

Figure 11: Spectral emissive power $E_{\lambda b}$ in dependence of the wavelength

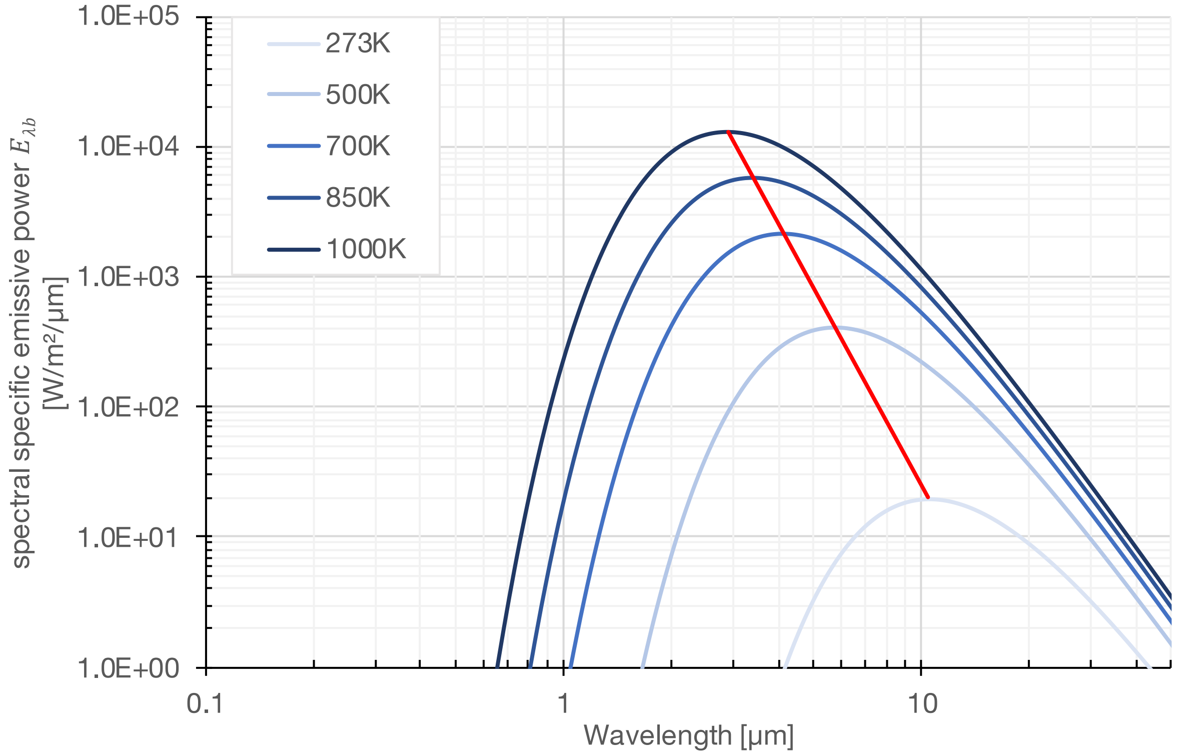

Figure 12: Spectral emissive power $E_{\lambda b}$ in dependence of the wavelength (logarithmic scale)

At each wavelength, the intensity of radiation increases with increasing temperature, accompanied by the characteristic shift of the maximum to small wavelengths. The maximum value of the emissive power $E_{\lambda b}(\lambda_{max},T)$ increases therefore rapidly with the dedicated temperature T. The law of this maxima-shift is also called *Wien's law* or *Wien's displacement law* (shown in Figure 11 in red). In the logarithmic scale (Figure 12), a linear relationship arises between the different maxima of the individual temperature isotherms. It can be seen that at elevated temperatures only some of the specific radiation is emitted in the spectrum of the visible light, which reaches from 0.40 µm to 0.75 µm. The temperature where our eyes can see bodies in dark surroundings is 798 K, respectively 525 °C. This point is called *Draper Point*. Such objects, like in this thesis hot steel samples, will first appear red.

The position of the different isotherm maxima on the *Wien's displacement line* can be calculated from the first deviation of $E_{\lambda b}$:

$$\frac{\partial E_{\lambda b}}{\partial \lambda} = 0, \tag{2-26}$$

resulting in the transcendental equation

$$\left(1 - \frac{c_2}{5\lambda T}\right) e^{(c_2/\lambda T)} = 1, \tag{2-27}$$

with the dedicated solution

$$\frac{c_2}{\lambda_{max} T} = 4.96511423, \tag{2-28}$$

or further converted

$$\lambda_{max} T = (2897.7686 \pm 0.0048)\ [\mu m K]. \tag{2-29}$$

As a simplification, the maximum wavelength at a specific temperature can be consequently given by the following equation

$$\lambda_{max} = \frac{2897.8}{T}\ [\mu m] \tag{2-30}$$

All observations made above apply to the radiation of a black body in vacuum. However, radiation in a medium behaves differently. For example, due to the reduced propagation velocity. This is called the refractive index n of the medium, which is then greater than one. However, refractive indices of the air or other gases are very close to one, which in turn is the reason why the change from exposure to vacuum is generally neglected [22].

2.5.3 **Specific emissive power in a defined spectrum**

The specific emissive power $E_b(T)$ of a black body is obtained by integrating $E_{\lambda b}(\lambda, T)$ over all wavelengths as it corresponds to the total area under the isotherms of Figure 11 and Figure 12. Further transformations and the use of dimensionless quantities (see [21,22,24]) lead to the *Stefan-Boltzmann law*, with the *Stefan-Boltzmann constant* σ:

$$E_b(T) = \int_0^\infty E_{\lambda b}(\lambda, T)\, d\lambda = \int_0^\infty \pi\, I_{\lambda b}(\lambda, T)\, d\lambda = \sigma\, T^4, \tag{2-31}$$

with

$$\sigma = \frac{c_1}{c_2^4}\frac{\pi}{15} = \frac{2\pi^5 k^4}{15\, c_0^2 h^3} = (5.670400 \pm 0.000040) \cdot 10^{-8} \frac{W}{m^2 K^4}. \tag{2-32}$$

In case of this dissertation (see Chapter 5.4) it is required to compute a specific emission in a given wavelength interval to calculate the emissivity of the specimens from the measured data. In order to calculate this, a ratio function $F(\lambda_1, \lambda_2)$ is necessary in which the two wavelengths λ_1 and λ_2 define the limits:

$$F(\lambda_1, \lambda_2) = \frac{\int_{\lambda_1}^{\lambda_2} E_{\lambda b}(\lambda, T) d\lambda}{\int_0^\infty E_{\lambda b}(\lambda, T) d\lambda} = \frac{1}{\sigma\, T^4} \int_{\lambda_1}^{\lambda_2} E_{\lambda b}(\lambda, T) d\lambda. \tag{2-33}$$

Equation (2-31) can be inserted in (2-33) and subsequently

$$F(\lambda_1, \lambda_2) = \frac{1}{\sigma\, T^4} \int_0^{\lambda_2} E_{\lambda b}(\lambda, T) d\lambda - \frac{1}{\sigma\, T^4} \int_0^{\lambda_1} E_{\lambda b}(\lambda, T) d\lambda \tag{2-34}$$

follows.

In addition, it is possible to evaluate the wavelength range in which a body emits its energy significantly. This can be determined by the ratio

$$\frac{E(T)}{E_b(T)} = \frac{\int_0^\lambda E_\lambda(\lambda, T)\, d\lambda}{\sigma\, T^4} \tag{2-35}$$

Consequently, it is possible to determine the proportion of the radiation from the total radiation emitted by a body in the wavelength interval from 0 to λ. This can be visualised more precisely by cumulative distribution curves. It can be clearly seen that, for example, the energy for the underlying research, in the temperature range from 0 °C (273 K) to 750 °C (1023 K), is transmitted at wavelength of 1 to 16 µm. Predominantly, at least for elevated temperatures, its radiated at smaller wavelengths.

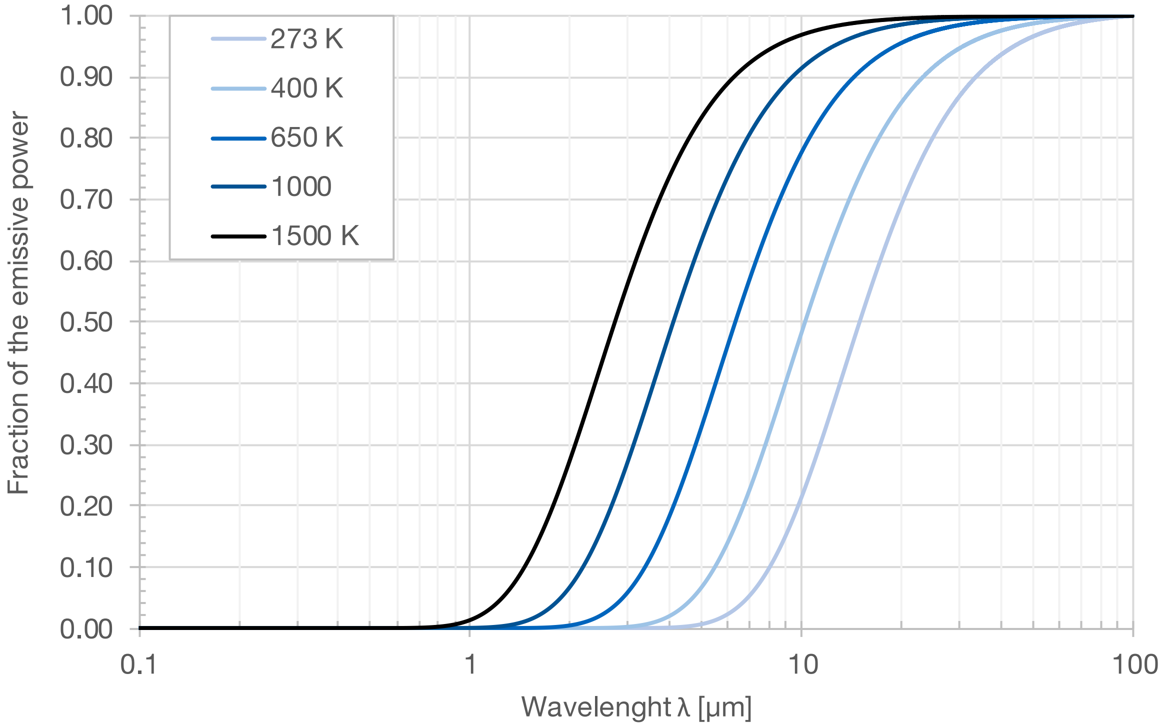

Figure 13: Spectral cumulative distribution of heat radiation energy

2.5.4 **Emissivity & Radiation of real bodies**

After the preceding explanation of the theory, the following section deals with the radiation properties of real bodies. Since real materials or real bodies have no physical ideal properties they differ in terms of radiation. In order to detect this deviation, different emissivity quantities have been introduced in science, which are explained in more detail below. As already mentioned at the beginning of Chapter 2, the following consideration underlie the electromagnetic theory of radiation.

The emissivity was introduced in physics in order to compare the radiation of real bodies to a black body at the same temperature. According to *Kirchhoff*, a black body radiates in any direction and at any wavelength the maximum possible radiation energy. In addition, as shown in Chapter 2.1.2, some radiation quantities are given to describe the exact behaviour of a black body. Therefore, the emissivity has to be linked to each of these four maximum radiation quantities of the hemisphere to reference a real body. Four different emissivity values can be assigned, which correspond to a dimensionless ratio and thus a material property of each body. For each applies:

$$\varepsilon \leq 1, \tag{2-36}$$

although the value ‘1’ can only be approximated by real bodies, as it is the maximum energy radiated by a black body. An overview of the definitions of the four emissivities is given in Table 6, based on the four radiance quantities of Chapter 2.1.2. Beginning with the directional spectral emissivity $\varepsilon_\lambda(\lambda,\vartheta,T)$, the other three values can be calculated.

Table 6: Different emissivity quantities

Directional spectral emissivity	
$\varepsilon_\lambda(\lambda,\vartheta,T) = \dfrac{I_\lambda(\lambda,\vartheta,T)}{I_{\lambda b}(\lambda,T)}$	*(2-37)*
Hemispherical spectral emissivity	
$\varepsilon_\lambda(\lambda,T) = \dfrac{E_\lambda(\lambda,T)}{E_{\lambda b}(\lambda,T)}$	*(2-38)*
$\varepsilon_\lambda(\lambda,T) = \dfrac{1}{\pi}\int_{\frown} \varepsilon_\lambda(\lambda,\vartheta,T)\cos\vartheta\, d\omega$	*(2-39)*
Directional total emissivity	
$\varepsilon(\vartheta,\varphi,T) = \dfrac{I(\vartheta,\varphi,T)}{I_b(T)} = \dfrac{\pi}{\sigma T^4} I(\vartheta,\varphi,T)$	*(2-40)*
$\varepsilon(\vartheta,\varphi,T) = \dfrac{1}{I_b(T)}\int_0^\infty \varepsilon_\lambda(\lambda,\vartheta,\varphi,T)\, I_{\lambda b}(\lambda,T)\, d\lambda$	*(2-41)*
Hemispherical total emissivity	
$\varepsilon(T) = \dfrac{E(T)}{E_b(T)} = \dfrac{E(T)}{\sigma T^4}$	*(2-42)*
$\varepsilon(T) = \dfrac{1}{E_b(T)}\int_0^\infty \varepsilon_\lambda(\lambda,T)\, E_{\lambda b}(\lambda,T)\, d\lambda = \dfrac{1}{\pi}\int_{\frown} \varepsilon(\vartheta,\varphi,T)\cos\vartheta\, d\omega$	*(2-43)*

$\varepsilon_\lambda(\lambda,\vartheta,T)$ characterize the directional and wavelength distribution of the emitted radiance by the ratio of the spectral radiative intensity of the body I_λ with the intensity of a black body $I_{\lambda b}$.

$\varepsilon_\lambda(\lambda,T)$ determines the wavelength dependence of the emitted radiation in the hemisphere by the ratio of the spectral specific emissive power E_λ of a real body to the black body $E_{\lambda b}$.

$\varepsilon(\vartheta,\varphi,T)$ specifies the direction (ϑ,φ) of the intensity over all wavelength. (The term “total” denotes that radiation of the whole spectrum is included).

$\varepsilon(T)$ represents the average emissivity over the wavelength and the direction. $\varepsilon(T)$ compares therefore the specific emissive power $E(T)$ of the real body with the emissive power of the black body $E_b(T)$ at the same temperature. In research or science, as well as in the following of this dissertation, $\varepsilon(T)$ is often referred to as the emissivity of a body.

Several physical quantities of real bodies can be derived from these relationships. The spectral specific emissive power E_λ of a real body can thus be calculated with the help of the emissivity ε_λ from the spectral specific quantity $E_{\lambda b}$ of the black body as follows:

$$E_\lambda(\lambda, T) = \varepsilon_\lambda(\lambda, T) E_{\lambda b}(\lambda, T) \tag{2-44}$$

As indicated by the index 'λ', the ratio depends on the wavelength and can be therefore different for every point in the spectrum.

In dependence of their behaviour, real objects can be separated into the following two categories:

- **Grey radiator**

A *Lambert radiator*, as shown in Chapter 2.5.1, is a body with a directional emissivity, thus radiating diffuse, which means evenly in all directions. In contrast, a *grey body* is, by definition, a radiator whose emissivity is the same for all wavelengths. Both cases provide simplifications for the important radiation calculations. Real bodies can thus be considered approximately as diffuse emitters and grey bodies. This approach allows an approximation for calculation of radiation exchange between two bodies and therefore for the explicit radiation behaviour of real bodies. For such an approach the *Lambert's cosine law* must apply, hence, such a body is often referred to as a *grey Lambert radiator*. Its radiant emissive power, depending on its temperature-dependent material property, corresponds to the emissivity $\varepsilon(T)$, of the black body. The emissivity $\varepsilon(T)$, which depends only on the temperature, is thus the only material function of the g*rey Lambert radiator*. Consequently, all four emissivities are the same by definition. The fact that real bodies are, to a good approximation, *Lambert* or grey emitters applies in most cases, but only if most or almost the complete spectral specific emission E_λ lies in wavelength ranges with nearly constant ε_λ.

- **Selective radiator**

If the emissivity of a real body varies greatly over different wavelength ranges, as shown in Figure 14, it is referred to as selective radiator. In fact, most real surfaces correspond to such radiators, but as highlighted previously, a body may not emit much energy in particular areas. In addition, it depends on the considered temperature range for every task and therefore a grey radiator can be considered sufficient.

Since bodies have a different radiation behaviour, they are divided into three categories of radiators. These are shown in Table 7and in Figure 14.

Table 7: Different radiators and their characteristics

Radiator	**Characteristic**	**Emissivity**
Black radiator / black body	The object emits the maximum energy for each wavelength and each temperature	$\varepsilon = 1$
Grey radiator / grey body	the object radiates at each wavelength the same fraction of the maximum energy. This fraction corresponds to the dedicated, constant emissivity	$\varepsilon \leq 1$
Selective radiator / selective body	The object emits variable in different wavelength spectra	ε varies depending on the wavelength λ

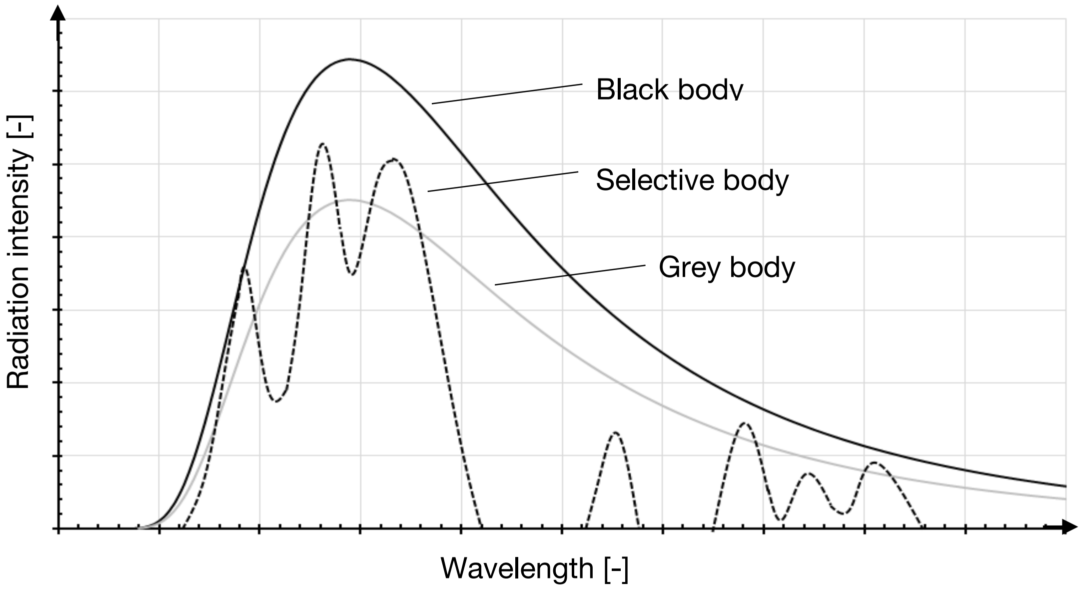

Figure 14: Radiation behaviour of different radiating bodies

3 Emissivity of metallic objects

Metal objects, which are opaque bodies, have a radiation behaviour which is described by the directed spectral emissivity $\varepsilon_\lambda(\lambda, \vartheta, T)$. In order to determine this experimentally, as done in the underlying experiments, extensive measurements are required. As shown by the arguments, the wavelength dependence as well as the dependence on direction and temperature have to be considered. Such comprehensive measurements have not been conclusively performed for every material. Science, especially engineering, often settles for determining the emissivity $\varepsilon_{\lambda,n}$ in the direction of the surface normal ($\vartheta = 0$) or the hemispherical total emissivity ε as shown in the previous Chapter 2. This is often due to technical reasons: As shown later in Chapter 5.2.6, there are atmospheric windows that cause such a limitation for the infrared measurement. In addition to roughness, superficial impurities also play a role. Even a thin oxide layer can completely change the radiation behaviour in comparison to the base material, resulting in many emissivity tables, which often differ in their data for the same material.

In regard of these problems, some theoretical approaches have been made to calculate the spectral emissivity. Therefore, the classical electromagnetic wave theory of *Maxwell* was used, which can combine the spectral emissivity ε_λ with optical material constants, the absorption coefficient k and the refractive index n. According to [22] these material constants form the complex refractive index $\bar{n}$:

$$\bar{n} = n - ik \tag{3-1}$$

In addition, the wave theory in the form of *Fresnel's* equations, describing the reflection and polarization of light at interfaces, provides the dedicated angular dependence of the directional emissivity. While this, by the assumption of isometry, has no dependence on the azimuth angle φ, a pure dependence on the polar angle θ is given. In order to ensure the validity of the electromagnetic theory (see [21]), a number of limitations are required, so that the emissivities derived from the theory do not always correspond to reality. Nevertheless, it provides important, qualitative valid approximations, which can serve as a good basis, especially in the absence of recorded data. In the following, this approach will be performed for metallic surfaces to double-check the findings in course of the research.

3.1 Metal surfaces – Drude Model

The electromagnetic waves impinging on metallic surfaces are damped very quickly in the material. As shown in [22], the absorption coefficient k is not zero and usually even greater than the refractive index n. Looking at the spectral emissivity $\varepsilon'_{\lambda,n}$ in direction of the surface normal, the following relationship arises from the electromagnetic theory

$$\varepsilon'_{\lambda}(n,k) = \frac{4n}{(n+1)^2 + k^2} \tag{3-2}$$

Some important findings could be made by theories from Drude or Hagen and Rubens (see [22]). For consideration at wavelengths which lie in the range of λ > 5 µm and additionally a small specific electrical resistance r_e, the material properties of the electrical conductors influencing the radiation can be described by a simplified version of the electromagnetic wave theory. In this theory, the refractive index n and the absorption coefficient k assume large values. According to [22], it applies

$$n = k = \sqrt{\frac{c_0 \mu_0 \lambda}{4\pi r_e}} = \sqrt{\frac{R_0 \lambda}{r_e}}, \tag{3-3}$$

where

c_0 Speed of light,

$\mu_0 = 4\pi \cdot 10^{-7} N/A^2$ magnetic field constant

and

$R_0 = \frac{c_0 \mu_0}{4\pi} = 29{,}979\ \Omega$ electrical resistance.

According to *Drude*'s *theory*, the spectral emissivity ε'_{λ}, as with most theories, depends only on the polar angle ϑ and not on the azimuth angle φ, and in this case it also depends on n, the refractive index. Up to a polar angle ϑ = 60 °, the emissivity can again be assumed to be approximately constant and in a circular form. From a polar angle of more than 80 °, the spectral emissivity ε'_{λ} assumes a maximum.

The directional spectral emissivity $\varepsilon'_{\lambda}(\vartheta, n)$ can be deduced from the *Drude Model* (see [22]), which is shown in Figure 15 and follows as:

$$\varepsilon'_{\lambda}(\vartheta, n) = 2n\cos\vartheta \left[\frac{1}{(n\cos\vartheta)^2 + (1 + n\cos\vartheta)^2} + \frac{1}{n^2 + (n + \cos\vartheta)^2}\right]. \tag{3-4}$$

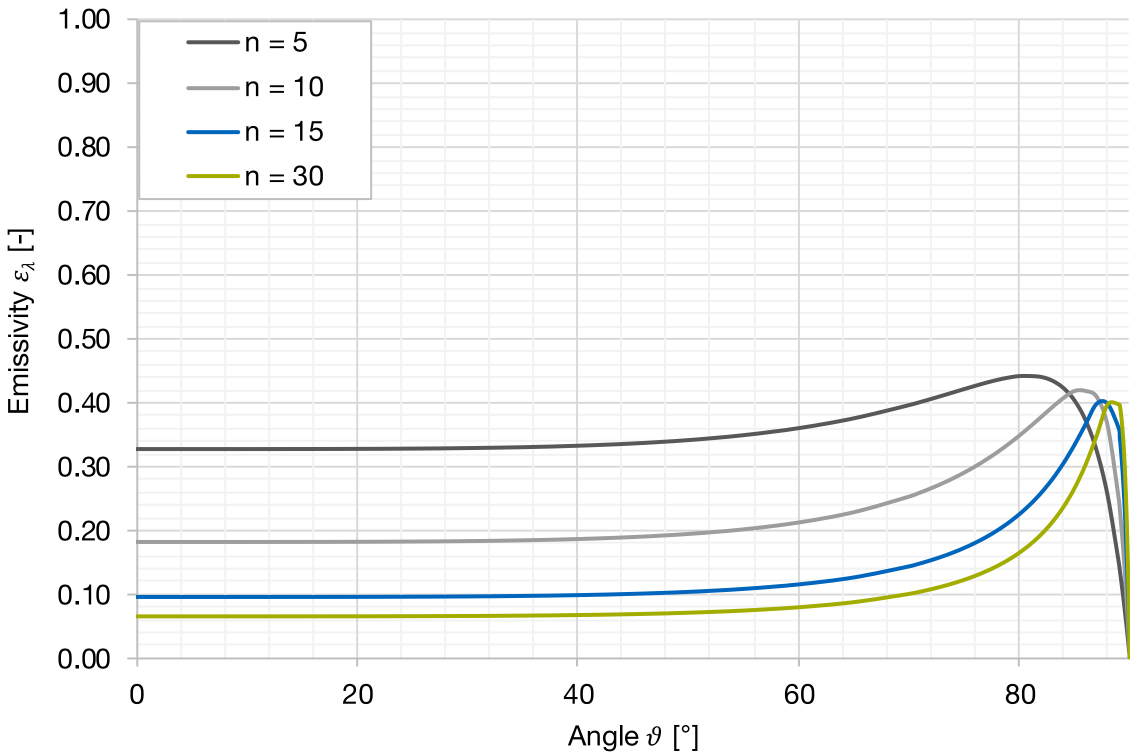

Figure 15: Directional spectral emissivity $\varepsilon'_\lambda(\vartheta, n)$ *of metals (according to the simplified electromagnetic theory)*

3.2 Emissivity of steel in literature

There are a variety of emissivity tables for materials from different manufacturers of infrared sensors (see [25]), but also for example by the association of German engineers – Verein Deutscher Ingenieure (VDI) [26]. However, for metals, these tables are rather approximate, and certainly not fixed, as the emissivity depends on several factors. These include, for example, the surface condition, the temperature and the angle of incidence. Therefore, in such cases, the experimental determination of the emissivity of the real measurement object under practical conditions is recommended. As a first indication, the values listed in VDI 3511 Part 4.5 [26] Table 2 per wavelength range of radiation thermometers according to VDI / VDE 3511 Part 4 [27] are listed in Table 8.

In contrast to other building materials such as concrete or wood, a larger range of wavelength-dependent emissivities is found for steel surfaces. Without considering the temperature dependence, the diversity can be already seen. Furthermore, the company Optris GmbH indicates emission levels in different wavelength ranges. Comparing both tables, it can be seen that partly even in the same spectra, the emissivities vary.

Table 8: Emissivity values of different materials from VDI/VDE 3511 Blatt 4.5 [26]

Surface/Material	**Wavelength range of the infrared sensor**					
	0.65	**0.7 - 1.1**	**1.45 - 1.7**	**2.0 - 2.5**	**4.5 - 5.5**	**8 - 14**
Concrete	-	-	-	-	-	0.55 - 0.65
Wood	-	-	-	-	-	0.80 - 0.90
Steel, tempered	0.75 - 0.80	0.70 - 0.85	0.70 - 0.85	0.45 - 0.70	0.30 - 0.60	0.30 - 0.60
Steel, blanc	0.45 - 0.55	0.40 - 0.45	0.30 - 0.40	0.20 - 0.35	0.10 - 0.30	0.10 - 0.30
Steel, rolled	0.50 - 0.60	0.45 - 0.55	0.35 - 0.50	0.25 - 0.40	0.20 - 0.30	0.20 - 0.30
Steel, oxidised	0.80 - 0.90	0.80 - 0.90	0.80 - 0.90	0.75 - 0.85	0.70 - 0.90	0.60 - 0.80

Table 9: Emissivity values of different materials from Optris [25]

Surface/Material	**Wavelength range of the infrared sensor**			
	1.0	**1.6**	**5.1**	**8 – 14**
Steel, polished	0.35	0.25	0.10	0.10
Steel, rust free	0.35	0.20 - 0.90	0.15 - 0.80	0.10 - 0.80
Steel, oxidised	0.80 - 0.90	0.80 - 0.90	0.70 - 0.90	0.70 - 0.90
Zinc, polished	0.50	0.05	0.03	0.02
Zinc, oxidised	0.60	0.15	0.10	0.10

Regardless of exact values, a dependence on the surface condition can be drawn from literature. While polished and thus smooth surfaces have a small emissivity, rough, oxidised surfaces tend to have high emissivities. This has to be verified in the course of this research.

3.3 Emissivity of hot-dip galvanized steel in literature

Radiation of metal surfaces, as seen in Chapter 2, is based on atomic and molecular level. *Sala* [28] states that the radiation behaviour depends on the chemical composition in a layer with a thickness of about 0 to 10^{-10} m. The radiation behaviour of galvanized surfaces should hence be provided exclusively by the alloy layer (40 to 250^{-6} m) or from the upper pure zinc layer alone, which is only a few micrometre thick.

Therefore, the emissivity of hot-dip galvanized steel members is influenced by the character of the layer formation, the oxidation of zinc and, since the melting point of zinc is at only 419 °C, the melting of the outer zinc layer. The emissivity is thus a variable depending on the temperature.

There is only little information in literature. *Elich & Hamerlinck* [29] described in 1990 that the emissivity of continuous produced galvanized (sendzimir process) 1 mm-steel sheetings, for temperatures up to 400 °C and 450 °C, is about 0.1 – 0.2. At higher temperatures, above the melting point of zinc the emissivity has, in turn, high values ($\varepsilon = 0.65 - 0.95$), depending on the original state of the tested old and new samples.

Newest research, done in Czech Republic by *Jirku* and *Wald* [30], offer an emissivity of about 0.32 for galvanized structures. This has been tested for an IPE 200 cross section and for hollow tube sections, in a furnace test and in a full-scale fire test.

In the course of this thesis, these findings have to be verified, scientifically reproduced and it has to be figured out why there is a possible better behaviour. Furthermore, a detailed temperature-dependent emissivity behaviour is sought, with respect to all dependencies provided in Chapter 2 and 3.

4 Specimens

The test samples for this research are divided into several groups. Specimens were produced for the emissivity experiments (see Chapter 5) as well as the full fire tests (see Chapter 6). Therefore, they are separated in a first step in small-scale and full-scale specimens. In addition, to cover a larger span various categories according to DIN EN 14713-2 [10] had to be tested, as for different classification, which depend on the chemical composition of the steel, the formation of each zinc coating differs (see Chapter 1.4). For tests specimens that have been hot-dip galvanized, it was category A, B and D, as shown in Table 10, as they are the most commonly used categories in structural steel construction. For comparative purposes, also some rusty samples were taken into account. The specimens were provided by W. Pilling, Max Bögl and ArcelorMittal. Missing information on the steel composition of the small and large samples were analysed by means of a spectral analysis in the laboratory of SLV in Munich. The results of the analysis of the most important two chemical elements, for hot-dip galvanizing, can be found in Table 10. The results show a perfect agreement with the desired categories.

Table 10: Composition of the steel for each specimen group measured by SLV München

Specimen Group	Category	Si [%]	P [%]	Si + 2.5 P [%]
Small-scale specimens	A I	0.01	0.009	0.0325
	B	0.18	0.024	0.24
	B II	0.19	0.012	0.22
	A II	0.01	0.010	0.035
	D*	0.4	0.03	0.475
Full-scale specmiens	A	0.01	0.010	0.035
	B ($A_m/V=62.5$)	0.22	0.02	0.035
	B ($A_m/V=76.7$)	0.22	0.015	0.2575
	D*	0.4	0.03	0.475

**according to manufacturer's data*

4.1 Hot-dip galvanizing of specimens

All specimens have been hot-dip galvanized in accordance with the zinc bath composition standards of DIN EN ISO 1461 [1] and the German “DASt-Richtline 022” [2]. The samples were galvanized in two different galvanizing plants of the companies Zinkpower Schörg GmbH & Co. KG and Wiegel Denkendorf Feuerverzinken GmbH.

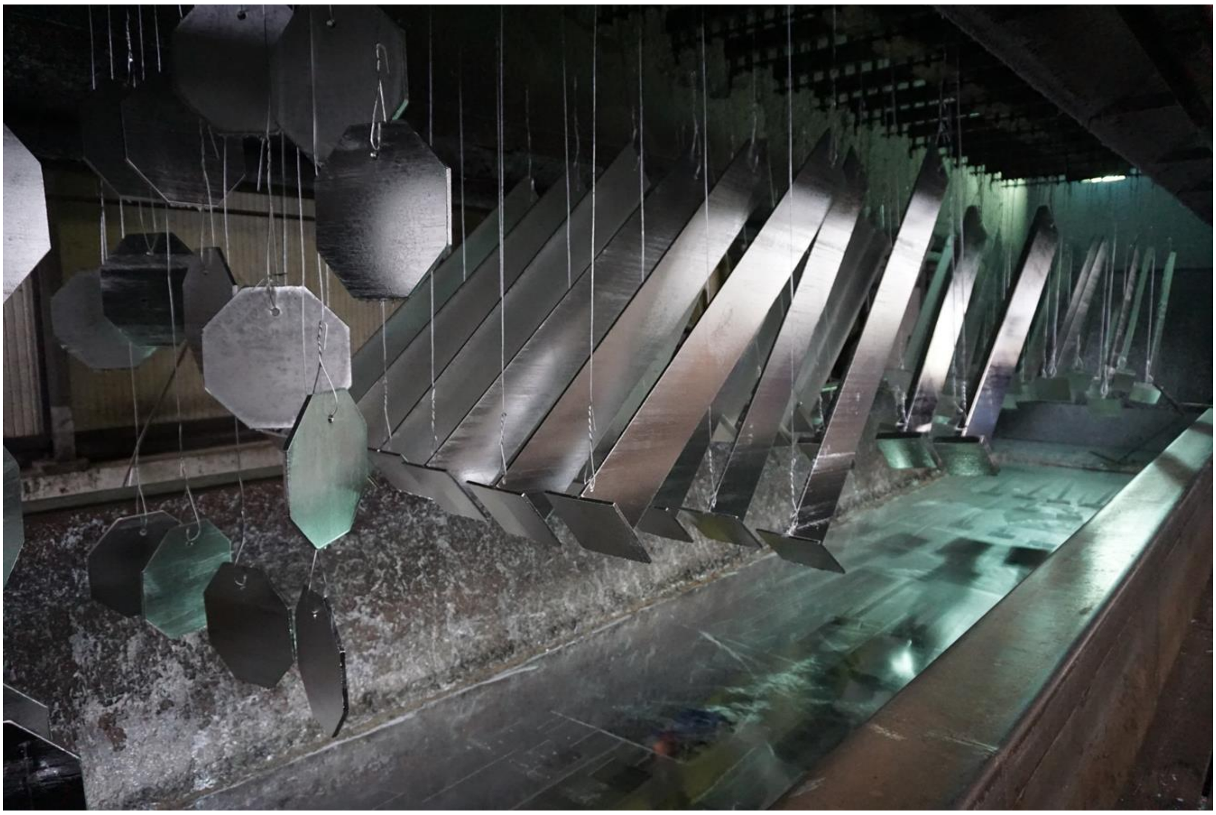

Figure 16: Hot-dip galvanizing of the test specimens

Other parameters like the temperature of the zinc bath have been chosen to be in the range of normal temperature galvanizing. The temperatures of the molten bath varied between 445 °C and 448 °C for samples of category A, B ($A_m/V=62.5$) and D of the first and second full-scale fire tests as well as for the “EP-T”-samples. The immersion time was around 11 minutes each. This duration was retained in the second plant were specimens of category B, with a section factor of 76.7, for the second full-scale test have been hot-dip galvanized at a similar temperature of 450 °C.

For the samples, the mean values (‘MV’) of the zinc layer thicknesses per category are listed below. The reactivity difference can be seen in Table 11. Low-silicon steel (category A) has a growth value of about 7-8 µm / min while high-silicon steel (category D), for example, has twice the value. According to the growth values, dedicated alloy coatings were formed. These correspond, per category, to the phase arrangements presented in Chapter 1.4. The corresponding coatings and phases are shown for the small-scale samples in microsections in Figure 17 and Figure 18 for categories A, B and D. More microsections can be found in Appendix ‘Microsections’.

Table 11: Coating thickness of specimen

	Category	**Mean value (MV)**	**lowest MV**	**highest MV**	**Growth value**
		[µm]	**[µm]**	**[µm]**	**[µm/min]**
Fire test No. 01	**A**[1]	84	80	90	8
	D[1]	186	175	196	17
Fire test No. 02	**A**[1]	81	71	91	7
	B[1]	154	134	194	14
	B[2]	306	262	330	28
	D[1]	152	129	172	14
EP-T	**A**[1]	88	80	100	8
	D[1]	200	175	227	18
	A[1,3]	90	88	93	8
	B[1]	232	225	244	21

[1] Zinkpower Schörg GmbH & Co. KG

[2] Wiegel Denkendorf Feuerverzinken GmbH

[3] dezinced & newly hot-dip galvanized

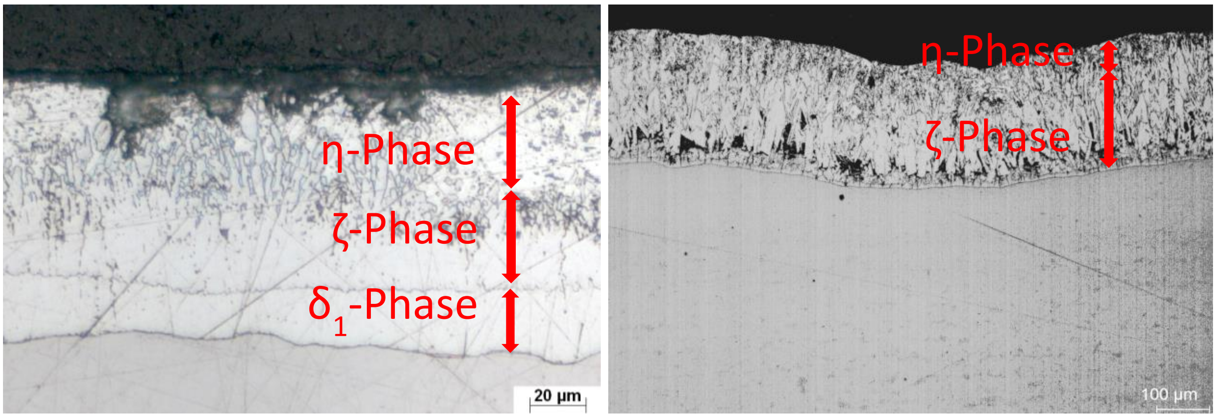

Figure 17: Microsection – left: category A; right: category B

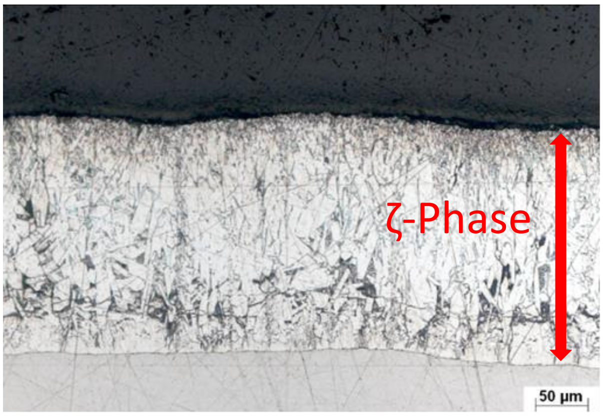

Figure 18: Microsection – category D

4.2 **Specimen – Full-scale tests**

The specimens for the full-scale fire tests were designed as rectangular steel sections. In addition, in order to avoid tilting of the specimens, a base plate was welded before galvanizing. Since no additional effects, such as shading effects of HEA or IPE profiles, appear on flat test samples, the measurement results are not sophisticated. It was thus possible to obtain more reliable test results for the present case.

The naming of the specimens will be explained on an example:

“X-Y-ZZZ”

where

X	indicates the thickness of a specimen: 1 or 4 [cm]
Y	indicates the category of the specimen: A, B or D
ZZZ	indicates the storage condition: *In* (inside) or *Out* (outside)

4.2.1 **Specimen – Full fire test No. 01**

In the first of both full fire tests, rusty and galvanized steel samples were used for the test to obtain information about a wide variety of surface scenarios. For this purpose, steel samples of category A and D were tested. As mentioned in Chapter 1.4, the different categories, due to different chemical compositions of the steel, have different zinc coatings. However, not only the zinc layers and their thickness but also the external appearance is different. This as well as the setup of the experiment is shown in Figure 19.

Overall, 24 steel samples were tested. In addition, to test different profile factors, they were again separated into two groups. Twelve samples were tested with a height of 1500 mm, a width of 200 mm and a thickness of 40 mm, while the twelve other samples were manufactured with the same dimensions except a different thickness of 10 mm. The following Table 12 shows the distribution of the sample categories:

Table 12: Specimen – Full fire test No. 01

Specimen			**Storage**		**Name of the specimen**
Dimensions	**Category**		**Inside**	**Outside**	
12x ***1500x200x40 mm***	*2*	rusty			*4-r*
	7	Cat. A	*5*	*2*	*4-A-In / 4-A-Out*
	3	Cat. D	*2*	*1*	*4-D-In / 4-D-Out*
12x ***1500x200x10 mm***	*2*	rusty			*1-r*
	7	Cat. A	*4*	*3*	*1-A-In / 1-A-Out*
	3	Cat. D	*2*	*1*	*1-D-In / 1-D-Out*

Figure 19: Setup of the first full fire test

As seen in Table 12, the galvanized samples were separated in their storage before the fire experiment. This will be discussed in further detail in the following section.

4.2.1.1 Storage

Hot-dip galvanized components are produced usually 'just in time' and therefore typically are delivered after a few days or weeks of storage directly to the building site, where they are incorporate. In order to produce the most unfavourable case in the first fire test, the samples were stored adversely after their delivery. Incorrect storage inevitably leads to visual and material impairments, such as white rust and corrosion products on the surface. Especially on freshly galvanized components, the storage conditions have a significant influence on the formation of the surface quality of HDG. At the beginning, a zinc coating is usually bright. Over time, it develops a patina and its appearance becomes darker. The patina itself is a weather-resistant protective layer of zinc oxide and zinc carbonate. In contrast, if no covering layer, along with its protective effect, has formed on specimen, white rust can form quickly. In order to obtain this adverse formation, the following steps (see notes from *Huckshold et al.* [31] and from the *Institut Feuerverzinken* [32]) were not kept:

- complete mutual contact of the individual components must be avoided,
- no cover by foils or tarpaulins (condensation),
- galvanized steel parts should be placed on dry substrates including a ground clearance of approximate 150 mm,
- the specimens should be stored on a slope,
- in case of high humidity, rain or snow, a longer, freely weathered storage should be avoided.

The consequence of non-compliance with these regulations means that the aforementioned cover layer could not be formed, because the zinc surfaces are moistened by water over a longer period of time. Consequently, the supply of air and thus the supply of CO_2 was insufficient. It inevitably formed white rust on the galvanized surface.

If such storage condition maintain only briefly, only small amounts of white rust would occur. After completion of an adverse storage, parts of the white rust formation can be transformed in a zinc protective topcoat. Since significant white rust formation was sought in the course of the test without completely destroying the zinc layers, the storage was maintained for 8 weeks. Due to that 'worst case' storage, a greenish, mucous mass also partially formed on the specimens.

As a result of this very unfavourable storage, different surface structures formed. These can be seen in Figure 20.

Figure 20: Consequences of adverse initial storage

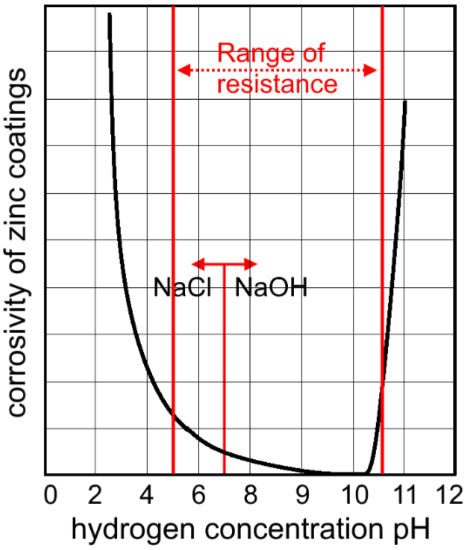

Figure 21: Corrosivity in dependence of the pH - value

Since a mucous mass on hot-dip galvanized objects is an uncommon case – which was previously unknown to this extent – the infestation was removed after this initial storage of eight weeks.

HDG offers high resistance to most chemical stresses such as oil, solvents, paints, etc., and is therefore resistant to many chemicals when the pH - value is in the range from 5.5 to 12.5 (see [31,32]). Due to this, the cleaning of the affected surfaces was carried out with an acetone solution (pH: 5 – 7) and a nonwoven abrasive.

After eight weeks of this initial adverse storage, the test samples were split into ‘inside’ and ‘outside’ stored specimens. Both storage variants were then maintained for one year. While the ‘inside’ samples were stored in a hall area with fresh air supply, the ‘outside’ stored samples were exposed to open weathering conditions.

For comparison, rusty samples were also examined. For this purpose, some of the samples intended for these experiments were completely removed from the zinc alloy by a pickling bath and then stored outside for six months. This resulted in rusted samples that represent a condition of components that would be repaired in construction at an early stage. Old rusty surfaces, which are characterized by a decomposing surface, with flaking layers, were not covered by this procedure.

4.2.2 **Specimen – Full fire test No. 02**

In the second full fire test, in addition to newly galvanized samples of categories A and D, samples in the Sebisty range, respectively category B, were tested. Thus, in this experiment, three categories had different zinc coatings according to their different chemical steel composition. For this experiment, only samples of approximately the same dimensions were tested. In addition, fewer samples were placed in the furnace to provide a greater distance among the samples and, especially, between the samples and the burner flames as this affected the results for the first fire test (see Chapter 6.4).

The segmentation of specimens is shown in Table 13:

Table 13: Specimen – Full fire test No. 02

Specimen			**Storage**		**Name of the specimen**
Dimensions	**Category**		**Inside**	**Outside**	
5x **1500x200x40 mm**	*2*	rusty		*2*	*4-r*
	2	Cat. A	*2*		*4-A-In*
	1	Cat. D	*1*		*4-D-In*
3x **1500x200x30 mm**	*3*	Cat. B	*3*		*4-B7-In*
4x **1500x160x40 mm**	*4*	Cat. B	*4*		*4-B6-In*

While all samples of category B were newly produced by the steel manufacturer and therefore hot-dip galvanized for the first time, the specimens of category A and D have been dezinced and newly galvanized as they have not been used for the first fire test. The reasons for this were that ‘newly’ hot-dip galvanized samples of these categories should be tested and to ascertain whether there is any poor influence on the behaviour for re-galvanized surfaces with respect to fire resistance. After galvanizing, the samples were stored inside a hall with fresh air supply. A white rust formation could be approximately excluded, due to a small storage time of two months.

The exact setup of the second fire test can be seen in the following Figure 22.

Figure 22: Setup of the second full fire test

4.3 Specimen – Small-scale test "EP-T"

4.3.1 Preparation

Before the 10 mm thick galvanized samples were completely finalised in a circular shape, with a diameter of 50 mm, by water jet cutting, the dimensions were significantly larger, given that no disturbing edge areas of the galvanizing process are in the measuring fields of the infrared sensors (see Chapter 5) and because several identically-galvanized and -treated steel samples with the same chemical composition could be obtained from the same samples' carrier plate. The latter had a shape of an octagon, with a diameter of 300 mm and a thickness of 10 mm. An example of the carrier plates, including the final test samples can be seen in Appendix 'EP-T'.

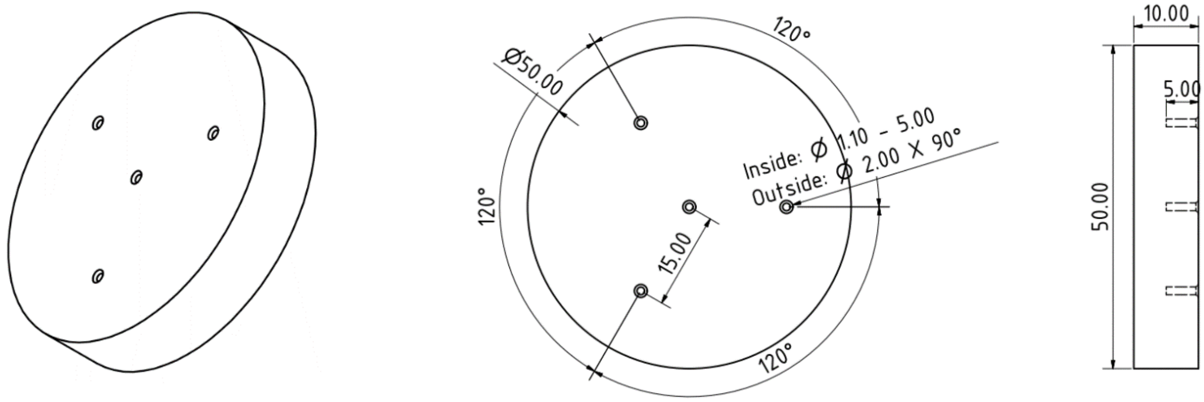

Figure 23: EP-T specimens [mm]

In further processing, the samples were provided with four 5.0 mm deep and 1.1 mm thick drilling holes from the back side to measure the temperature in the sample by incorporated thermocouples during the experiment (see Chapter 5). In order to reduce the notch effect on the outer hole's edge, the hole was minimal widened on the surface with a slightly larger driller of 2.0 mm. Consequently, a conic outer ring, with a 1.1 mm inner hole could be provided, as shown in Figure 23. The implementation of the thermocouples on the front side has been omitted to produce no unwanted influences starting from the surface to be measured by the infrared sensors as described in Chapter 3. The four holes were arranged in a way that a holistic temperature profile could be generated on the sample. In addition, a redundant system of temperature measurement could be guaranteed.

4.3.2 Storage

Different surface conditions of the small specimens were striven for a wider range of results. Therefore, the following four states were investigated:

- freshly galvanized; stored inside (experiments after the formation of the topcoat, shortest storage time: 4 weeks)
- galvanized; stored unfavourably for 8 weeks -> stored inside afterwards
- galvanized; stored unfavourably for 8 weeks -> stored outside afterwards at weathering conditions
- rusty

The storage conditions of the adverse stored samples corresponded to the storage of the full-scale test samples of the first fire test (see Chapter 4.2.1.1).

5 Emissivity Performance-Test (EP-T)

In the course of the thesis it was necessary to develop a test setup [33], which allows the verification of a temperature-dependent emissivity of steel surfaces. In order to realize such a test, some influence factors, inter alia the heating, the controlling and the emissivity measurement, had to be evaluated. Due to its importance for this research, the evaluation of the emissivity measurement variant is shown in the following, before the final setup is described in further detail.

5.1 Determination of the Emissivity

There are several recognized methods in science for the emissivity determination on opaque materials.

1. On the surface of the test object, a special varnish or adhesive tape is partially applied. Its emissivity is usually in the range of ε = 0.90 - 0.95 and remains constant up to defined temperature. By alternately measuring the temperatures of this part and the objects surface with its unknown emissivity, the emissivity of the pyrometer can be adjusted untill it indicates the same temperature. This adjusted value then corresponds to the actual emissivity at the current temperature and the current measurement parameters (e.g. angle or wavelength). Unfortunately, this is not applicable for higher temperatures, due to the evaporation of the varnish or the glue of a tape.
2. The measurement object is provided with a borehole on the surface. The ratio of the depth to the diameter must be at least 1:5. This produces an approximately black radiator in which the radiation is caught. The emissivity is therefore in the range of $\varepsilon \approx 0.95$. A detailed mathematical solution for an effective emissivity of a cylindrical cavity can be found in *Bramsen et al.* [23]. For this purpose, it is necessary that the measuring field diameter (spot diameter on the surface) of the pyrometer is smaller than the diameter of the borehole. By comparative measurements, first in the hole and then on another measurement point on the non-prepared surface, the emissivity is adjusted until the same temperature is displayed at both positions. Similar to variant 1, this adjusted value corresponds to the actual emissivity at the current temperature and the current measurement parameters.
3. The temperature of the test object is determined with implemented thermocouples or contact thermometers. For example, a borehole for thermocouples is applicate at an appropriate large sample. Alternatively, the surface temperature is measured using a

suitable surface temperature sensor. However, it is important to have a continuous fixation here.

An additional pyrometer is aligned at the surface to be measured of the object, whereby the measurement should be as close as possible to the measurement of the thermocouples. Subsequently, the emissivity ε of the radiation thermometer has to be adjusted until both measurement variants indicate the same temperature. Again, as with both other variants, this adjusted value corresponds to the actual emissivity at the current temperature and the current measurement parameters.

The last variant is the most accurate and for the desired range of temperatures (20 – 850 °C) the most suitable method for this research. Further advantages of pyrometers are their quite delay-free measurement and their possibility of measuring moving objects without any contact. Therefore, this method was used and formed the basis for the development of the Emissivity Performance – Test.

5.2 EP-T setup

Due to the requirements of the emissivity measuring variant, the self-designed test stand consists of the following components:

- Table
- Radiation shield
- Rotateable plate incl. stepper motor
- Heating modul
- Light source
- Electric switch panel
- Sensor- & Camera bracket
- IR-pyrometer / IR-camera
- Temperature sensors / HBM mearuring system
- Camera
- Test specimen
- Computer incl. control software

Originating from these parts, only the most important will be discussed in the following.

5.2.1 **Radiation shield**

It is important to minimize a variety of error sources. One of them, in non-contact temperature measurement, is the unwanted measurement of the apparent temperature of the test object. In this case, the infrared sensor measures, the reflected temperature or background temperature on the surface of the sample, since the radiation energy of them is reflected from the object's surface into the camera. For objects with high emissivity the influence is rather small. For objects with a lower emissivity – like this is the case for polished metal surfaces – this gets an important influence factor. The sensor thus detects less the actual emitted radiation, but more the reflection of the environment, which inevitably leads to false measurement results.

In order to avoid this and exclude additional radiation influences from the environment, such as from light bulbs, a coverage was designed. Only openings for the two IR sensors and the camera were provided.

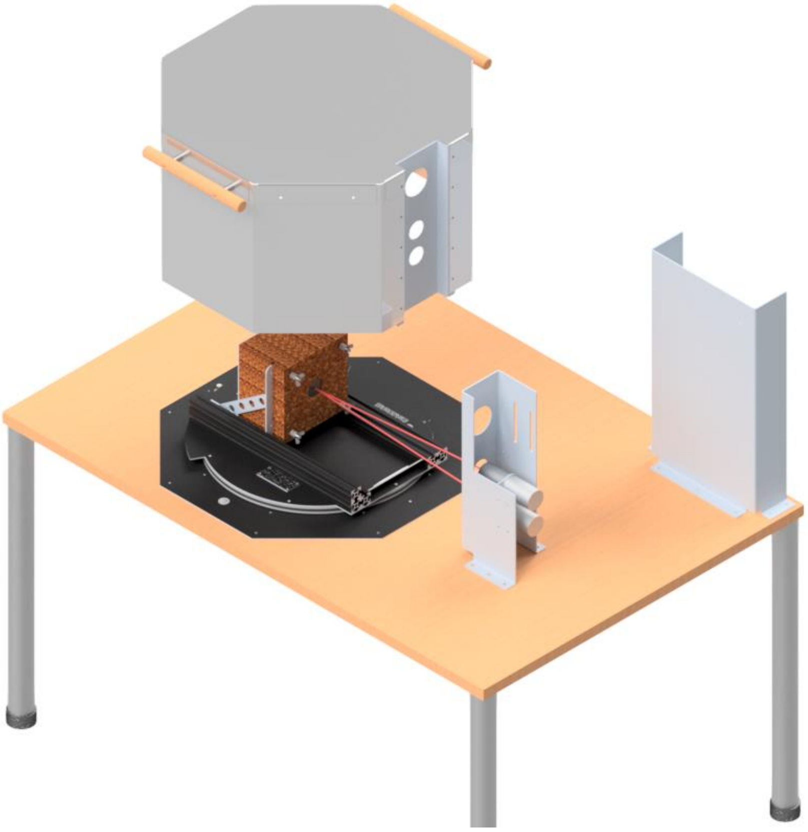

Figure 24: Setup of the Emissivity Perfomance-Test

5.2.2 **Rotatable mounting plate incl. stepper motor**

The aim of the experimental setup was, inter alia, to measure the angle-dependent emissivity of surfaces. In order to avoid manual errors in the angle adjustment, a variant with a turntable was chosen, which could be controlled during the tests by a self-coded control software.

For this purpose, the rotatable mounting plate was controlled via a stepper motor from Trinamic of the type PD42-3-1141. This was done by developing an own software. Thus, a rotation angle with an accuracy of a tenths of a degree could be reached. Due to the mounting of the test sample and the associated limitation of the measuring angle, the control was limited from - 45° to 45° starting from the perpendicular plane.

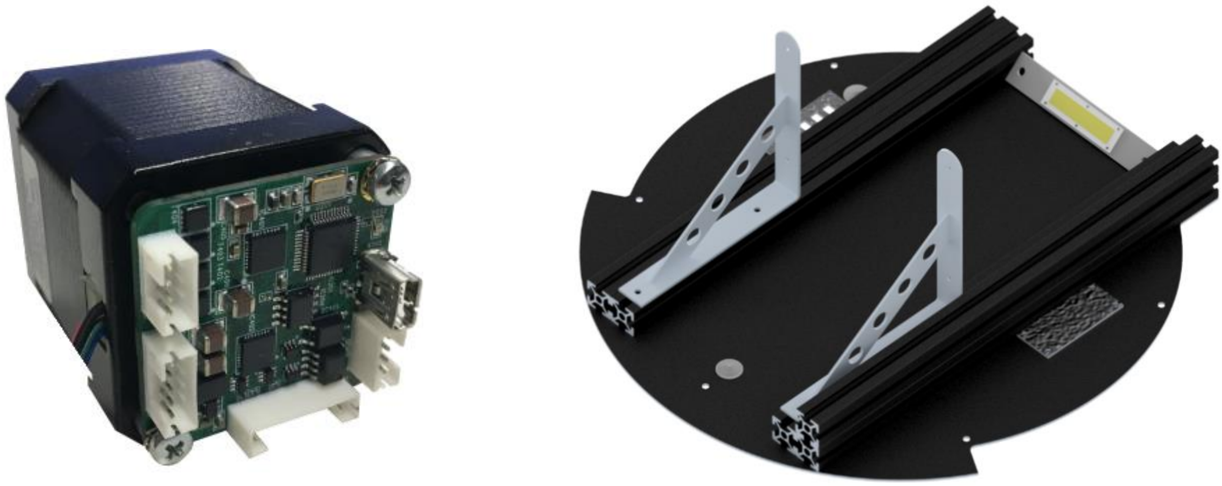

Figure 25: Stepper motor PD42-3-1141 from Trinamic (left); rotateable mounting plate (right)

Furthermore, aluminium profiles and angles were placed on the turntable, providing a mounting frame for the heating module. Special attention had to be paid to the cables, such as measuring and power cables. Since the rotating functionality could easily catch cables and would lead in the worst case to the termination of the measurement attempt. Therefore, the cable lines were placed through an opening underneath the plate through the table.

In addition, the self-programmed stepper motor was linked to other components of the test stand. These include a voltage regulator, which regulates the heat release of the heating module, as well as an LED light source.

5.2.3 Heating module

The self-built heating module was made from several vermiculite plates. Vermiculite itself offers excellent properties for this application. Among other things, for example, a high melting point (about 1315 °C) and excellent insulation properties, which reduces the heat dissipation enormously. The radiation interference of and therefore in the test stand can thus be set almost to zero.

The test specimens held in a separate vermiculite plate are brought to the appropriate temperature by a heating module. This is done by heating the FeCrAl wire installed behind the sample (alloy components: Cr 22 %, Al 5.8 %, Fe 72.2 %) using electricity. Based on the existing resistance 11.5 Ω/m and the diameter of Ø 0.40 mm, the length to be used could be calculated from the electric switch control so that a desired total resistance of 55 Ω was obtained.

$$R = \frac{l * \rho}{A} \tag{5-1}$$

$$l = \frac{R * A}{\rho} = \frac{55\Omega * (\frac{0.40mm}{2})^2 * \pi}{1.45 \ \frac{\Omega * \mathrm{mm}^2}{m}} = 4.783m \tag{5-2}$$

The reproducible, self-wound wire, with a maximum working temperature of 1400 °C, was integrated into the electricity circuit via two poles. The heating of the test samples is thus regulated only by the voltage, so that a dedicated heating curve can be evolved.

The total package of the heating module thus allows heating from the ambient temperature up to about 900 °C of a test specimen.

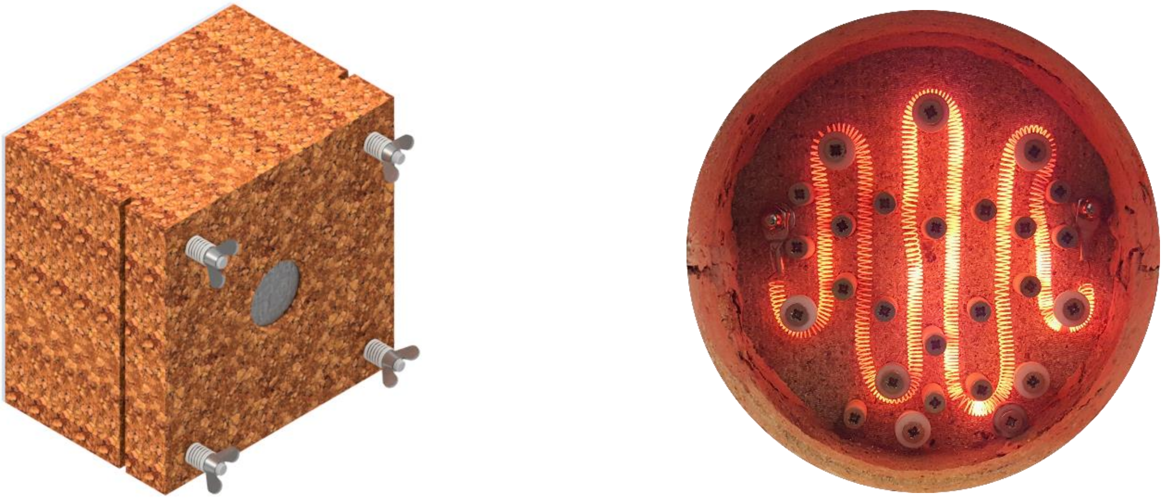

Figure 26: Illustration of the heating module incl. a sample (left); heating wire in the module (right)

5.2.4 Electric switch panel

To operate the measuring technology used, the stepper motor and especially for controlling the heating module, an installation box (KV 9330) from Hensel was used. An additional voltage regulator enabled the current flow in the heating module to be regulated outside the coverage. In order to control everything via the self-developed control software, this had to be coupled with the stepper motor.

5.2.5 Light source

For the simultaneous video and photo documentation during the experiment, a light source had to be implemented. However, only a LED panel is suitable, since a light bulb emits heat radiation in the infrared range and would lead to incorrect measurements. The light source was controlled by the stepper motor using the self-programmed software and could be turned on and off as desired.

5.2.6 Infrared sensors

For non-contact temperature measurement pyrometers have been used for decades. These infrared (IR) sensors can, via the heat radiation, determine the temperatures without contact to their measurement objects. In this case, the infrared radiation emanating from the object is directed by means of a superior optical system to an infrared detector element, for example a photodiode, which converts the incident radiation into a corresponding electrical signal. This signal is then processed and amplified by further digital steps in such a way that the output quantity can be used to deduce the dedicated object temperature.

In addition to the integrated display of a pyrometer, infrared thermometers / sensors also feature digital interfaces (e.g. USB). These digital interfaces can also be used for device setting and as practiced in this experimental setup also for digital control and data query.

To measure the temperature in the EP-T, two IR sensors from Optris GmbH were selected. The first sensor *LT* measures in a spectral range of 8 – 14 µm while the other pyrometer *3MH1* measures only in the range around the wavelength of 2.3 µm. Both fit perfectly into the atmospheric windows, which can be seen in Figure 27 of the VDI in [26]. Atmospheric windows respectively infrared windows, in turn, provide spectral ranges where radiation can pass without disturbance or energy loss.

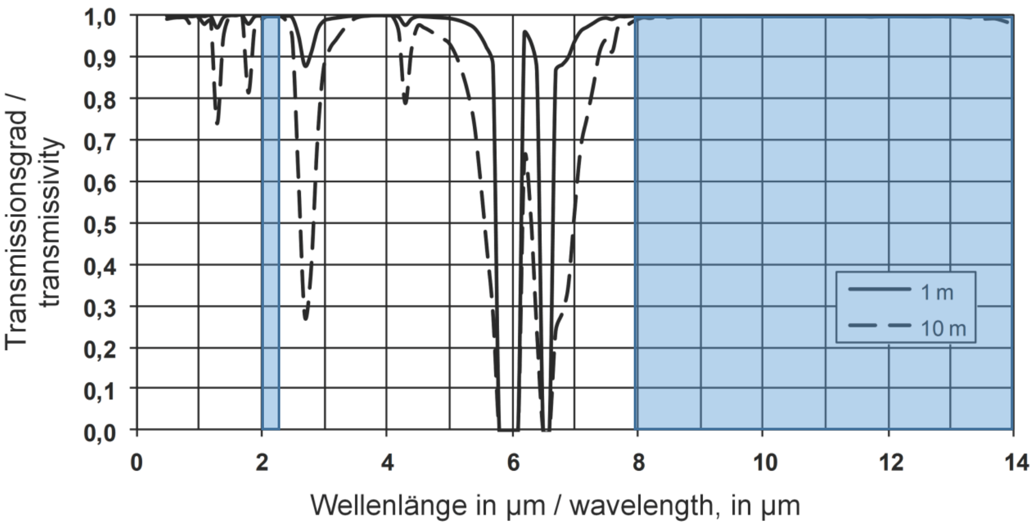

Figure 27: Spectral transmissivity of air at ambient temperature of 25 °C, a pressure of 1 bar, 98 % relative humidity and 0.03 % CO2 content for 1 m and 10 m distance; from [26]

Since the radiated energy is distributed in dependence of the temperature over the total spectral range, only a certain temperature range can be covered by each individual IR-sensor. The most important information about the two pyrometers can be found in Table 14.

Table 14: Technical information of the infrared sensors

Model	**Temperature range**	**Spectral range**	**System accuracy**	**Temperature resolution**	**Setting time**	**Optic**
	[°C]	**[µm]**	**[K/°C]**	**[K/°C]**	**[ms]**	
LT	-50 bis 975	8 - 14	±1 °C or ±1 %	0.1	120	CF4
3MH1	150 bis 1000	2.3	±(0.3 % T_{Mess} +2 °C)	0.1	1	CF4

The distance of the sensors corresponds to a safe distance to the heat source to produce no unnecessary temperature effect on the sensitive measuring heads. In addition, the optics and therefore the spot size on the sample has been chosen in a way that it is completely on the test sample, even with a rotated measuring angle. The measuring spot of the two used sensors *3MH1* - CF4 and LT - CF4 corresponds to a diameter of 1.5 mm respectively 5.9 mm at a distance of 450 mm. In order to fix the position, a support structure has been developed that holds both the IR sensors and a digital camera in their respective positions and thus contributes to a trouble-free measurement.

5.2.7 **Temperature sensors / HBM Measurement system**

To measure the temperatures in the steel samples, four type K sheath thermocouples (TC) were used. In this case, stainless steel (1.4841) thermocouples, which are suitable for measuring temperatures in more demanding environments, such as elevated temperatures up to 1100 °C. These thermocouples with a diameter of 1.0 mm are bent to the corresponding measuring point and remain fixed in their position hole without changing the thermal properties. In order to get a precise statement of the temperature distribution across the sample the thermocouples were placed in a defined way from the back of the sample. By measuring the temperature from behind, it was possible to measure undisturbed with the IR sensors at the front side. One of the TC was placed in the middle of the sample, whereas the others were uniformly distributed around in a circle with an angle in between the measurement spots of 120°. To get no notch stress into the TC the hole was drilled with a diameter of 1.1 mm and then widened, at the surface, with a slightly greater diameter (see Figure 23 in Chapter 4.3.1). In order to provide a good heat conduction between the thermocouple and the steel sample, the whole had to be cleaned from any drilling oil. This was done by cleaning with acetone and short pulses of air pressures. In addition, a copper paste was applied before implementing the thermocouples tip to improve the conduction behaviour.

An HBM QuantumX MX 1609 KB amplifier was used to record and convert the voltages from the thermocouples into temperatures.

5.2.8 **Computer incl. control software**

To control the test stand including the stepper motor – respectively light, angle of rotation and heating – as well as the two infrared sensors, a program with an appropriate user interface was created with the programming language Python.

The graphical user interface (GUI) is shown in the following Figure 28. It comprises two parts. The first part is the sensor control, which is in the upper part of the GUI. In order to interact with the plugged IR sensors, it is necessary to use the correct serial port of the computer. After the successful installation of the pyrometers, it is possible to access the device by clicking the opening port button. Subsequently, it is possible to change the emissivity and the measurement interval of the sensors by editing the entry in the input boxes. This is also possible during the test. Before starting a test, it is recommended to create a new output file by editing the name assignment box. Using the same name again, will lead to an ongoing editing of the last file. Every change in an input box has to be confirmed by clicking the related ‘OK’-button. The second part of the GUI is the stepper motor control. Again, it is important to set and open the right serial port, after installing, to interact with the stepper motor. In the two input boxes it is possible to handle the speed and the acceleration. Activating, the changed entries, is done by clicking the ‘Ok’-button. Furthermore, the rotation angle is controlled by two buttons, each providing +/-5°-steps in both directions. The current angle is shown in real-time below the buttons. As previously mentioned, the light is controlled by the stepper motor and therefore controlled via two buttons on the right side of the GUI. It can be switch on and off the whole time. The same appears for the electrical dimmer. Again, two buttons, one for the higher default level of electrical voltage and one for the lower default voltage level.

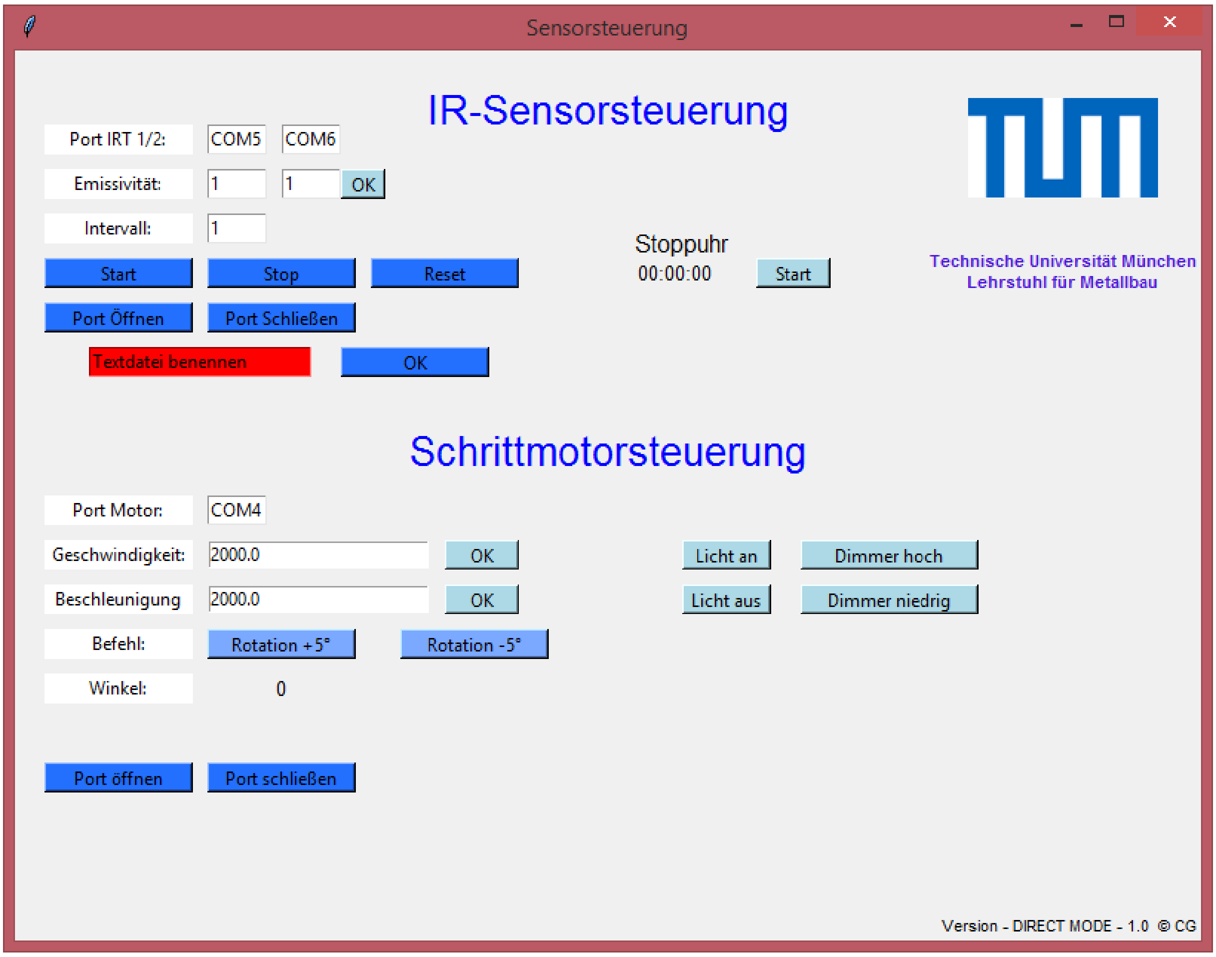

Port IRT 1/2: COM5 COM6
Emissivität: 1 1
Intervall: 1
Stoppuhr 00:00:00
Port Motor: COM4
Geschwindigkeit: 2000.0
Beschleunigung 2000.0
Winkel: 0
Version - DIRECT MODE - 1.0 © CG

Figure 28: Graphical User Interface (GUI) of the self-programmed control software

Due to the direct control, the setting can be changed and adjusted directly during the test procedure. Therefore, it was possible to control the EP-T setup of a test and record every input and in turn measurement output to optimize the evaluation procedure afterwards.

Changing the settings was logged automatically in different generated text files. For this purpose, a program internal clock was implemented. Analysing, comparing and further processing of the different measured and logged parameters (e.g. temperature, angle and emissivity) can be done with any programs in the next step. For this thesis, this was done by self-generated VBA-programmed Excel tools.

5.2.9 Processing of the measured data

In the beginning of the tests, it was necessary to change the emissivity values manually in the self-made EP-T control software (GUI). Therefore, the system was run in a direct mode. By data logging, it was possible to create a temperature dependent emissivity.

With more tests, and an ongoing proof of the setup, the measurement method could be changed. With increasingly more data, it was possible to determine the emissivity after the test automatically. By calculating with the exact radiation intensities for every temperature, as shown in Chapter 2.5.3, of the specimen and the dedicated measured intensities of the sensors, it was possible to calculate the related emissivity for every step during the test. The calculation was done for each sensor in their dedicated measuring wavelength range. This results in a more detailed and exact determination of the temperature-dependent emissivity.

5.3 Possibility of measuring errors

Pyrometers have a very short response time. In contrast, measuring temperatures with thermocouples, the probe indicates the temperature of its tip. The temperature of the tip changes due to heat conduction, which in turn takes more time. Systematic errors in the contact temperature measurement lead only – if any – to a minimal error in the determination of the emissivity. In the case of the Optris IR sensors *3MH1* and *LT* used in this approach, a settling time with 90 % of the signal is present at 1 ms and 120 ms, respectively.

The methods differ not only in their setting time, but also in their fault tolerance. For the thermocouples based on nickel-chromium (type K) and the two pyrometers used from Optris GmbH (*LT* or *3MH1*), the following maximum possible error tolerances, shown in Figure 29 result over a temperature range of 0 to 1000 °C.

At shorter wavelengths it is only possible to measure radiated energy in case of higher temperatures. The radiation intensity shifts, as already mentioned in Chapter 2, with increasing temperature to smaller wavelengths. While at low temperatures no radiation occurs in the range of the 2.3 µm sensor, this sensor is at temperatures above 400 °C exposed to a significantly higher radiation intensity than a sensor that measures in the longer wavelength range, as this is the case for the *LT*-sensor. This situation is shown in Figure 29. The higher the radiation intensity the lower the susceptibility to deviations and the more likely is an accurate measurement. This also implies that for the *3MH1* sensor only results from temperatures approximate above 200 °C are meaningful.

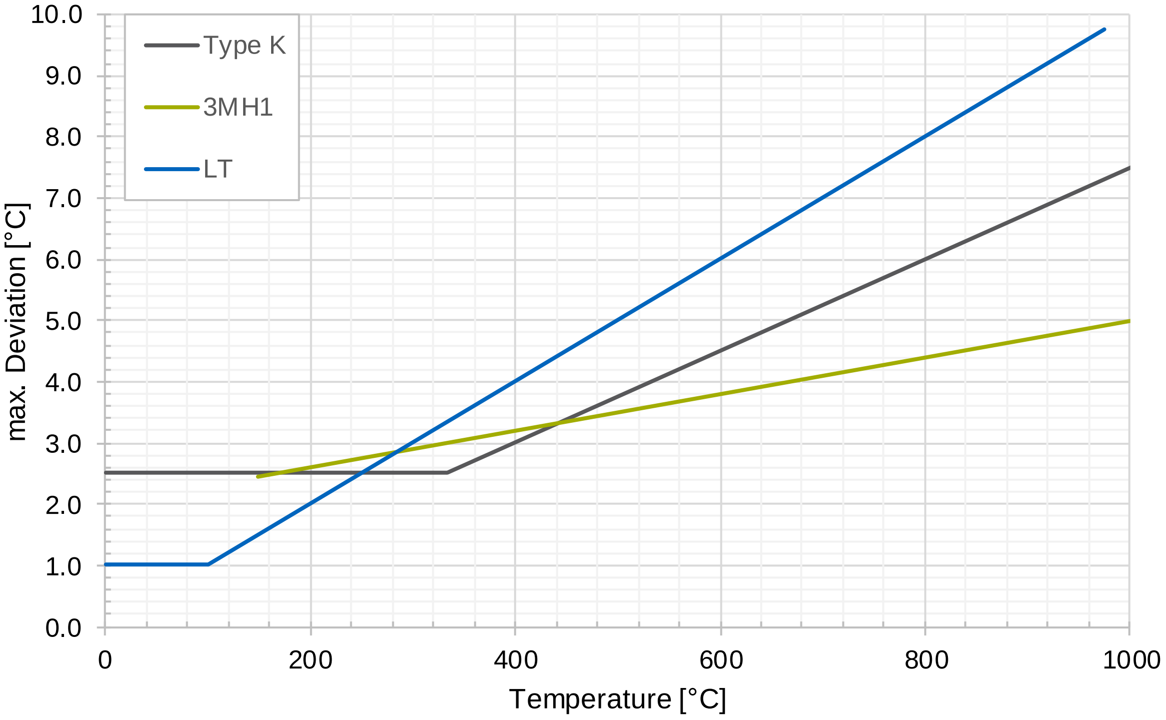

Figure 29: Maximal deviation depending on the measuring method (Thermoelements type 'K'; Optris IR-sensors 3MH1 and LT)

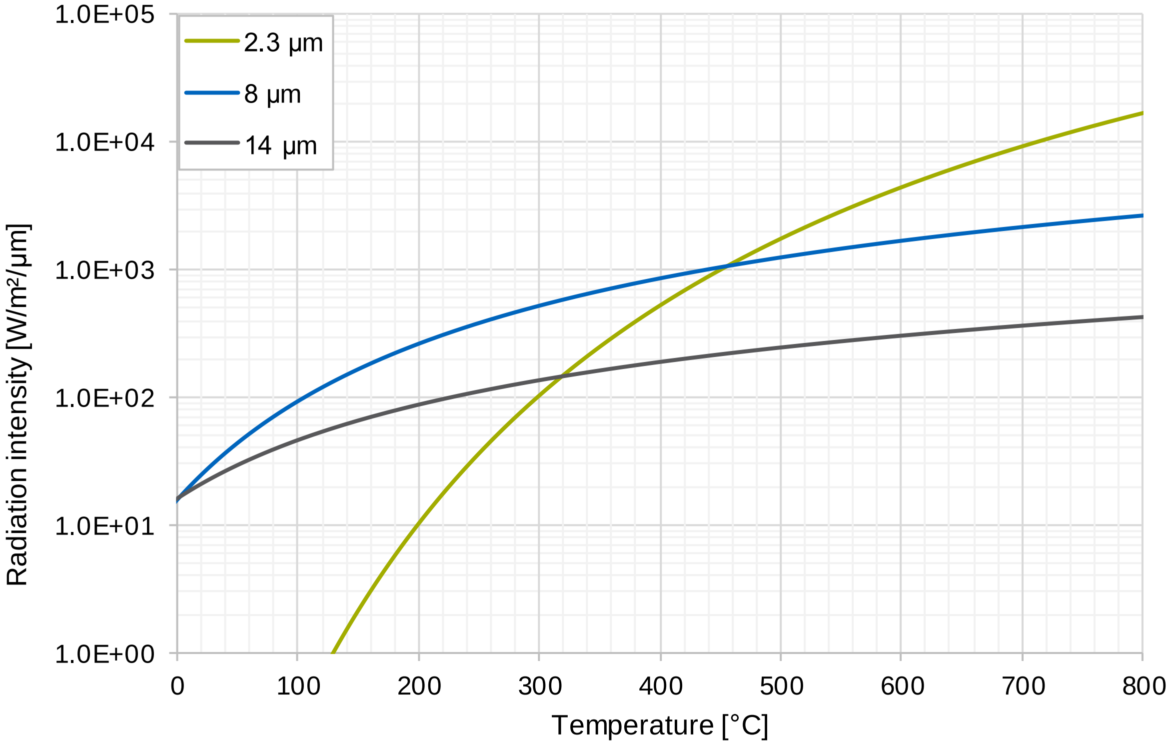

Figure 30: Radiation intensity in dependence of the wavelength and the temperature

Essentially, for smooth metallic surfaces, one should measure in wavelengths, which are as small as possible to avoid an increased susceptibility to errors. For rougher surfaces or plastic surfaces, IR sensors measuring in a longer wavelength can be used.

5.4 Evaluation of the EP-T

In order to obtain a precise statement of the emissivity, a large number of experiments were necessary. Especially, to provide a fundamental basis for all possible surface conditions and the variety of the alloy layering. Therefore, 147 tests, with changing parameters, have been done for this doctoral thesis. An overview is given in Table 15.

Table 15: Number of experiments of different specimens

Specimen/Category	**Name (Abbreviation)**	**Number of tests**	**Condition**
Specimen of Category A	'A'	71	Stored inside / outside *
	'A_N'	8	Newly HDG; stored inside
	'A (P)'	2	passivated
Specimen of Category D	'D'	34	Stored inside / outside *
	'D (P)'	2	passivated
Specimen of Category B	'B'	11	Stored inside / outside
	'B(CZ)'	3	HDG in Czech Republic; stored inside
Rusty		19	Stored outside
	In total:	**147**	

** the specimens were stored adverse for 8 weeks and were separated afterwards by storing them 'inside' or 'outside'*

The evaluation starts at temperatures of 250 °C. Due to *Wien's displacement law*, the dedicated radiated energy is too low below this temperature. Consequently, the error susceptibility is too high, as it was described in Chapter 5.3 above. However, based on this research, this low temperature range up to 250 °C is not relevant because at the beginning of a fire convection transfers most of the energy. This can be seen in Figure 6 of Chapter 1.7.1. After 6 – 7 minutes of a nominal standard fire (ISO 834) more energy is transmitted by radiation. At this time, depending on the profile factor, the beams are already approximate 150 °C warm. The difference is therefore nearly negligible.

The evaluation of the results is done individually for each category, all based on the same procedure of the evaluation routine:

1. Determination of the mean value of all samples of the same ‘sample-carrier plate’
2. Median above the mean to reduce measurement noise
   → ‘MV sample-carrier plate’
3. Mean value over all sample-carrier plates (the number of tests per ‘sample-carrier plate’ is taken into account as a weighting factor) per category and storage condition

   Distinction: total mean value (‘MV’); total mean value ‘Inside” (‘MV (Inside)’), total mean value ‘outside” (‘MV (Outside)’); total mean value ‘new” (‘MV (New)’)

In addition, a statistical evaluation for each step (1st to 3rd) was done with respect to the standard deviation, the standard error and the variance. The formulas can be extracted from Appendix ‘EP-T’. Consequently, it is possible to provide information on the dispersion of the values collected per sample category and on the accuracy of the mean per category.

For reasons of clarity, only the overall mean values, ‘MV’, ‘MV (Inside)’, ‘MV (Outside)’ and ‘MV (New)’, of all samples in a category will be discussed. Each category will be first analysed separately in the following.

5.4.1 **Category A**

For category A, and thus a steel in the low-silicon range, the largest number of experiments was carried out. Specifically, samples of various surface conditions were tested. As explained in Chapter 4.3, it was of interest to do a 'worst case' / 'best case' analysis, by covering a wide variety of influences on the zinc layer. These influences can be seen in detail in Figure 31 on the surface of the specimens. While newly hot-dip galvanized specimens are bright and shiny, specimens with an adverse initial storage show a visual duller surface. Accompanied by a longer storage under weathering condition this additionally leads to a higher amount of white rust. Comparing Figure 31and Figure 32 one can see each specimens before and after the thermal exposure in the EP-T, with their related strong surface changes. Even after the thermal impact, one can see a distinct difference between these three different surface conditions.

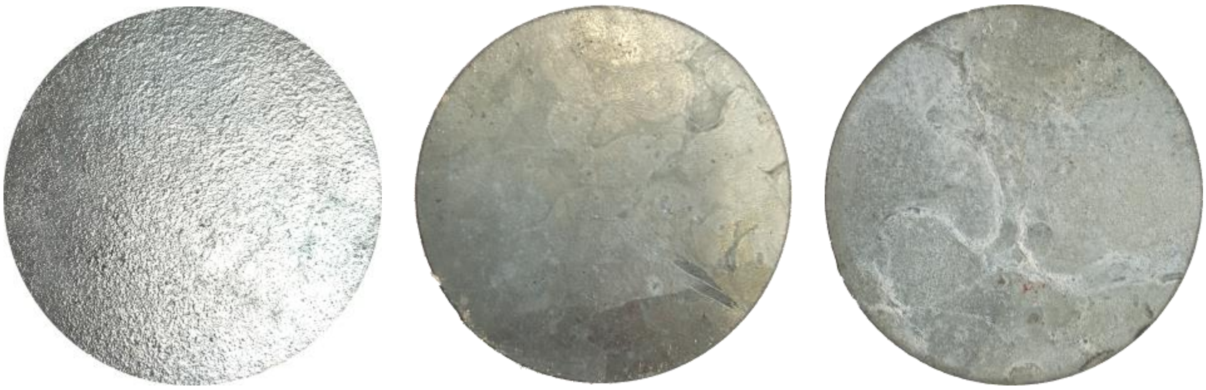

Figure 31: Specimen of category A. Newly HDG (Left); White rust on samples with respective adverse initial storage (Middle: afterwards stored 'inside'; Right: afterwards stored 'outside')

Figure 32: Same specimen of category A as in Figure 31 after the thermal exposure of the EP-T: Newly HDG after 714 °C (left); two samples with respective adverse initial storage: afterwards stored 'inside' (middle) and afterwards stored 'outside' (right) each after 850 °C

The chemical reactions, induced by higher temperatures, differ strongly in depends of the initial condition of the surface. Comparing a ‘newly’ hot-dip galvanized specimen before (Figure 31 on the left) and after (Figure 32 on the left) the EP-T, with a maximum temperature of 714 °C, one can see a distinct colouration change. In addition, these samples exhibit a relatively smooth surface after the thermal impact. Samples with white rust formation, before the test, on their surface reveal an even more pronounced change. As seen at the specimens in the middle and the right of Figure 31and Figure 32 the reaction is higher not only by their colour change but also in terms of roughness. The visual white rust entities can be recognized again at the appropriate parts on the surface after the thermal exposure. In this case they were exposed to temperatures up to 850 °C. With higher temperatures the zinc precipitate as white zinc oxide on the surface. The influence of the temperature is analysed in further detail in Chapter 7.

To these visual findings dedicated measured emissivity curves are shown in the diagrams of both sensors in Figure 33 and Figure 34. In the following, the mean value of the measured emissivity of the different sample groups (distinguished by their storage and properties) is discussed.

Essentially, all ε-T curves have a significantly better behaviour, independent of their surface state, than the Eurocode would specify with a constant value of ε_{EC} = 0.70 throughout the entire temperature range. Towards the end of the measured range, at a temperature slightly below 650 – 750 ° C, the gradients approach or partly exceed this limit value. Both, the curves gained by measuring in the long-wave spectrum, as well as the curves measured in the short-wave range by the pyrometers, show similar patterns of the temperature-time behaviour, although – depending on their surface texture – they are slightly offset from each other.

Independent of the sample properties, the resistance limits of the η- and ζ-phases can be clearly seen. At these points, not only the structure of the dedicated zinc layer changes, but also the respective emissivity. The two resistance limits at 419 °C of the η-phase and at 530 °C of the ζ-phase are marked in red in the related diagrams. The functionality of the EP-T could therefore be verified.

Freshly galvanized samples ‘MV (New)’, with their very shiny surface (see Figure 31, left), have a very low initial emissivity. Their initial value is below $\varepsilon \leq 0.10$. After reaching the first resistance limit, the emissivity increases slightly. After the melting point of the η-phase, where there is no significant high impact, the emissivity remains at a level of about ε = 0.10 – 0.15. In contrast, after exceeding the second resistance limit at approximately 530 °C the emissivity increases significantly and rapidly, independent of the measured wavelength range.

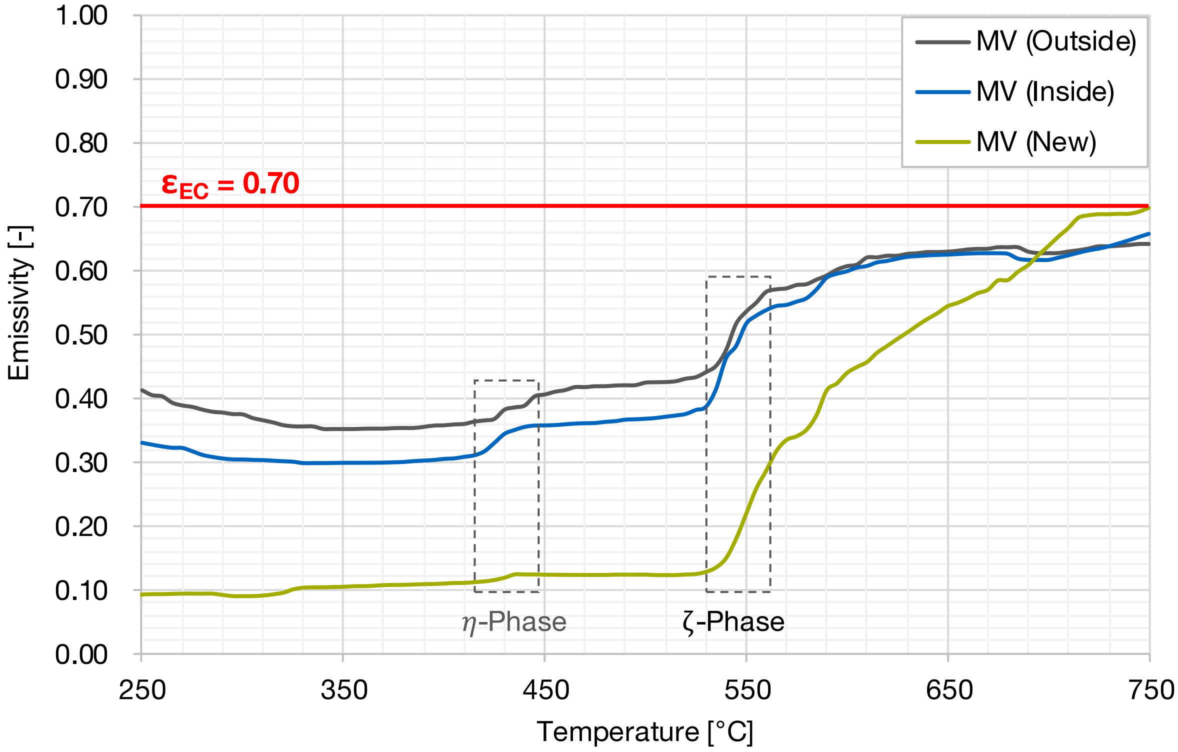

Figure 33: Emissivity evaluation of category A specimen; Wavelength range 3MH1: 2.3 μm

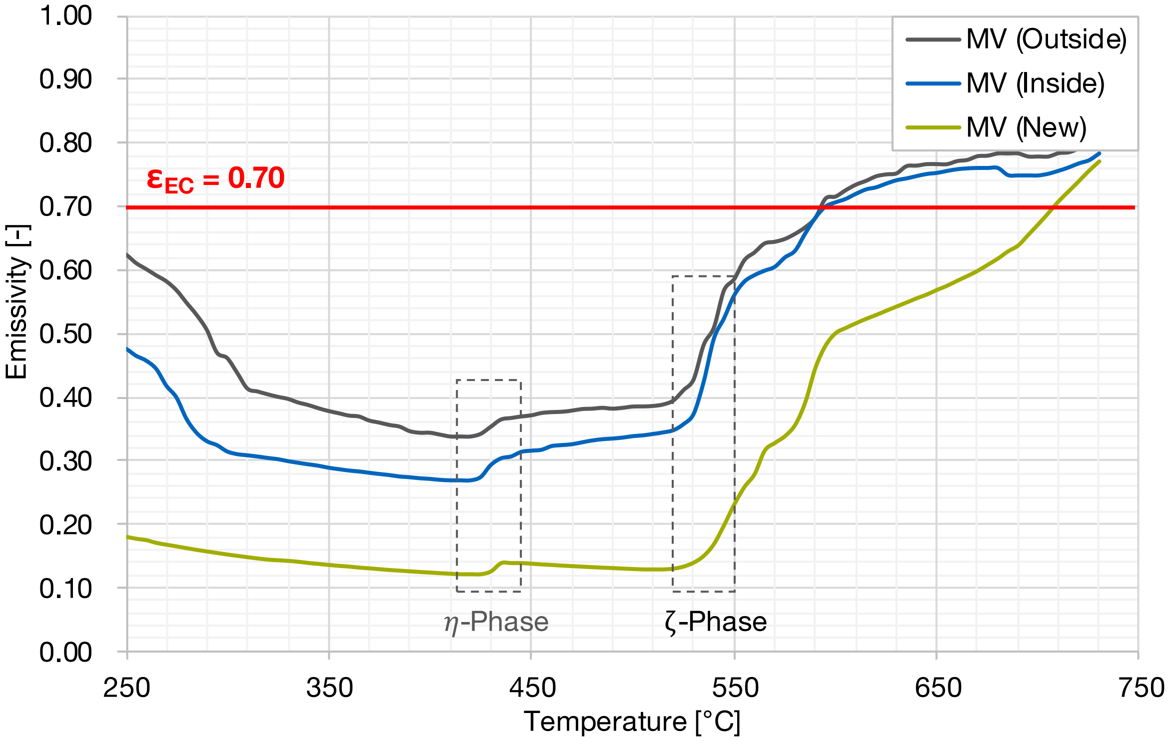

Figure 34: Emissivity evaluation of category A specimen; Wavelength range LT: 8 – 14 μm

Samples that have been initially stored very unfavourably, and thus cover a case that will not occur in reality, exhibit significantly higher emissivities compared to relatively newly galvanized samples. This behaviour occurs regardless of their subsequent storage. The reason for this is the existing white rust on the surface, which, depending on the further storage, was more or less pronounced on the sample surface. This can be clearly seen in Figure 33 over the total temperature range up to 700 °C.

Even the subsequent storage condition has a distinct influence on the samples. Although the initial status of the surface was the same, a stronger white rust contaminated surface appears on the specimens ‘MV (Outside)’ with an additional outside storage of one year (see Figure 31). The emissivity is again 5 to 10 % higher than for specimens that have been stored subsequently inside ‘MV (Inside)’. Nevertheless, in both cases the emissivity exhibits at the beginning, for example at 350 °C, a level of ε = 0.30 – 0.35, which is lower by half compared to ε_{EC} = 0.70. As seen before, the emissivity increases at both resistance limits. While the influence of the η-phase is more pronounced than by newly HDG samples, the ζ-phases again has the same major influence, which leads in turn to a strong increase of the emissivity. In higher temperature segments, a value around 0.70 is reached.

Essentially, it can be concluded that a pure zinc coating, as it is the case with category A, provides a very small and thus good emissivity with respect to the steel structures in fire. An even better emissivity results for specimen with an unweathered state. With increasing white rust formations on a surface, the emissivity increases. The influence of the white rust can be seen especially at the beginning of the temperature impact. With an increasing temperature the white rust influence disappears mostly. Due to the roughness of the oxidation layer, a larger emissivity is achieved compared to the smooth η-phase surface. More details follow in Chapter 7.3.

The mean values, of the total data, shown in Figure 33 and Figure 34 can be found in Appendix ‘EP-T’. The dedicated statistical values show that the respective averages provide very good representative results. For category A, as shown in Table 16, the maximum standard error of the mean (MV) is only about 1 – 3 % for the *3MH1* infrared sensor. In addition, the maximum values of variance and standard deviation, calculated for the complete measured data of the analysis in the temperature range of 250 – 750 °C, are shown for a measuring wavelength of 2.3 µm.

Table 16: Statistical analysis of the EP-T for category A

Category **(number of specimens)**	**max. variance (S^2) [-]**	**max. standard deviation (S) [-]**	**max. standard error (SE) [-]**
MV Total (38)	0.0046	0.0675	0.0109
MV Inside (21)	0.0064	0.0801	0.0130
MV Outside (17)	0.0050	0.0709	0.0115
MV New (6)	0.0064	0.0801	0.0289

5.4.2 **Category B**

Different samples with different HDG conditions have been tested for category B. Due to the collaboration with Prof. František Wald of the Czech Technical University (CTU) in Prague, it was possible to get different surface conditions for this category, which is not only based on their storage situation but also for their alloy formation. In the following, the mean value of the measured emissivity of different sample groups (distinguished by their storage and properties) is discussed.

First the samples, which have been produced in Germany, will be discussed. The tested specimens were partly stored inside (‘MV (Inside)’) and partly stored outside (‘MV (Outside)’) after the HDG as described in Chapter 4.3.2. The consequential influence on their surface can be seen in Figure 35. Being influenced by weathering conditions, the surface loses its shiny optic over time. However, a visual white rust formation, in contrast to category A, could not be spotted. Again, the samples can be compared before (Figure 35) and after (Figure 36) the thermal exposure.

Figure 35: Specimen of category B: Stored inside (left); stored outside (middle); specimen of CTU, stored inside (right)

Figure 36: Same specimen of category B as in Figure 35 after a thermal impact of 750 °C in the EP-T: Stored inside (left); stored outside (middle); specimen of CTU, stored inside (right)

Category B samples show, in the unweathered condition, a slightly higher emissivity over the complete temperature range compared to galvanized samples of the category A. The curves in the long-wave and short-wave range, show similar behaviour patterns. Since, if at all, only a very thin pure zinc coating is present in category B, the resistance limit of the η-phase is almost not visible in the ε-T curve. On the contrary, the resistance limit of 530 °C is again clearly apparent due to the existing thick ζ-phase in the alloy layer. Consequently, a nearly constant emissivity of ε = 0.30 results up to a temperature of about 530 °C. After reaching this tipping point, the emissivity increases in stages, which is an indication of layers with different iron contents within the crystal structure of the ζ-phase. At temperatures of approximately 600 °C to 700 °C the emissivity reaches a plateau of ε = 0.45 – 0.50. In the elevated temperature range of over 700 °C the emissivity increases again and equalizes to the value of the Eurocode and thus has a level of ε_{EC} = 0.70 again.

Externally stored samples 'MV (Outside)' exhibit an increased emissivity. This difference is even more pronounced than in category A. Looking at the diagrams in Figure 37 and Figure 38 one can see that the samples approach an emissivity of about ε = 0.55, if they were stored for several month in weathered conditions. Reaching the melting point of the ζ-phase leads to an increasing emissivity. In complete contrast to all other tested samples the emissivity falls again after rising until a temperature of just below 600°C. According to the scientifically proven theory, the emissivity rises accompanied by an increasing temperature at constant surface conditions. Therefore, a phase transformation, with an alteration of the top zinc alloy layer must has been preceded. At temperatures above 650 °C, the emissivity values of both sample groups align again and have an emissivity of ε = 0.70 towards the end of the measured temperature.

Since roughness dominates the surface of these category B samples, a measurement in a higher spectrum of 8 – 14 µm, especially in the range of temperatures up to approximately 550 °C, is more reliable than the measurements in a short wavelength range. This is clearly visible in the area of the ζ-phase resistant temperature around 530 °C, which is not recognizable in the short-wave spectrum. This fact arises also the lack of information for materials such as concrete and wood in Table 8 of the VDI / VDE in Chapter 3.2. However, at higher temperatures the measurements of the shorter wavelength spectrum get more reliable again.

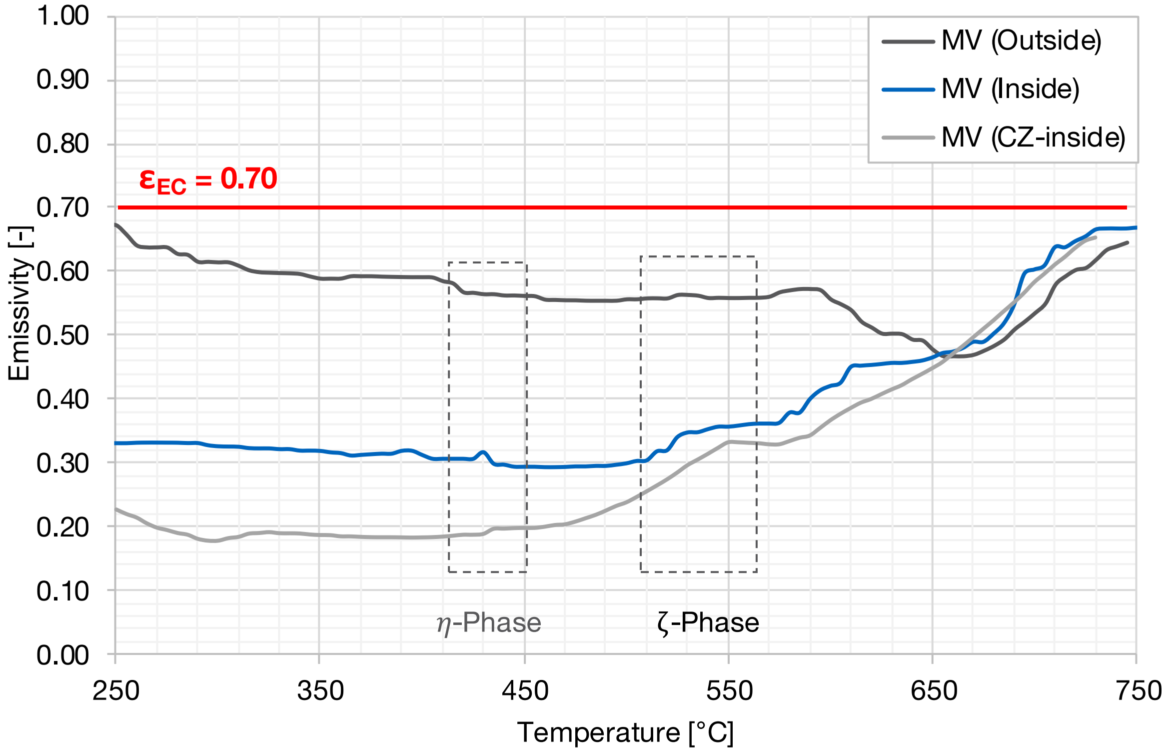

Figure 37: Emissivity evaluation of category B specimen; Wavelength range 3MH1: 2.3 μm

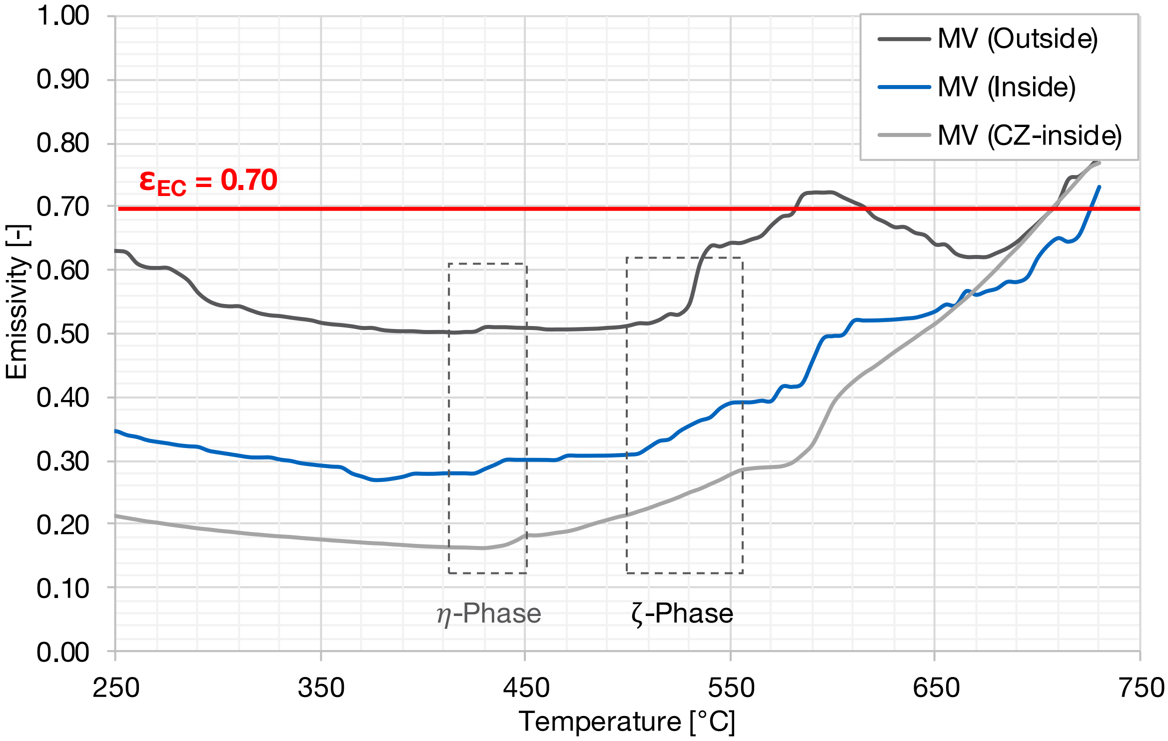

Figure 38: Emissivity evaluation of category B specimen; Wavelength range LT: 8 – 14 μm

The surfaces of the Czech test sample (right sample in Figure 35) show a different, smoother surface compared to the other specimen groups of category B. This is due to their different silicon content and their different galvanizing. As a result, the reduced roughness of the different surfaces leads to different, lower emissivity values. In addition, to the measurement problematic before, the infrared sensor *3MH1* shows again good results. Consequently, the measured ε- T curves of the different wavelength are more or less identical. With an initial emissivity of about $\varepsilon \leq 0.20$, it is 10 % lower than the comparable mean value of the 'MV (Inside)' emissivity. A small change at the first resistance level of 419 °C indicates a very thin η-phase. At around 500 °C the ε- T curve starts to rise, reaches a short plateau at 550 °C and rises again until the curve aligns with the other curves of category B samples.

The related mean values shown in Figure 35 and Figure 36 are shown in Appendix 'EP-T'. The dedicated statistical values show that the respective averages provide good representative results. In contrast to category A, as shown in Table 17, the maximum standard error of the mean (MV) is slightly higher with about 7%.

Table 17: Statistical analysis of the EP-T for category B

Category (number of specimens)	**max. variance (S^2) [-]**	**max. standard deviation (S) [-]**	**max. standard error (SE) [-]**
MV Inside (7)	0.033	0.182	0.069
MV Outside (4)	0.032	0.178	0.067
MV CZ-inside (3)	0.004	0.066	0.038

5.4.3 **Category D**

Category D is also based on a high number of tests. Since this high-silicon region forms the complete counterpart to the low-silicon region regarding the zinc layer formation, the samples had exactly the same storage conditions. After an adverse initial storage for eight weeks, as described in Chapter 4.3.2, one part of the samples was stored inside and the other outside for up to one year. Consequently, some specimen exhibit also a white rust contaminated surface. Examples for different surface conditions are shown in Figure 39.

Figure 39: Specimen of category D: samples with respective adverse initial storage (Left and middle: afterwards stored 'inside'; Right: afterwards stored 'outside')

Figure 40: Same specimen of category D as in Figure 39 after the thermal impact of the EP-T: samples with respective adverse initial storage after 800 °C (left) and 850 °C (middle & right)

It can be seen that, according to the differences in the zinc alloy formation of the particular categories, also a different image of emissivity occurs. All ε-T curves, regardless of the measured wavelength range, have a significantly higher initial level than the samples of category A and B. While for lower temperatures up to 400 °C the emissivity is very high and constant, it falls in the range of 400 – 530 °C for about 10 % before rising again after exceeding the ζ-phase resistant limit at 530 °C. This in-between behaviour can be attributed to a white rust formation on the surface, disappearing after a certain level of temperature. This category is based on a behaviour closest to the Eurocode with values between ε = 0.50 – 0.75

in the entire temperature range. The difference between the samples stored ‘inside’ and ‘outside’ with adverse initial storage is, as with category A, in the range of 5 – 10 %.

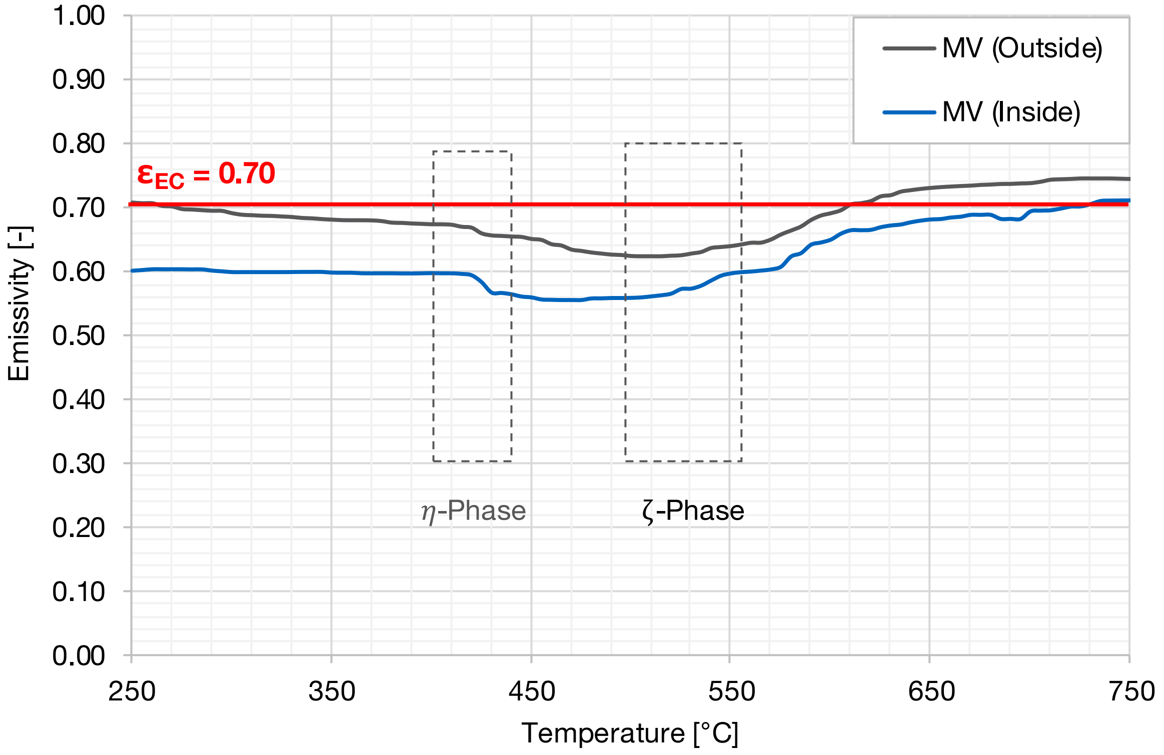

Figure 41: Emissivity evaluation of category D specimen; Wavelength range 3MH1: 2.3 µm

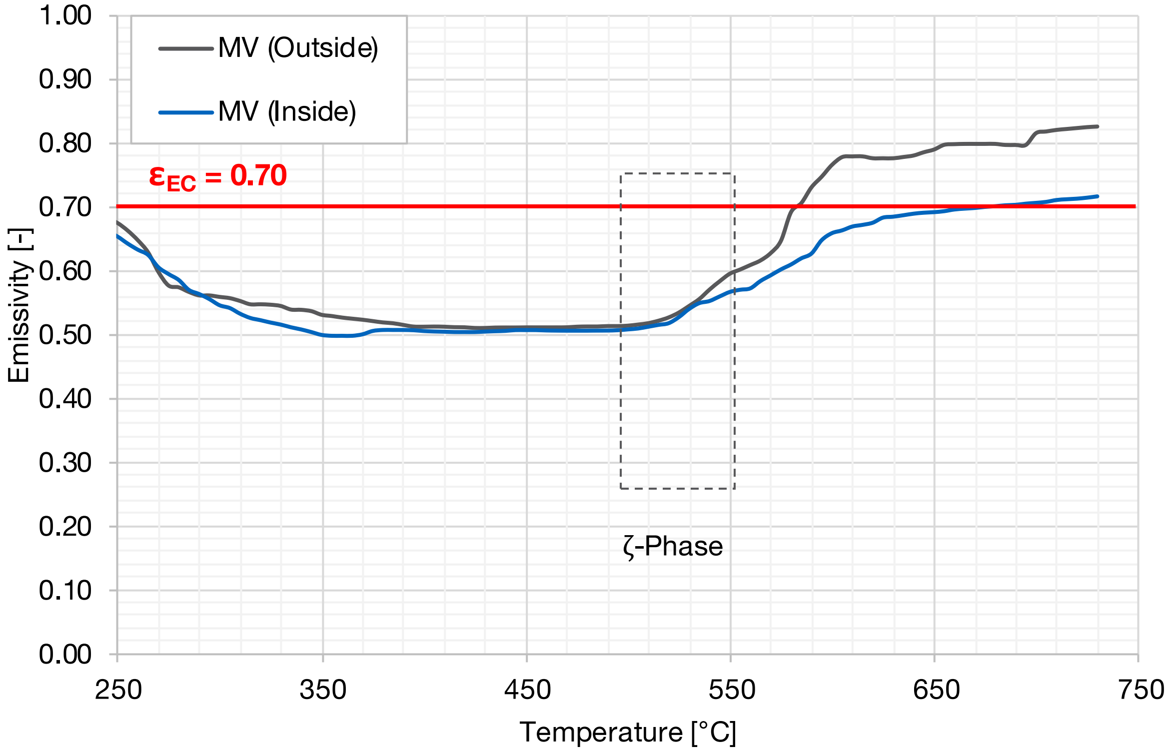

Figure 42: Emissivity evaluation of category A specimen; Wavelength range LT: 8 – 14 µm

The chemical reactions, taking place on surfaces of category D, are stronger compared to these of the other two categories. This can be seen not only by the colouration in Figure 40, but also by the final roughness of the surface after the thermal impact. Places of white rust formations can be recognized even after the temperature influence. In some cases, as this can be seen in Figure 40 in the middle, the zinc alloy layer gets separated from the steel substrate. Consequently, bubbles with a thin but hard zinc oxide shells result.

The mean values shown in Figure 41 and Figure 42 can be found in Appendix ‘EP-T’. The dedicated statistical values show that the respective averages provide very good representative results. The maximum standard error of the mean (MV) is in total in the range of 1.5 %. For measured values of the unfavourable and externally stored samples this value is slightly increased (3 %), given that the samples were contaminated with varying degrees of white rust.

Table 18: Statistical analysis of the EP-T for category D

Category (number of specimens)	**max. variance (S^2) [-]**	**max. standard deviation (S) [-]**	**max. standard error (SE) [-]**
MV Total (23)	0.0049	0.0702	0.0146
MV Inside (12)	0.0023	0.0484	0.0140
MV Outside (11)	0.0091	0.0953	0.0287

5.5 **Infrared camera experiments**

As an additional method of analysis, an infrared thermal imaging camera was used. The aim was to validate the results of the pyrometer measurements and to get a more detailed look at the differences of a galvanized surface. Zinc flowers, visible or invisible to the human eye, have different reactivity with respect to corrosion resistance according to *Seré et al.* [11]. In the visible range, there is also an optical colour difference. Hence, it can be concluded that also different emissivities are to be expected. In order to quantify this, the experiments were again carried out in the test stand (EP-T), developed for this research, by implementing an additional thermal imaging camera of the type PI 400 from Optris GmbH.

The PI 400 measures in the range of 7.5 – 13 µm and is therefore located in the rather long-wave spectrum for metal surfaces. Since errors in the measurement of metallic surfaces increase with accompany increasing wavelengths due to the radiation intensity, there are also special metal surface cameras that measure in a correspondingly very small wavelength range of 0.50 to 0.54 microns. However, due to the shift in the radiation spectrum (see Chapter 2), these cameras can only record infrared radiation above a temperature of 900 °C. However, in the underlying research project, the results in the temperature range from 20 °C to a maximum of 850 °C are of interest. The chosen IR thermal imaging camera delivers these. With a sensor resolution of 382 x 288 pixels, it offers 80 frames per second in the temperature range up to 900 °C. Despite possibly existing error rate, the PI 400 provides the necessary insights.

5.5.1 **Setup of the tests**

For the purpose of validating the EP-T experiments with the IR-camera, the IR-pyrometer with the wavelength range of around 2.3 µm was additionally used for comparison purposes in the experiments. In addition, for the first test a reference measuring point – a 'black emitter' – was implemented in the specimen. The latter was done with the help of a hole in the ratio diameter / depth < 1:5. The procedure for this is described in Chapter 5.1.

The complete experimental procedure was carried out according to the Emissivity Performance-Tests (EP-T) of the pyrometers. Again, the actual temperatures of the specimens were determined by four thermocouples. In addition, the analysis was carried out by the detected heat energy using the thermal imaging camera and the pyrometer. The calculation of the emissivity from the pyrometer *3MH1* was carried out analogously to the procedure before. In contrast, the evaluation of the emissivity of the IR-camera was carried out in 25 °C steps. Depending on the thermocouple temperature measurement, the emissivity of the radiated temperature was digitally adjusted every 25 °C via the associated software 'PI-

Connect’ from Optris GmbH of the thermal imaging camera until the displayed temperature also had the same multiple of 25 °C. This was done continuously for the temperature steps up to a maximum temperature of 800 °C. From this, a graph that is dependent on both the temperature and the emissivity and the respective measuring field of the sample surface can be generated.

In order to illustrate the images of the thermal camera, a setting was chosen, which indicates less radiating areas white and emission-rich and therefore strongly radiating areas black. The result is an adaptable colour scale. Consequently, an explicit colour does not correspond to a defined temperature, but adapts itself to each measuring step of the occurring maximum and minimum temperature, so that the colours stand at all times in reference to all present temperatures on the surface of the dedicated temperature step.

Figure 43: Temperature depending colour scale for the IR thermal camera

5.5.2 Evaluation of the IR-camera tests

Due to the parallel measurement of the short-wave measuring pyrometer at 2.3 μm and the long-range thermal imaging camera at 7.5 – 13 μm, the evaluated emissivity can be compared with each other at least in one measuring spot. However, under certain circumstances this can also be problematic since a single pyrometer measuring spot can have quite different properties than the remaining surface.

When comparing the two measurements, it should be noted – based on Figure 12 – that at lower temperatures up to 400 °C, one is situated in a longer wavelength spectrum. Consequently, according to the *Planck’s radiation law*, the thermal camera measures a higher radiation intensity in the range between 7.5 – 13 μm than the pyrometer *3MH1*. Above 400 °C, the wavelengths are sufficiently short and the pyrometer experiences a higher radiation intensity than the IR-camera. Depending on the area, the measuring system with the highest radiation intensity provides the, least error-prone, value for the emissivity. This is discussed in further detail in the analysis of Chapter 7.2.

5.5.2.1 Category A – Low silicon steel

The test specimens used for these experiments correspond to the ‘inside’ and ‘outside’ stored samples, with initial adverse storage. Therefore, the surface is, in addition, partly loaded with white rust. The surface of the galvanized low-silicon samples can be divided into lighter and darker areas. This is related to the zinc flowers as already mentioned.

Below are images of the IR-camera in combination with a photo of the category A sample ‘10’ before (left column) and after (right column) the experiment and superimposed step by step with the IR-image by 20 %; 60 %, 100 %. This ‘layering’ can thus illustrate the radiation behaviour on the surface. The sample is shown stepwise at temperatures of T = 200 °C, 400 °C, 600 °C and 800 °C.

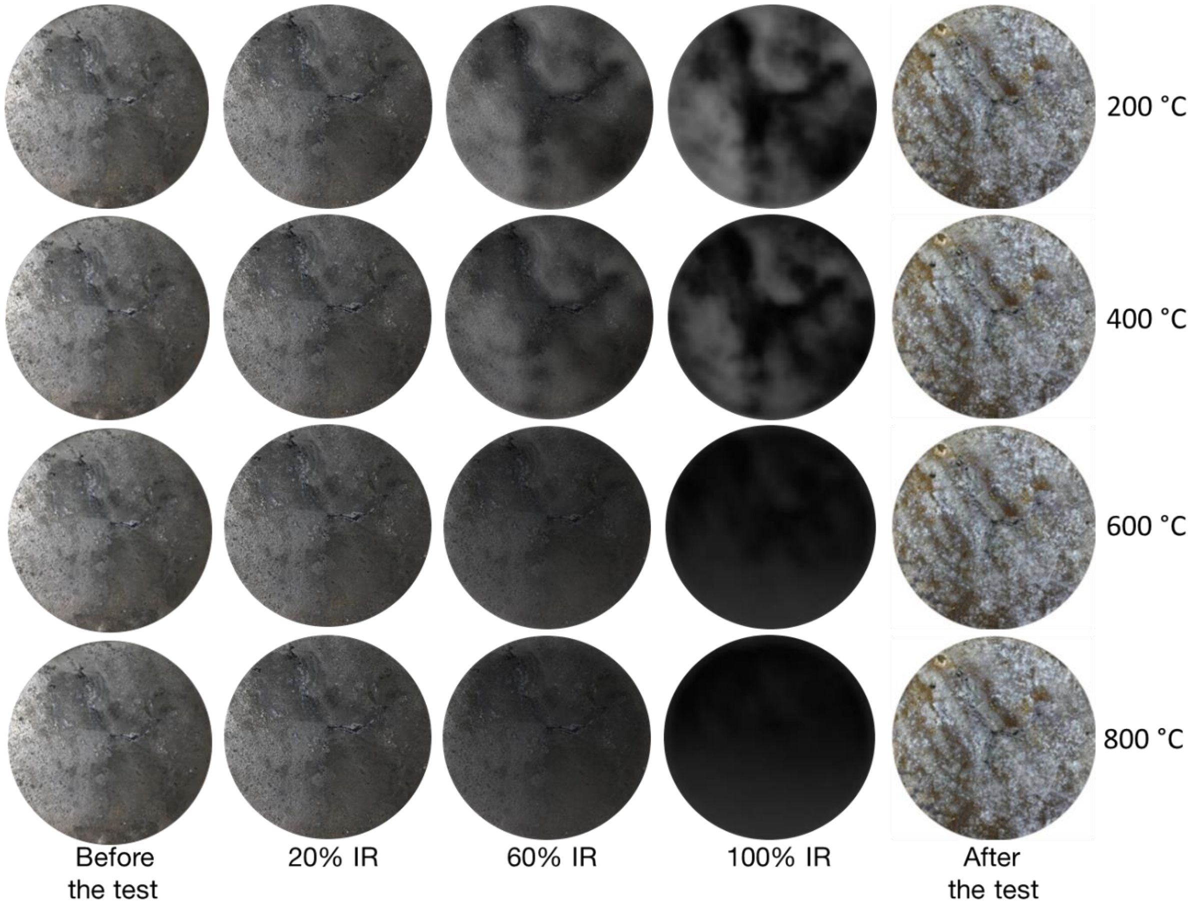

Figure 44: Superimposition of the IR-camera picture with the original picture of a category A sample at different temperatures

As the temperature increases, the sample becomes darker according to the colour setting of the thermal infrared camera. It can be seen that areas of brighter and darker appearance are present. For areas of the darker surfaces, this results in a higher emission compared to areas of the brighter surfaces.

By analysing the 200 °C series (1st line in Figure 44), one can clearly see that the bright areas of the galvanized surface are in line with the bright spots of the IR-camera, which illustrate a range of lower emissivity. Conversely, the optically darker appearing areas of the uninfluenced sample also have darker colours in the thermal image. As the temperature increases step by step from 200 °C to 800 °C, the contrast between these areas decreases, as the shift to the short-wave range provides a generally very high level of radiation on the surface. In addition, for temperatures of 419 °C and higher, the pure zinc coating (η-phase) begins to melt. Above 530 °C, the resistance limit of the ζ-phase is exceeded, which leads to an approximately equal iron-zinc layer at the top of the surface. Consequently, the heat radiation behaviour of the areas approximates and exhibit similar colours for thermal imaging at 600 °C and 800 °C.

To determine the emissivities, several measuring points were evaluated in both bright and dark areas of the surface. An average value was calculated from the obtained emissivity of the respective measuring spots of each specific region. The latter are shown and compared to the analysis of the *3MH1* infrared sensor in the following diagram.

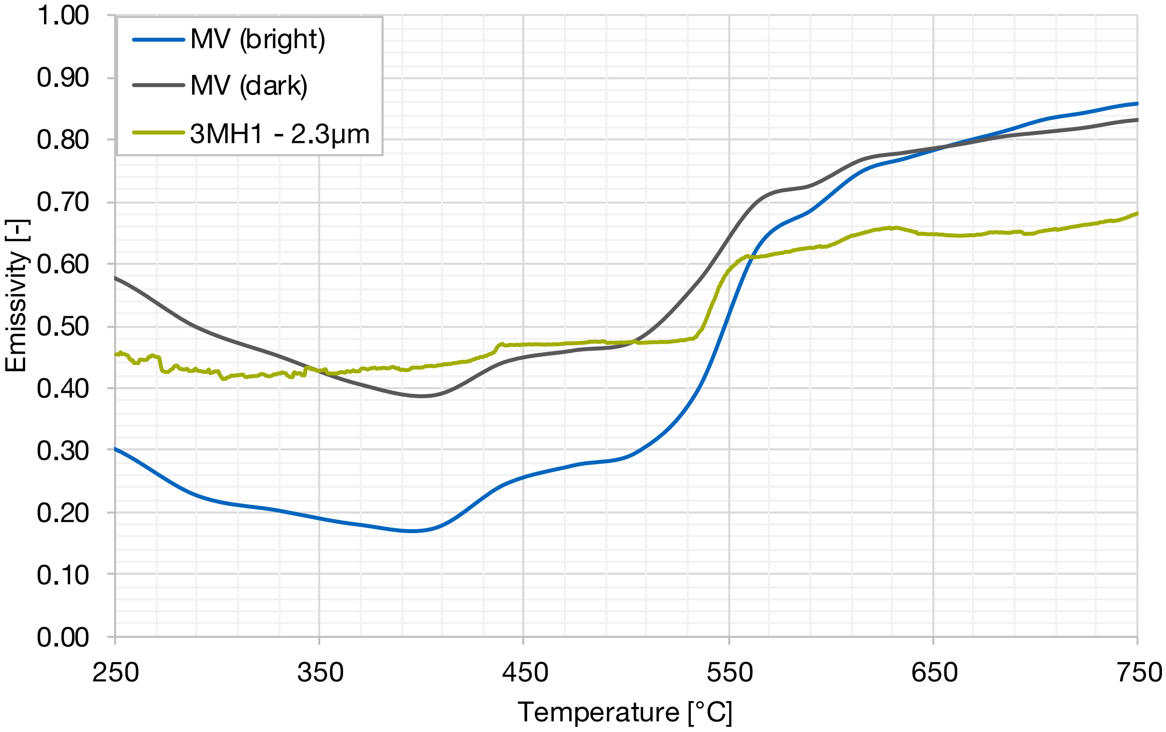

Figure 45: Evaluated emissivity for bright and dark spots/spangles of category A (IR-camera) in comparison to the infrared sensor (3MH1 – 2.3 µm)

The optical findings can be quantitatively confirmed by the results of the thermal imaging camera. Brighter and darker spangles have significantly different emissivities. At the beginning of the emissivity-temperature curve, a larger difference of the two areas can be seen. The maximum difference in emissivity in this test is 0.20 at a temperature of about

525 °C. Thereafter, the different curves of the two areas approach due to the inhomogeneous outer zinc layers, which change their composition from this point on. This will be discussed in further detail in Chapter 7.6. Towards the end, both emissivity curves are in a range of $\varepsilon > 0.70$. However, due to the measurement inaccuracy in the relatively long-wavelength spectrum of the camera, these results are no longer applicable in the higher temperature range and have a character of an informative data.

The influence of the white rust on this adverse stored specimen can be seen at the beginning. However, it decreases with increasing temperatures as already seen in Chapter 5.4 of the EP - T. A complete summary for this effect is given in Chapter 7.3.

5.5.2.2 Category B – Sebisty steel

Samples of Sebisty steel (category B) have a bright but rougher appearance. Due to a stronger reaction of the zinc and the iron in the process of HDG, the iron can partly disturb the outer zinc alloy phase. Therefore, there might be some areas on the surface, which appear visually darker than the rest of the surface.

If an image of a newly hot-dip galvanized category B sample before the test (in Figure 46 left column) is superimposed with infrared thermal images of the same sample during the measurement at temperatures of T = 200 °C, 400 °C and 600 °C the following depiction can be given. For comparison purposes, the image of the same sample after the heating is also shown on the right side of each row in Figure 46.

Whereas at the beginning some zinc spangle can be highlighted by the picture of the infrared camera, the spangles disappear later on. The surface gets more homogenous, after the transformation of the ζ-phase, if the temperature rises up to about 600 °C. For lower temperatures, there is quite no difference visible between the temperature steps 200 °C and 400 °C, by this analysis method. Comparing the depiction of Figure 46 with the measured temperature-dependent emissivity curve of Figure 47, one can see that this is in line with the curves, since there is no change in the emissivity of the surface. The emissivity – independent of the measuring infrared spectrum – is very low at the beginning. The *3MH1* sensor, which measures at a wavelength of 2.3 µm, exhibits an emissivity of 0.23 until a temperature up to 500 °C, whereas the camera shows an even lower value of 0.10 – 0.15 depending on bright or duller spangles. Subsequently, each curve raises and ends at an emissivity $\varepsilon < 0.60$. As the surface of the Sebisty steel is rougher, the temperature-emissivity curves of the different measurement methods match better.

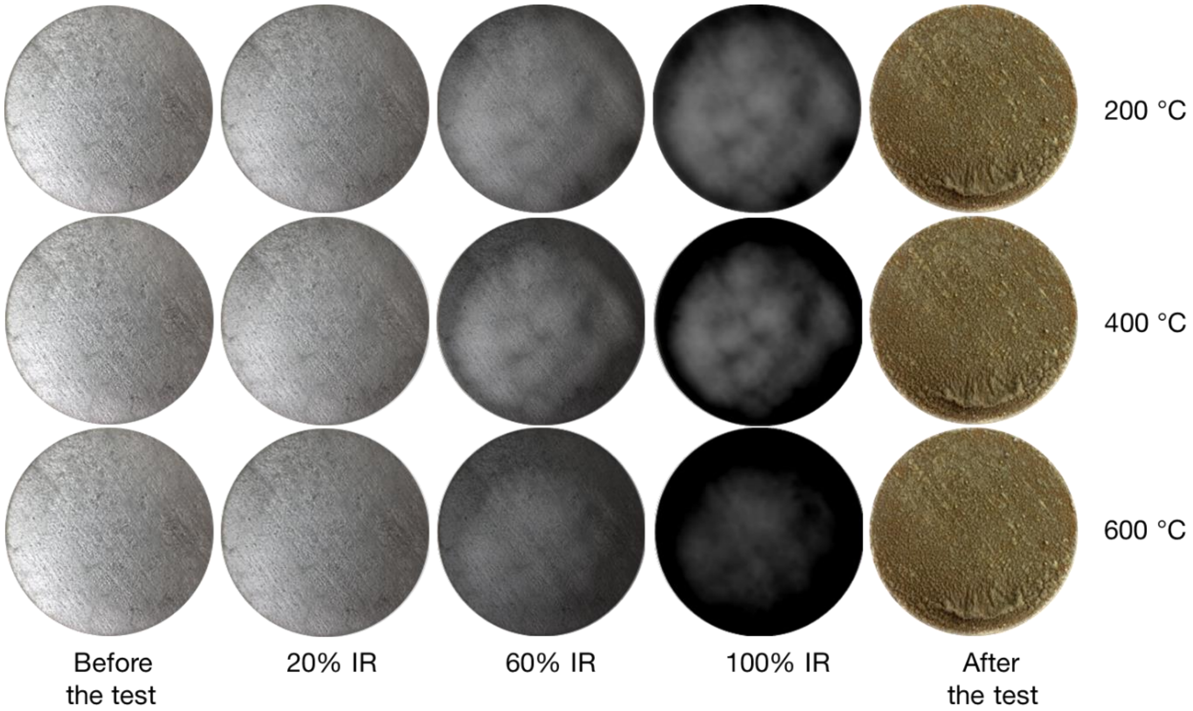

Figure 46: Superimposition of the IR-camera picture with the original picture of a category A sample at different temperatures.

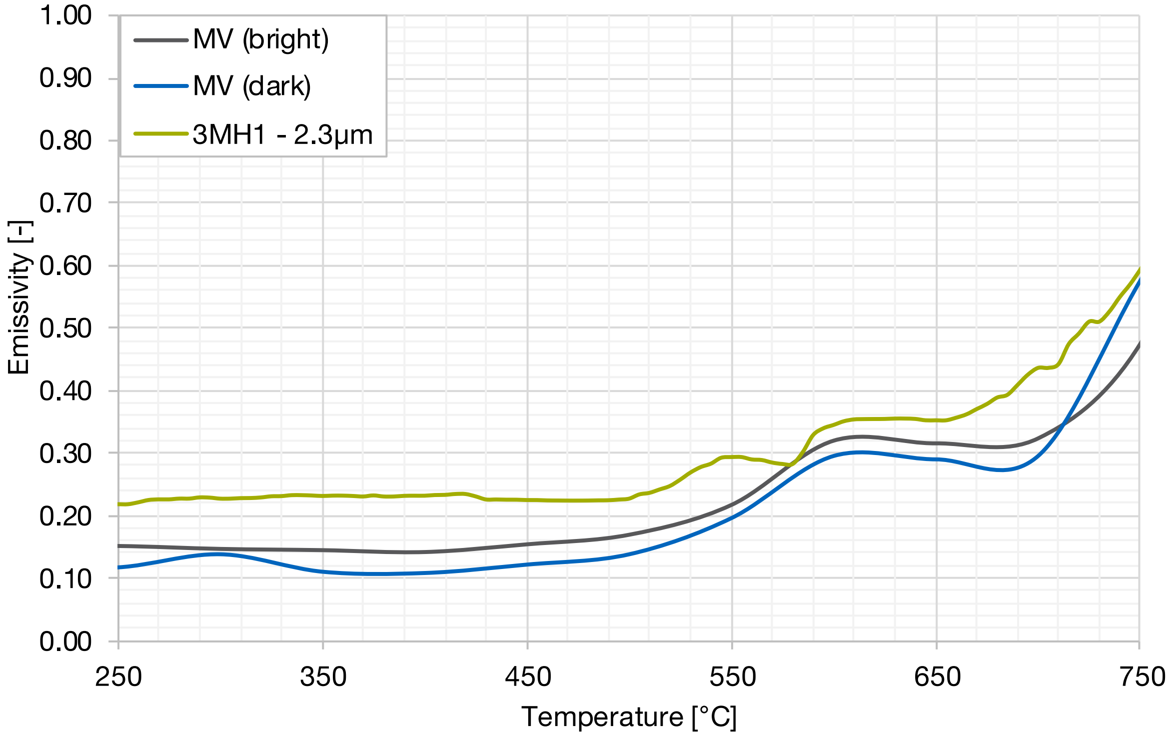

Figure 47: Evaluated emissivity for bright and dark spots/spangles of category B (IR-camera) in comparison to the infrared sensor (3MH1 – 2.3 µm)

5.5.2.3 Category D – High-silicon steel

Compared to the low-silicon steel, the samples of high-silicon steel have a more homogeneous colouration. Due to the higher iron content of the outer iron-zinc alloy phase and, thereby, a lower zinc content, they appear visibly darker and duller than samples of category A.

If an image of a category D sample before the test (in figure 34 left) is superimposed with infrared thermal images of the same sample during the measurement at temperatures of T = 200 °C, 400 °C and 600 °C the following depiction can be given. For comparison purposes, the image of the same sample after the heating is also shown on the right side of Figure 48.

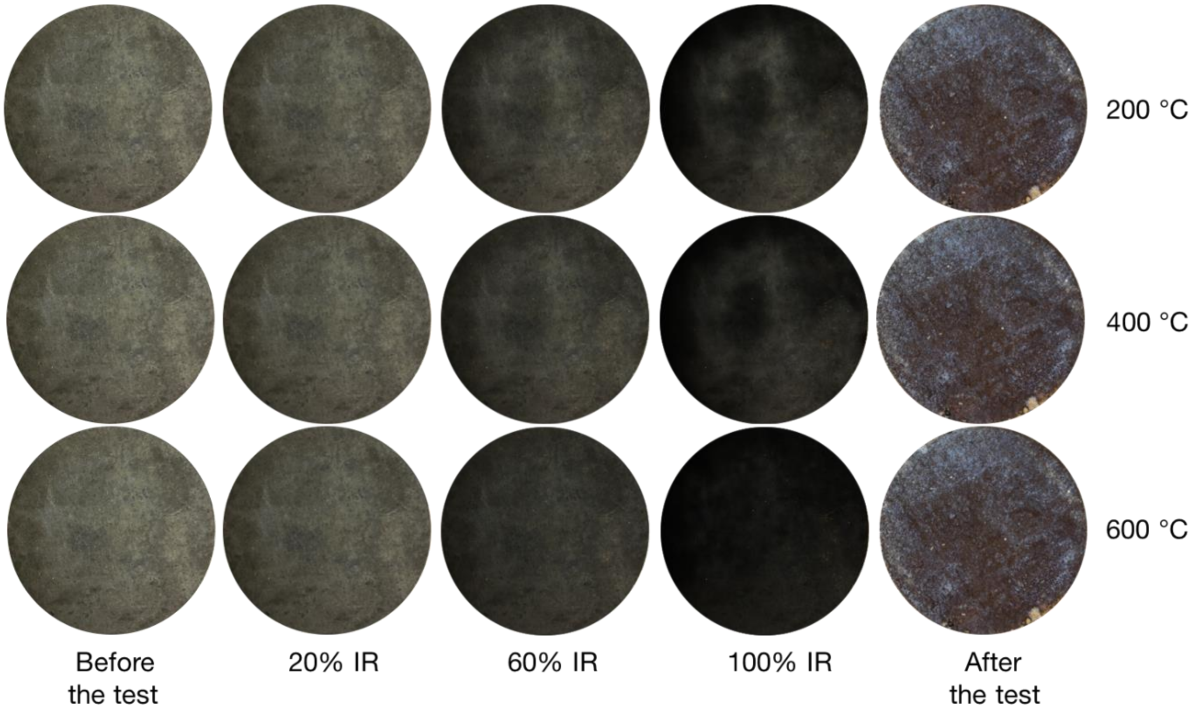

Figure 48: Superimposition of the IR-camera picture with the original picture of a category D sample at different temperatures.

While there are almost no differences visible on the sample surface besides the white rust, the images of the thermal camera additionally show bright and dark spots. Each of these areas was again evaluated, using several measuring points. Both the thermography and the determined emissivity curve in Figure 49 show that even category D samples exhibit stronger and weaker radiating areas. The present emissivity differences illustrate that spangles also occur on galvanized high-silicon steel specimens, although these are not always visually recognizable. Since the emissivities correlate with each other after the resistance limit of the outer ζ-phase, the assumption that the emissivity-influencing spangles are present only in the uppermost layers and are dependent on the prevailing crystallographic orientation can be made. This has to be analysed in detail (see Chapter 7.6).

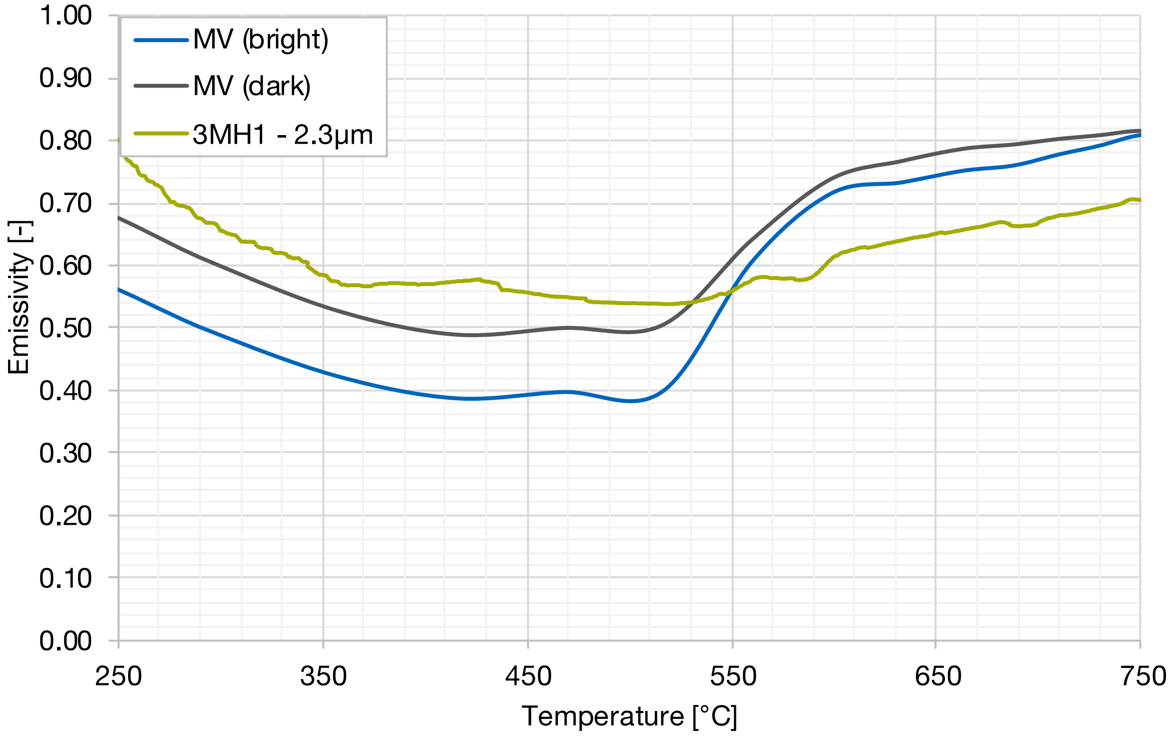

Figure 49: Evaluated emissivity for bright and dark spots/spangles of category D (IR-camera) in comparison to the infrared sensor (3MH1 – 2.3 µm)

As with category A, the white rust influence of the adverse storage conditions is again evident. Despite this influence, the difference between bright and darker areas up to the resistance limit at 530 °C is, throughout the course of the curve, approximately 10 %. Compared to category A, both emissivity curves, as in the EP-T experiments in Chapter 5.4, are significantly higher and thus exhibit greater emissivities. However, the bright areas of category D are approximately in the range of the darker areas of category A.

In addition, one can see that for a longer wavelength spectrum, the emissivity is lower until the resistant limit of the ζ-phase, and higher afterwards, if it is compared to the short wavelength spectrum of the *3MH1* sensor.

5.6 **Total emissivity of the EP-T**

If the emissivity, which was gained from the EP-T, is summarized over both wavelength ranges of the two infrared sensors *3MH1* and *LT* stepwise over the temperature, the following values represented in Table 19, Table 20 and Table 21 are obtained. As previously mentioned, the measured values below 250 °C are not taken into account due to the measurement inaccuracy of the sensors.

5.6.1 **Category A**

Category A offers lower values, especially in comparison to the Eurocode (ε =0.70). Although a situation was produced with the samples ‘MV (Inside)’ and ‘MV (Outside)’, the values are better, with respect to the fire resistance. In addition, freshly hot-dip galvanized samples ‘MV (New)’ show an even superior behaviour. It should be highlighted once again that these components ‘MV (Inside)’ and ‘MV (Outside)’ have been stored against any regulations. This unfavourable condition would not be accepted by an owner of a building site. In practice, due to storage and transportation, a surface condition between ‘MV (New)’ and ‘MV (Inside)’ will occur. With 0.125 and 0.327, the dedicated emissivity values for temperatures up to 530 °C are much better than the comparative normative value of 0.70 from the Eurocode [17]. Even after the temperature of the resistant limit of the ζ-phase, the mean values of both investigated conditions are below this stated emissivity ε_{EC}.

Table 19: Total emissivity (EP-T) of category A

Temperature range [°C]	MV (Inside)	MV (Outside)	MW (New)	EC
250-530	0.327	0.399	0.125	0.700
530-650	0.603	0.623	0.386	0.700
650-750	0.698	0.711	0.657	0.700

In order to guarantee a simple incorporation and application of the achieved results for engineers on the one side and for the construction industry on the other side, a two-stage emissivity is used. This is shown in the following Figure 50, in which again the exact measured values from the Emissivity Performance-Tests are shown.

Due to this two-stage system ($\varepsilon = 0.35 \leq 500$ °C; $\varepsilon = 0.70 > 500$ °C), the unfavourable case for category A can be completely covered. Minor exceedances in the range up to 500 °C can be compensated by the significantly higher values of the simplification in comparison to the measured emissivity for temperatures above 500 °C.

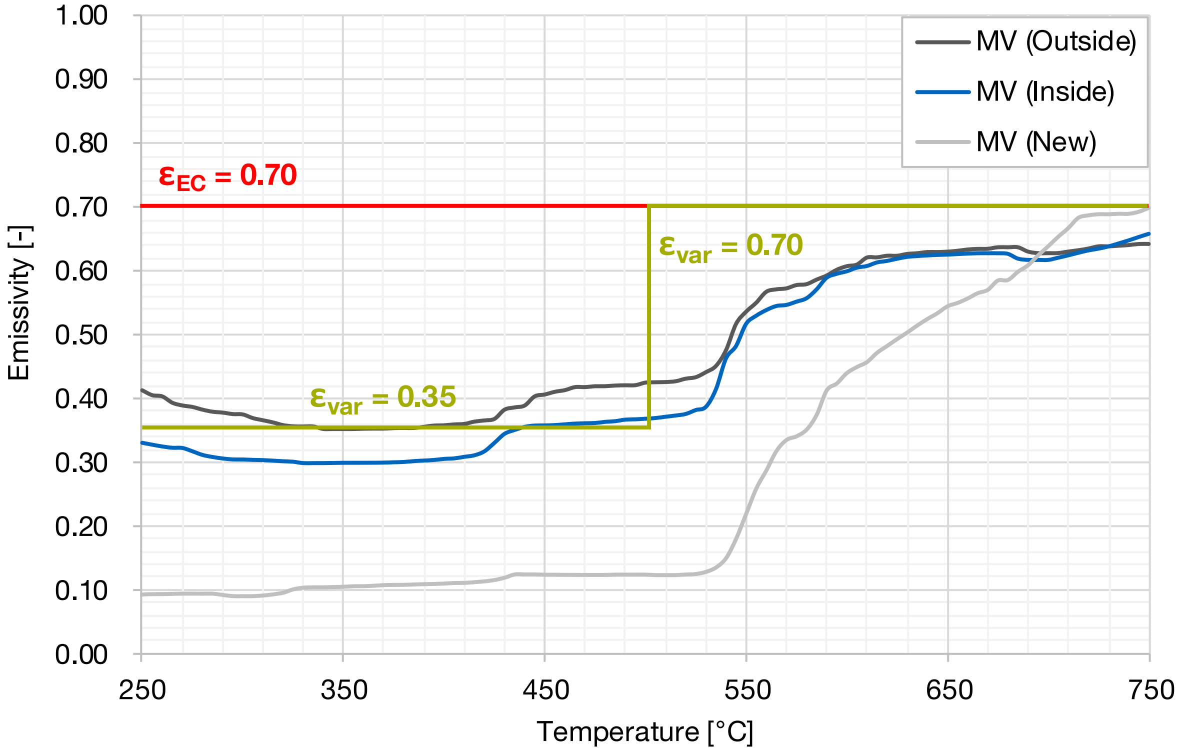

Figure 50: Comparison of the normative emissivity with a two-stage emissivity approach for category A

5.6.2 **Category B**

For category B, the influence of the storage condition is more pronounced. Internally stored samples form a patina, where a positive surface condition is maintained. If steel members are stored unfavourable after galvanizing, a condition is developed which leads to a minor positive effect regarding fire protection. This effect can be seen by the mean values of the emissivity for different temperature steps.

Table 20: Total emissivity (EP-T) of category B

Temperature range [°C]	**MV (Inside)**	**MW (Outside)**	**MV (CZ)**	**EC**
250 – 530	0.309	0.557	0.206	0.700
530 – 650	0.435	0.604	0.364	0.700
650 – 750	0.619	0.622	0.547	0.700

The standard case for hot-dip galvanized components of category B, ‘MW (Indoor)’, as well as the better emissivity of the Czech samples (CZ), can be covered by the previously introduced two-stage emissivity approach. For higher temperatures, an additional positive effect can be achieved for category B, since the emissivity remains distinct below the value ε_{EC} = 0.70.

For the unfavourable case ‘MV (Outside)’ a comparison has to be made. Figure 51 compares constant emissivities with the variable, two-stage approach for a 30-minute thermal load according to the standard temperature-time curve ISO 834 [16]. For the adverse case ‘MV (Outside)’ of category B the curves ε = 0.55 and ε = 0.60 apply. It can be seen that even for $k_{sh}A_m/V$ ≥ 80 similar temperatures or temperatures, which are on the safe side, are achieved with the variable two-stage system (ε_{var} = 0.35 ≤ 500 °C; ε_{var} = 0.70 > 500 °C).

The two-stage emissivity approach, calculated for categories A and B, has to be confirmed in large-scale tests.

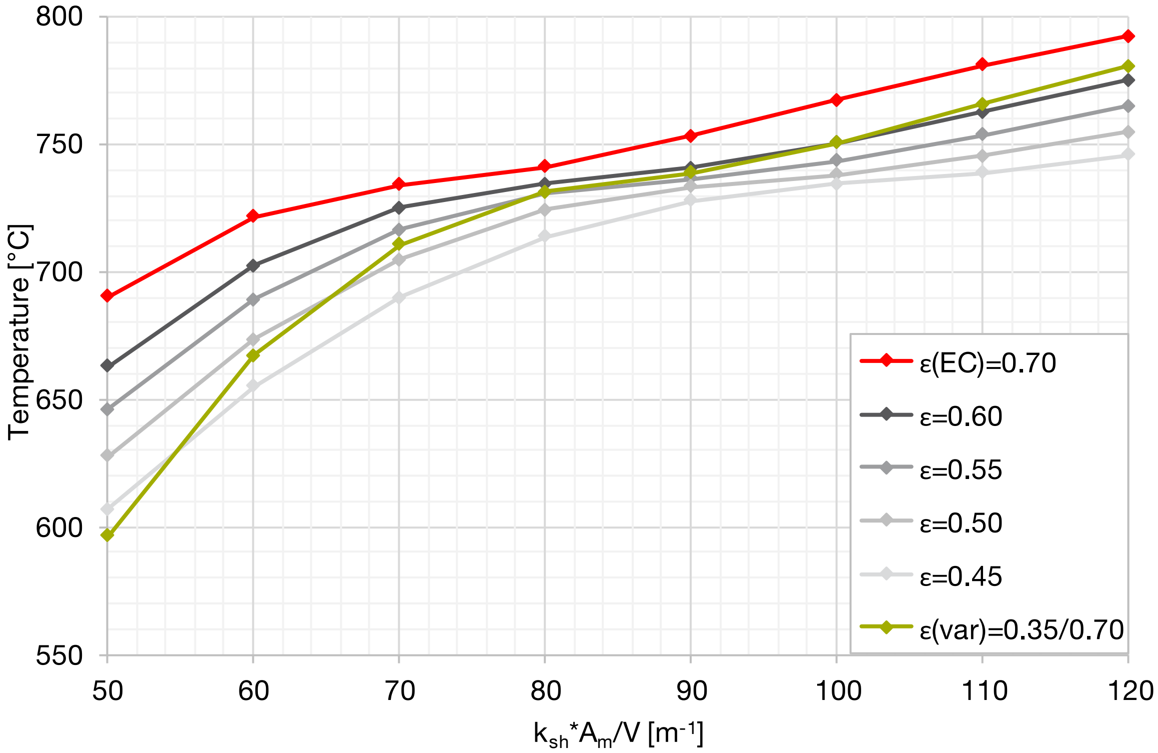

Figure 51: Comparison of steel section temperatures in dependence of their modified $k_{sh}A_m/V$ section factor for different emissivity levels after a fire duration of 30 minutes according to an ISO 834 fire

5.6.3 Category D

Compared to the Eurocode, category D – as previously mentioned – shows an approximately similar behaviour. The total emissivity values are only marginally smaller.

Table 21: Total emissivity (EP-T) of category D

Temperature range [°C]	MV (Inside)	MW (Outside)	EC
250 – 530	0.555	0.602	0.700
530 – 650	0.635	0.695	0.700
650 – 750	0.703	0.778	0.700

A significant positive effect of category D can be ruled out according to the EP-T analysis. Nevertheless, this has to be proven in the full fire tests.

6 Full fire tests

In the course of the research, two major fire tests were performed to prove the findings gained from the Emissivity Performance - Test (EP-T) and confirm them scientifically in large-scale tests. These tests took place in the Fire Testing and Research Laboratory of the Technical University of Munich and were carried out according to the requirements of fire resistance tests in DIN EN 1363-1 [15] for 30 minutes each.

Different setups have been used for two fire tests to cover a wide range of hot-dip galvanized test samples with different surface properties. Before describing the differences, the common features will be described first in further detail.

6.1 Temperature measurement

Most important for the entire test was the measurement of the dedicated temperature in each specimen during the test. As seen in Chapter 4.2, the test samples were flat with a rectangular section. In order to quantify the correct heating and avoid falsifications due to the inflow of hot ambient temperatures or material weakening in the measuring point during the fire test, the insertion of the thermocouples was ensured via 50 mm deep drilled holes from the short side of the specimens.

Thermocouples (TC) are based on a thermoelectric effect, found in 1821 by *Seebeck*. By connecting two cores, made of different materials, a voltage can be measured when their junction point – in this case at the wire ends in the specimen – has a different temperature level than their free ends. The thermocouple produces a temperature-dependent voltage and as a result, this voltage can be interpreted to a dedicated temperature. Due to the high ambient temperatures in the fire test, the thermocouples had to exhibit a higher resistance against thermal impact. The 2.3 mm thick TC, consisting of type K conductor pairs, are, therefore, isolated by multiple glasfiber-layers. Type K thermocouples are composed by two different wires (nickel-chromium / nickel-aluminium) according to DIN EN 60584-1 [34]. The fault tolerance occurring with this measuring method is limited by the DIN EN 60584-1 [34] to the maximum of 2.5 °C or 0.75 % of the temperature and is therefore within the acceptable range for the measurement.

As mentioned above, the thermocouple wires had a diameter of 2.3 mm. Due to the frailty of thin drills and the susceptibility of drifting boreholes, drill holes of a greater diameter (3.9 mm) were pre-drilled and then widened with a reamer to 4.0 mm diameter. In order to fill the formed mismatch, perfect fitting tubes were made out of the same material. Built in the lathe, so that the inside diameter was 2.3 mm and the outside diameter was 4.0 mm, they fitted in the internal diameter of the holes drilled in the specimen and provided a perfect pipe for the thermocouple wires. By installing the tubes, a sufficiently deep hole with the desired hole diameter for the thermocouples was achieved. In addition, to avoid any disturbance of the measurement, a heat-resistant adhesive sealed the point of insertion.

For each specimen, four of these measuring points, with a spacing of 300 mm each, were drilled, alternating laterally over the height. In order to prevent the thermocouple wires from damage by the partly strong air turbulence in the furnace, the cables were bundled and laid on the ground via previously laid non-inflammable cable routes.

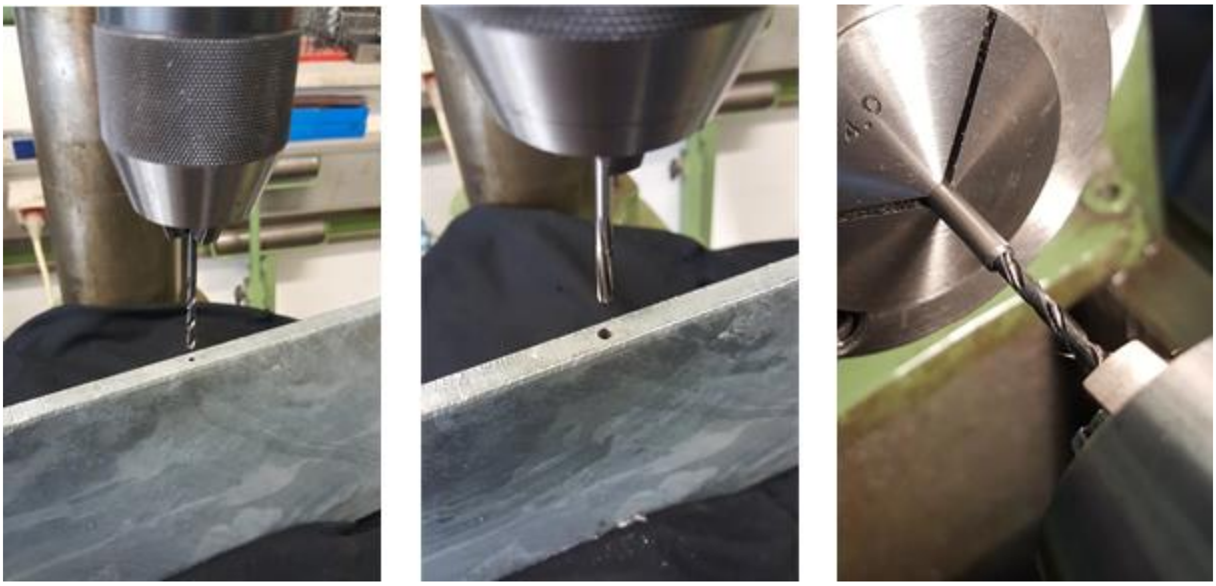

Figure 52: Preparation steps for the insertion of the thermocouples. From left to right: 1. Pre-drilling (Ø 3.9 mm); 2. Reamer (Ø 4.0 mm) 3. Preparation of the tubes (inside: Ø 2.3 mm; outside: Ø 4.0 mm)

6.2 Furnace control

Via external oil burners, the temperature in the fire compartment is introduced and regulated. In both experiments, four burners in total were mounted on both sides at the provided openings. While on the left side of the furnace the two burners were fixed in the lower level at a height of 0.50 m, the burners on the opposite right side were positioned on the top level at a height of 2.50 m. Consequently, a defined air flow in the fire room develops and results in a heat exchange.

Plate thermometers were used to control the rising temperatures in the furnace according to DIN EN 1361-1 [15]. These comprise a folded nickel plate, a fixed thermocouple and a thermal insulation. The distribution of the plate thermometers should provide a reliable indication of the mean temperature in the vicinity of the upper half of the specimens. In both tests, six of them were used.

The average temperature in the fire test must be controlled to satisfy the following relation:

$$T = 345 \log_{10}(8t + 1) + 20 \tag{6-1}$$

where

T is the average furnace temperature [°C]

and

t is the time [min].

The curve of heating, which corresponds to the standard temperature-time curve – also known as ISO 834 curve – presented in Chapter 1.5, may deviate only slightly. The limits are to be taken from DIN EN 1363-1 [15] and are shown in each fire test diagram in Figure 96 and Figure 98.

6.3 Emissivity assumption

In the ongoing analysis, the results of both fire tests will be compared to the temperature-time curve with a constant emissivity of $\varepsilon = 0.70$ of the DIN EN 1993-1-2 [17], calculated for specimens with an A_m/V - value of 60 and as well with an A_m/V - value of 210. In addition, originating from the EP-T results of Chapter 5.6, for both groups a temperature-time curve will be determined with the following emissivity values to get a first approach of the heating behaviour of the test samples:

$\varepsilon_{var} = 0.35 < 500$ °C and

$\varepsilon_{var} = 0.65 > 500$ °C.

6.4 **Full fire test – No. 01**

6.4.1 **Experimental setup**

The sample arrangement was set up with a grid spacing of 0.50 m to 0.50 m. Grouping of the same sample types was avoided because in a furnace a quite different temperature distribution may occur. Therefore, same samples were separated and equally distributed within the fire area. There were five rows with four specimens each and two rows of only two specimens (see Figure 53). The reason for a reduced number of samples in the two outer rows is given that the burners were arranged on the left side at the bottom corners in the fire room. The temperatures in this area are much higher, which in turn leads to incorrect measurements. Figure 95 in Appendix 'Full Fire Test' shows the schematic setup of the fire furnace (3.0 m x 4.0 m).

The 24 specimens were placed as follows in Table 22. Detailed information of the specimens can be found in Chapter 4.

Table 22: Line setup of the specimens for the first fire test

1. Row	**Specimen**	**2. Row**	**Specimen**	**3. Row**	**Specimen**	**4. Row**	**Specimen**
1	4-r	3	4-A-Out	7	4-A-In	11	1-A-Out
2	4-A-In	4	1-D-In	8	1-A-Out	12	1-A-In
		5	1-D-Out	9	1-A-In	13	4-D-In
		6	4-D-In	10	1-r	14	4-A-In

5. Row	**Specimen**	**6. Row**	**Specimen**	**7. Row**	**Specimen**
15	*1-A-In*	19	*1-D-In*	23	*1-r*
16	*4-A-In*	20	*4-A-Out*	24	*1-A-Out*
17	*4-r*	21	*4-A-In*		
18	*1-A-In*	22	*4-D-Out*		

6.4.2 **Measurements**

Besides the six plate thermometers, 96 thermocouples, with a total length of approximate 560 m, were used for the temperature measurement in the steel samples for the first full fire test. In addition, eight further temperature measurements were carried out at two spots in the fire compartment. Each with four thermocouples at the respective measurement heights of the samples to measure the temperature near a specimen. Consequently, it was possible to visualise any temperature gradients over the heights in the furnace. The data analysis was completed with further pressure and oxygen measurements. The internal pressure of the furnace can thus be controlled via the associated chimney and opening regulators. During the test, a data logger records the data of the overall 112 in-situ measurements.

6.4.3 Test execution and evaluation

The fire test was planned for 30 minutes of fire. In Figure 95 of the Apendix ‘Full Fire Test’, one can see that the average temperature in the room fits the normative demands.

Before analysing the detailed data, one can see that the specimens have been highly affected by the thermal exposure. The visual inspection shows high chemical reactions on the galvanized surfaces. The 10 mm thin steel samples have partially tipped over by the softening of the material. However, the last effect happened after 30 minutes of the test, when the burners were still activated until the 36th minute. The following Figure 53 shows the setup and compares the test samples before and after the first experiment:

Figure 53: Setup of the first fire test before (left) and after (right) the thermal exposure

For an analysis, the results will be divided into several parts, based on the different section factors. This leads to two different analysis-categories. By looking at specimens of the same dimensions, the heating can be directly compared and the analysis is therefore more detailed.

In each analysis the mean values (MV) of the measured temperature-time curves of the test samples are compared to the previously calculated temperature-time curves, with different emission levels as described in Chapter 5.6. The latter are categorized as followed:

- red-dashed	≙ constant emissivity:	ε_{EC} = 0.70 (according to DIN EN 1993-1-2 [17])
- green-dashed	≙ variable emissivity:	ε_{var} = 0.35 < 500 °C and ε_{var} = 0.65 > 500 °C

6.4.3.1 Analysis of the 40 mm thick specimen ($A_m/V = 60$)

The following diagram in Figure 54 shows the curves of different samples. The categorization is assigned as follows:

Category A	≙	grey
Category D	≙	blue
Rusty sample	≙	red

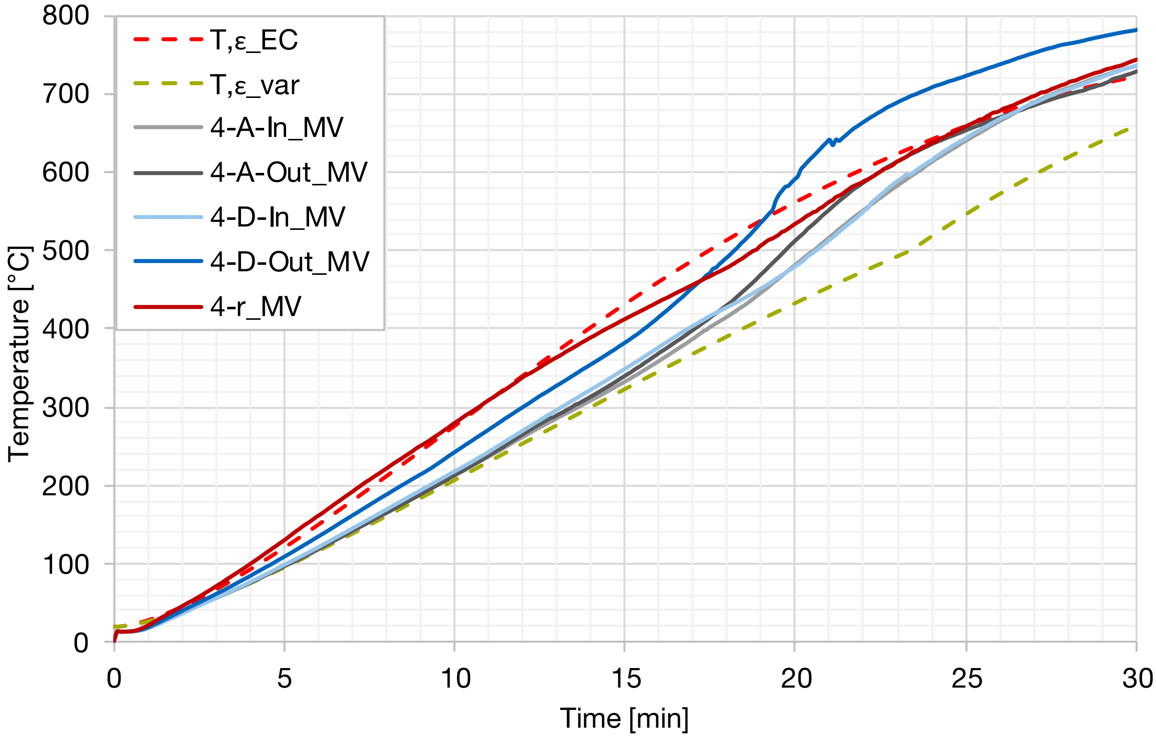

Figure 54: Comparison of the temperature-time curves from the first fire test of specimens ($A_m/V = 60$) of category A, category D and rusty samples with the calculated heating behaviour of such specimens

During the test, the behaviour and more specifically the heating of the specimens changed. This can be seen in Figure 54 between the minutes 15 to 20 where the heating increased rapidly. With regard of this situation, the following analysis will be separated additionally in two time periods.

Time slot up to 15 minutes

Within the first 15 minutes, the samples behaved as expected and predicted. The curve of the comparative rusty sample ‘4-r’ is very similar to the calculated development of the Eurocode, with a constant emissivity ε of 0.70.

If one compares the heating curves of the galvanized samples with the two calculated temperature-time profiles for these cross-sections ($A_m/V=60$), one can see a distinct affinity for the newly generated emissivity curve gained by the EP-T. Surprisingly both category D, samples with higher zinc layer thicknesses, and category A samples, with their glossy appearance, showed an almost perfect match with the predicted heating curve. Likewise, in this time interval of the first 15 minutes, the storage type played no significant role.

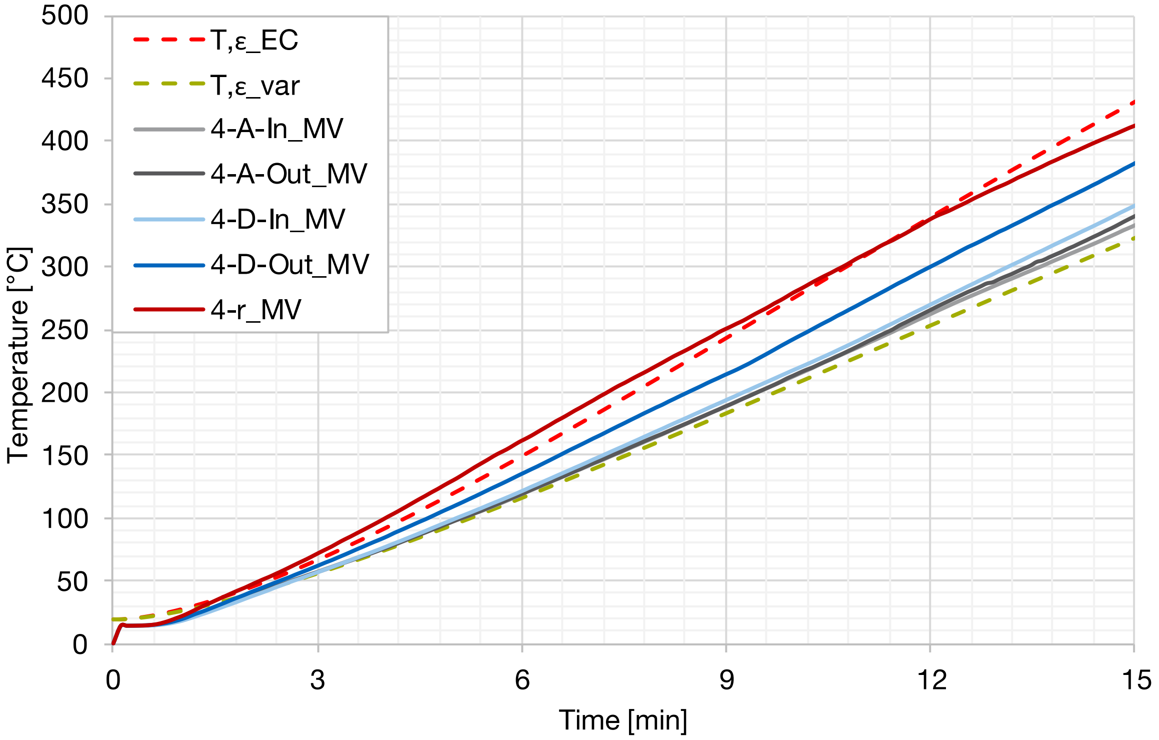

Figure 55: Comparison of the measured temperature-time curves of the mean values (MV) with the calculated curves for the first 15 minutes

Time slot 15 – 30 minutes

The rusty steel sample still shows the expected behaviour and, with minor deviations, is identical to the normative based heating curve.

However, the galvanized samples show a completely different behaviour. Regardless of their different surface properties, the temperature-time curves have an increasing deviation from the predicted curve within the duration of the test. This behaviour will be explained in detail after taken the thinner samples into account.

6.4.3.2 Analysis of the 10 mm thick specimen ($A_m/V = 210$)

The following diagram, in Figure 56, shows the curves of different samples with a section factor of 210. The categorization is assigned as follows:

Category A	≙	grey
Category D	≙	blue
Rusty sample	≙	red

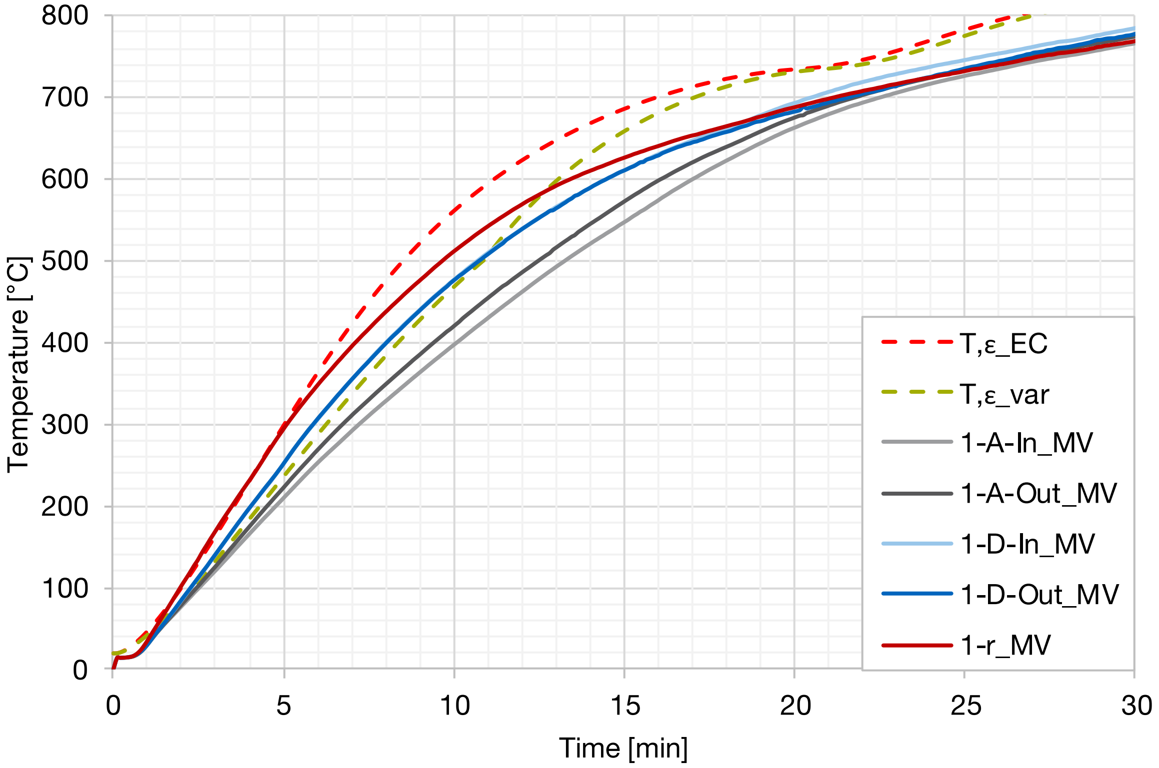

Figure 56: Comparison of the temperature-time curves from the fire test of the mean values (MV) of the specimens ($A_m/V = 210$) of category A, category D and rusty samples with the calculated heating behaviour of specimens ($A_m/V = 210$)

A well-known effect, regardless of the surface properties, is a faster heating with an increasing A_m/V ratio. Comparing the diagrams of Figure 55 and Figure 56 one can clearly see this effect, due to different thicknesses of specimens by the related higher temperatures at different points in time.

Again, the analysis is separated into two time slots. The first from 0 up to 5 minutes and the second one from 5 to 30 minutes.

Time slot up to 5 minutes

In the initial 5 minutes, the expected behaviour appears again. The rusty comparative sample (dark red) shows the dedicated heating behaviour of the temperature-time curve with a constant emissivity of ε_{EC} = 0.70.

In turn, all galvanized samples show a more positive behaviour. Their heating, independent of their previous storage conditions, fits to the prediction from the EP-T emissivity measurements. Although they follow mostly the variable emissivity line of the EP-T, some had partially an even better behaviour. This especially appears for specimens of category A and even more pronounced for samples that have been additionally stored inside. Specimens of category D, in turn, showed the same heating behaviour. Therefore, in the diagram of Figure 57, one cannot distinguish between the two heating curves of the mean values '1-D-In_MV' and '1-D-Out_MV'.

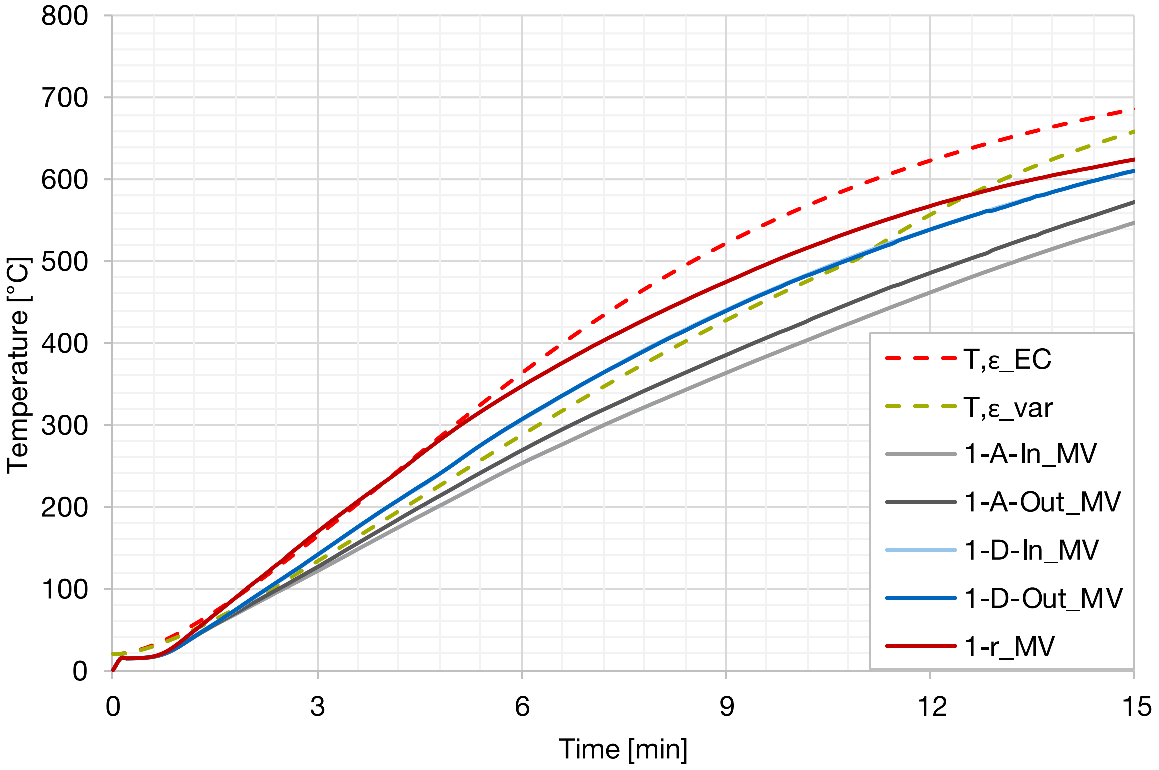

Figure 57: Comparison of the measured temperature-time curves of the mean values (MV) with the calculated curves for the first 15 minutes (A_m/V = 210)

Time slot 5 – 30 minutes

After the first five minutes, a clearly changed situation appears. All samples deviate to varying degrees, depending on their characteristics, from the predictions.

The rusty steel sample shows a much better behaviour than one could expect with a temperature of 626 °C after 15 minutes. This is 61 °C below the predicted temperature of 687 °C. The tendency persists also in the further course of the experiment, with the same temperature difference at the end of the fire test of around 61 °C.

The behaviour of galvanized steel samples, with an A_m/V ratio of 210, is identical to this. Although the category D samples are hotter in comparison to the category A samples, the difference to the predicted heating curves is huge. The following table shows the deviation from the two comparison curves:

Table 23: Deviations of the measured results of the first fire test to the calculated heating curves

Specimen category	**Deviation to the 'Eurocode-curve' (ε_{EC})**		**Deviation to the generated curve (ε_{var})**	
	15. Minute	**30. Minute**	**15. Minute**	**30. Minute**
Category A	-130 °C	-60 °C	-103 °C	-58 °C
Category D	-75 °C	-46 °C	-48 °C	-44 °C
Rusty	-61 °C	-61 °C	-33 °C	-59 °C

As seen in Table 23, the thin specimens perform, independent of their surface condition, much better than they should. The measured temperatures are in a range of -130 °C to -46 °C colder, in dependence of the test specimen and the time, than predicted by the Eurocode calculation method. Nevertheless, at 15 minutes one can see that the tendency of their behaviour among themselves is as expected. The rusty specimen is the hottest, whereas the specimen of category A is the coldest. Looking at the deviations to the predicted temperatures of the generated curve, calculated by an variable emissivity ε_{var}, one can see that they are a bit smaller, but still not negligible. The measured temperatures, for example, for category A are still 103 °C colder after 15 minutes and 58 °C after 30 minutes of the test than the calculated ones.

It can be concluded that the specimen with a higher section factor must have given heat to samples with a smaller profile factor. The thesis that has to be proved is, therefore:

The 'thinner' samples heated up the 'thicker' samples!

As stated in Chapter 1.5, heat is always distributed from a higher potential level to a lower level, hence from objects with higher temperatures to objects with lower temperatures – in the present case, from the thinner, warmer samples to the thicker, colder samples. In order to prove the thesis, the radiation exchange in the furnace has to be taken into account as far as possible. With such a diverse setup where each sample is affected by many other objects, it is difficult to calculate the interactions. On the one hand, an object absorbs heat, but on the other hand delivers heat energy to other objects. This happens all under the influence of constantly changing surrounding parameters. It should be emphasized that such a calculation can only be made by a number of assumptions and that the results only allow drawing conclusions about tendencies of the proceeded processes.

6.4.3.3 Interaction between the specimens

In order to approximate the interactions that have taken place, a stationary system is gradually assumed. In each time step, the heat exchange in the form of radiant energy between the main interaction partners is calculated. From this temperature gain $+\Delta T$, or in turn temperature loss $-\Delta T$, the actual temperature of the steel sample can be determined from the previously calculated temperature:

$$\begin{aligned} T_{act,x} &= T_{cal,x} + \Delta T_{y1\rightarrow x} + \Delta T_{y2\rightarrow x} + \Delta T_{y3\rightarrow x} + \Delta T_{y4\rightarrow x} + \cdots \\ &-\Delta T_{x\rightarrow y_1} - \Delta T_{x\rightarrow y_2} - \Delta T_{x\rightarrow y_3} - \cdots \end{aligned} \tag{6-2}$$

where

$T_{act,x}$ is the actual temperature of the specimen x,

$T_{cal,x}$ is the calculated temperature of the specimen x,

$\Delta T_{y1\rightarrow x}$ is the temperature gain of the radiation exchange with another specimen,

and

$\Delta T_{x\rightarrow y_1}$ is the temperature loss of the radiation exchange with another specimen.

To calculate the radiation exchange for the simple case between two opposing, grey radiating surfaces, the following equation, according to [35], can be used:

$$Q_{12} = \frac{\sigma \varepsilon_1 \varepsilon_2 A_1 \varphi_{12}}{1-(1-\varepsilon_1)(1-\varepsilon_2)\varphi_{12}\varphi_{21}}(T_1^4 - T_2^4) \tag{6-3}$$

where

σ is the Stefan-Blotzmann constant,

ε is the emissivity of each surface,

and

φ is the configuration factor.

Originating from this induced energy one can calculate the temperature change in a body:

$$\Delta T = \frac{\dot{Q}_{12}}{(mc)} \tag{6-4}$$

with

m mass of the body [kg]

c specific heat capacity [J/(kg K)].

In cases where two object surfaces are spatially opposed, not all of the emitted radiation of one surface will impinge on the other surface. The radiation component of a surface i, which affects the other object surface k, based on the total emitted radiation, is called the configuration factor φ_{ik}. The determination of this geometric parameter is often the most difficult part in radiation exchange computation. However, since this is the evaluation of a purely geometrical problem, already calculated angular relationships exist for many geometrical configurations. Simplifications for certain conditions are offered by the VDI [35] or *Howell et al.* [24]. The latter provide an even more detailed derivation and evaluation of a wide range of geometric relationships. In the course of the retroactive calculation of this experiment therefore only the test samples were taken into account, which were in the immediate vicinity, and in addition had a relatively free 'field of view' on each other. Two different kind of geometrical factors have to be calculated for this fire test. The equations for both configuration factor φ_{ik} are listed below.

For two parallel, equal-sized, opposite rectangular areas (A_1 and A_2), the configuration factor can be calculated, according to [24], as follows:

$$\varphi_{12} = \frac{2}{\pi XY}\left\{\ln\left[\frac{(1+X^2)(1+Y^2)}{1+X^2+Y^2}\right]^{1/2} + X\sqrt{1+Y^2}\,\arctan\frac{X}{\sqrt{1+Y^2}} + Y\sqrt{1+X^2}\,\arctan\frac{Y}{\sqrt{1+X^2}} - X\arctan X - Y\arctan Y\right. \tag{6-5}$$

where, with respect to Figure 58:

$X = \frac{a}{c}$ and $Y = \frac{b}{c}$.

The configuration factor for the reverse approach then results in:

$$\varphi_{21} = \frac{A_1}{A_2}\varphi_{12} \tag{6-6}$$

In case of two parallel but offset surfaces, the following configuration factor results:

$$\varphi_{12} = \frac{1}{(x_2 - x_1)(y_2 - y_1)} \sum_{l=1}^{2} \sum_{k=1}^{2} \sum_{j=1}^{2} \sum_{i=1}^{2} (-1)^{(i+j+k+l)} G(x_i, y_j, \eta_k, \zeta_l) \tag{6-7}$$

where

$$\begin{aligned} G = \frac{1}{2\pi} \Bigg(& (y-\eta)[(x-\zeta)^2 + z^2]^{\frac{1}{2}} \arctan\left\{\frac{y-\eta}{[(x-\zeta)^2 + z^2]^{1/2}}\right\} \\ & + (x-\zeta)[(y-\eta)^2 + z^2]^{1/2} \arctan\left\{\frac{x-\zeta}{[(y-\eta)^2 + z^2]^{1/2}}\right\} \\ & - \frac{z^2}{2} \ln[(x-\zeta)^2 + (y-\eta)^2 + z^2] \Bigg) \end{aligned} \tag{6-8}$$

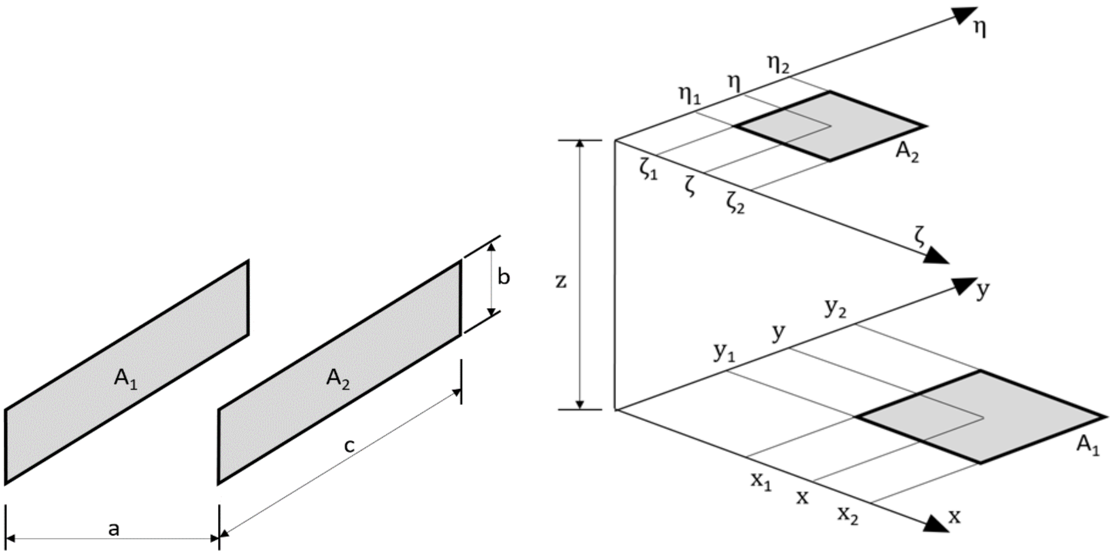

Figure 58: Geometrical coherences of two opposite surfaces

The procedure is demonstrated stepwise, as an example, with sample ‘4-A-Out_3’ – hereafter simplified as sample no. ‘3’:

1. The main interaction-specimen have to be determined. In the case of sample ‘3’, these are sample nos. 1, 2, 7, 8, 9 and 12.
2. The heat transfers from and to these samples shall be determined according to formulas above. The determination of the configuration factors was carried out according to [24]:

	1 & 7 → 3	2 & 8 → 3	12 → 3	9 → 3
$\boldsymbol{\varphi_{12}}$	0.15268	0.05268	0.04240	0.01093

Various emissivity values were taken into account, with respect to the different surface properties. As previously mentioned, constant values for the entire temperature range have been chosen as a simplification:

	ε_m **(≤ 500°C)**	ε_m **(> 500°C)**
Rusty (ε_{rust})	0.70	
Cat. A. (ε_A)	0.35	0.65
Cat. D. (ε_D)	0.45	0.65

3. The individual temperature changes are to be added / substracted according to Equation (6-2). This results in an additional temperature of 9.2 °C for sample ‘3’, at the end of the fire test, by taking the five greatest influences in account.

	$+\Delta \boldsymbol{T}_{1\to3}$	$+\Delta \boldsymbol{T}_{8\to3}$	$+\Delta \boldsymbol{T}_{12\to3}$	$+\Delta \boldsymbol{T}_{7\to3}$	$+\Delta \boldsymbol{T}_{2\to3}$
4A_3	2.7	2.6	1.6	1.1	1.1

**Only the five greatest influences are provided*

4. This temperature difference has to be added to the calculated forecasted temperatures according DIN EN 1993-1-2 [17], on both, the constant ($\varepsilon_{EC,const}$) and the variable (ε_{var}) approach:

$$T^*{}_{EC,3} = T_{EC} + 9.2 = 721.3 + 9.2 = 730.4\,°C$$

$$T^*_{\varepsilon,var,3} = T_{\varepsilon,var,3} + 9.2 = 658.7 + 9.2 = 667.9\,°C$$

Finally, a better comparison can be drawn since the mutual influence is approximated. As a result of this consideration, an adapted temperature-time curve is obtained. For example, on the sample ‘4-A-Out_3’ it can be seen in Figure 59 that the temperature prognosis with a variable emissivity ensures much better statements about the temperature development of galvanized specimens, than the Eurocode. A fixed emissivity of $\varepsilon = 0.70$ is therefore not applicable for all surfaces in a fire scenario.

These additional effects were calculated for more test samples. As a simplification, only the five greatest influences were taken into account.

Table 24: Overview of additional effects $+\Delta T_{y\to x}$ of some sample interactions

Specimen	$\boldsymbol{T}_{cal}$	$+\Delta \boldsymbol{T}_{1\to x}$	$+\Delta \boldsymbol{T}_{2\to x}$	$+\Delta \boldsymbol{T}_{3\to x}$	$+\Delta \boldsymbol{T}_{4\to x}$	$+\Delta \boldsymbol{T}_{5\to x}$	$+\Delta \boldsymbol{T}^*_{tot}$	$\boldsymbol{T}_{new}$
4A_3	658.7	$2.7_{1\to3}$	$2.6_{8\to3}$	$1.6_{12\to3}$	$1.1_{7\to3}$	$1.1_{2\to3}$	**9.2**	667.9
4A_16	658.7	$5.7_{12\to16}$	$3.6_{20\to16}$	$2.9_{19\to16}$	$2.2_{11\to16}$	$2.2_{23\to16}$	**16.7**	675.4
4D_13	694.5	$5.3_{9\to13}$	$3.2_{10\to13}$	$2.7_{8\to13}$	$2.5_{18\to13}$	$1.9_{4\to13}$	**15.7**	710.2

** only the five greatest effects are taken into account*
** calculated according to [24]*

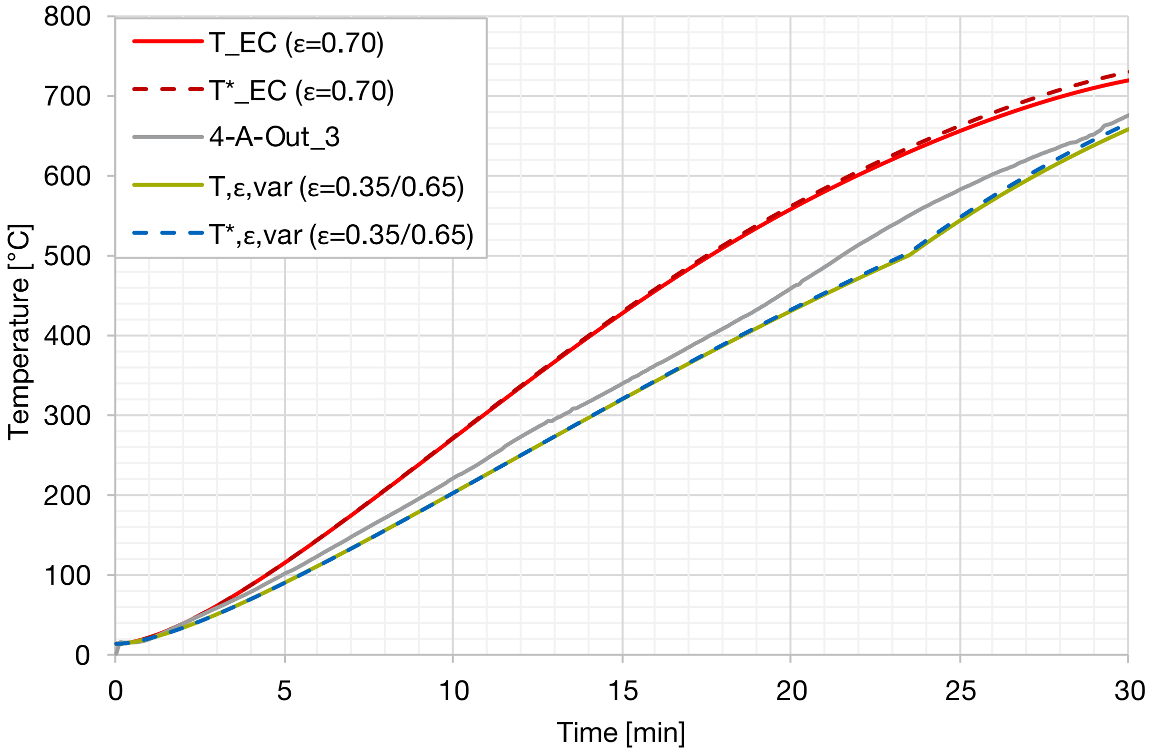

Figure 59: Comparison of the improved calculated temperature-time curves with the heating of the sample '4-A-Out_3'

By comparing the adjusted temperature values T^* after a fire duration of 30 minutes with the dedicated measured temperatures of the fire test ($T_{x,measured}$) a more accurately analysis can be achieved.

Table 25: Comparison of modified calculated temperatures T^*_{EC} and $T^*_{\varepsilon,var}$ with measured temperatures

Specimen	$\boldsymbol{T_{x,measured}}$	$\boldsymbol{T^*_{EC}}$	$\Delta(\boldsymbol{T^*_{EC}-T_x})$	$\boldsymbol{T^*_{\varepsilon,var}}$	$\Delta(\boldsymbol{T^*_{\varepsilon,var}-T_x})$
4A_3	675.4	730.4	+55	667.9	-7.5
4A_16	702.3	738.3	+36	675.4	-26.9
4D_13	721.1	737.3	+16.2	710.2	-10.9

The deviation of the temperature calculations by means of a variable two-stage emissivity is in each case much lower and indicates that the assumptions are correct. The previously established thesis can be confirmed. The thinner samples ($A_m/V = 210$) heated up the thicker samples ($A_m/V = 60$). A more detailed view is waived, since the interactions in a constantly changing fire area cannot be calculated exactly. A further confirmation of the emissivity assumption had to be made in the second fire test.

6.4.3.4 Effects on the hot-dip galvanized surfaces

In the following, the individual areas of the test specimen are dealt with in further detail – in particular on the surface change. Depending on the existing surface condition before the thermal impact, different reactions can be seen. For example, for samples with a previous white rust load, the reaction is more pronounced. The same applies to surfaces with a higher sample temperature.

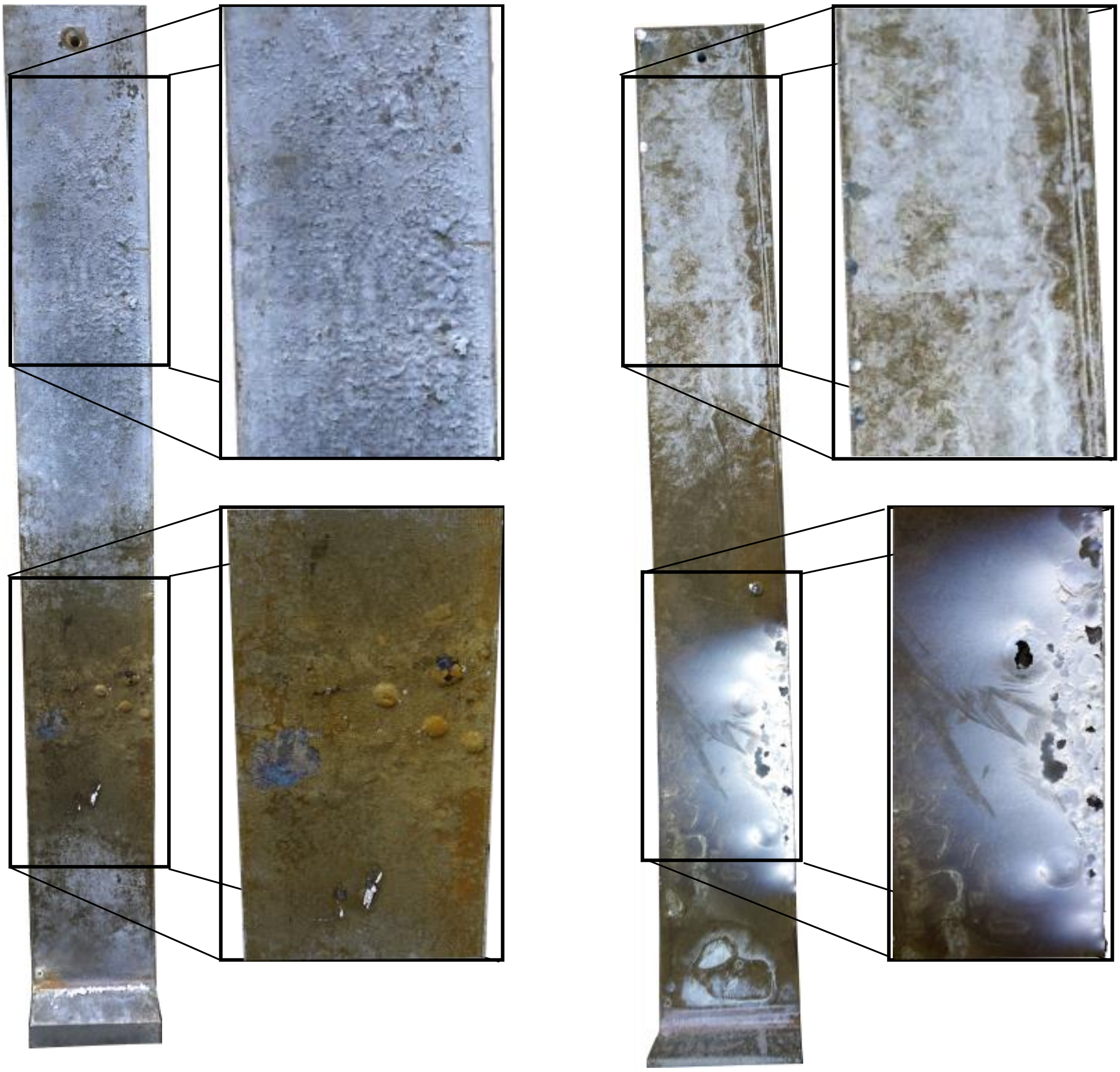

Figure 60: Left: ‘4-A-In_02’ (40 mm thick sample of category A, stored 'inside' after the adverse initial storage); right: ‘1-A-Out_24’ (10 mm thick sample of category A, stored 'outside' after the adverse initial storage

Both samples shown in Figure 60 have different effects of temperature impacts. The left sample ‘4-A-In_02’ is a 40 mm thick sample stored ‘inside’ after an unfavourable initial storage. The right sample ‘1-A-Out_24’ represents a specimen of the thinner, 10 mm thick, category, which was stored outside after an adverse initial storage. However, both test samples are based on the same position relative to the burner in the fire area. As shown in Figure 95 in Annex ‘Full Fire Test’, these are the two outer samples, each affected by the lower burner flame. The flame influence can be seen in the bottom area of both samples. With higher prevailed sample temperatures stronger reactions on the surface turned out compared to other surface areas of the same specimen. While the temperatures in the rest of the 40 mm thick sample parts were around 815 °C after 36 minutes of fire, the temperature in the bottom highlighted area was additionally 30 °C higher. Furthermore, the temperatures in this part of the sample was higher for a longer duration. As a result, another chemically composed oxide layer with a changed crystal structure occurs. Zinc oxide also plays a major role in colouration and the related thermochromism of zinc oxide. More details about thermochromism can be found in Chapter 7.7.4.

Sample ‘1-A-Out_24’ heats up much faster due to the thinner cross section and was thus exposed to high temperatures for a longer duration. The consequence is a stronger chemical reaction over the entire sample surface. In the lower area, which was influenced by the burner, respectively the flame of the burner, there was even a precipitation of the zinc in the form of white zinc oxide powder. In order to make this possible, the topmost pure zinc layer (η-phase) had to evaporate and then react chemically with the oxygen present in the fire compartment. This can only take place for temperatures of the zinc above 907 °C.

6.5 Full fire test – No. 02

6.5.1 Experimental setup

The sample arrangement had a grid spacing of 0.75 m to 0.50 m. Grouping of samples with the same properties (e.g. galvanizing coating) was, like in the first full fire test, prevented by distributing the samples equally throughout the fire area. In the second test, only twelve specimens were tested due to the interactions and the influence of the burners of the first experiment, with three rows having four samples each. Figure 97 in Appendix ‘Full Fire Test’ shows the setup in the furnace. The specimens were placed as follows:

Table 26: Line setup of the specimens for the second fire test

1. Row	Specimen	2. Row	Specimen	3. Row	Specimen
11	*4-A-In*	**21**	*4-B7-In*	**31**	*4-B6-In*
12	*4-B7-In*	**22**	*4-B6-In*	**32**	*4-r*
13	*4-r*	**23**	*4-A-In*	**33**	*4-B6-In*
14	*4-B6-In*	**24**	*4-B7-In*	**34**	*4-D-In*

More detailed information on the specimens can be found in Chapter 4.

6.5.2 Measurements

Overall 48 thermocouples with an added cable length of 262 m were used for the second full fire test. Furthermore, six additional plate thermometers – according to the first fire test – were used to control the temperature in the fire compartment. Their positions are shown in Figure 97 in Appendix ‘Full Fire Test’.

6.5.3 Test execution and evaluation

The experiment was again planned as a 30 minutes’ fire test. The temperature development in the fire area was, with one exception, within the scope of standardization. The average combustion chamber temperature (referred to as ‘BR’) and the distribution of the temperature in the fire compartment itself can be seen in Figure 98 in Appendix ‘Full Fire Test’. The reason for the shortfall below the normative limit temperature was a brief failure of a burner. Consequently, the temperature did not rise to the desired extent in a minor time slot. However, after the reactivation of the burner, the desired temperature could be generated again in the fire compartment. Consequently, a perfect room temperature was achieved.

The deviation from the normative regulation can be neglected and accepted within this research since the emissivity values are calculated back from the actual combustion chamber temperature and are not assumed by the ISO 834 [16] as done in usual fire protection tests. Therefore, the findings drawn from the experiment are independent of this – anyway only minimal – deviation.

It becomes clear that, as in a real fire, the room temperature is not evenly distributed over the fire area, but places of higher temperature and lower temperature occur. In this experiment, it is a gradient from the north-western part to the southern part of the fire area. With an average deviation of about 65 °C. The effect of temperature again showed its influence on the sample surfaces. There are significant changes due to chemical reactions and diffusion processes. The following Figure 61 compares the samples before and after the thermal exposure.

Figure 61: Setup of the second fire test before (left) and after (right) the thermal impact

For the analysis of the test results, the specimen will be separated according to their profile factors. This leads to three different specimen analysis-categories. However, looking at specimens of the same dimensions, the heating can be directly compared and the analysis is thus more detailed.

In each analysis the measured temperature-time curves of the test samples are compared to the previously calculated temperature-time curves, with different emission levels as described in Chapter 5.6. The latter are categorized as followed:

- red-dashed ≙ constant emissivity: ε = 0.70
  (according to DIN EN 1993-1-2 [17])
- green-dashed ≙ variable emissivity: ε_{var} = 0.35 < 500 °C and
  ε_{var} = 0.65 > 500 °C

6.5.3.1 Analysis of the 200 x 40 mm thick specimen ($A_m/V = 60$)

The following diagram in Figure 62 shows the courses of mean values (MV) of different samples. The categorization is assigned as follows:

Category A	≙	grey
Category D	≙	blue
Rusty sample	≙	red

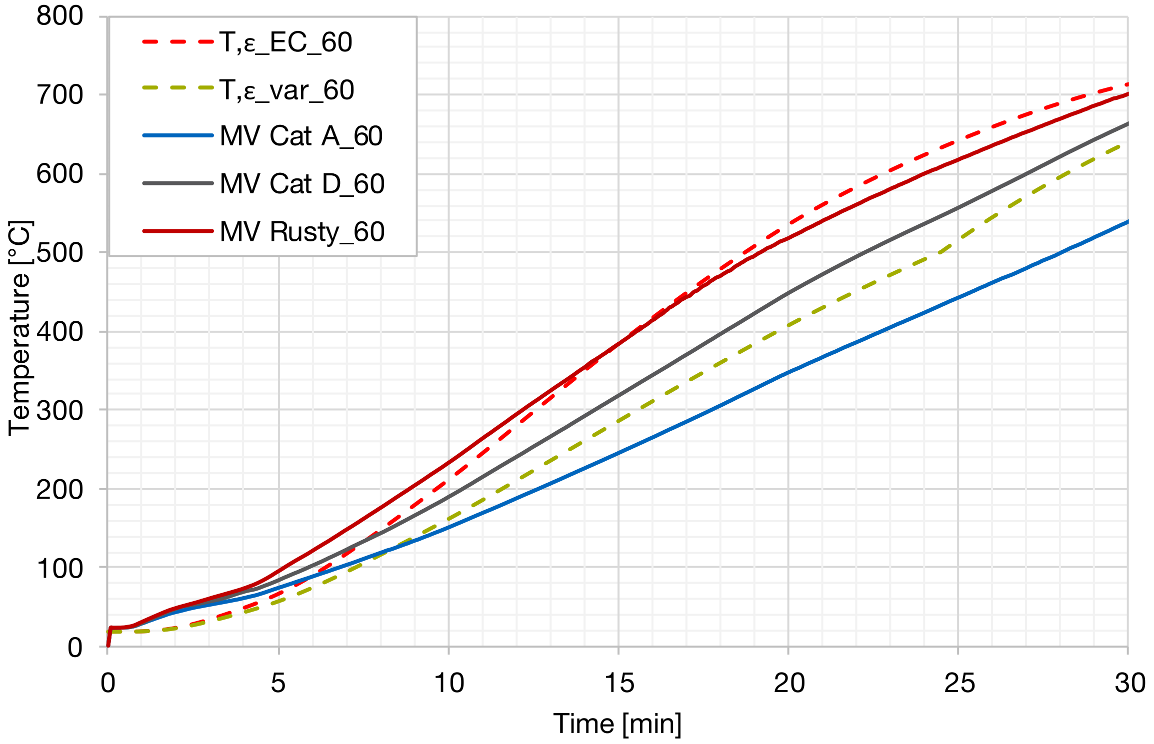

Figure 62: Comparison of the temperature-time curves of the mean values (MV) from the second fire test of specimens ($A_m/V = 60$) of category A, category D and rusty samples with the calculated heating behaviour of specimens ($A_m/V = 60$)

If one compares only the three measured curves, it can be seen that the same different behaviours reveal as seen in the fire test No. 01. The samples of the category A behave much better, and have therefore a slower heating than the sample of the category D. The worst result regarding fire resistance and thus an intense heating can be seen by the rusty sample.

Table 27: Average deviation of samples with an A_m/V – factor of 60 per category from the calculation

Specimen	**Deviation to the 'Eurocode-curve' (ε_{EC})**		**Deviation to the generated curve (ε_{var})**	
	15. Minute (384 °C)	**30. Minute (713 °C)**	**15. Minute (286 °C)**	**30. Minute (639 °C)**
Category A	-140 (244 °C)	-175 (538 °C)	-42 (244 °C)	-101 (538 °C)
Category D	-66 (318 °C)	-50 (663 °C)	+32 (318 °C)	+24 (663 °C)
Rusty	-2 (382 °C)	-13 (700 °C)	+96 (382 °C)	+61 (700 °C)

The rusted steel sample shows a similar heating response in comparison with the temperature-time curve of the Eurocode and is with 382 °C only 2 °C cooler than the predicted Eurocode temperature of 384 °C after 15 minutes of fire. This tendency remains almost the same in the ongoing of the experiment (see Figure 62). Towards the end of the fire test the temperature difference is around -13 °C.

The two galvanized categories behaved differently. Category D already shows a better behaviour than the rusty samples. The deviations from the temperature-time curve of the Eurocode are obvious. With deviations of - 66 °C after 15 minutes and -50 °C after 30 minutes of the heat exposure, there is a strong advantage regarding the residual strengths (see Chapter 1.6). In comparison with the predicted temperature-time curve of a variable emissivity ($\varepsilon = 0.35 < 500$ °C and $\varepsilon = 0.65 > 500$ °C), a slightly better match can be seen here. Deviations of +32 °C (15th minute) and +24 °C (30th minute) emphasize that.

Category A shows an even slower warming behaviour. Temperatures of 244 °C after 15 minutes and 538 °C after 30 minutes in an ISO fire, each deviate more than -140 °C from the predicted temperature of the Eurocode. Therefore, a fundamental different behaviour can be used as a basis, compared to the normative heating course. Furthermore, the behaviour strongly deviates in comparison to the predicted curve with a two-stage, variable emissivity. Although the deviations are in a smaller range, there remains a non-negligible deviation, in the positive sense.

Considering the samples of category A and D, not only a significant better behaviour compared to the Eurocode can be seen, but also a better behaviour compared to the first fire test. This clearly highlights that the surface texture, at the time of thermal exposure, has a serious influence on its emissivity. While for the first fire test, specimen with the worst surface condition were aspired, the second fire test should cover also specimens with an almost white rust-free surface. The specimens were therefore stored for about one and a half month before the test. This treatment is more comparable with real, just in time, produced steel components and results is an even better emissivity.

6.5.3.2 Analysis of the 160 x 40 mm thick specimen ($A_m/V = 62.5$)

The following diagram, in Figure 63, shows the courses of different samples. The categorization is assigned as follows:

All samples of Category B ≙ grey

Mean value of Category B ≙ blue

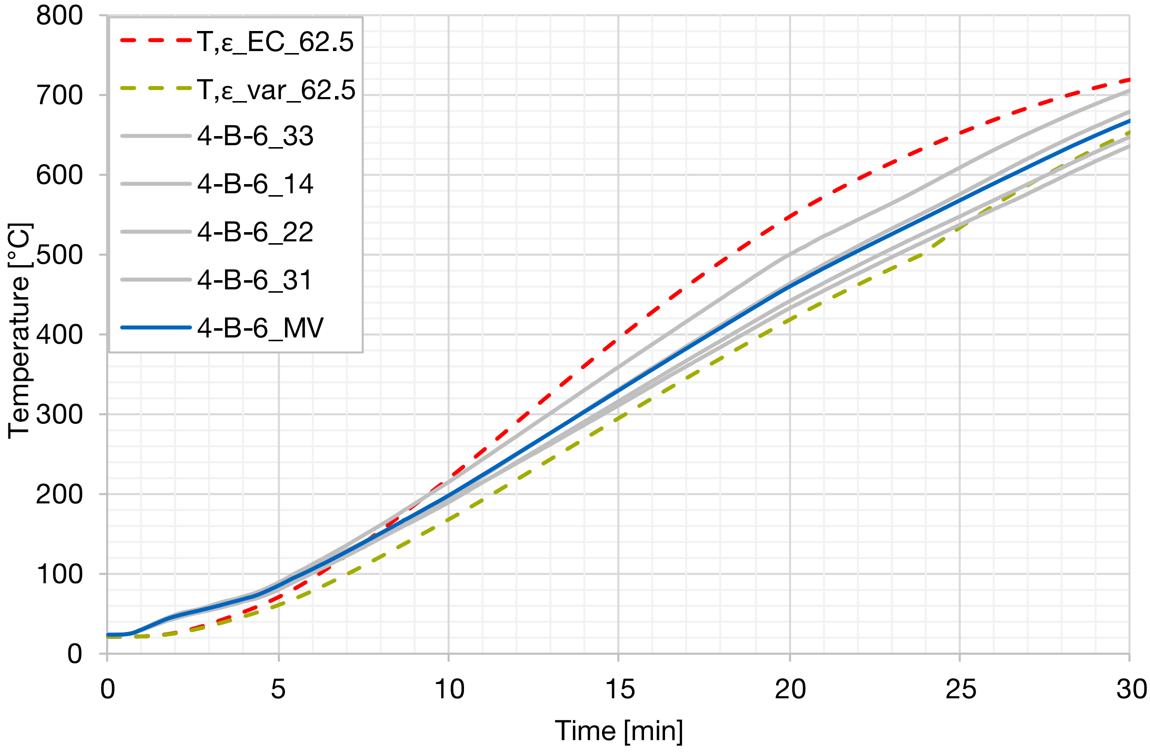

Figure 63: Comparison of the temperature-time curves of the mean values (MV) from the second fire test of specimens ($A_m/V = 62.5$) of category B with the calculated heating behaviour of specimens ($A_m/V = 62.5$)

Looking at the individual temperature-time curves of the different samples, one can clearly see that all samples are within a similar range. Sample '4-B-6_33' is the only one that deviates and shows a slightly higher temperature. A reason for this is the different room temperature prevailing in the furnace. As previously mentioned, the temperature on the north-western corner is higher. The deviation in the furnace area is consistent with the deviation of the sample, compared to the other samples of the same type. With respect to this approximately same behaviour, only the mean value (MV) of all four samples is considered in the following.

Comparing the mean temperature-time curve of the samples with the curves of the Eurocode and the prediction of the EP-T, a good agreement with the curve of the variable emissivity is shown. Deviations of +12 °C (see Table 28) from the temperature-time curve, calculated with a variable emissivity, at the end of the fire test emphasize this. If one omits the outlier '4-B-6_33' a deviation of only 1.12 °C at the end of the fire test (30. Minute) can be calculated, which thus matches perfectly with the final temperature.

Table 28: Average deviation of samples with an A_m/V – factor of 62.5 per category from the calculation

Specimen category	**Deviation to the 'Eurocode-curve' (ε_{EC})**		**Deviation to the generated curve (ε_{var})**	
	15. Minute **(395 °C)**	**30. Minute** **(719 °C)**	**15. Minute** **(295 °C)**	**30. Minute** **(654 °C)**
Category B	-68 (327 °C)	-53 (666 °C)	32 (327 °C)	12 (666 °C)

6.5.3.3 Analysis of the 200 x 30 mm thick specimen ($A_m/V = 76.7$)

The following diagram in Figure 64 shows the courses of different samples. The categorization is assigned as follows:

All samples of Category B ≙ grey

Mean value of Category B ≙ blue

The category B samples with an A_m/V ratio of 76.7, and thus a lower mass compared to the previous samples, heat up faster. Consequently, it can be seen that the difference between the two predicted curves – one with a constant emissivity and one with a two-stage emissivity – becomes smaller towards the end of the 30-minute fire exposure. If there is a lack of mass, it is a matter of time when the temperatures of both pre-calculated curves will align at the end. In the present case, despite the smaller mass, a difference remains visible. The mean value of the temperature-time curves is quite in the middle between the graph of the predicted curve of the Eurocode and the two-stage forecast. This behaviour persists only until minute 20. Subsequently the variable curve fits better to the behaviour of the test samples. Comparing the final temperatures (see Table 29) one can see that the prediction of the variable emissivity approach fits perfectly to the mean value of the measured temperatures of the specimens.

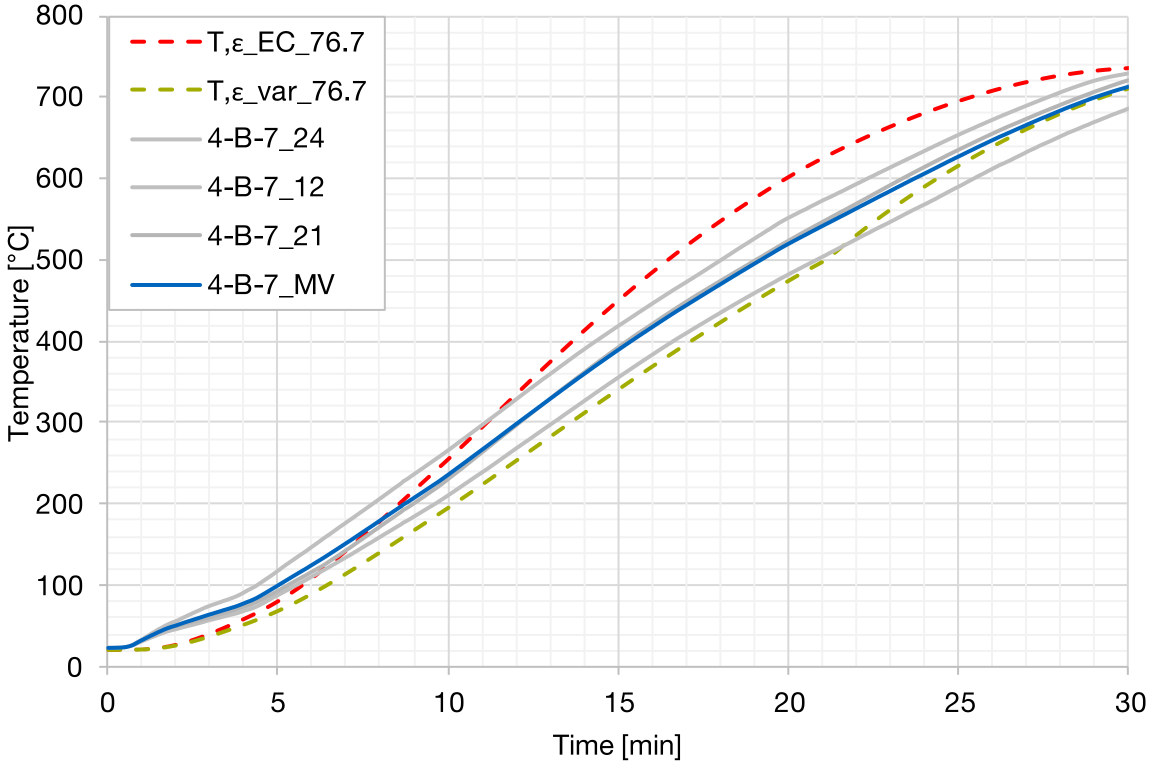

Figure 64: Comparison of the temperature-time curves of the mean values (MV) from the second fire test of specimens ($A_m/V = 76.7$) of category B with the calculated heating behaviour of specimens ($A_m/V = 76.7$)

Table 29: Average deviation of samples with an A_m/V – factor of 76.7 per category from the calculation

Specimen category	**Deviation to the 'Eurocode-curve' (ε_{EC})**		**Deviation to the generated curve (ε_{var})**	
	15. Minute **(449 °C)**	**30. Minute** **(736 °C)**	**15. Minute** **(341 °C)**	**30. Minute** **(711 °C)**
Category B	-63 (386 °C)	-25 (711 °C)	45 (386 °C)	0 (711 °C)

Nevertheless, neither the one nor the other predicted temperature-time curve is correct during the heating. As seen in Chapter 3 as well as in Chapter 5 in the EP-T the emissivity is not only a value. It changes during a rising thermal exposure and cannot be simplified perfectly by one or a two-stage emissivity values. In the following Chapter 6.6, the emissivity values were therefore recalculated from the fire test.

6.6 **Emissivity – recalculated from the full fire tests**

The emissivity of the specimens in a fire test can be approximately recalculated, by knowing the exact setups, temperatures in the furnace and their distribution. It is important to mention that emissivity at the beginning of a fire in a furnace test, according to DIN EN 1363-1 [15], cannot be recalculated. There are two reasons for this:

First reason is the normative method of measuring room temperatures with shielded plate thermometer. The burners heat up the fire area by hot jets, including flames (with an emissivity ε_f). The room temperature is measured at the points of the thermometer plates. Due to the radiation shields, the flames radiation cannot completely be taken into account. However, in fact all specimens get the heat radiation from the flames.

The second reason is shown in Figure 6 of Chapter 1.7.2. As previously mentioned, the heating of a sample is influenced by convection and radiation. However, each influence varies during a fire. In the first minutes, the heating of a specimen is mainly affected by convection. With a radiation amount of about 20 % of the net heat flux, a change of the emissivity has no major influence in the calculated heating of a sample.

As a result, for example if a specimen has a higher temperature than the actual calculated one, the emissivity has to be changed to a higher value to compensate this difference. In order to fulfil this requirement, it is possible that the emissivity has to be partially greater than 1.0, which is physically impossible. This problem can be recognized, for example, in Figure 62, Figure 63 and Figure 64. In the range of the first five minutes, neither the calculated temperature-time curve with an emissivity of $\varepsilon = 0.70$ nor the curve with the starting emissivity $\varepsilon = 0.35$ approximates, not even partially, the measured temperatures.

6.6.1 **Emissivity – Full fire test no. 01**

In the first full fire test, various interactions between the samples took place. In addition, a simplification for the emissivity had to be made as a basis to calculate the influences between the specimen. Based on these circumstances, it is quite impossible to recalculate reliable emissivity values for the whole test, for every sample. Nevertheless, the simplifications showed good results in the first 15 minutes of the test. A recalculation was done until the interaction is too high for each sample. Therefore, the emissivity for the most samples is available until a temperature of 500 °C.

For specimens with a section factor of $A_m/V = 60$ the emissivity can be seen in Figure 65, whereas for specimens with a A_m/V factor of 210 the emissivity can be seen in Figure 66.

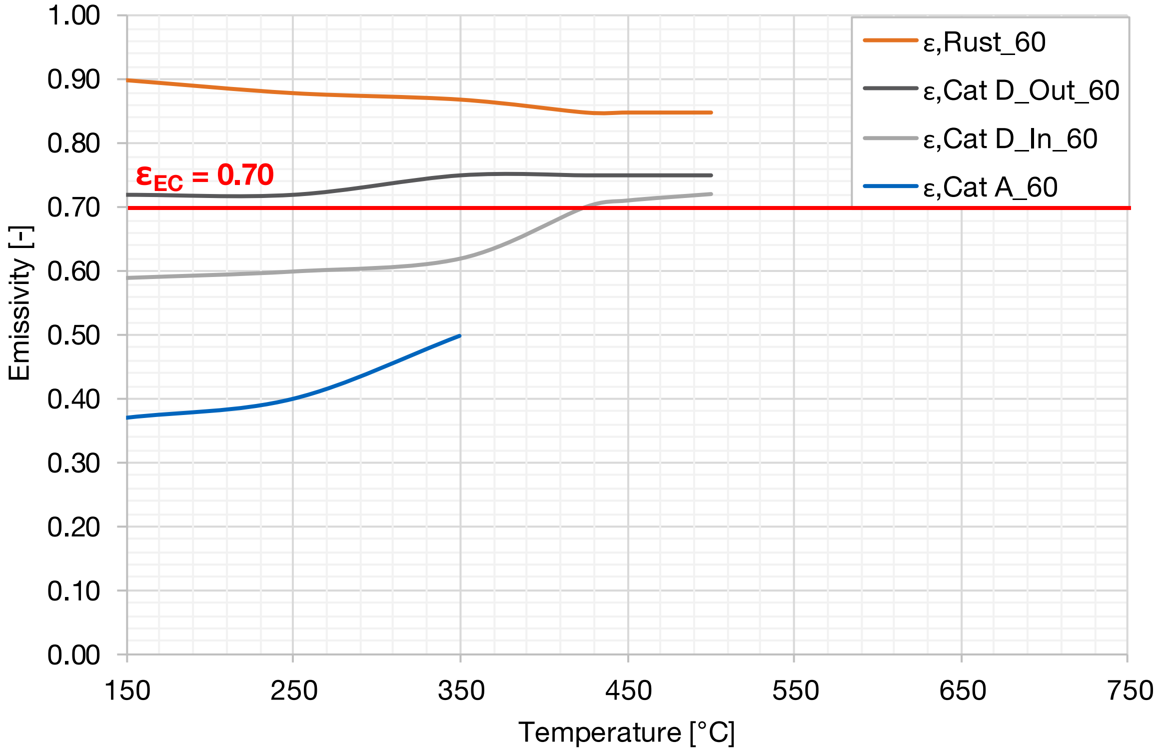

Figure 65: Recalculated emissivity of the first fire test for specimens with an A_m/V-factor of 60 [m^{-1}]

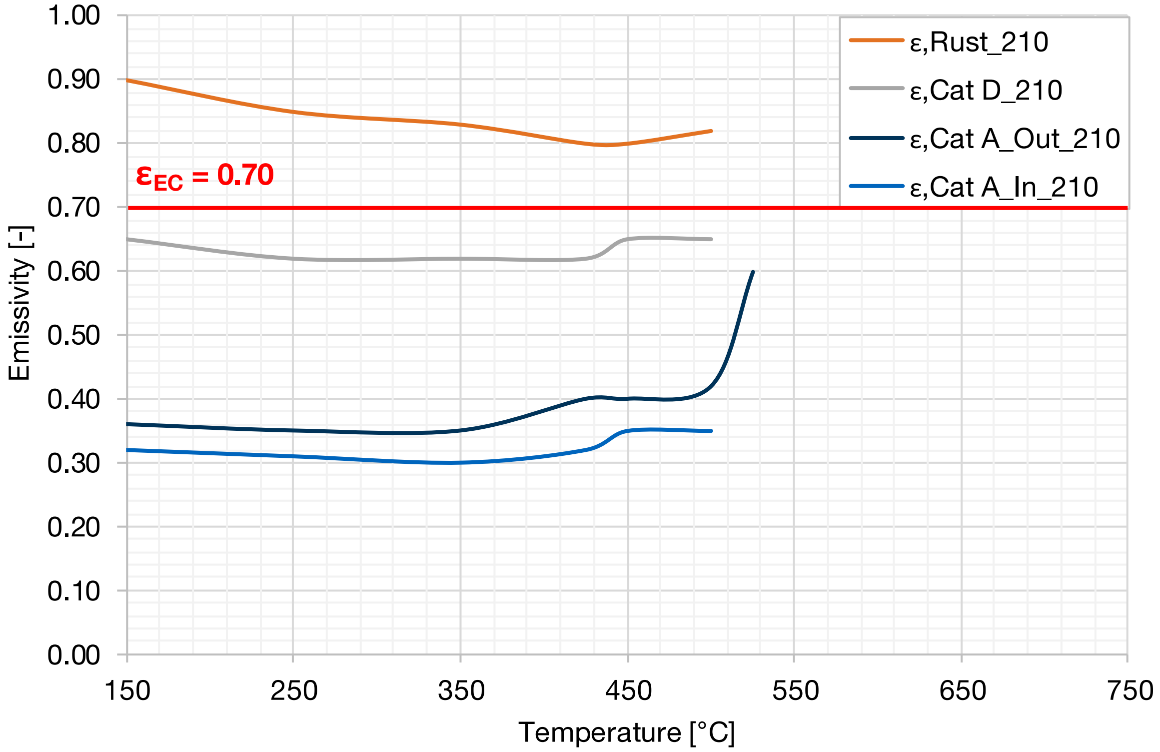

Figure 66: Recalculated emissivity of the first fire test for specimens with an A_m/V-factor of 210 [m^{-1}]

Following the correlations of the individual temperature-time curves of each sample category of Chapter 6.4.3, the related emissivity curves have the same relationships among each other. Independent of the section factor, one can see that category A has the lowest, rusty samples the highest emissivity and category D is in between them. In addition, the emissivity of samples which have been stored inside are always lower than their equivalent counterpart samples which have been stored outside.

However, better results can be achieved by analysing the second full fire test, as the specimens did not affact each other.

6.6.2 **Emissivity – Full fire test no. 02**

For the second full fire test the emissivity is calculated for higher temperatures than 150 °C. For each steel category and each section factor an own emissivity-time curve was determined. The result can be seen in the following Figure 67.

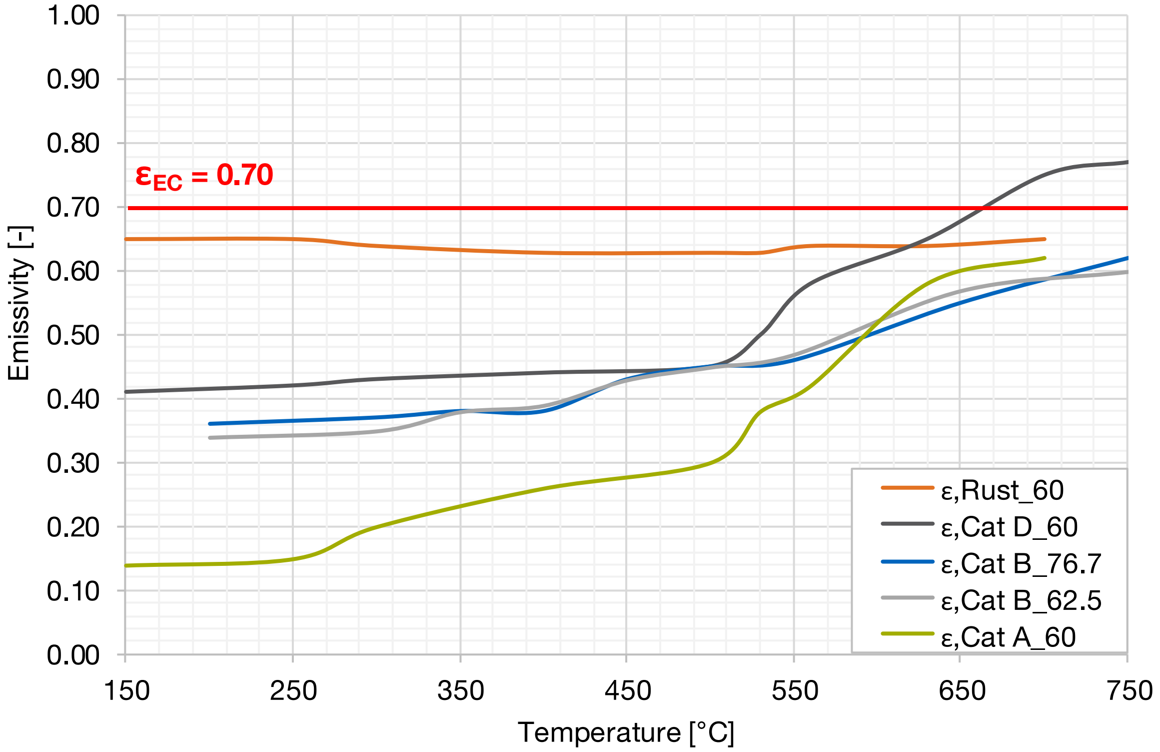

Figure 67: Calculated emissivity curves in dependence of the temperature for specimens of the second fire test

Again, the same relationship occurs between the emissivity curves in dependence of the temperature. Category A exhibit the lowest emissivity, category B the second lowest, category D the highest value for hot-dip galvanized steel samples and the rusty steel has the highest value of all tested categories.

The emissivity of category A starts at a very low level, at about $\varepsilon = 0.12$. In the ongoing of the fire tests the emissivity increases with increasing temperatures. This behaviour is in line with the theory presented in Chapter 3. At a temperature of about 530 °C the emissivity rises strongly and ends for temperatures of about 650 °C and higher at a level of ε = 0.65. This increase for temperatures at the resistance limit of the ζ-phase is typical for steel compositions in the low-silicon content steel and was already seen in the EP-T (see Chapter 5).

The emissivity of category D shows a very constant behaviour at around ε = 0.45 up to a component temperature of about 510 °C. At the resistance limit of the ζ-phase an increase of the emissivity can be seen. For temperatures above 650 °C the emissivity exceeds the default emissivity ε_{EC} = 0.70 of the Eurocode and has therefore a worse heating behaviour with respect to the fire resistance of structural steel.

Emissivities calculated from the two differently sized samples of category B (A_m/V = 62.5 and A_m/V = 76.7) result in a value around ε = 0.35 - 0.40. From a temperature of about 540 °C, which is almost identical, to that of category A and D, the emissivity increases continuously and ends at ε = 0.60 - 0.65 for temperatures of the specimens of about 750 °C.

The comparative rusty sample exhibits a relatively constant emissivity of ε = 0.65 and is therefore approximately the same as the default value of the Eurocode.

7 Effects on the emissivity

In the following, some influences found in literature as well as in the EP-T and the full fire tests, such as the white rust or the angle dependence of the emissivity and its impact on the total emissivity will be discussed.

In addition, a deeper analysis is provided for hot-dip galvanized structural steel members in fire, with respect to the characteristic variable emissivity in the investigated temperature range.

7.1 Viewing angle

The angle dependence was experimental evaluated in the EP-T to prove the theoretical dependence of the emissivity of hot-dip galvanized surfaces. This was done, as described in Chapter 5, during the tests with the self-programmed remote control and a rotatable plate in the limits of +45° to – 45°. At the beginning, the angle was adjusted every few seconds by 5°- steps. The time interval was limited to the response time of the measuring tools (IR-Sensor and TC). The change by a five-degree offset, if any, is not greater than 1 – 2%, which is within the limits of accuracy of the measurements. As there were no major differences in emissivity by this adjustment, the following analysis compares measurements with a fixed measuring angle over the complete temperature range. This was done for samples of the category A and D, as they define the limits within the iron-zinc alloy surfaces.

In Figure 68 the specimen '10N_2', which was measured by a viewing angle of +30° to the normal direction, is compared with two other samples ('10N_3' and '10N_4') of newly galvanized surfaces, which were measured perpendicular to the surface. All specimens are from the same category A carrier plate ('10N'). Therefore, they have the same steel composition, the same alloy layer and the same surface appearance. One can see that there is quite no difference for temperatures up to 530 °C. For smooth surface conditions, as this is provided by category A, this is in line with the theoretical approach shown in Chapter 3. Subsequently, as the surface condition changes due to the diffusion processes and the oxidation of the outer zinc layer, a rougher surface occurs and the influence seems to become slightly greater. The variation can be quantified up to 10 % for an angle offset of 30°. Nevertheless, looking at the other two test samples one can see that the difference does not has to be ascribed by the angle. Due to transformation of the zinc coating, which is activated by temperatures above the resistance level of the ζ-phase, different surface condition may occur independent of the measuring angle.

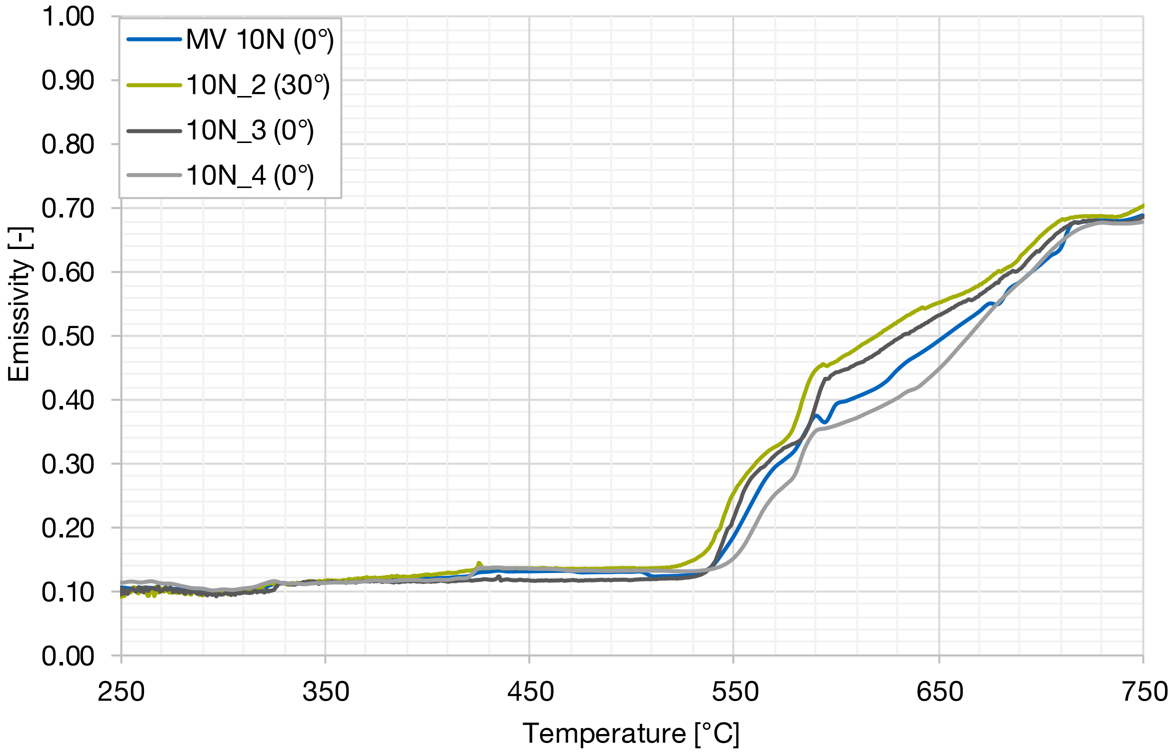

Figure 68: Comparison of angle dependence on sample '10N' (category A)

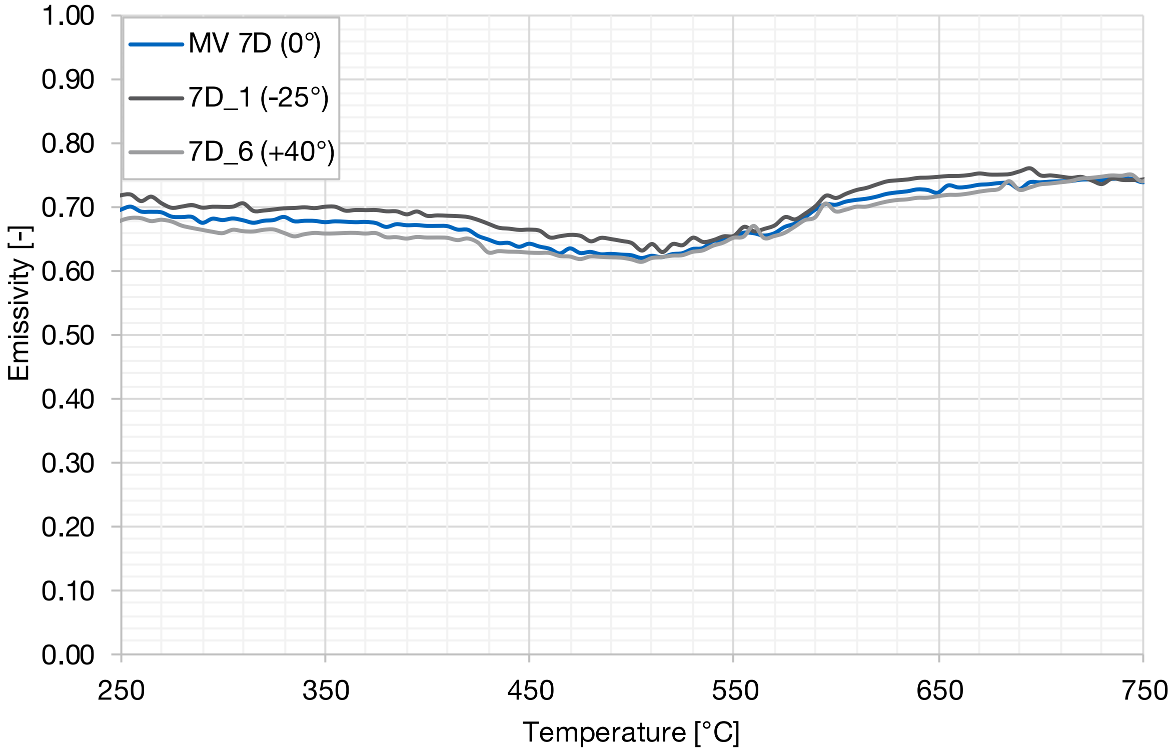

Figure 69: Comparison of angle dependence on sample '7D' (category D)

The same analysis was done for test specimens of category D. Figure 69 shows the temperature-time curve of the mean value of all specimens from the carrier plate '7D' in comparison to the curve of specimen ‘7D_1’, with a viewing angle of -25°, and in comparison to test sample ‘7D_6’, with an viewing angle of +40°.

In case of a rougher surface, the influence is a little higher. For both directions, the difference compared to the mean value is less than 5 %. Again, as already stated, this deviation is within the limits of accuracy of the measurements and within the dependence of the individual surface change of each zinc coating.

Consequently, the dependence of the emissivity in the angular range of -40° to +40° degree can be neglected. The theoretical approach in Chapter 3.1 was therefore proven in this angle range. Looking at angles with a greater offset than 40°, the theoretical approach of the *Drudes Model* (see [21,24]) as seen in Figure 15 shows higher emissivity values for metals, especially for viewing angles which are greater than 60°. However, this approach is only valid for wavelengths $\lambda > 5$ µm. By contrast, the angular distribution of the directional emissive power E_λ degreases (see Chapter 2.5, Figure 10) with an increasing viewing angle. Therefore, the influence of angles, which are greater than 40° can also be neglected.

7.2 **Wavelength**

7.2.1 **Wavelength dependence at both IR-sensors**

As already mentioned, the infrared wavelength, at which the IR sensors measure metallic surfaces, should be as small as possible, to minimize the error of the measurement. For smooth zinc alloy layers, the measurement of the *3MH1*-sensor, which measures at a wavelength of 2.3 µm is therefore more accurate.

Since roughness dominates the surface at higher temperatures of HDG samples, a measurement in a higher spectrum of 7.5 – 13 or 8 – 14 µm, especially in the range of temperatures of 550 °C and higher, can be more reliable, than the measurements in a short wavelength range. This was clearly visible at category B in Figure 37, for the resistant temperature of the ζ-phase around 530 °C, which was not recognizable in the short-wave spectrum. This fact arises also the lack of information for materials such as concrete and wood in Table 8 of the VDI [26] in Chapter 3.2. However, due to a higher amount of radiated energy at even higher temperatures, the measurements of the shorter wavelength spectrum get more reliable again.

The wavelength dependence is shown in the following with respect to category A and B surfaces. Due to their reactions and, accompanied, a surface change due to the thermal influence, the differences are of better apparent effects.

Looking at the curves in Figure 70 and in Figure 71, one can see that the differences between the measurements in both spectra (2.3 µm and 8 – 14 µm) are quite identical. The average deviation in most cases is not greater than 5 % for temperatures below 530 °C. For higher temperatures the difference varies in dependence of each case, with a highest deviation of about 15 %. However, the radiated energy at the lower spectrum of around 2.3 µm is by a multiple higher and consequently should be more accurate. This was shown in Figure 12 of Chapter 2.5 and can be calculated exactly with the equations of Chapter 2.5.3.

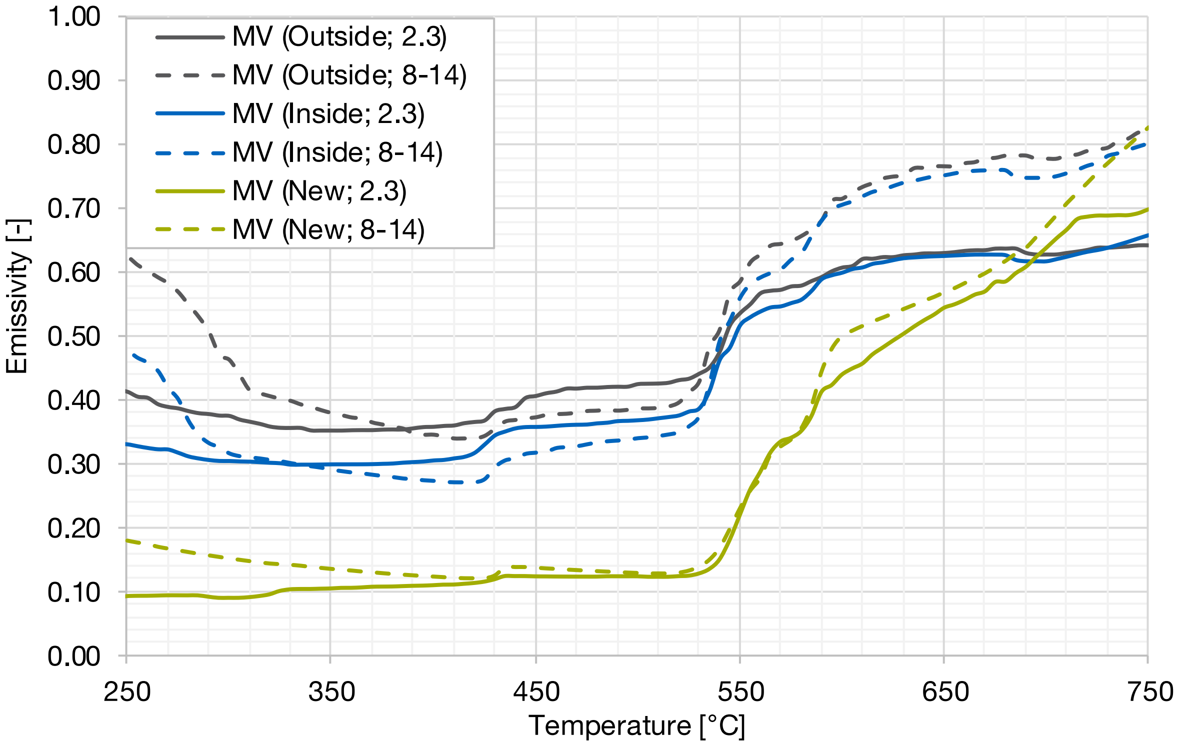

Figure 70: Comparison of the measured emissivity of category A in different wavelength spectra

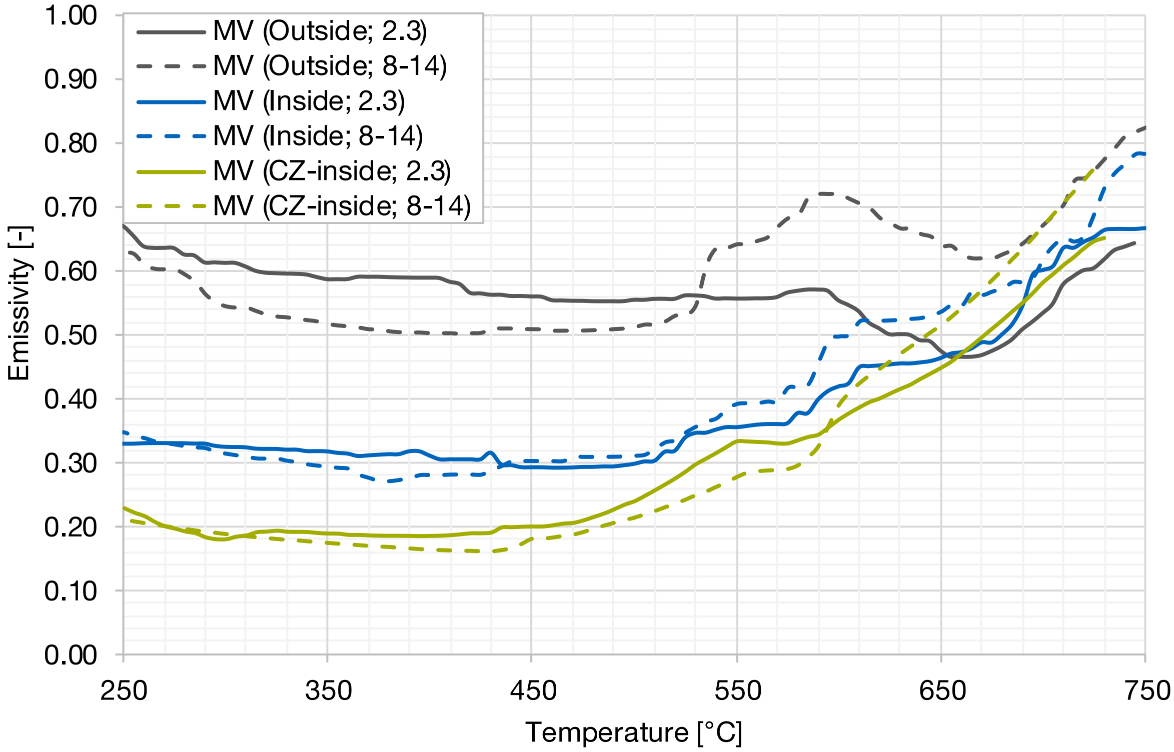

Figure 71: Comparison of the measured emissivity of category B in different wavelength spectra

The analysis of the infrared camera, in Chapter 5.5, reveals distinct lower emissivity curves over the temperature range up to 530 °C, for a wavelength spectrum of 7.5 – 13 µm, and marginal higher emissivity curves for higher temperatures.

7.2.2 **Comparison to literature**

Overall, there is a moderate dependence of the measured wavelength range. However, as seen in the analysis of the infrared camera, an even higher dependence can be seen, for hot-dip galvanized samples, on the measuring spot on the surface. For rougher surfaces, as this is the case for category B and D, it was proven that a measurement at larger wavelength also exhibits good results. Nevertheless, as mentioned in Chapter 5.2.6, for metal surface one should take the smallest possible wavelength to minimize errors.

Emissivity in literature, provided in Chapter 3.2, shows a decreasing value accompanied by an increase of the measuring wavelength spectrum. This effect is independent of the provider of these information and can be seen in Table 8 and Table 9. The findings in this thesis show that this behaviour is only valid for temperature ranges lower than 530 °C. Subsequently, at least for hot-dip galvanized samples, the emissivity measured by longer wavelengths is higher.

Comparing the data of literature with the evaluated emissivity values of this thesis in the spectra, in which the two infrared sensors and the thermal camera measured, one can say that newly hot-dip galvanized surfaces are in line with the provided values for blanc or even polished steel. Samples with white rust are, in contrast, in line with the provided data for oxidised steel.

7.3 **White rust**

According to the theory, as for example described in *Siegel et al.* [21], the emissivity of metallic surfaces should steadily increase with increasing temperature. Thus, the lowest emission value has to occur at the beginning of the temperature measurement range. However, this is not the case for samples covered by white rust, in the range of low temperatures up to approximate 300 °C. Depending on the severity, this more or less affects the emissivity. The influence decreases in the case of rising temperatures and disappears at temperatures of about 350 °C. Subsequently, the emissivity of the actual existing surface is found. Depending on the previous weathering or storage conditions and thus the outer zinc layer phase, obtained after depositing the white rust formation, a certain characteristic level of emissivity occurs. In case of a more pronounced, initial oxide layer, this level is higher than for less significant formations. The influence is therefore strong at the beginning of the heat impact.

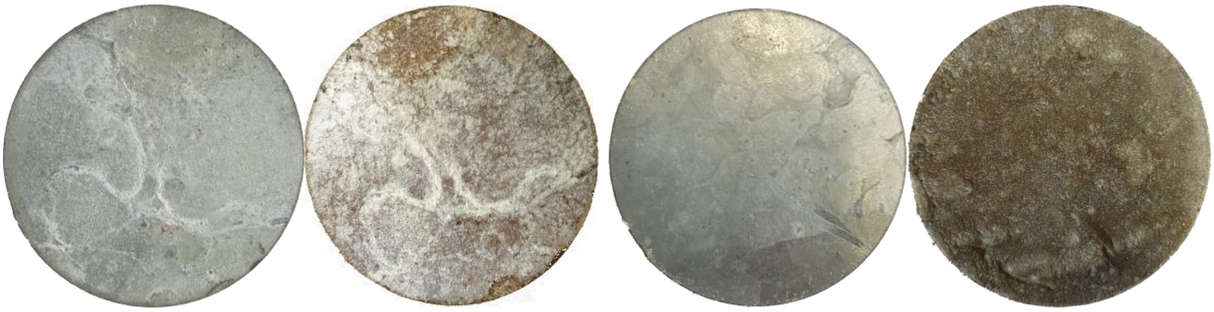

Figure 72: Two specimens of category A each before and after the thermal impact

The reactions of specimen, which have been covered with white rust, differ. Due to zinc oxide layers before the thermal exposure, different chemical products and therefore different surface optics arise on the surface. This can be seen in Figure 72.

However, the influence of the white rust is diminished by the fact that the majority of the transmitted energy is transmitted at the beginning of a fire by convection and not by radiation (see Figure 6 in Chapter 1.7.2). The white rust leads, taking both effects into account, to a moderate influence.

7.4 **Re-galvanizing**

As it was shown in the second full fire test, in Chapter 6.5, there is no major influence, if samples are dezinced and re-galvanized. Even if the surface has some pimples, the emissivity is, with quite no deviation, the same as for newly hot-dip galvanized structural steel members. This is especially for old buildings an important added value for building refurbishment.

7.5 **Roughness**

Two categories of surfaces can be identified regarding the roughness of a surface: optical smooth surfaces and real rough surfaces. The spectral emissivity for ideal optical smooth surfaces can be determined by Equation (3-3) as it was shown in Chapter 3.1. As hot-dip galvanized surfaces, under the influence of temperature, are of a rougher type and therefore vary strongly regarding their roughness, this attempt was not used for the following analysis.

To investigate the differences in the emissivities of the specimen, haptic roughness measurements were carried out at the IKS in Dresden and at the Technical University of Munich. Several measurement methods, depending on the order of the roughness, were investigated to research their influence. Therefore, a short overview of the different roughness order is given:

With respect to DIN 4760 [36], six different orders of surface deviations can be measured. The 1st, 2nd and 3rd order are a form of geometrical failures (e.g. a flatness deviation, waviness) and can be covered by the analysis of Chapter 7.1. Whereas, the 4th order takes different roughness values into account, the 5th and 6th order considers the microstructure and the lattice structure. Thus, only the 4th order is examined in this chapter in detail.

Modern surface measuring devices output a large number of different surface characteristics, the significance of each is quite different. The following paragraph gives an overview of the determination and validity of the most important parameters.

The arithmetic mean roughness R_a represents the arithmetic average deviation of the absolute values of the profile from the middle line. It cannot distinguish between peaks and grooves, nor can it recognize different profile shapes. However, R_a is widely adopted in engineering, since it gives a good general description of the height variations in the surface.

$$R_a = \frac{1}{l_r}\int_0^l |z(x)|dx, \tag{7-1}$$

where z is the heights and l_r is the single measurement length.

R_q is the root mean square roughness of the profile deviation. It is defined in a similar way as R_a, but is more sensitive to single peaks and grooves. It is calculated by taking the root of the variance of Equation (7-1). R_q is thus defined as

$$R_q = \sqrt{\frac{1}{l_r}\int_0^l |z^2(x)|dx}\,. \tag{7-2}$$

In addition, for each length l_r of each measurement section, the mean roughness depth R_z is defined as the sum of the height, of the largest peak, and the depth of the largest valley. R_z results from averaging the individual results of five measurement sections.

$$R_z = \frac{1}{5}\sum_{i=1}^{5} R_z(i) \tag{7-3}$$

7.5.1 Surface parameter roughness of 4th order

The first analysis was done for samples, which were stored inside and outside, of category A and D, with an initial adverse storage. On the one hand for samples before and on the other hand for samples after the temperature exposure. Mean roughness depths R_z, as shown in Figure 73, exhibit a good tendency to show how the emissivity is related to the individual samples.

Comparing the roughness R_z of category A and D among each other, one clearly sees a difference. For example, in case of indoor stored samples the roughness depth R_z is more than 60 % higher for samples of category D compared to samples of category A.

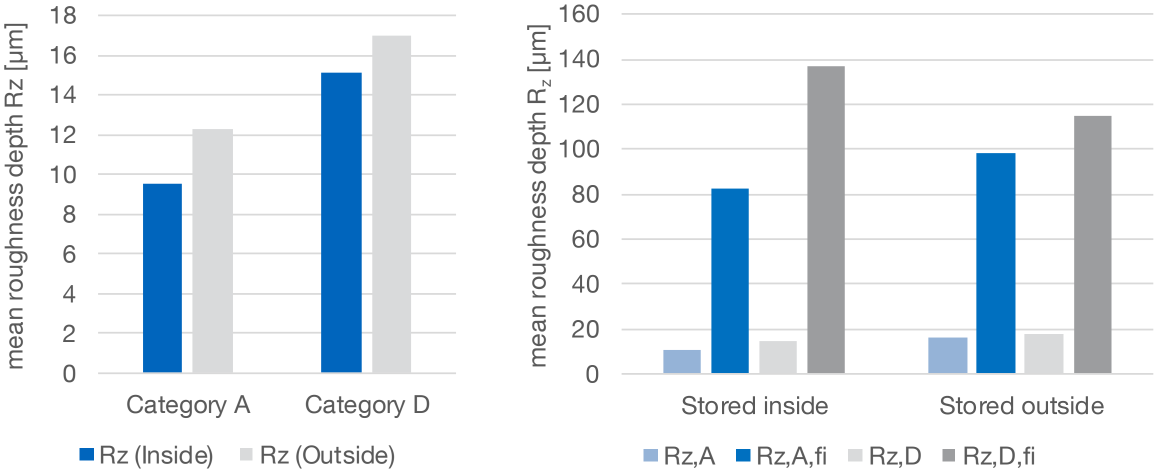

Figure 73: Measured roughness R_z for specimens of category A and D, before and after the thermal exposure

Differences also can be seen within each category. Samples stored outside have a surface roughness of about 15 – 30 % higher than those stored inside. Consequently, there is a good correlation with the measured emissivity ratios in Chapter 5. If one compares samples before and after the effect of temperature, the roughness R_z at the end assumes a value which is 6 to 8 times higher. Due to the subtleties in the nanometre range, the emissivity can only be estimated from this surface parameter.

Since radiation can be ‘caught’ in the surface structure of peaks and valleys, the emissivity and therefore the heat absorption also considerably depends on the roughness of the surface. An increase in the emissivity is consequently associated with the continuous increase in temperature and thus an increase in roughness.

According to *Siegel et al.* [21], the hemispherical emissivity increases when the root mean square roughness R_q is greater than the wavelength λ of the incident thermal radiation. The reason for this are multiple reflections of the rays in the valleys of the surface profile. This in turn is physically possible due to smaller radiation wavelengths compared to the cavities. This increases the degree of absorption and, consequently, according to *Kirchoff's law*, increases the emissivity. The wavelength therefore has a direct influence on the emissivity. As shown in Chapter 2, the wavelength of heat radiation also has a significant influence on the transmitted energy. For a complete spectrum, an effective part of the wavelength can be assigned, which influences the heating behaviour to a decisive extent. For the effective part of the total emitted power the range applies as:

$$\frac{R_q}{\lambda} > 1 \tag{7-4}$$

The root mean square roughness R_q of the different hot-dip galvanized steel specimens in this thesis can be seen in the following table:

Table 30: Root mean square roughness R_q measured on different specimens

	HDG steel			**Rusted steel**
Category	**A**	**D**	**B**	**rust**
R_q	4.533	5.171	12.680	8.914

With Equation (7-4), it can thus be estimated which proportion of the radiated energy at which temperature per category has an influence on the emissivity. With an increasing temperature the influence of this ‘effective energy’ increases, due to decreasing wavelengths of the radiation. Looking at Table 31, it can be seen that, for example, category A and D differ by about 10 % for the whole temperature range. Looking at this difference, it indicates that heat intake in category D tends to be consistently higher. If one compares the temperature-dependent emissivities of the EP-T experiments (see Chapter 5.4), this coincide with the results. Even higher is the effective ratio of rusty samples. Again, parallels can be drawn to the emissivity. The fact that the emissivity cannot be deduced from the pure square mean roughness R_q is shown by the sample of category B. The R_q value is several times higher than that of category A and category D, but the emissivity measured and analysed via the EP-T is exactly between the two categories. One reason for this exception is the fact that the root mean square roughness R_q changes differently during heating for each category. The ratio of the individual R_q is not the same for the complete temperature range. In addition, the roughness is only one influencing factor of many.

Table 31: Ratio of the absorbed effective energy, in dependence of the roughness of each category, of the total radiated energy for several temperatures

	Ratio of the effective energy from the total radiated energy [%]			
Temperature [°C]	**A**	**D**	**Rust**	**B**
300	18.4	26.7	65.2	83.0
419	30.6	40.1	75.5	88.8
530	41.3	51.0	82.0	92.1
650	51.5	60.5	86.7	94.4
750	58.6	66.9	89.5	95.6

7.6 **Microstructure**

If the outer phase of the iron-zinc alloy is an η-phase, as it is for category A, it was shown that the emissivity is, at the beginning of the thermal exposure, very low. For a present outer ζ-phase, as it is for specimens of category D, the emissivity is quite high. In the following, the differences in the microstructure are shown and are linked to the emissivity.

7.6.1 **Texture of the outer alloy phase**

In case of an upper η-phase, the layer consists practically of pure zinc or the zinc bath composition and is formed by simple solidification of the zinc melt. The iron content is about 0.08 %. Zinc, as shown in Chapter 1.4, crystallized in the hexagonal system (hcp).

The intermetallic ζ-phase can be defined stoichiometrically as $FeZn_{13}$. As it can be seen in Table 4, the iron content is about 6 %. While pure zinc still crystallizes in the hexagonal closest packing, this phase crystallises differently. In literature, most references point to a monoclinic, base-centred lattice (C2/m symmetry). However, their lattice constants strongly differ from those of iron and zinc. Thus according to *Liu et al.* [37] the lattice constants have the following values $a = 1.3408 \cdot 10^{-9}$ m, $b = 0.7605 \cdot 10^{-9}$ m, $c = 0.5074 \cdot 10^{-9}$ m. These were also confirmed by Pokorny *et al.* [38]. Depending on the growing rate, different amounts of iron are bound to the near-surface layer and thus a different atomic lattice structure is present for different steel grades. As it can be seen from microsections, even in category A the ζ-phase appears to some extent at the surface, which partially increases the iron content. With different lattice structure different emissivity values occur.

7.6.2 **Spangles**

The results of the infrared camera exhibit major differences in the emissivity of dark and bright zinc spangles. As mentioned in Chapter 1.4.2.5, the appearance of these different spangles is related to a changed crystallographic orientation (see Chapter 1.2). Bright crystal structures are based on a basal texture, whereas matt crystals have a crystallographic orientation of pyramidal (10.2) (10.3), (11.2), or prismatic planes (10.0) parallel to the surface.

In addition to the duller or darker appearance, the pyramidal crystal structure leads to higher emissivity values, while, planes (00.2), parallel to the surface exhibit a brighter appearance and lower emissivity values. This is in line with the findings of *Seré et al*. [11], where bright areas on the surface had a higher corrosion resistance while darker spangles had higher corrosion rates.

Zinc spangles were found by the infrared camera, on every category, even if these were not visible to the human eye. Since the emissivities measured, in Chapter 5.5, for dark and bright crystallographic structures of category D correlate with each other after the resistance limit of the outer ζ-phase, the emissivity-influencing spangles are only present in the uppermost layers and have to be dependent on the prevailing crystallographic orientation.

7.6.3 **Microstructure in the alloy layer**

The emissivity of a component depends on the microstructure of a very thin layer beneath the surface. Quite no research has been done on the property changes of hot-dip galvanized steel parts in case of a higher thermal influences. Essentially, hot-dip galvanized alloy coatings have a good thermal resistance for both low and high temperatures. In the area of atmospheric load, the upper temperature limit is usually given as 200 °C (see *Peissker* [39]). If temperatures above this limit affect the iron-zinc alloy, the diffusion processes between the two materials zinc and steel, respectively iron, and their phases, restart at reduced speed.

This effect is also called *Kirkendall effect* (see *Schulz et al.* [3]). After some time and high temperatures, as it is the case in this research project, this can lead to exfoliation of the outer pure zinc coating. According to *Maaß et al.* [40], this can be attributed to different diffusion rates.

As shown in Chapter 1.4.2, the different alloy phases have different structures. An emissivity difference can therefore also be set by a different structure. Due to the temperature dependence of the individual phases, some changes are expected in the course of heating. In order to analyse the zinc coating, microsections of test specimens from the Emissivity Performance-Test have been made before and after the thermal impact. Comparing these microsections before and after the thermal exposure one can clearly see a change in the layer structure. Figure 74 shows this situation for a specimen of category A, Figure 75 for category B and Figure 76 for category D. Whereas the iron-zinc layer exhibits different phases before the heating, these phase transitions disappear afterwards. All microsections on the right side of these three Figures have the same appearance. Independent of the category, the *Kirkendall effect* may lead to a more homogeneous layer structure after the thermal impact, due to an iron diffusion into the different phases.

The analysis of microsections was done for all surface conditions and for each category. Always leading to the same findings. More Microsections can therefore be found in Appendix 'Microsections'.

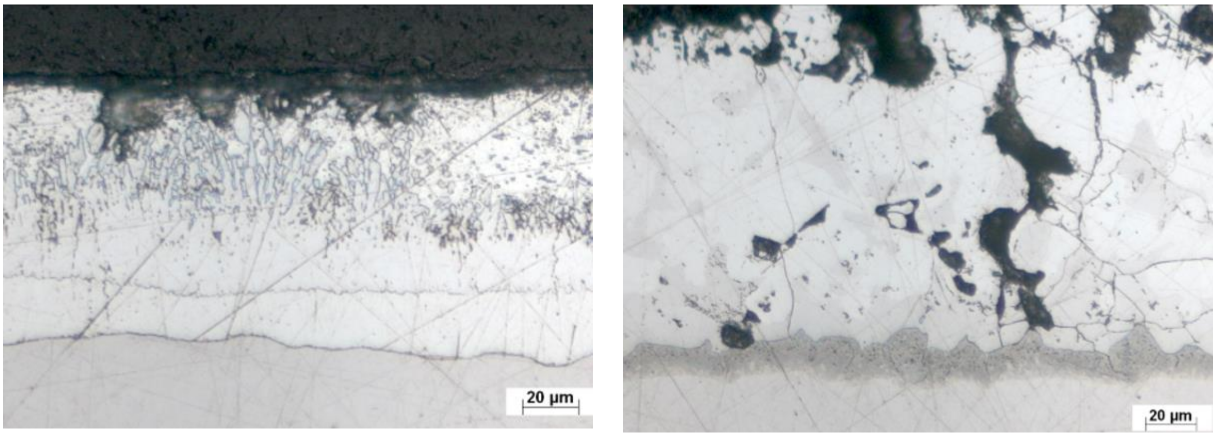

Figure 74: Microsections of category A before (left) and after (right) the thermal impact

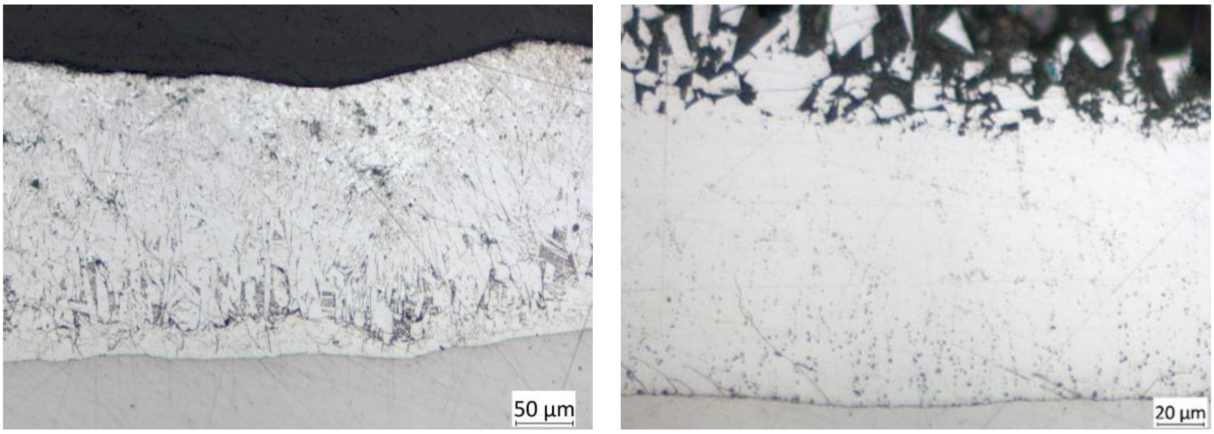

Figure 75: Microsections of category B before (left) and after (right) the thermal impact

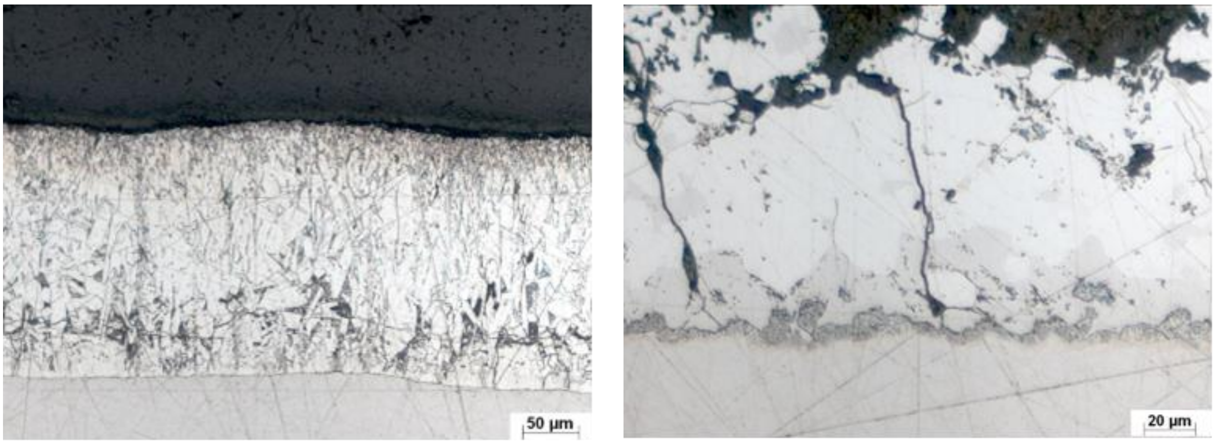

Figure 76: Microsections of category D before (left) and after (right) the thermal impact

In order to estimate the diffusion processes, REM/EDX analysis were performed on the zinc layer of each category A, B and D, on samples before and after thermal exposure. With the help of line scans, it was possible to see the weight percent (*wt.%*) of different elements. In the course of the thesis, it was of interest to know the different ratios of the elements iron (Fe), zinc (Zn) and oxygen (O). The measurements were carried out again in cooperation with the IKS in Dresden.

While at the line scan of the original state (Figure 77) the individual phases can be identified by their corresponding iron content, the line scan after the heating (Figure 78) shows that the transitions between the individual phases have been altered by diffusion processes and have been shifted to the surface. This shift of the phase boundaries (*Kirkendall effect*) and the diffusion of the iron into the zinc results, as already seen in the microsections, in an entirely different alloy layer compared to the originate one. A more detailed analysis on this effect is done in the next chapter.

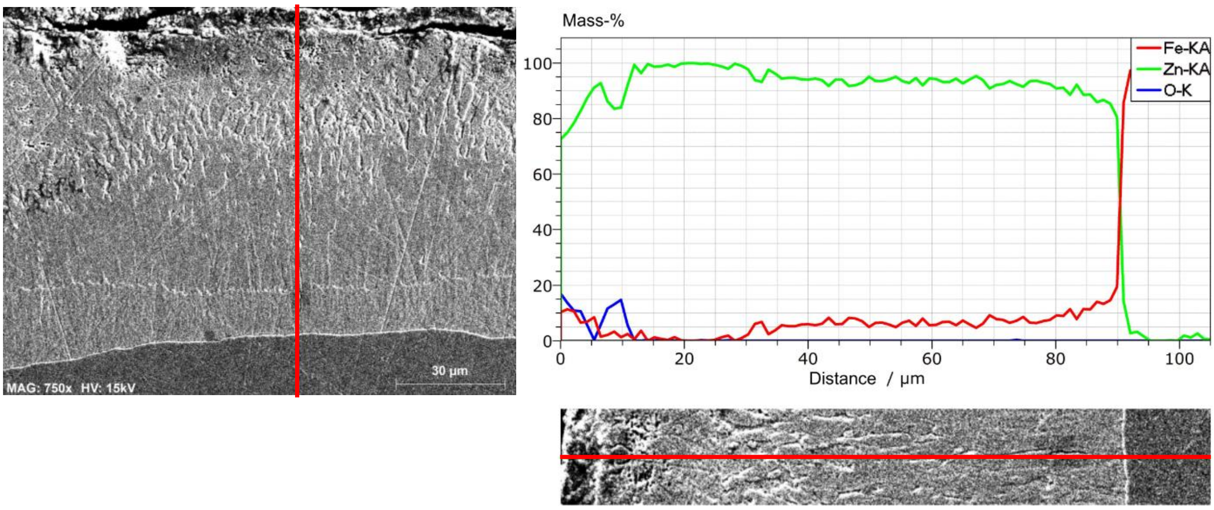

Figure 77: Line scan (REM/EDX) before thermal exposure on a specimen of category A

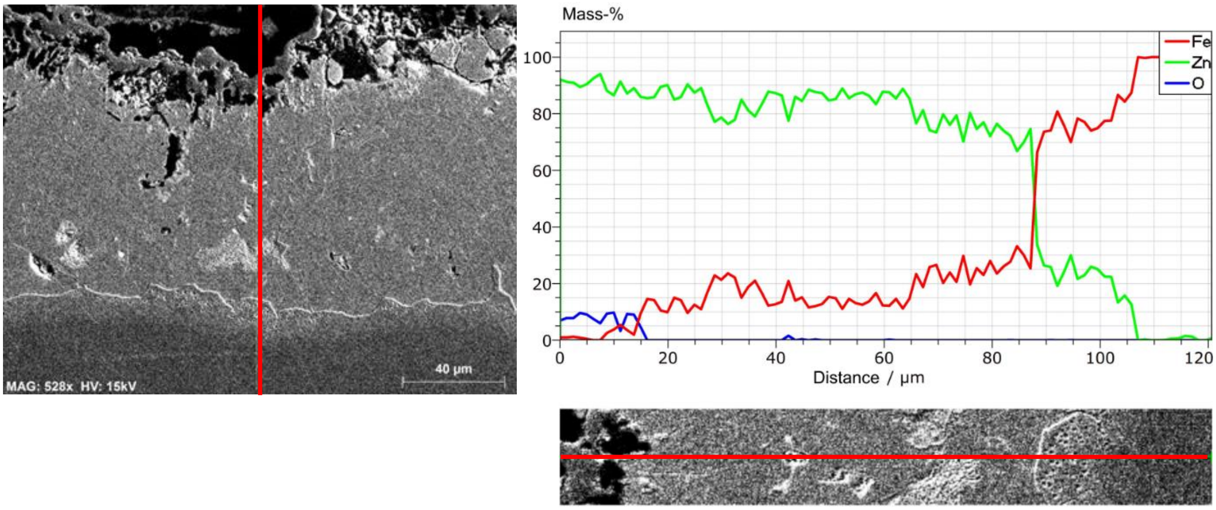

Figure 78: Line scan (REM/EDX) after thermal exposure of 850 °C on a specimen of category A

7.7 Temperature influence on the surface condition

7.7.1 Continuous heating of a hot-dip galvanized specimen

The influence of high temperatures leads to a change in the surface appearance, not only by the colour but also by the roughness. Some tests have been made to identify the different surface conditions at different temperature stages. Therefore, the heating was regulated to different levels. The levels were, in turn, defined by possible temperatures, which could be reached during a fire scenario by steel members and where defined between the resistant limits of the different alloy phases. The visual surface change can be seen for category A in Figure 79 and in Figure 80 for category B.

Both categories exhibit major changes, visible on the surface. With an increasing temperature, the surface changes from bright and 'grey' to dull and 'brown'. For temperatures higher than 700 °C the surface roughness additionally gets more pronounced. Whereas the iron-zinc alloy is very hard in the original state, the layers become porous and fragile. The latter sometimes leads to spalling as it can be seen in the lower part of the last specimen in Figure 80. An additional effect are bubbles, which appear if the temperature becomes even higher.

Figure 79: Samples of the same carrier plate of category A ('3N'), which have been affected by different temperature stages. From left to right: 1. Row: Original sample (20 °C); after 497 °C and 564 °C; 2. Row: after 693 °C, 808 °C and 846 °C

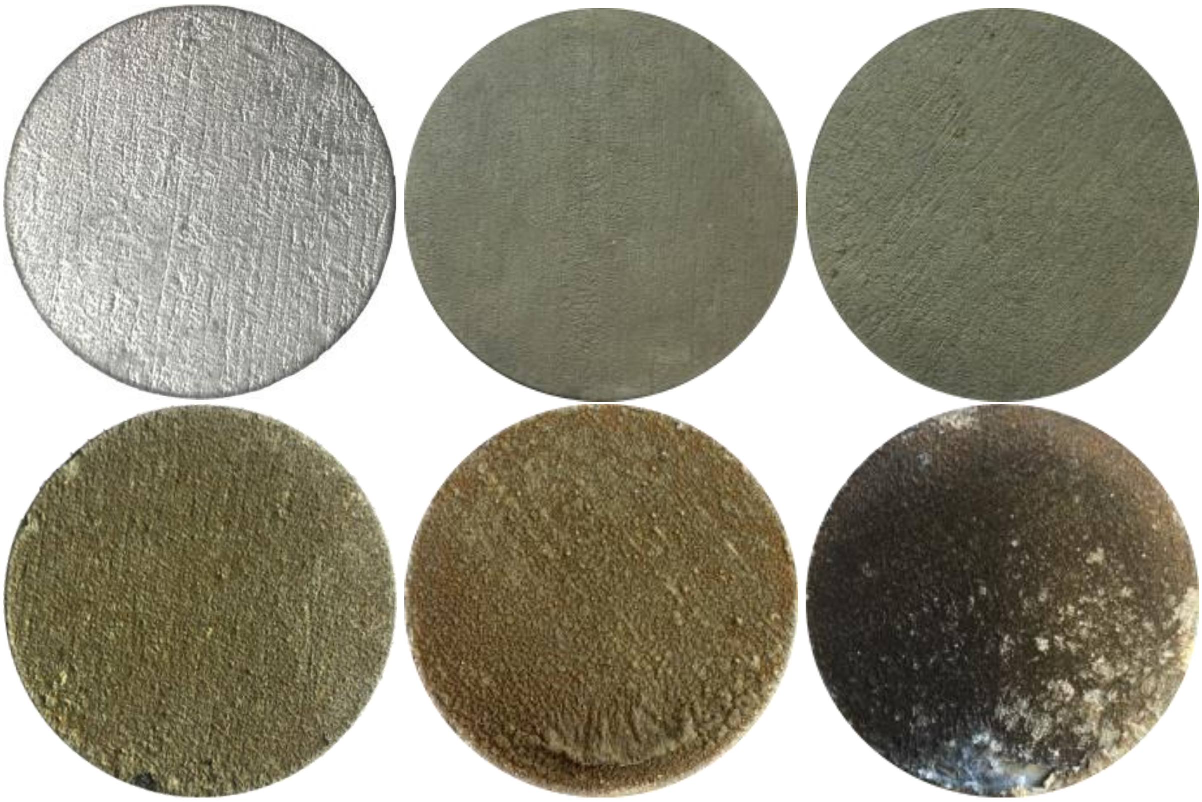

Figure 80: Samples of the same carrier plate of category B, which have been affected by different temperature stages. From left to right: 1. Row: Original sample (20 °C); after 562 °C and 606 °C; 2. Row: after 755 °C, 846 °C and 908 °C

As a conclusion, it follows that reactions of smooth samples are weaker than for specimens with a rougher initial surface.

Microsections and line scans, of the REM/EDX analysis, are used again for analysing the differences beneath the surface. The peaks in the following Figure 82, Figure 83 and Figure 84 can be referred to cracks in or in-between alloy layer phases and are therefore neglectable. In addition, due to the fragility of the iron-zinc alloy layers, the microsections are partly destroyed during grinding of the section. The analysis is first done for a new hot-dip galvanized specimen of category A.

As seen in the REM/EDX analysis in Chapter 7.6, before a thermal exposure each phase of the iron-zinc coating can be identified by their iron content. The original state in Figure 81, where the η-, ζ-, and δ_1-phases are clearly seen, is compared to line scans after a thermal exposure up to 564 °C, 693 °C and up to 698 °C. With a higher temperature impact, the diffusion processes take place stronger. Consequently, increasingly more iron is transferred to the surface. Whereas quite no iron is at the surface at the original state, about 8 – 10 % iron is concentrated at the surface for an impacted temperature of 564 °C. With a higher temperature of 693 °C, respectively 698 °C, an increased iron content of more than 10 % can be measured. This observation applies for all alloy phases. Each phase exhibits a higher amount of iron after the thermal exposure. In addition, the line scan of 693 °C in Figure 83 reveals the mentioned fragility, as the surface is not flat but more a fracture plane due to grinding of the section. With the line scan in Figure 84 of a temperature of 698 °C one can see how a microsection would look like, at higher temperatures, if there is no break out of the material.

A quite constant and equally distributed iron content, without any visible phase transitions, leads to only one residual phase above the δ_1-phase. Even if the iron content is very high, the new phase can be assigned as a ζ-phase.

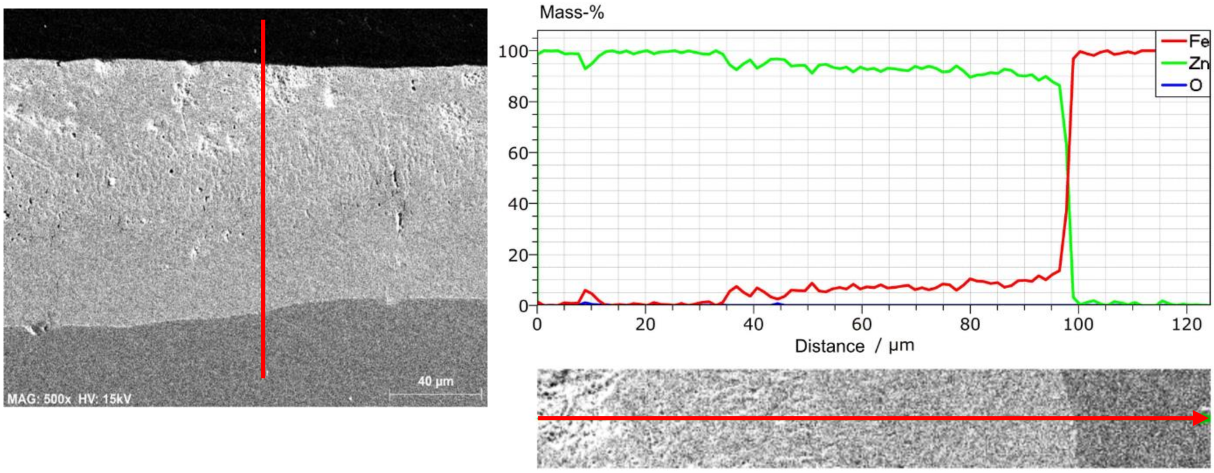

Figure 81: Line scan (REM/EDX) before thermal exposure on a new hot-dip galvanized specimen of category A ('3N_1')

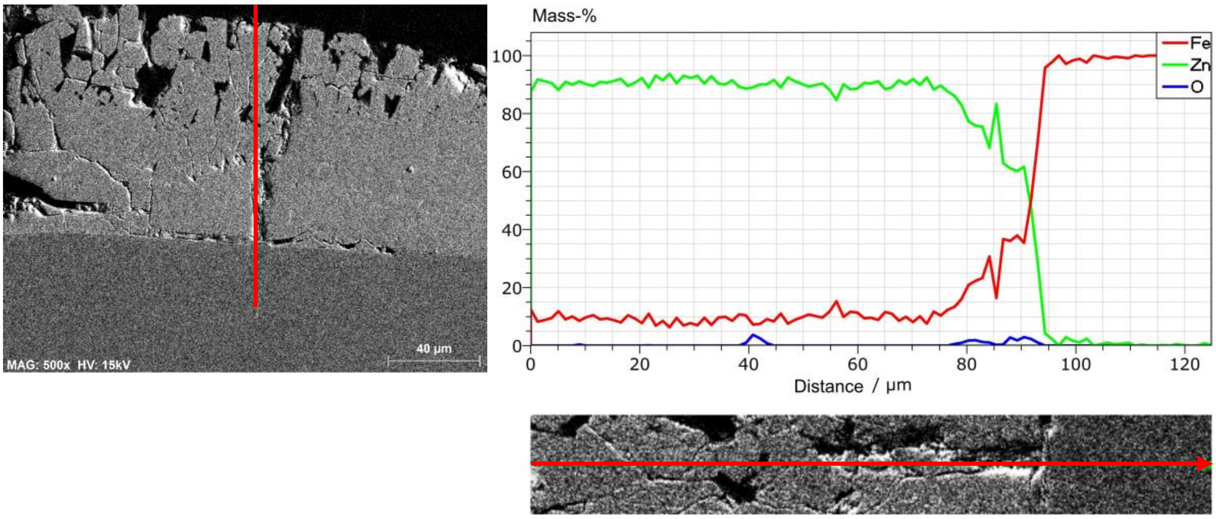

Figure 82: Line scan (REM/EDX) after a thermal exposure until 564 °C on a new hot-dip galvanized specimen of category A ('3N_3')

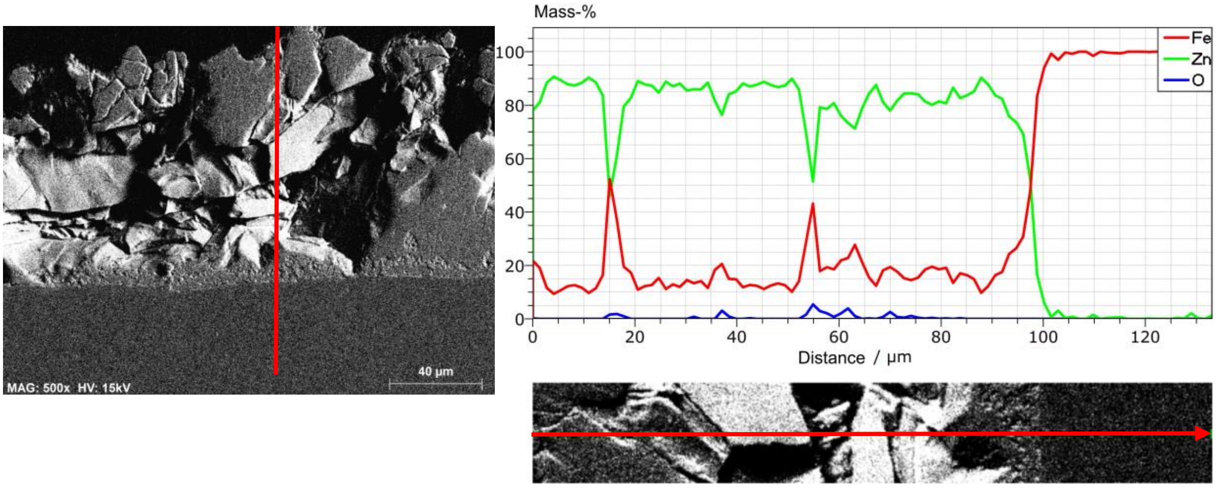

Figure 83: Line scan (REM/EDX) after a thermal exposure until 693 °C on a new hot-dip galvanized specimen of category A ('3N_1')

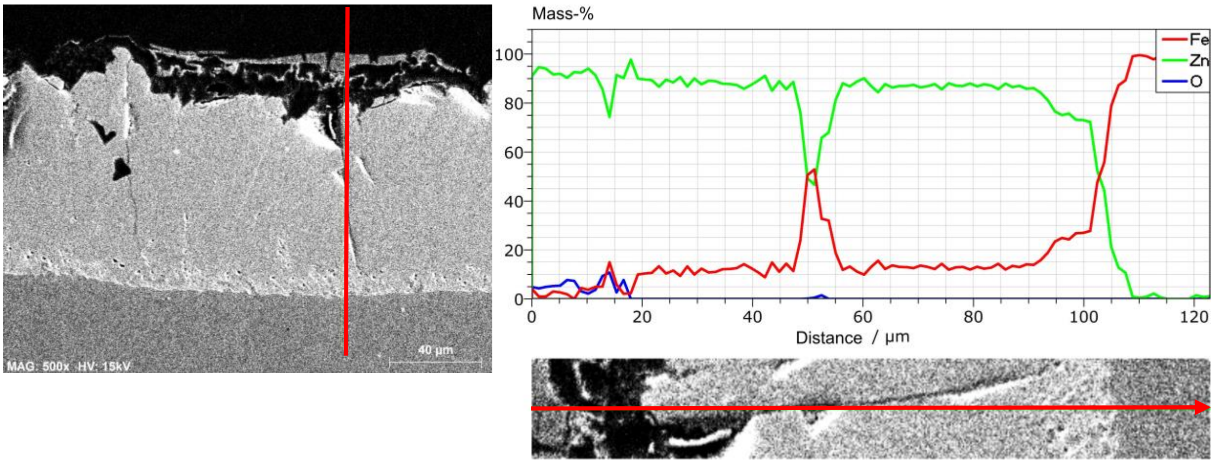

Figure 84: Line scan (REM/EDX) after a thermal exposure until 698 °C on hot-dip galvanized specimen of category A, which have been stored inside for one year after an adverse storage of eight weeks

The same analysis was done for category B. Comparing a line scan before a thermal exposure (Figure 85) with a line scan after a thermal impact of 608 °C (Figure 86) one can see the same changes into the same residual phase. Via REM/EDX, again a quite constant and equally distributed iron content, without any visible phase transitions, appears. The residual phase is therefore assigned as a ζ-phase.

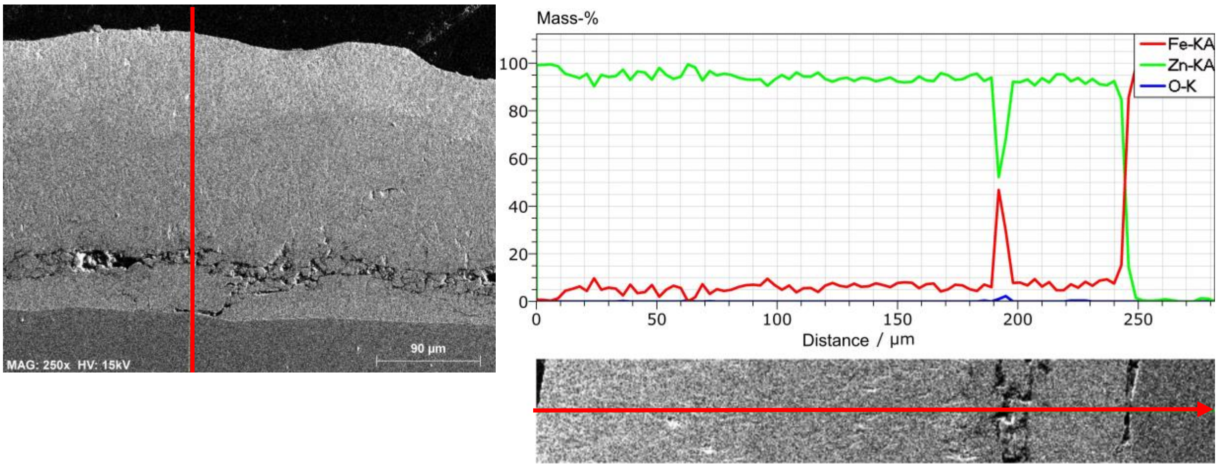

Figure 85: Line scan before thermal exposure on a new hot-dip galvanized specimen of category B ('B1')

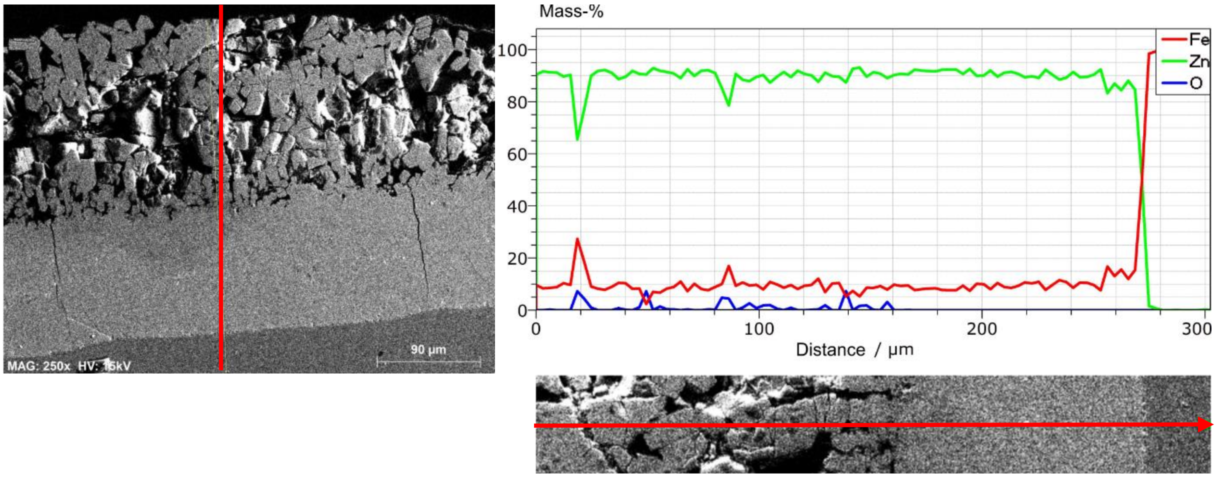

Figure 86: Line scan (REM/EDX) after a thermal exposure until 608 °C on a new hot-dip galvanized specimen of category B

7.7.2 Spectral analysis

During temperature increase, the pure zinc of the η-phase precipitates. It partially exfoliates or turns into chemical compounds such as zinc oxide. In addition, the iron accumulates on the surface. Spectral analysis of a category A sample heated above 850 °C yielded the following elements:

Table 32: Spectral analysis of the surface of a specimen (category A) heated over 850 °C

	Ratio of the elements [%]							
Spectrum	**C**	**O**	**Mg**	**Al**	**Si**	**Mn**	**Fe**	**Zn**
4-1618-1	3.84	8.6	0.75	3.99	1.05	1.72	32.87	47.17
4-1618-2	3.25	7.36	0.46	4.09	0.55	1.09	43.46	39.75
4-1618-3	5.87	10.51	0	0.21	0.16	7.75	11.33	64.18
4-1618-4	2.82	1.37	0	0.03	0.07	0.03	29.45	66.23
4-1618-5	2.44	1.59	0	0.01	0.12	0.07	28.56	67.21
4-1618-6	3.17	6.25	0.49	1.93	0.5	0.92	48.33	38.41
Mean value	**3.56**	**5.95**	**0.28**	**1.71**	**0.41**	**1.93**	**32.33**	**53.83**

7.7.3 Sudden temperature impact

In the course of the thesis, it was of interest, if a high temperature has another effect if it is not introduced continuously, but suddenly. Therefore, a hot-dip galvanized surface was exposed suddenly to a temperature of over 907 °C, which is the evaporation temperature of zinc. As assumed, the outer pure zinc layer evaporates and precipitates in a white powder. The powder partly remains attached on the sample and partly falls to the ground. An analysation showed that it is mainly composed by combinations of zinc oxide, as it can be seen in Table 33.

Table 33: Spectral analysis of powder of a specimen (category A), which was heated suddenly to 920 °C

Spectrum	**C**	**O**	**Al**	**Zn**	**Sum (%)**
4-1618-7	1.55	8.57	0.27	89.61	**100**
4-1618-8	2.74	8.21	0.19	88.86	**100**
4-1618-9	1.91	8.94	0.10	89.05	**100**
4-1618-10	2.2	9.09	-	88.71	**100**
4-1618-11	5.19	9.21	-	85.60	**100**
4-1618-12	3.93	8.93	-	87.14	**100**
Mean value	**2.92**	**8.82**	**0.19**	**88.16**	

7.7.4 Thermochromism

During heating the specimens offer a thermochromism. Thermochromism refers to the property of substances to change their colour when the temperature rises. With increasing temperatures, the surface (zinc oxide) changes its colour. Pure zinc oxide would be white in its original state (as mentioned in the previous Chapter 7.7.3) and gets yellow at higher temperatures. Due to other chemical compositions, the visible colouration deviates from a pure yellow. Reasons for these colour shifts are changes in the molecular or crystal structure. This process, which can be seen in Figure 87, is reversible. After cooling, the substance normally returns to its original colouration.

Figure 87: Thermochromism during heating of a hot-dip galvanized sample. From left to right: 22 °C, 340 °C, 510 °C, 650 °C, 810 °C

7.7.5 Analyse method for buildings after a thermal exposure

As shown in this chapter, hot-dip galvanized steel members offer a temperature-related surface appearance. Therefore, it is possible to estimate the highest temperature – which was introduced in a steel section – during a fire.

7.8 Passivation

Passivation is a subsequent treatment that is arranged after the HDG procedure. Passivation prevents temporarily the chemical reaction of the zinc coating with substances in the environment. Thus, additional layers of passivation improve the corrosion behaviour. As described in Chapter 4, white rust is mainly a problem with freshly hot-dip galvanized parts, since at the beginning no protective cover layers have formed. In order to ascertain the influence of passivation on the emissivity of hot-dip galvanized steel at thermal exposure, two different passivation systems were applied on test samples of category A and D.

One passivation system is a water-based lacquer and the other is a phosphating application. Both systems have, according to the producers a gloss retention effect and both slow down the formation of white rust. The selected passivation methods were applied to the zinc surfaces in a dipping process.

Analysing Emissivity Performance-Tests with passivated, newly hot dip galvanized specimen of category A ('MV (Passivation)'), one can see that the temperature-dependent emissivity curves still exhibit their low starting level. For comparison to the mean value of indoor stored specimen, also a sample ('1P (Outside)') with an outdoor storage under weathering conditions of two months was tested. A small difference appears after the first resistant limit of the outer η-phase of about 420 °C. Between this temperature and 650 °C the emissivity is about 5 % higher. Subsequently the deviation disappears and the curves approximate each other again.

By comparing the passivated emissivity curves with the temperature-dependent emissivity curves of Chapter 5.4.1 it can be seen that the typical abrupt increase is missing. In addition, the emissivity increases at a higher temperature. Towards the end of the measured temperature range the emissivity curves exhibit the same end values.

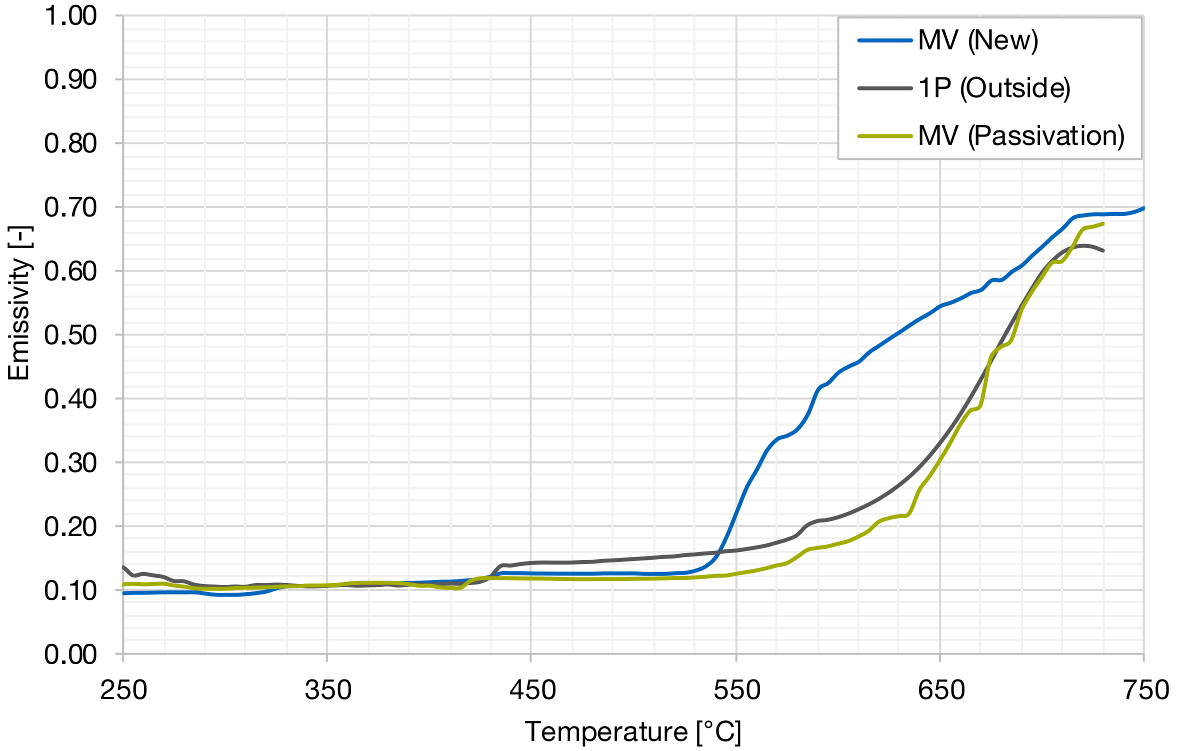

Figure 88: Comparison of passivated specimens with newly HDG specimens of category A (MV (New))

Passivated samples of category D exhibit quite the same emissivity curves as without a passivation. As shown in Figure 89 the influence is not significant. Since both passivation systems have a boiling point of about 110 °C, this behaviour can be explained as follows. The passivation has a beneficial influence on the surface in terms of white rust prevention. The starting levels of the emissivity is therefore as low as it would be on newly hot-dip galvanized surfaces. After a steel temperature of 110 °C there is no significant influence of the passivation on the emissivity, neither good nor bad.

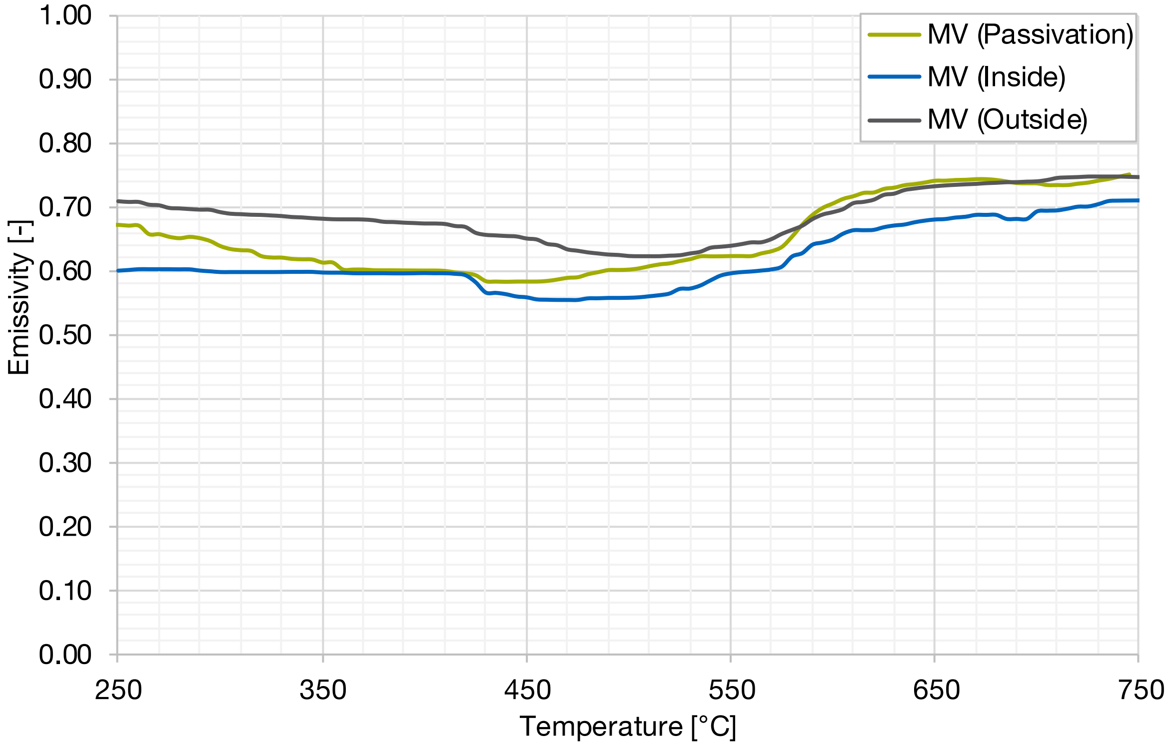

Figure 89: Comparison of passivated specimens with newly HDG specimens of category D (‘MV (Inside)’, ‘MV (Outside)’)

Consequently, a passivation can be used and due to the lack of white rust it may help that an even better fire resistance behaviour can be provided.

8 Total emissivity of HDG structural steel

In engineering, as it is the desired practical field for this research, it is necessary to provide a total emissivity for the verification methods in the Eurocodes, for example the DIN EN 1993-1-2 [17]. This physical quantity was achieved by taking all effects (see Chapter 2.5.4 and Chapter 7) into account. This resulted in a two-stage emissivity approach for category A and B, which was derived from 147 Emissivity Performance-Tests, and was proved by the full-scale tests. For practical reasons, and to be on the safe side with respect to uncertainties of the surface condition and with respect to fire safety, the total emissivity of hot-dip galvanized components therefore is assigned as follows:

$\varepsilon = 0.35 \leq 500$ °C and $\varepsilon = 0.70 > 500$ °C

For category D a total emissivity of $\varepsilon = 0.65$ can be assigned from the EP-T and is, therefore neglectable and will not be considered any further.

In the following benefits, design tools as well as a calculation example of this emissivity approach will be provided.

8.1 Nomograms

For the verification according to DIN EN 1993-1-2 [17] nomograms have been established. The development of the steel temperature can be directly received as a function of the fire duration and the modified section factor $k_{sh}A_m/V$.

8.1.1 Section factor - dependent nomogram for unprotected steel members

The positive effect of the new approach (ε_{var} = 0.35/0.70) can be shown by comparison with the Eurocode concept (ε_{EC} = 0.70) based on a nomogram for unprotected steel members subjected to the ISO 834 fire curve, for different time durations. Figure 90 shows this for fire durations of 15 and 30 minutes of the standard temperature-time curve (ISO 834).

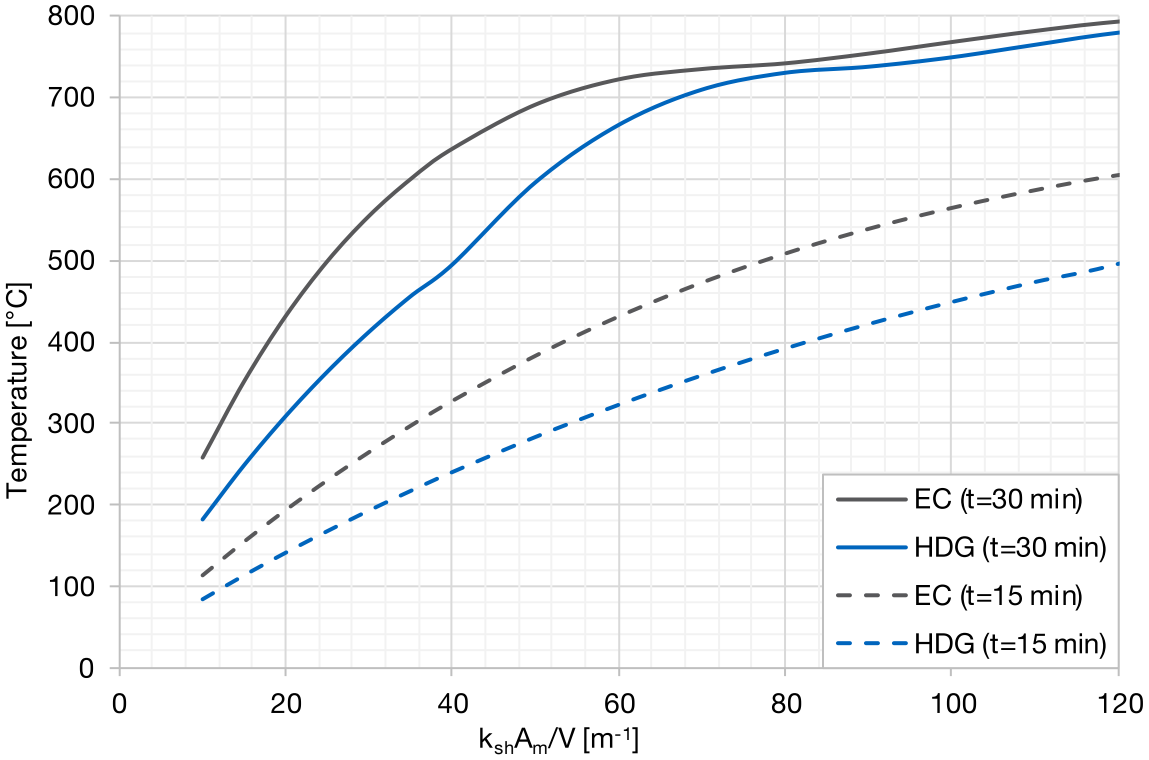

Figure 90: Influence of the emissivity of hot-dip galvanized steel profiles in dependence of the modified section factor $k_{sh}A_m/V$ for an ISO 834 fire up to 15 and 30 minutes

8.1.2 Temperature-time nomogram for unprotected steel members

A nomogram for unprotected steel members in a fire scenario according to ISO 834 fire curve is shown in Figure 91 for up to 30 minutes. Nomograms for a longer fire duration can be found in Appendix 'Nomograms'. In addition, due to the dependence to the modified section factors, these factors can be found in Table 38 and Table 39 in the same Appendix.

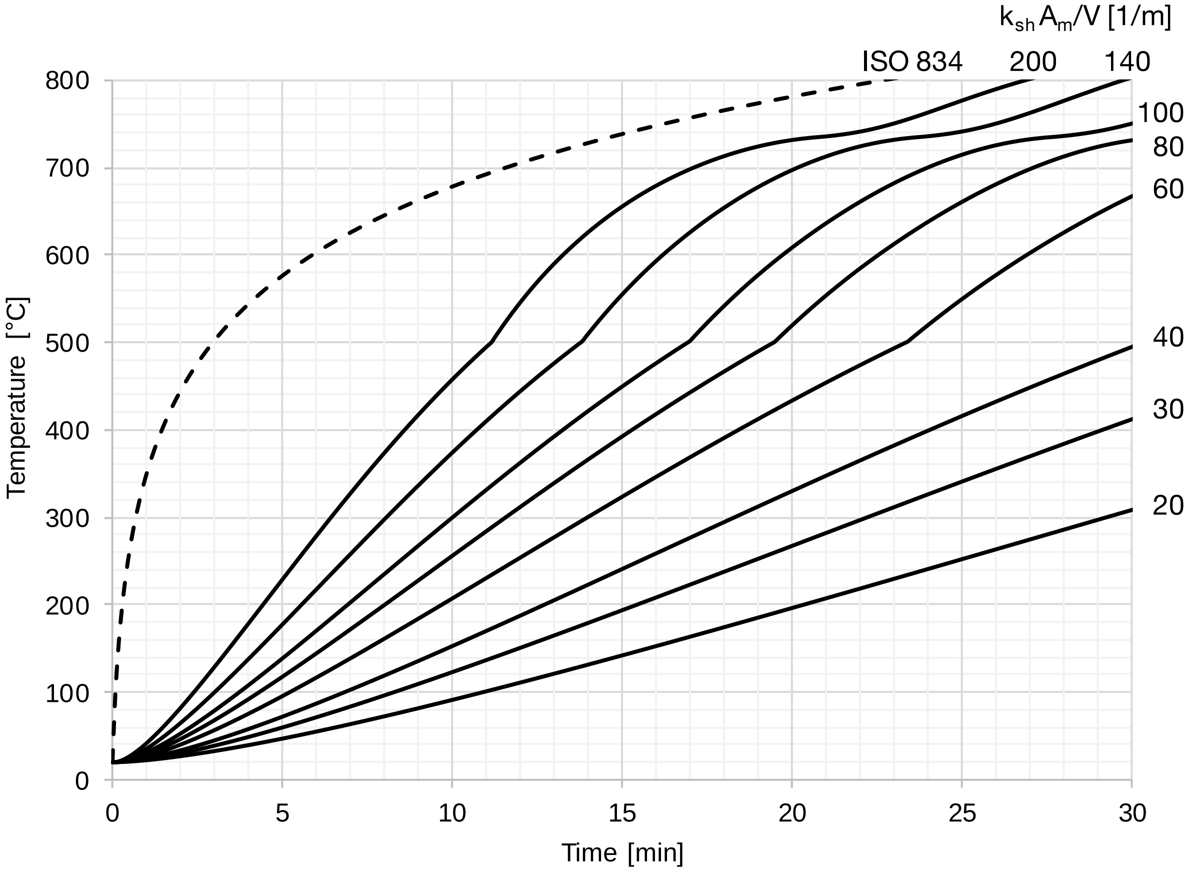

Figure 91: Nomogram for unprotected hot-dip galvanized steel members in dependence of the modified section factor $k_{sh}A_m/V$ *for an ISO 834 fire*

8.1.3 Nomograms connected to the reduction factor

Nomograms can be used in cooperation with the reduction factor η_{fi} of Chapter 1.7. This evaluation can be found in Appendix 'Nomograms' in full scale, while in the following Figure 92 a scheme for the usage of the application is given.

First, they can be used, as it is indicated by the red procedure in Figure 92, starting with a known reduction factor η_{fi} (1), via the adaption factor for the non-uniform temperature distribution in the structural system (2), to the known modified section factor $k_{sh}A_m/V$ (3) of the specimen to get a resulting time t^* for the fire resistance.

Second, they can be used – starting again with a known reduction factor η_{fi} (1), via the adaption factor for the non-uniform temperature distribution in the structural system (2) – to find the unknown modified section factor $k_{sh}A_m/V$ of the specimen by knowing the mandatory fire resistance time.

Third, they can be used – as indicated by the blue procedure in Figure 92 – starting again with a known fire resistance time (1), via a known modified section factor $k_{sh}A_m/V$ (2) and the adaption factor to find the highest possible reduction factor η_{fi} as this indicated the maximum residual strength in fire.

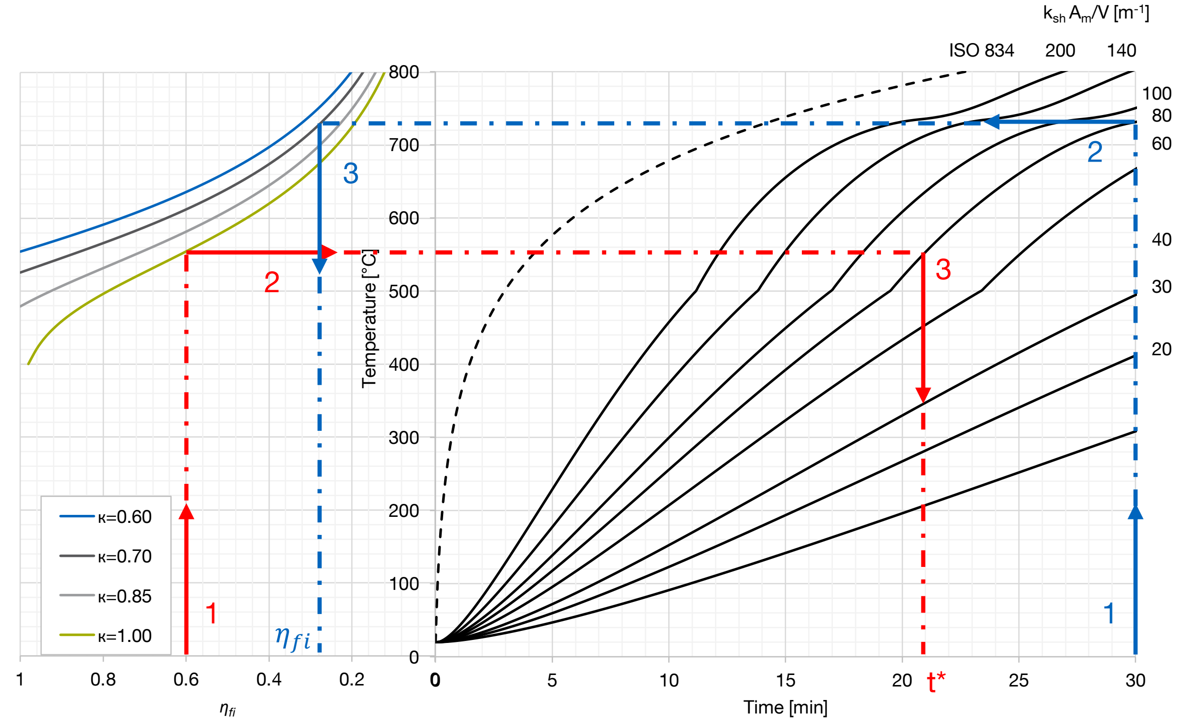

Figure 92: Scheme of the usage of a nomogram in cooperation with the reduction factor η_{fi}

8.2 Example: 3-sided hot-dip galvanized steel member in fire

In the following, a single steel beam (HEB 400) flamed on three sides is considered in a composite beam system. The beam is calculated separately from the system. No stud connectors are used and therefore no composite action is assumed, which ensures an easy comparability. The verification is carried out according to DIN EN 1993-1-2 [17] and the corresponding national appendix [41]. The nominal fire is based on the ISO 834 [16] with a fire duration of 30 minutes. The component temperature is determined in accordance with Chapter 1.7, first for a constant emissivity ε_{EC} = 0.70 of the Eurocode and second with the variable two-stage emissivity ε_{var} presented at the beginning of Chapter 8 for hot-dip galvanized steel. Table 34 shows the calculated temperatures and the resulting temperature difference.

Table 34: Calculated temperatures according to DIN EN 1993-1-2 [17]

	Variant		**Temperature difference**
	$\boldsymbol{\varepsilon_{EC}}$	$\boldsymbol{\varepsilon_{var}}$	$\boldsymbol{\Delta T}$ **[°C]**
Temperature T [°C]	690.3	596.0	94.2

The material-dependent reduction factors can be determined from the calculated temperatures in accordance with Chapter 1.6. It is shown that a temperature difference of 94.2 °C, after 30 minutes of an ISO 834 fire scenario, increase the load-bearing capacity by 90.4 % in the event of fire (see Table 35). This increase was calculated as follows:

$$Increase\ in\ yield\ strength\ [\%] = \frac{k_{y,\theta,HDG} - k_{y,\theta,EC}}{k_{y,\theta,EC}} \tag{8-1}$$

Calculated temperatures according to DIN EN 1993-1-2 [17]

Table 35: Calculated effective yield strength according to DIN EN 1993-1-2 [17]

	Variant		**Increase in yield strength**
	ε_{EC}	ε_{var}	[%]
Effective yield strength [%]	25.3	48.2	90.4

With the present example, an *R30* fire requirement can be achieved for galvanized steel members for almost all building and load categories. In contrast, the variant according to the Eurocode would not fulfil the requirements.

9 Conclusion

Each analysis – the two full-scale tests as well as the 147 Emissivity Perfomance-Tests – exhibits important insights for the heating behaviour of hot-dip galvanized steel members in the accidental fire situation.

It turned out that different steel categories, accompanying with different hot-dip galvanized alloy layers on steel members, have different behaviour patterns. In general, this was always more favourable with respect to a *R30* fire protection requirement than the normative specifications given by the DIN EN 1993-1-2 [17]. However, the economic value depends strongly on the prevailing alloy layer. While very good results could be achieved for categories A and B with an outer pure zinc layer, the positive effect in the high-silicon range (category D) is lower.

In the thesis, the causal parameter for this different behaviour was determined. While DIN EN 1993-1-2 [17] and DIN EN 1994-1-2 [18] refer to a simplified, surface-independent constant emissivity $\varepsilon = 0.70$ for structural steel, hot-dip galvanized surfaces show a strong temperature-dependent emissivity. This parameter was recalculated from the full fire tests and explicitly determined in the EP-T. For this purpose, all physical dependencies of this highly complex value were taken into account to make an exact statement. The temperature-dependent emissivity was determined for various hot-dip galvanized surfaces. Therefore, category A, B and D (according to DIN EN ISO 14713-2 [10]) were tested, combined with all possible surface conditions. The influence of weathering, for example, as well as the negative influence of an adverse storage were shown.

Arising from the results, it is important to preserve the outer pure zinc layer. The latter can be obtained by observing the instructions of the *Institut Feuerverzinken* regarding delivery and storage conditions [32].

The lower emissivity, for temperatures up to 500 °C, can lead to an *R30* fire protection requirement being achieved without additional measures, especially in case of stouter profiles or in composite construction.

From this research, a new concept for the consideration of the emissivity of hot-dip galvanized components in case of fire is derived. Due to a beneficially outer pure zinc coating (η-phase), this approach is only applicable, in the field of normal temperature galvanizing, for the A and B. As seen in Chapters 5 and 6, it is strongly variable in the relevant temperature range. For practical reasons, the implementation is based on a safe side two-stage approach. The following Table 36 shows this concept, which is based on DIN EN 1993-1-2 [17].

This two-stage emissivity approach enables a simple implementation in design methods of the Eurocodes DIN EN 1993-1-2 [17] and DIN EN 1994-1-2 [18], since the design process is not changed.

In addition, it has to be mentioned that this concept is already implemented in the new drafts of the next generation of structural Eurocodes.

Table 36: New draft approach for structural eurocodes

Type of steel	**ε_m ≤ 500 °C**	**ε_m > 500 °C**
Carbon steel	0.70	
HDG steel [1]	0.35	0.70

[1] Steel that has been hot-dip galvanized according to EN ISO 1461[1] and with a steel composition according to category A or B of EN ISO 14713-2 [10]

10 Outlook

In the course of this thesis, it has been shown that an outer pure zinc layer offers higher benefits, with respect to the fire resistance of hot-dip galvanized structures. This was done for normal temperature galvanizing and for zinc bath compositions standards according to DIN EN ISO 1461 [1] and the 'DASt-Richtline 022' [2]. If one considers the research of *Schulz et al.* [3] or *Katzung et al.* [9] it can be assumed that for other batch temperatures or additives in the zinc bath, the same favourable effect may occur, even in other steel categories.

As shown in Chapter 1.4.2, in case of normal temperature galvanizing up to 460 °C, the iron-zinc alloy formation has a high dependence on temperature. In case of high-temperature galvanizing, this dependence continues. *Schulz et al*. [3] provide a good basis of data for all categories at higher temperatures. In dependence of the silicon content, the dipping time and the zinc bath temperature it can be seen in [3] that according to their layer thickness it is beneficially especially for steel in the Sandelin range.

However, it is difficult to estimate the structure of an iron-zinc alloy only based on the final layer thickness. An important indicator, as shown in Chapter 4, is the growth value. The increase in layer thickness per minute, in turn, can be assigned to a dedicated layer formation. Such values can be derived from *Katzung et al.* [9] as well as from *Schulz et al.* [3]

Recent research in the field of HDG has been conducted with respect to the effects of different zinc bath additives. Despite not being state of the art at present, these findings can have additional positive effects for the heating behaviour with respect to the layer formation. In the following, some of these, including a short description of their effects, are listed.

- Aluminium: Added to the zinc bath, even in a minimal amount, it leads to a reduction of the layer thickness [3,9]. According to *Horstmann* [7], this can be assigned to the development of a thin intermetallic phase ($FeAl_3$ or Fe_2Al_5) on the steel member, which inhibits the formation of the iron-zinc alloy for a certain time. This effect increases with increasing silicon content in the steel member. In addition, aluminium has a melting point of 660 °C, which may have additional benefits due to a possible shift of the resistance limits towards higher temperatures. As an positive side effect, the surface becomes more shiny [39,40]. That can be a first hint that the emissivity should be lower.
- Nickel reduces the layer thickness especially in the Sandelin range [3] and to a small amount in the Sebisty range. The structure of the coating changes considerably. The

typical Sandelin structure becomes an alloy layer with phases that are similar to low-silicon steel. In addition, the appearance gets brighter.

However, each of these additives may have benefits with respect to the appearance and the emissivity – and therefore to the heating behaviour – although as they are findings of most recent research they may also offer some disadvantages.

Looking at fire resistance of steel members, the knowledge provided in this thesis opens new perspectives and with new technologies this may have an even more pronounced effect.

Appendix ‘EP-T’

EP-T – Preparation of the specimen

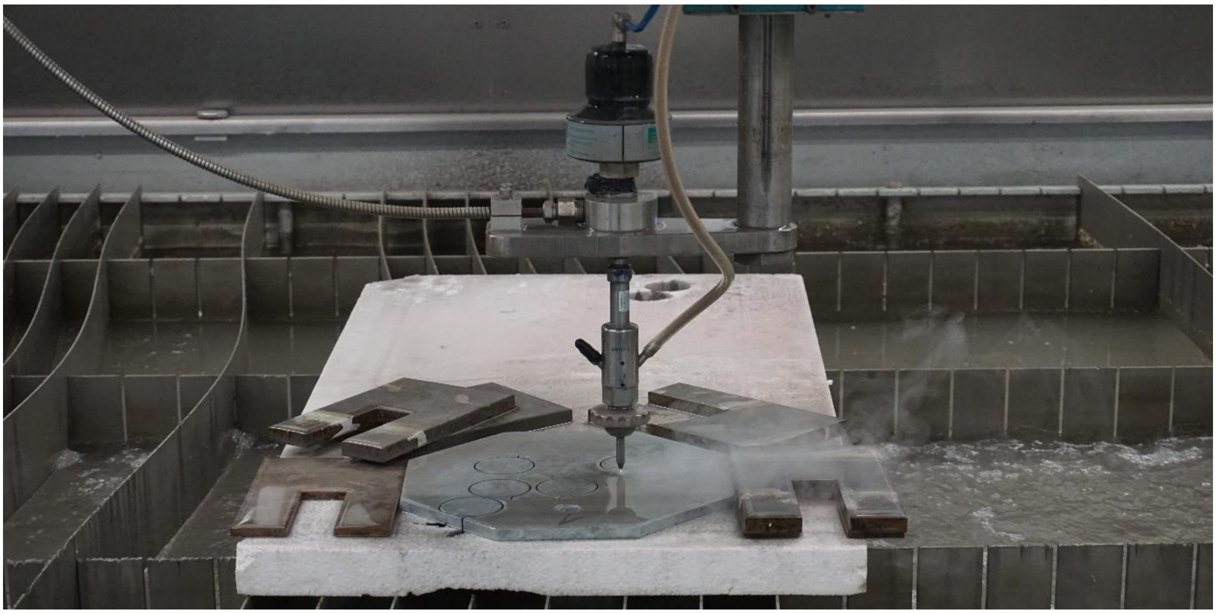

Figure 93: Preparation of the test samples (d =50 mm) out of the octagon carrier plate by water jetting

Figure 94: Carrier plates after water jetting with the corresponding test samples

Statistical approach

The statistical evaluation and the measurement results of the Emissivity Performance Test will be discussed. The statistical evaluation was carried out using the following statistical formulas:

- Mean value (MV):

$$\bar{x} = \frac{1}{n}\sum_{i=1}^{n} x_i \qquad \text{(A1-1)}$$

- Variance (S^2):

$$S^2 = \frac{1}{n}\sum_{i=1}^{n} (x_i - \bar{x})^2 \qquad \text{(A1-2)}$$

- Standard deviation (S):

$$S = \sqrt{\frac{1}{n}\sum_{i=1}^{n} (x_i - \bar{x})^2} \qquad \text{(A1-3)}$$

- Standard error (SE):

$$SE = \frac{S}{\sqrt{n}} = \frac{\sqrt{\frac{1}{n}\sum_{i=1}^{n}(x_i - \bar{x})^2}}{\sqrt{n}} \qquad \text{(A1-4)}$$

EP-T Category A – MV, MV (Inside), MV (Outside)

For reasons of clarity, not all the detailed measured data and information is provided. The evaluated data is, therefore, provided in steps of 25 °C.

3MH1 (2.3 µm) data

Category A	**Mean values of carrier plates**									
	‘1’	**‘2’**	**‘3’**	**‘4’**	**‘5’**	**‘9’**	**‘12’**	**‘13’**	**‘14’**	**‘15’**
Storage	**Outside**	**Outside**	**Inside**	**Inside**	**Outside**	**Inside**	**Inside**	**Inside**	**Inside**	**Inside**
Temperature [°C]										
250	0.413	0.423	0.366	0.289	0.369	0.335	0.301	0.256	0.342	0.341
300	0.376	0.381	0.343	0.275	0.329	0.296	0.293	0.243	0.328	0.321
325	0.357	0.373	0.341	0.274	0.319	0.286	0.312	0.242	0.324	0.318
350	0.353	0.369	0.340	0.277	0.318	0.285	0.305	0.245	0.324	0.316
375	0.354	0.368	0.339	0.277	0.311	0.285	0.305	0.249	0.328	0.312
400	0.359	0.372	0.345	0.284	0.312	0.290	0.310	0.255	0.334	0.312
425	0.369	0.396	0.373	0.298	0.321	0.296	0.342	0.299	0.350	0.331
450	0.407	0.416	0.392	0.337	0.360	0.343	0.356	0.325	0.382	0.339
475	0.421	0.420	0.396	0.340	0.367	0.344	0.349	0.330	0.387	0.338
500	0.425	0.426	0.400	0.352	0.375	0.355	0.351	0.340	0.393	0.335
525	0.434	0.442	0.409	0.358	0.383	0.361	0.382	0.345	0.412	0.343
550	0.526	0.541	0.564	0.473	0.527	0.533	0.543	0.428	0.520	0.439
575	0.577	0.566	0.586	0.503	0.572	0.552	0.560	0.503	0.581	0.521
600	0.607	0.596	0.611	0.569	0.604	0.577	0.608	0.585	0.614	0.567
625	0.623	0.609	0.617	0.596	0.632	0.606	0.628	0.618	0.623	0.581
650	0.629	0.608	0.618	0.602	0.644	0.614	0.637	0.638	0.620	0.595
675	0.636	0.606	0.612	0.605	0.644	0.618	0.637	0.651	0.620	0.601
700	0.627	0.580	0.577	0.587	0.627	0.596	0.640	0.651	0.627	0.602
725	0.637	0.596	0.599	0.607	0.637	0.612	0.657	0.666	0.645	0.637
750	0.641	0.614	0.627	0.631	0.660		0.677	0.676	0.668	0.659

Category A – newly hot-dip galvanized

Carrier plate	**'3N'**			**'10N'**		
Specimen	**'3N_1'**	**'3N_3'**	**'3N_5'**	**'10N_1'**	**'10N_2'**	**'10N_3'**
Storage	**Inside**	**Inside**	**Inside**	**Inside**	**Inside**	**Inside**
Temperature [°C]						
250	0.091	0.073	0.095	0.097	0.105	0.103
275	0.092	0.089	0.098	0.097	0.101	0.101
300	0.087	0.080	0.090	0.094	0.099	0.096
325	0.095	0.089	0.101	0.107	0.113	0.104
350	0.095	0.089	0.108	0.109	0.117	0.114
355	0.097	0.090	0.109	0.111	0.118	0.115
360	0.096	0.092	0.109	0.110	0.118	0.113
365	0.096	0.092	0.109	0.110	0.120	0.114
370	0.098	0.093	0.110	0.111	0.122	0.116
375	0.097	0.093	0.110	0.113	0.122	0.116
400	0.097	0.096	0.112	0.116	0.127	0.116
425	0.103	0.100	0.116	0.121	0.139	0.118
450	0.124	0.121	0.121	0.131	0.137	0.117
475	0.124	0.120	0.120		0.136	0.117
500	0.127	0.120	0.121		0.137	0.118
525	0.129	0.121	0.124	0.099	0.143	0.121
550	0.213	0.150	0.231	0.116	0.253	0.218
575	0.331		0.344	0.296	0.336	0.325
600	0.455		0.464	0.304	0.460	0.443
625	0.498		0.504	0.326	0.511	0.485
650			0.552	0.435	0.552	0.532
675	0.599		0.586	0.500	0.590	0.575
700	0.617		0.647	0.538	0.656	0.635
725	0.639		0.693	0.000	0.688	0.680
750	0.641	0.614	0.627	0.631	0.660	

LT (8 – 14 µm) data

Category A	**Mean values of carrier plates**									
	‘1’	**‘2’**	**‘3’**	**‘4’**	**‘5’**	**‘9’**	**‘12’**	**‘13’**	**‘14’**	**‘15’**
Storage	**Outside**	**Outside**	**Inside**	**Inside**	**Outside**	**Inside**	**Inside**	**Inside**	**Inside**	**Inside**
Temperature [°C]										
250	0.724	0.625	0.547	0.000	0.631	0.538	0.417	0.308	0.587	0.697
275	0.634	0.507	0.448	0.331	0.583	0.485	0.367	0.283	0.492	0.475
300	0.534	0.420	0.350	0.278	0.471	0.370	0.282	0.261	0.349	0.457
325	0.456	0.401	0.339	0.271	0.400	0.351	0.276	0.242	0.338	0.440
350	0.413	0.379	0.320	0.266	0.377	0.331	0.265	0.225	0.329	0.425
375	0.397	0.361	0.313	0.257	0.340	0.317	0.259	0.211	0.321	0.407
400	0.379	0.345	0.305	0.251	0.321	0.305	0.251	0.203	0.316	0.392
425	0.381	0.343	0.302	0.246	0.311	0.304	0.268	0.216	0.313	0.392
450	0.408	0.372	0.330	0.290	0.338	0.367	0.292	0.270	0.349	0.410
475	0.438	0.382	0.331	0.298	0.353	0.389	0.308	0.291	0.359	0.410
500	0.447	0.386	0.331	0.306	0.362	0.412	0.308	0.313	0.364	0.410
525	0.459	0.412	0.336	0.306	0.371	0.434	0.365	0.330	0.376	0.414
550	0.615	0.561	0.643	0.458	0.573	0.675	0.585	0.444	0.556	0.547
575	0.710	0.598	0.671	0.518	0.645	0.703	0.638	0.544	0.645	0.649
600	0.754	0.653	0.749	0.619	0.713	0.759	0.705	0.677	0.731	0.735
625	0.783		0.761	0.657	0.748	0.792	0.742	0.716	0.749	0.758
650	0.802		0.773	0.677	0.767	0.808	0.759		0.764	
675	0.814		0.773	0.689	0.779	0.819	0.770		0.771	
700	0.816		0.717	0.666	0.779	0.817	0.753		0.794	
725	0.834		0.744	0.691	0.791	0.836	0.774		0.821	

Category A - newly hot-dip galvanized

Carrier plate	**‘3N’**			**‘10N’**	
Specimen	**‘3N_1’**	**‘3N_3’**	**‘3N_5’**	**‘10N_2’**	**‘10N_3’**
Storage	**Innen**	**Innen**	**Innen**	**Innen**	**Innen**
Temperature [°C]					
250	0.172	0.174	0.178	0.181	0.187
275	0.158	0.160	0.163	0.166	0.170
300	0.146	0.148	0.151	0.153	0.157
325	0.138	0.139	0.142	0.145	0.146
350	0.131	0.131	0.136	0.137	0.139
375	0.057	0.124	0.129	0.130	0.132
400	0.058	0.119	0.124	0.126	0.126
425	0.059	0.115	0.120	0.126	0.121
450	0.082	0.135	0.137	0.141	0.137
475	0.082	0.130	0.133	0.137	0.132
500	0.082	0.126	0.128	0.135	0.128
525	0.086	0.122	0.127	0.160	0.124
550	0.177	0.155	0.250	0.283	0.238
575	0.306		0.345	0.341	0.323
600	0.472		0.507	0.500	0.491
625	0.511		0.542	0.532	0.530
650	0.543		0.576	0.561	0.564
675	0.594		0.611	0.609	0.604
700	0.635		0.673	0.683	0.663
725	0.658		0.756	0.764	0.752
750				0.835	

EP-T Category A – Statistical evaluation

3MH1 (2.3 µm) data

	Total				Inside				Outside			
	MV Total	**S^2**	**S**	**SE**	**MV Inside**	**S^2**	**S**	**SE**	**MV Outside**	**S^2**	**S**	**SE**
max. value		0.005	0.067	0.011		0.006	0.080	0.013		0.005	0.071	0.011
Temperature [°C]												
250	0.349	0.002	0.045	0.007	0.323	0.002	0.043	0.007	0.406	0.003	0.050	0.008
275	0.332	0.001	0.038	0.006	0.313	0.002	0.041	0.007	0.383	0.002	0.044	0.007
300	0.322	0.001	0.034	0.006	0.296	0.001	0.034	0.006	0.360	0.002	0.041	0.007
325	0.320	0.001	0.028	0.005	0.306	0.001	0.028	0.005	0.346	0.001	0.031	0.005
350	0.317	0.001	0.027	0.004	0.301	0.001	0.026	0.004	0.338	0.001	0.031	0.005
375	0.316	0.001	0.027	0.004	0.302	0.001	0.025	0.004	0.333	0.001	0.030	0.005
400	0.319	0.001	0.027	0.004	0.304	0.001	0.023	0.004	0.332	0.001	0.030	0.005
425	0.338	0.001	0.029	0.005	0.311	0.001	0.023	0.004	0.335	0.001	0.031	0.005
450	0.367	0.001	0.025	0.004	0.349	0.001	0.023	0.004	0.362	0.001	0.036	0.006
455	0.366	0.001	0.027	0.004	0.353	0.000	0.021	0.003	0.370	0.001	0.031	0.005
475	0.369	0.001	0.028	0.005	0.351	0.001	0.023	0.004	0.384	0.001	0.032	0.005
500	0.375	0.001	0.029	0.005	0.357	0.001	0.024	0.004	0.392	0.001	0.031	0.005
525	0.390	0.001	0.028	0.005	0.360	0.001	0.026	0.004	0.398	0.001	0.032	0.005
550	0.523	0.001	0.030	0.005	0.420	0.002	0.040	0.006	0.435	0.001	0.038	0.006
575	0.560	0.000	0.021	0.003	0.540	0.001	0.035	0.006	0.557	0.000	0.011	0.002
600	0.599	0.000	0.014	0.002	0.570	0.001	0.023	0.004	0.580	0.000	0.007	0.001
625	0.620	0.000	0.014	0.002	0.605	0.000	0.016	0.003	0.618	0.000	0.009	0.002
650	0.627	0.000	0.016	0.003	0.620	0.000	0.016	0.003	0.628	0.000	0.012	0.002
675	0.629	0.000	0.015	0.002	0.624	0.000	0.015	0.002	0.633	0.000	0.015	0.002
700	0.618	0.000	0.022	0.004	0.621	0.000	0.018	0.003	0.629	0.000	0.022	0.004
725	0.634	0.000	0.021	0.003	0.628	0.000	0.022	0.004	0.618	0.000	0.017	0.003
750					0.647	0.000	0.022	0.004	0.631	0.000	0.020	0.003

Category A_N – newly hot-dip galvanized

	MV Inside	S^2	S	SE
max. value:		0.0064	0.0801	0.0289
Temperature [°C]				
250	0.093	0.00011	0.01043	0.00426
275	0.095	0.00002	0.00431	0.00176
300	0.091	0.00004	0.00634	0.00259
325	0.102	0.00006	0.00777	0.00317
350	0.105	0.00010	0.01015	0.00414
375	0.108	0.00011	0.01034	0.00422
400	0.111	0.00012	0.01093	0.00446
425	0.116	0.00016	0.01269	0.00518
450	0.125	0.00005	0.00675	0.00276
475	0.124	0.00004	0.00663	0.00271
500	0.125	0.00005	0.00704	0.00287
525	0.123	0.00017	0.01285	0.00524
550	0.197	0.00230	0.04794	0.01957
575	0.327	0.00027	0.01643	0.00671
600	0.424	0.00370	0.06080	0.02482
625	0.465	0.00486	0.06972	0.02846
650	0.517	0.00235	0.04853	0.01981
675	0.570	0.00128	0.03573	0.01459
700	0.618	0.00178	0.04218	0.01722
725	0.675	0.00045	0.02125	0.00868
750	0.690	0.00006	0.00779	0.00318

LT (8 – 14 µm) data

	Total				Inside				Outside			
	MV Total	S^2	S	SE	MV Inside	S^2	S	SE	MV Outside	S^2	S	SE
max. value		0.117	0.342	0.056		0.105	0.325	0.053		0.132	0.363	0.059
Temperature [°C]												
250	0.536	0.027	0.166	0.027	0.446	0.039	0.197	0.032	0.646	0.013	0.116	0.019
275	0.482	0.010	0.100	0.016	0.408	0.010	0.099	0.016	0.574	0.010	0.101	0.016
300	0.389	0.008	0.088	0.014	0.323	0.008	0.087	0.014	0.470	0.008	0.089	0.014
325	0.356	0.004	0.065	0.010	0.312	0.005	0.069	0.011	0.410	0.003	0.058	0.009
350	0.337	0.003	0.057	0.009	0.300	0.004	0.064	0.010	0.384	0.002	0.048	0.008
375	0.319	0.003	0.051	0.008	0.290	0.003	0.057	0.009	0.355	0.002	0.042	0.007
400	0.306	0.002	0.047	0.008	0.282	0.003	0.053	0.009	0.337	0.001	0.037	0.006
425	0.307	0.002	0.042	0.007	0.288	0.002	0.046	0.007	0.331	0.001	0.036	0.006
450	0.339	0.002	0.040	0.006	0.323	0.002	0.045	0.007	0.359	0.001	0.033	0.005
475	0.353	0.002	0.041	0.007	0.336	0.002	0.043	0.007	0.375	0.001	0.038	0.006
500	0.360	0.002	0.043	0.007	0.342	0.002	0.047	0.008	0.383	0.001	0.039	0.006
525	0.383	0.001	0.037	0.006	0.372	0.001	0.037	0.006	0.396	0.001	0.036	0.006
550	0.576	0.002	0.048	0.008	0.574	0.004	0.063	0.010	0.578	0.000	0.018	0.003
575	0.640	0.002	0.044	0.007	0.635	0.002	0.050	0.008	0.645	0.001	0.036	0.006
600	0.709	0.001	0.036	0.006	0.712	0.001	0.037	0.006	0.706	0.001	0.033	0.005
625	0.745	0.059	0.243	0.039	0.743	0.001	0.033	0.005	0.578	0.131	0.362	0.059
650	0.764	0.108	0.329	0.053	0.651	0.084	0.291	0.047	0.593	0.138	0.371	0.060
675	0.774	0.111	0.333	0.054	0.660	0.086	0.294	0.048	0.602	0.141	0.376	0.061
700	0.763	0.108	0.329	0.053	0.650	0.085	0.291	0.047	0.602	0.138	0.371	0.060
725	0.784	0.114	0.338	0.055	0.670	0.089	0.299	0.049	0.613	0.145	0.381	0.062

Category A - newly hot-dip galvanized

	MV Inside	S²	S	SE
max. value		0.0064	0.0801	0.0219
Temperature [°C]				
250	0.179	0.000	0.005	0.002
275	0.164	0.000	0.004	0.002
300	0.151	0.000	0.004	0.002
325	0.142	0.000	0.003	0.002
350	0.135	0.000	0.003	0.001
375	0.115	0.001	0.029	0.013
400	0.111	0.001	0.026	0.012
425	0.109	0.001	0.025	0.011
450	0.126	0.001	0.022	0.010
475	0.123	0.000	0.021	0.009
500	0.120	0.000	0.019	0.009
525	0.124	0.001	0.024	0.011
550	0.220	0.002	0.047	0.021
575	0.329	0.000	0.016	0.007
600	0.492	0.000	0.013	0.006
625	0.529	0.000	0.011	0.005
650	0.561	0.000	0.012	0.005
675	0.604	0.000	0.007	0.003
700	0.663	0.000	0.018	0.008
725	0.733	0.002	0.043	0.019
750	0.822	0.000	0.000	0.000

EP-T Category B – MV, MV (Inside), MV (Outside)

3MH1 (2.3 µm) data

Category B Specimen – Inside

	‘B_1’	**‘B_9’**	**‘B_10’**	**‘B_12’**	**‘B_17’**	**‘B_18’**	**‘B_121’**	**‘CZ1_1’**	**‘CZ1_1’**	**‘CZ1_1’**
Storage	**Inside**	**Inside**	**Inside**	**Inside**	**Inside**	**Inside**	**Inside**	**Inside**	**Inside**	**Inside**
Temperature [°]										
250	0.213	0.211	0.645	0.384	0.240	0.247	0.355		0.304	0.173
275	0.226	0.209	0.650	0.381	0.251	0.261	0.337		0.249	0.150
300		0.206	0.628	0.390	0.225	0.259	0.331		0.212	0.146
325	0.232	0.208	0.603	0.379	0.231	0.265	0.331	0.246	0.196	0.143
350	0.232	0.206	0.577	0.378	0.229	0.265	0.319	0.234	0.183	0.149
375	0.230	0.204	0.223	0.379	0.223		0.317	0.230	0.175	0.150
400	0.232	0.201	0.550	0.378	0.223		0.320	0.233	0.168	0.152
425	0.239		0.491	0.379	0.232	0.259	0.319	0.236	0.170	0.159
450	0.225	0.207	0.480	0.323	0.235	0.260	0.315	0.249	0.177	0.673
475		0.209	0.477	0.318	0.232	0.263	0.318	0.255	0.178	0.181
500	0.228	0.213	0.498	0.320	0.233	0.271	0.321	0.288	0.197	0.214
525	0.258		0.570	0.341	0.243	0.315	0.353	0.336	0.240	0.249
550	0.306	0.261	0.544	0.383	0.273	0.359	0.389	0.390	0.293	0.289
575	0.278	0.276	0.607	0.364			0.362	0.367	0.323	0.299
600	0.346	0.429	0.598	0.418	0.312		0.416	0.382	0.336	0.348
625	0.357	0.470	0.572	0.432			0.440	0.409	0.394	0.399
630	0.356	0.477	0.568	0.433			0.445	0.414	0.403	0.407
650	0.351	0.501	0.558	0.447			0.465	0.436	0.440	0.444
675	0.379	0.538	0.591				0.499	0.492	0.495	0.503
700	0.422	0.587	0.840	0.907			0.556	0.556	0.573	0.570
725	0.476		0.780	0.935			0.630	0.617	0.656	0.636
750	0.700		0.797				0.707			

Category B	**Specimen – Outside**			
	'BA_1'	**'BA_20'**	**'BA_22'**	**'BA_26'**
Storage	**Outside**	**Outside**	**Outside**	**Outside**
Temperature [°]				
250	0.601	0.823	0.565	0.849
275	0.594	0.737	0.545	0.772
300	0.579	0.686	0.535	0.728
325	0.564	0.645	0.531	0.700
350		0.629	0.537	0.671
375	0.558	0.613	0.526	0.668
400	0.555	0.613	0.527	0.666
425	0.545	0.599	0.386	0.638
450	0.532	0.581	0.499	0.630
475	0.526	0.568	0.492	0.630
500	0.522	0.565	0.492	0.630
525	0.532	0.561	0.502	0.653
550	0.543	0.574	0.496	0.614
575		0.581	0.485	0.633
600		0.615	0.509	0.589
625	0.480	0.573	0.488	0.537
650	0.418	0.523	0.463	0.498
675	0.388	0.507	0.470	0.506
700	0.402	0.561	0.519	0.598
725	0.496	0.612	0.591	0.667
750	0.596		0.652	0.710

LT (8 – 14 µm) data

Category B – specimen

	‘B_9’	**‘B_10’**	**‘B_12’**	**‘B_17’**	**‘B_18’**	**‘B_121’**	**‘CZ1_1’**	**‘CZ1_2’**	**‘CZ1_3’**
Storage	**Inside**	**Inside**	**Inside**	**Inside**	**Inside**	**Inside**	**Inside**	**Inside**	**Inside**
Temperature [°]									
250	0.273	0.490	0.321	0.359	0.282	0.319		0.238	0.189
275	0.258	0.476	0.310	0.345	0.269	0.305		0.226	0.176
300	0.247	0.462	0.301	0.320	0.256	0.292		0.216	0.164
325	0.236	0.448	0.293	0.306	0.247	0.281	0.182	0.209	0.156
350	0.227	0.437	0.287	0.293	0.238	0.272	0.173	0.202	0.149
375	0.220	0.000	0.281	0.280		0.265	0.167	0.196	0.143
400	0.214	0.423	0.278	0.268		0.261	0.163	0.191	0.138
425		0.425	0.276	0.263	0.240	0.265	0.159	0.189	0.135
450	0.226	0.543	0.231	0.299	0.236	0.272	0.187	0.188	0.157
475	0.224	0.541	0.276	0.300	0.235	0.272	0.203	0.204	0.170
500	0.223	0.542	0.275	0.305	0.239	0.274	0.248	0.212	0.208
525		0.563	0.287	0.321	0.293	0.313	0.299	0.236	0.236
550	0.274	0.627	0.321	0.357	0.349	0.371	0.360	0.271	0.268
575	0.298	0.686	0.315			0.367	0.370	0.303	0.274
600	0.470	0.763	0.398	0.420		0.432	0.473	0.352	0.361
625	0.465	0.774	0.408			0.440	0.516	0.458	0.437
650	0.476	0.781	0.414			0.448	0.560	0.517	0.493
675	0.507	0.786				0.473	0.639	0.574	0.568
700	0.574	0.787	0.757			0.541	0.722	0.651	0.655
725		0.000	0.682			0.661	0.796	0.740	0.748
750		0.800				0.813	0.857		

Category B

Storage	‘BA_20’ Outside	‘BA_22’ Outside
Temperature [°]		
250	0.649	0.649
275	0.621	0.629
300	0.559	0.568
325	0.540	0.544
350		0.531
375	0.521	0.520
400	0.516	0.516
425	0.520	0.516
450	0.525	0.522
475	0.524	0.519
500	0.526	0.523
525	0.543	0.509
550	0.635	0.609
575		0.646
600		0.736
625	0.677	0.695
650	0.620	0.654
675	0.579	0.625
700	0.594	0.687
725	0.709	0.766
750	0.825	

EP-T Category B – Statistical evaluation

3MH1 (2.3 µm) data

	Total				**Inside**				**Outside**			
	MV Total	**S^2**	**S**	**SE**	**MV Inside**	**S^2**	**S**	**SE**	**MV Outside**	**S^2**	**S**	**SE**
max. value:		0.256	0.271	0.477		0.033	0.182	0.069		0.032	0.178	0.089
Temperature [°C]												
250	0.467	0.053	0.230	0.069	0.329	0.021	0.144	0.054	0.758	0.012	0.111	
275	0.331	0.042	0.204	0.061	0.330	0.020	0.142	0.054	0.701	0.006	0.077	0.038
300	0.340	0.035	0.188	0.057	0.324	0.021	0.143	0.054	0.664	0.004	0.063	0.031
325	0.321	0.031	0.177	0.053	0.321	0.016	0.128	0.048	0.636	0.003	0.056	0.028
350	0.315	0.030	0.172	0.052	0.317	0.014	0.120	0.045	0.650	0.000	0.021	0.011
375	0.263	0.029	0.172	0.052	0.291	0.004	0.063	0.024	0.613	0.002	0.045	0.023
400	0.317	0.028	0.167	0.050	0.311	0.015	0.121	0.046	0.611	0.002	0.045	0.023
425	0.320	0.021	0.144	0.043	0.305	0.008	0.092	0.035	0.594	0.001	0.038	0.019
450	0.292	0.022	0.149	0.045	0.292	0.008	0.087	0.033	0.581	0.002	0.040	0.020
475	0.303	0.021	0.144	0.043	0.293	0.008	0.088	0.033	0.575	0.002	0.042	0.021
500	0.298	0.021	0.146	0.044	0.298	0.008	0.091	0.034	0.573	0.002	0.044	0.022
525	0.347	0.019	0.139	0.042	0.339	0.012	0.108	0.041	0.582	0.003	0.052	0.026
550	0.359	0.015	0.121	0.037	0.355	0.008	0.089	0.034	0.577	0.001	0.029	0.015
575	0.378	0.019	0.138	0.041	0.362	0.015	0.121	0.046	0.607	0.001	0.026	0.013
600	0.420	0.011	0.106	0.032	0.420	0.008	0.090	0.034	0.602	0.000	0.013	0.006
625	0.454	0.004	0.066	0.020	0.454	0.005	0.070	0.026	0.530	0.001	0.039	0.019
650	0.464	0.003	0.057	0.017	0.464	0.005	0.068	0.026	0.480	0.002	0.045	0.022
675	0.502	0.004	0.067	0.020	0.489	0.006	0.078	0.029	0.467	0.003	0.056	0.028
700	0.662	0.026	0.161	0.048	0.603	0.033	0.182	0.069	0.521	0.007	0.085	0.043
725	0.705	0.020	0.140	0.042	0.655	0.029	0.171	0.065	0.592	0.005	0.071	0.036
750	0.735	0.004	0.061	0.018	0.669	0.002	0.044	0.017	0.653	0.003	0.057	0.028

Category B (CZ)	**Statistical evaluation**			
	MV	**S^2**	**S**	**SE**
max. value:		**0.048**	**0.219**	**0.126**
Temperature [°C]				
250	0.239	0.004	0.065	0.038
275	0.199	0.002	0.050	0.029
300	0.179	0.001	0.033	0.019
325	0.195	0.002	0.042	0.024
350	0.189	0.001	0.035	0.020
375	0.185	0.001	0.033	0.019
400	0.184	0.001	0.035	0.020
425	0.188	0.001	0.034	0.020
450	0.366	0.048	0.219	0.126
475	0.205	0.001	0.036	0.021
500	0.233	0.002	0.040	0.023
525	0.275	0.002	0.043	0.025
550	0.324	0.002	0.047	0.027
575	0.330	0.001	0.028	0.016
600	0.355	0.000	0.020	0.011
625	0.401	0.000	0.006	0.003
650	0.440	0.000	0.003	0.002
675	0.497	0.000	0.005	0.003
700	0.566	0.000	0.007	0.004
725	0.636	0.000	0.016	0.009

LT (8 – 14 µm) data

	Total				Inside				Outside			
	MV Total	S^2	S	SE	MV Inside	S^2	S	SE	MV Outside	S^2	S	SE
max. value:		0.256	0.271	0.477		0.166	0.170	0.767		0.032	0.178	0.089
Temperature [°]												
250	0.418	0.022	0.148	0.052	0.346	0.072	0.030	0.346	0.649	0.000	0.000	0.000
275	0.392	0.021	0.143	0.051	0.327	0.072	0.030	0.327	0.625	0.000	0.004	0.003
300	0.372	0.016	0.125	0.044	0.313	0.071	0.029	0.313	0.564	0.000	0.004	0.003
325	0.362	0.014	0.120	0.043	0.305	0.070	0.028	0.305	0.541	0.000	0.002	0.001
350	0.350	0.011	0.105	0.037	0.292	0.069	0.028	0.292	0.531	0.000	0.000	0.000
375	0.333	0.015	0.124	0.044	0.257	0.025	0.010	0.257	0.521	0.000	0.000	0.000
400	0.339	0.014	0.119	0.042	0.280	0.071	0.029	0.280	0.516	0.000	0.000	0.000
425	0.347	0.013	0.116	0.041	0.280	0.067	0.027	0.280	0.518	0.000	0.002	0.002
450	0.357	0.019	0.136	0.048	0.302	0.111	0.045	0.302	0.523	0.000	0.001	0.001
475	0.361	0.017	0.131	0.046	0.308	0.108	0.044	0.308	0.521	0.000	0.003	0.002
500	0.363	0.017	0.131	0.046	0.310	0.107	0.044	0.310	0.524	0.000	0.002	0.001
525	0.387	0.014	0.118	0.042	0.347	0.105	0.043	0.347	0.531	0.000	0.017	0.012
550	0.431	0.020	0.143	0.051	0.391	0.113	0.046	0.391	0.622	0.000	0.013	0.009
575	0.465	0.028	0.168	0.059	0.417	0.158	0.064	0.417	0.646	0.000	0.000	0.000
600	0.561	0.023	0.153	0.054	0.497	0.135	0.055	0.497	0.734	0.000	0.000	0.000
625	0.579	0.020	0.143	0.051	0.522	0.147	0.060	0.522	0.686	0.000	0.009	0.006
650	0.570	0.017	0.130	0.046	0.536	0.147	0.060	0.536	0.644	0.000	0.017	0.012
675	0.583	0.012	0.110	0.039	0.567	0.140	0.057	0.567	0.604	0.001	0.023	0.016
700	0.632	0.009	0.093	0.033	0.620	0.108	0.044	0.620	0.641	0.002	0.047	0.033
725	0.705	0.002	0.039	0.014	0.691	0.010	0.004	0.691	0.738	0.001	0.028	0.020
750	0.800	0.000	0.010	0.004	0.782	0.006	0.000	0.782	0.817	0.000	0.000	0.000

EP-T Category D – MV, MV (Inside), MV (Outside)

3MH1 (2.3 µm) data

Category D	**Mean values of carrier plates**					
	‘1D’	**‘2D’**	**‘4D’**	**‘5D’**	**‘7D’**	**‘8D’**
Storage	**Inside**	**Outside**	**Inside**	**Outside**	**Outside**	**Outside**
Number of specimen per plate	4	2	8	1	7	1
Temperature [°C]						
250	0.589	0.514	0.614	0.750	0.694	0.679
275	0.593	0.516	0.612	0.725	0.686	0.684
300	0.586	0.512	0.610	0.706	0.681	0.689
325	0.584	0.508	0.613	0.692	0.680	0.688
350	0.581	0.505	0.614	0.683	0.679	0.683
375	0.576	0.497	0.617	0.675	0.676	0.687
400	0.578	0.496	0.614	0.670	0.672	0.681
425	0.555	0.507	0.609	0.660	0.656	0.664
450	0.514	0.514	0.603	0.648	0.640	0.666
475	0.512	0.523	0.598	0.627	0.630	0.640
500	0.522	0.531	0.594	0.620	0.626	0.627
525	0.547	0.540	0.597	0.620	0.630	0.627
550	0.580	0.562	0.613	0.630	0.654	0.636
575	0.581	0.590	0.632	0.642	0.670	0.663
600	0.632	0.626	0.665	0.683	0.706	0.687
625	0.635	0.653	0.701	0.700	0.722	0.734
650	0.646	0.659	0.715	0.719	0.729	0.748
675	0.646	0.670	0.730	0.724	0.737	0.749
700	0.655	0.675	0.731	0.729	0.740	0.749
725	0.668	0.688	0.733	0.740	0.744	0.757
750	0.641	0.614	0.627	0.631	0.660	0.755

LT (8 – 14 µm) data

Category D	**Mean values of carrier plates**					
	‘1D’	**‘2D’**	**‘4D’**	**‘5D’**	**‘7D’**	**‘8D’**
Storage	**Inside**	**Outside**	**Inside**	**Outside**	**Outside**	**Outside**
Number of specimen per plate	4	2	8	1	7	1
Temperature [°C]						
250	0.415	0.762	0.738	0.686	0.676	0.540
275	0.406	0.739	0.708	0.589	0.578	0.490
300	0.395	0.665	0.645	0.563	0.560	0.434
325	0.384	0.637	0.612	0.517	0.548	0.431
350	0.367	0.614	0.607	0.469	0.532	0.426
375	0.358	0.587	0.590	0.509	0.522	0.421
400	0.351	0.568	0.587	0.516	0.514	0.417
425	0.354	0.560	0.584	0.515	0.512	0.417
450	0.364	0.563	0.584	0.525	0.513	0.416
475	0.367	0.567	0.585	0.524	0.514	0.412
500	0.378	0.571	0.586	0.530	0.515	0.412
525	0.413	0.580	0.594	0.570	0.536	0.421
550	0.517	0.638	0.622	0.654	0.596	0.428
575	0.605	0.704	0.656	0.675	0.648	0.479
600	0.767	0.766	0.709	0.774	0.703	0.497
625	0.776	0.800	0.724	0.800	0.711	0.529
650	0.790	0.806	0.733	0.810	0.712	0.536
675	0.799	0.812	0.742	0.819	0.724	0.543
700	0.816	0.818	0.748	0.824	0.727	0.550
725	0.833	0.825	0.754	0.835	0.731	0.558
750	0.641	0.614	0.627	0.631	0.660	0.577

EP-T Category D – Statistical evaluation

3MH1 (2.3 µm) data

	Total				Inside				Outside			
	MV Total	**S^2**	**S**	**SE**	**MV Inside**	**S^2**	**S**	**SE**	**MV Outside**	**S^2**	**S**	**SE**
max. value		0.005	0.067	0.011		0.006	0.080	0.013		0.005	0.071	0.011
Temperature [°C]												
250	0.634	0.004	0.059	0.012	0.605	0.001	0.031	0.009	0.665	0.006	0.080	0.024
275	0.631	0.003	0.054	0.011	0.606	0.001	0.027	0.008	0.659	0.005	0.074	0.022
300	0.627	0.003	0.053	0.011	0.602	0.001	0.027	0.008	0.653	0.005	0.072	0.022
325	0.626	0.003	0.053	0.011	0.603	0.001	0.026	0.008	0.650	0.005	0.072	0.022
350	0.625	0.003	0.053	0.011	0.603	0.001	0.027	0.008	0.648	0.005	0.072	0.022
375	0.623	0.003	0.054	0.011	0.603	0.001	0.028	0.008	0.645	0.005	0.073	0.022
400	0.621	0.003	0.052	0.011	0.602	0.001	0.025	0.007	0.641	0.005	0.071	0.021
425	0.610	0.002	0.048	0.010	0.591	0.001	0.031	0.009	0.630	0.004	0.062	0.019
450	0.596	0.003	0.052	0.011	0.574	0.002	0.048	0.014	0.620	0.003	0.056	0.017
475	0.589	0.002	0.046	0.010	0.569	0.002	0.045	0.013	0.611	0.002	0.047	0.014
500	0.588	0.002	0.040	0.008	0.570	0.002	0.039	0.011	0.608	0.002	0.042	0.013
525	0.596	0.001	0.033	0.007	0.580	0.001	0.028	0.008	0.612	0.001	0.038	0.011
550	0.617	0.001	0.031	0.006	0.602	0.000	0.022	0.006	0.633	0.001	0.039	0.012
575	0.633	0.001	0.033	0.007	0.615	0.001	0.030	0.009	0.652	0.001	0.036	0.011
600	0.670	0.001	0.029	0.006	0.654	0.000	0.022	0.006	0.687	0.001	0.035	0.010
625	0.693	0.001	0.033	0.007	0.679	0.001	0.034	0.010	0.708	0.001	0.031	0.009
650	0.704	0.001	0.033	0.007	0.692	0.001	0.035	0.010	0.717	0.001	0.031	0.009
675	0.713	0.001	0.036	0.007	0.702	0.002	0.041	0.012	0.725	0.001	0.029	0.009
700	0.716	0.001	0.033	0.007	0.706	0.001	0.037	0.011	0.728	0.001	0.028	0.008
725	0.723	0.001	0.029	0.006	0.712	0.001	0.033	0.010	0.735	0.001	0.025	0.008
750	0.726	0.000	0.022	0.005	0.718	0.001	0.023	0.007	0.735	0.000	0.020	0.006

LT (8 – 14 µm) data

	Total				Inside				Outside			
	MV Total	**S^2**	**S**	**SE**	**MV Inside**	**S^2**	**S**	**SE**	**MV Outside**	**S^2**	**S**	**SE**
max. value		0.005	0.067	0.011		0.006	0.080	0.013		0.005	0.071	0.011
Temperature [°C]												
250	0.654	0.014	0.119	0.025	0.631	0.024	0.154	0.044	0.680	0.004	0.061	0.018
275	0.604	0.013	0.114	0.024	0.608	0.020	0.143	0.041	0.600	0.005	0.070	0.021
300	0.565	0.009	0.094	0.020	0.562	0.014	0.118	0.034	0.568	0.003	0.058	0.018
325	0.543	0.007	0.086	0.018	0.536	0.012	0.108	0.031	0.551	0.003	0.053	0.016
350	0.529	0.008	0.089	0.019	0.527	0.013	0.113	0.033	0.532	0.003	0.051	0.015
375	0.518	0.007	0.084	0.018	0.513	0.012	0.109	0.032	0.524	0.002	0.042	0.013
400	0.512	0.007	0.084	0.018	0.509	0.012	0.111	0.032	0.515	0.001	0.037	0.011
425	0.510	0.007	0.082	0.017	0.507	0.012	0.108	0.031	0.512	0.001	0.035	0.011
450	0.512	0.006	0.079	0.016	0.511	0.011	0.104	0.030	0.514	0.001	0.036	0.011
475	0.514	0.006	0.079	0.016	0.513	0.011	0.103	0.030	0.515	0.001	0.038	0.012
500	0.517	0.006	0.076	0.016	0.517	0.010	0.098	0.028	0.517	0.002	0.039	0.012
525	0.535	0.005	0.068	0.014	0.534	0.007	0.085	0.025	0.536	0.002	0.041	0.012
550	0.590	0.003	0.053	0.011	0.587	0.002	0.050	0.014	0.594	0.003	0.057	0.017
575	0.642	0.002	0.043	0.009	0.639	0.001	0.024	0.007	0.645	0.003	0.057	0.017
600	0.716	0.003	0.054	0.011	0.728	0.001	0.030	0.009	0.702	0.005	0.072	0.022
625	0.730	0.003	0.054	0.011	0.741	0.001	0.027	0.008	0.719	0.005	0.072	0.022
650	0.738	0.003	0.056	0.012	0.752	0.001	0.031	0.009	0.722	0.005	0.074	0.022
675	0.747	0.003	0.055	0.012	0.761	0.001	0.030	0.009	0.732	0.005	0.073	0.022
700	0.754	0.003	0.057	0.012	0.770	0.001	0.036	0.010	0.736	0.005	0.074	0.022
725	0.762	0.004	0.060	0.012	0.780	0.002	0.042	0.012	0.742	0.006	0.075	0.023
750	0.777	0.004	0.060	0.012	0.799	0.002	0.045	0.013	0.752	0.005	0.073	0.022

Appendix 'Full Fire Test'

Full fire test no.01

Figure 95 shows the setup of the fire furnace (3.0 m x 4.0 m) with specimen (blue) and thermocouple wires (grey). In addition, the positions of the six temperature measuring plates are indicated (dark grey).

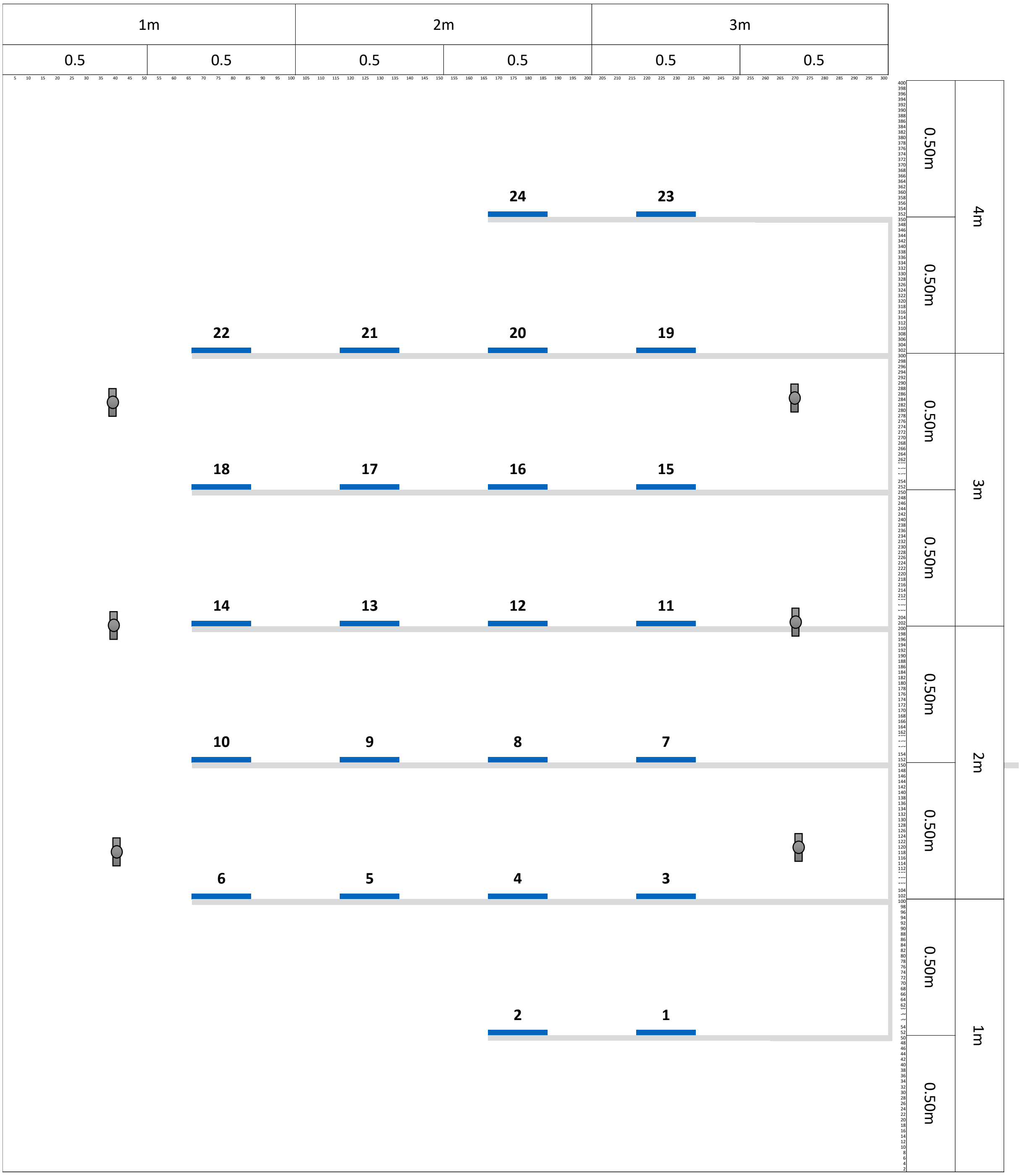

Figure 95: Setup of the first full fire test no.01

The 24 specimens were placed as follows:

1. Row	**Specimen**	**2. Row**	**Specimen**	**3. Row**	**Specimen**	**4. Row**	**Specimen**
1	4-r	3	4-A-Out	7	4-A-In	11	1-A-Out
2	4-A-In	4	1-D-In	8	1-A-Out	12	1-A-In
		5	1-D-Out	9	1-A-In	13	4-D-In
		6	4-D-In	10	1-r	14	4-A-In

5. Row	**Specimen**	**6. Row**	**Specimen**	**7. Row**	**Specimen**
15	1-A-In	19	1-D-In	23	1-r
16	4-A-In	20	4-A-Out	24	1-A-Out
17	4-r	21	4-A-In		
18	1-A-In	22	4-D-Out		

Test procedure

In Figure 97 one can see a comparison of the average room temperature of the compartment with the normative limitations of the DIN EN 1363-1 [15].

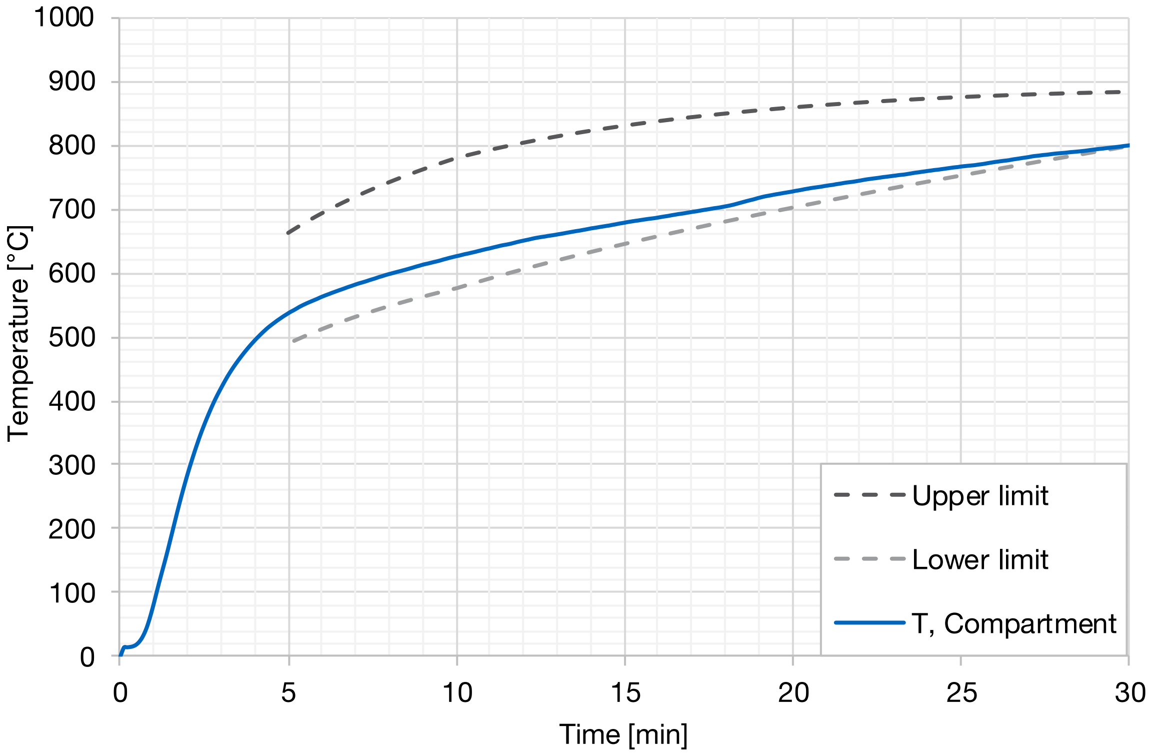

Figure 96: Comparison of the average measured room temperature of the first full fire with the normative limitations of the DIN EN 1363-1 [15].

Full fire test no.02

Setup

Figure 97 shows the layout of the furnace (3.0 m x 4.0 m) with specimen (blue) and thermocouple wires (grey). In addition, the positions of the six temperature measuring plates are indicated (dark grey).

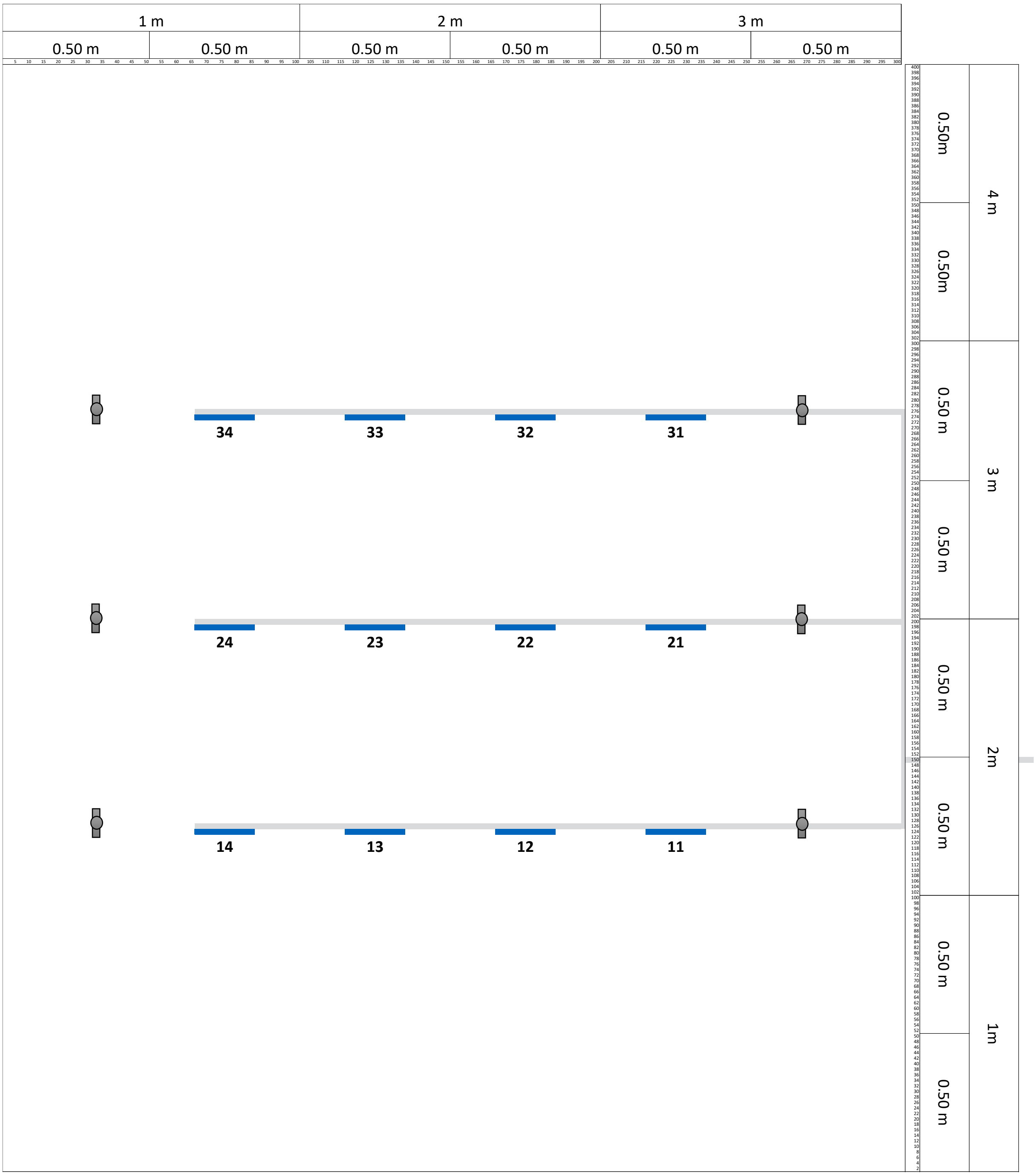

Figure 97: Setup of the first full fire test no.02

The 12 specimens were placed as follows:

1. Row	Specimen	2. Row	Specimen	3. Row	Specimen
11	4-A-In	21	4-B7-In	31	4-B6-In
12	4-B7-In	22	4-B6-In	32	4-r
13	4-r	23	4-A-In	33	4-B6-In
14	4-B6-In	24	4-B7-In	34	4-D-In

Test procedure

In the following Figure 98, one can see the average fire compartment temperature (‘T, Compartment’) of the second fire rest as well as the temperature distribution, separated by cardinal points.

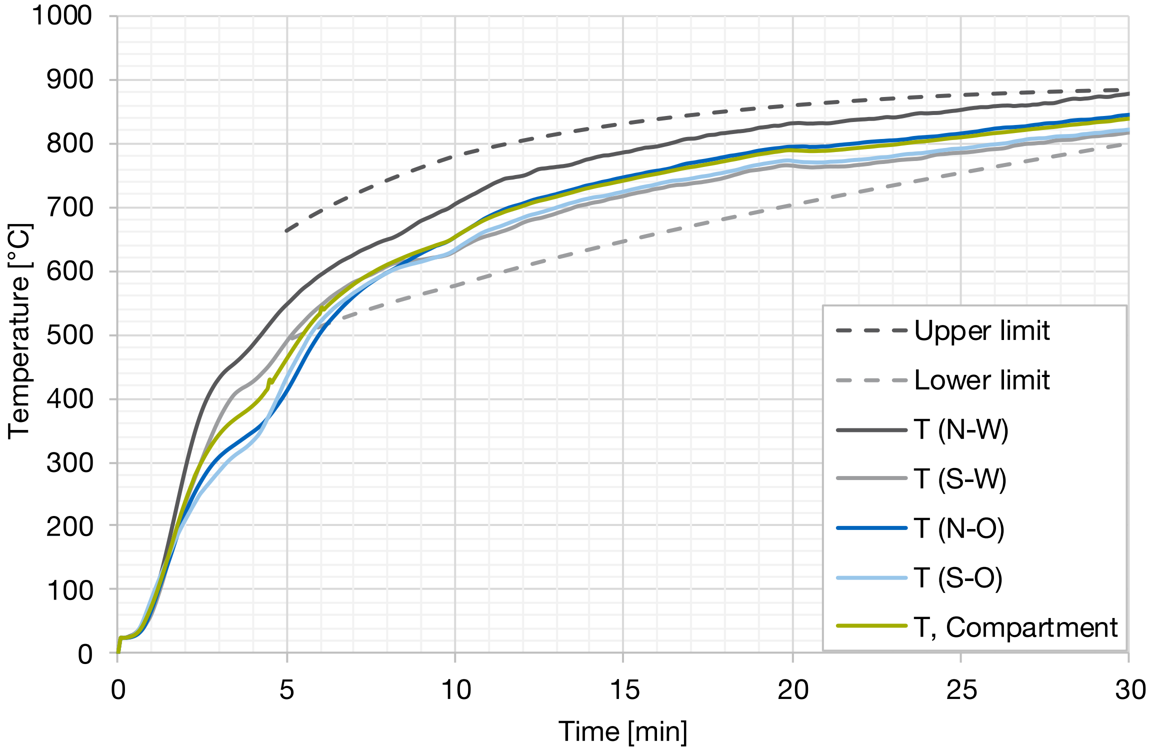

Figure 98: Comparison of the average measured room temperature of the second full fire with the normative limitations of the DIN EN 1363-1 [15]

Appendix ‘Micosections’

In the following microsections of several samples are provided. Table 37 gives an overview.

Table 37: List of microsections

Specimen	Category	Figure	Note
1	A	Figure 99	Microsection before the thermal impact
3	A	Figure 100	Microsection before the thermal impact
3N	A	Figure 101	Microsection before the thermal impact
1D	D	Figure 102	Microsection before the thermal impact
4D	D	Figure 103	Microsection before the thermal impact
1B	B	Figure 104	Microsection before the thermal impact
1	A	Figure 105	Microsection after the thermal impact
14	A	Figure 106	Microsection after the thermal impact
3N	A	Figure 107	Microsection after the thermal impact
B17	B	Figure 108	Microsection after the thermal impact
4D	D	Figure 109	Microsection after the thermal impact
7D	D	Figure 110	Microsection after the thermal impact

Microsection before the thermal impact

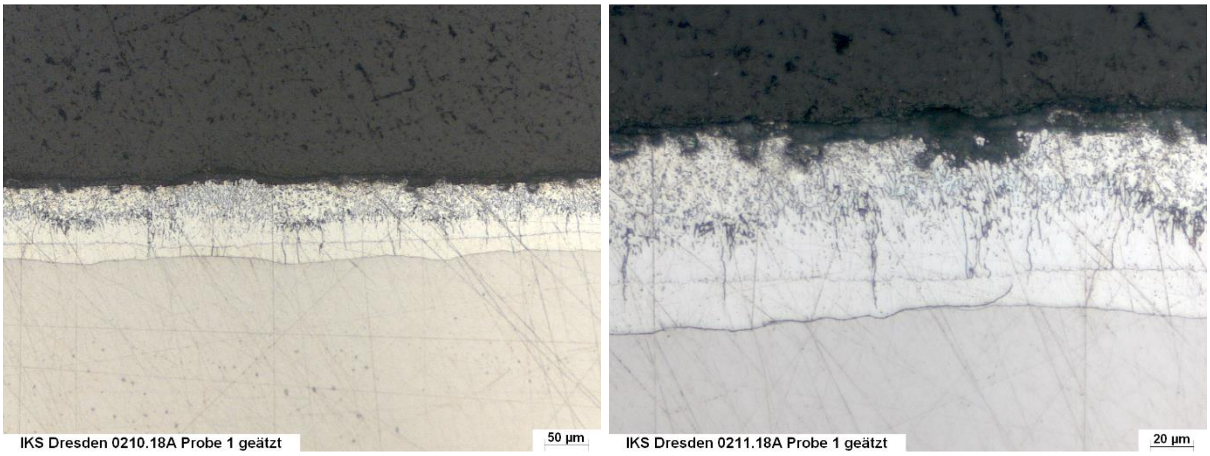

Figure 99: Microsection before the thermal impact specimen ‘1’

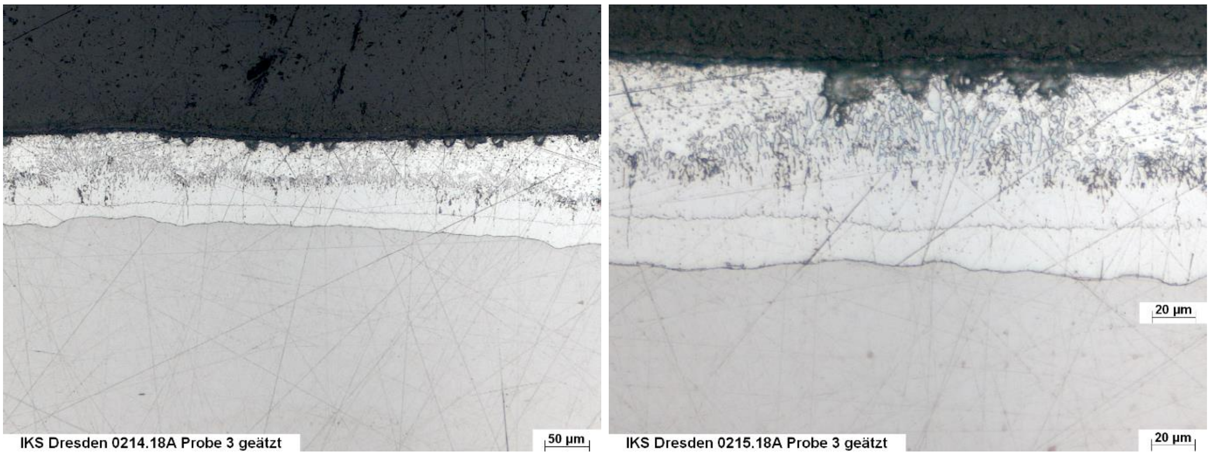

Figure 100: Microsection before the thermal impact specimen ‘3’

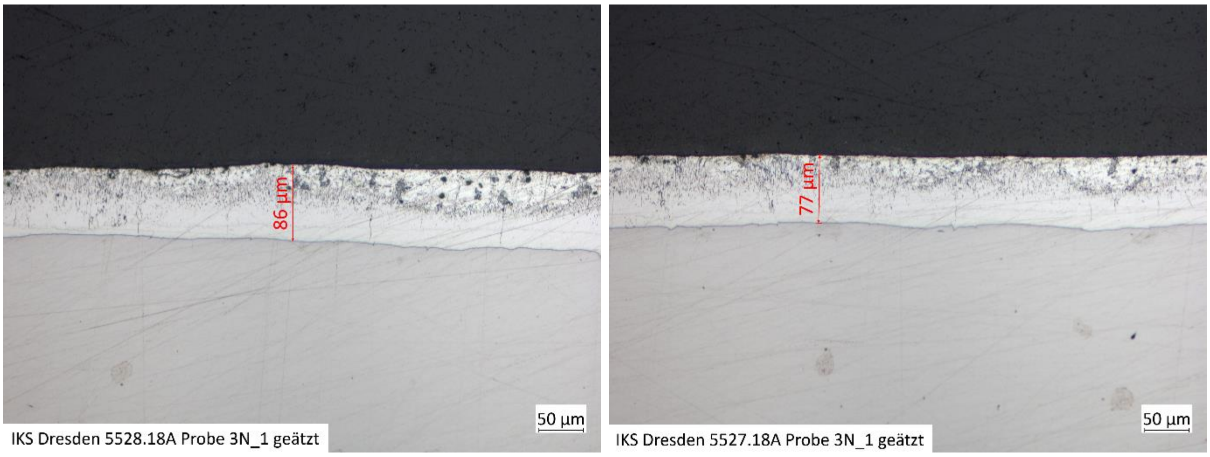

Figure 101: Microsection before the thermal impact specimen ‘3N’

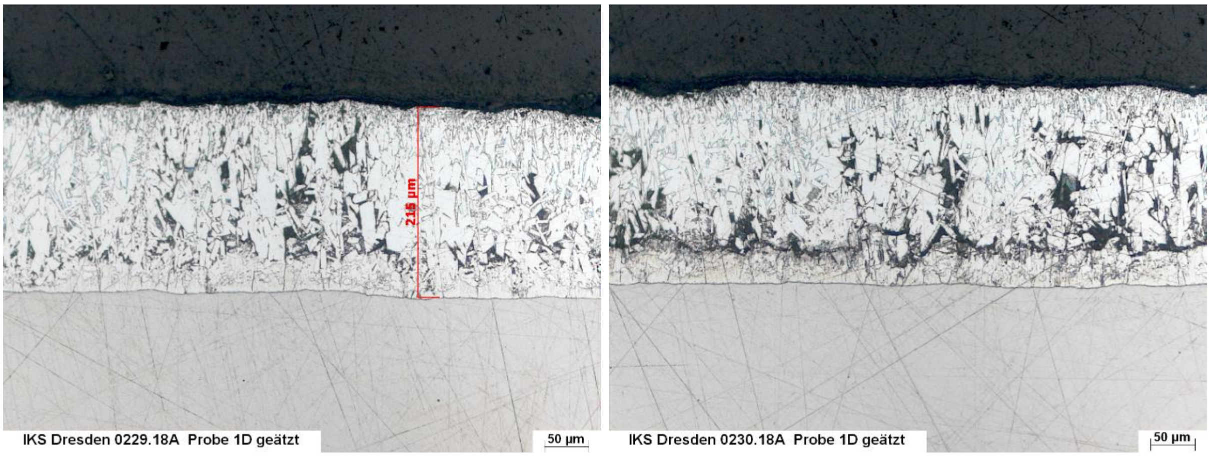

Figure 102: Microsection before the thermal impact specimen ‘1D’

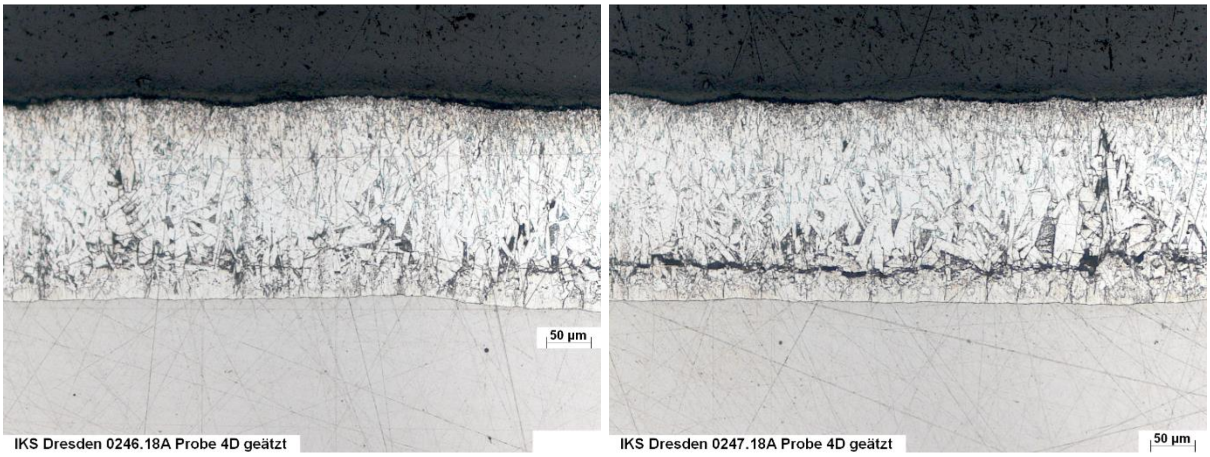

Figure 103: Microsection before the thermal impact specimen ‘4D’

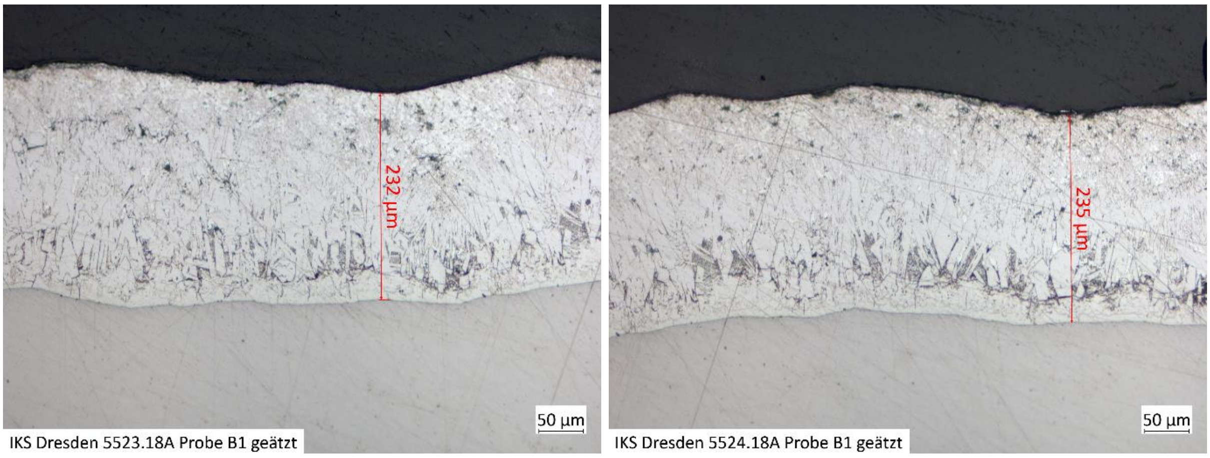

Figure 104: Microsection before the thermal impact specimen ‘1B’

Microsection after the thermal impact

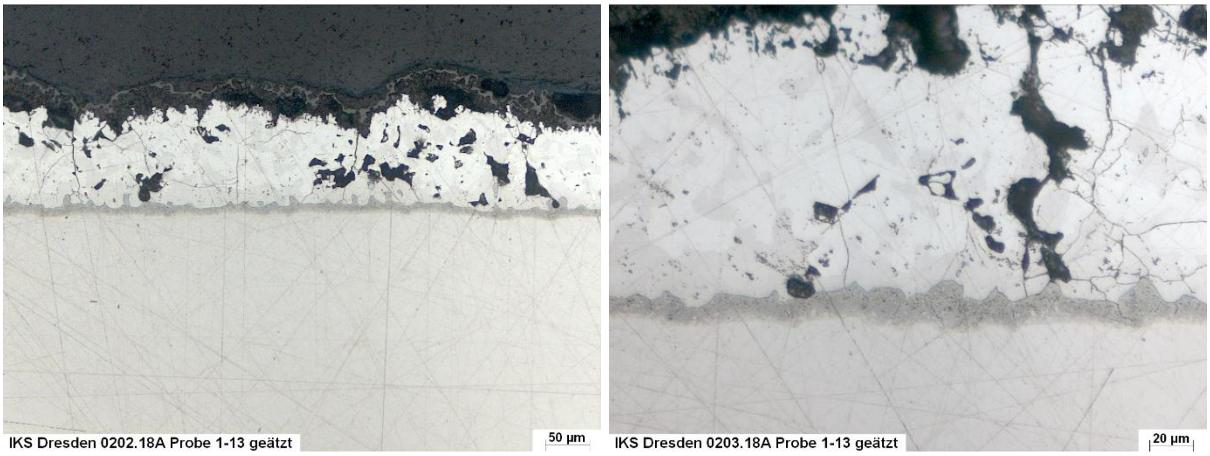

Figure 105: Microsection after the thermal impact specimen ‘1_13’

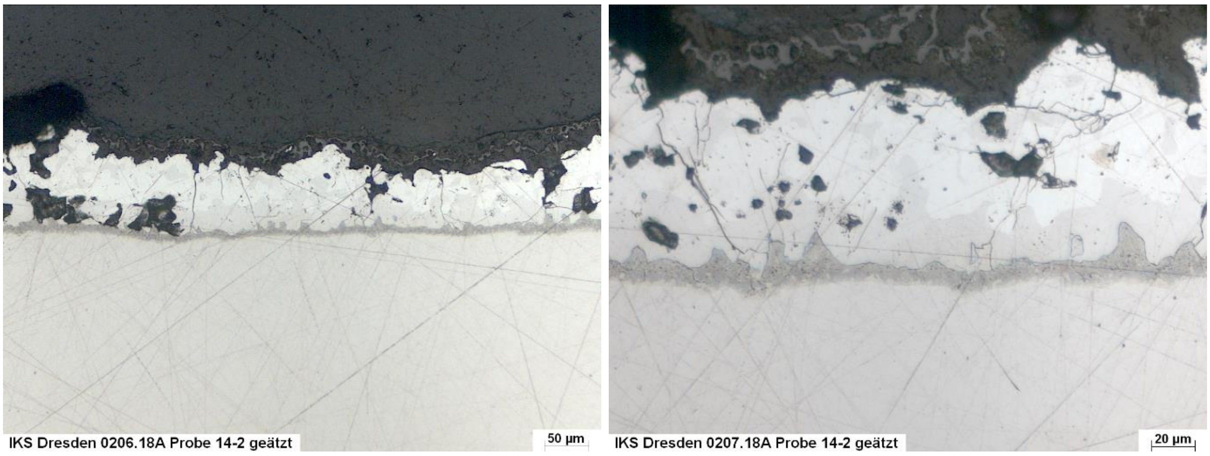

Figure 106: Microsection after the thermal impact specimen ‘14_2’

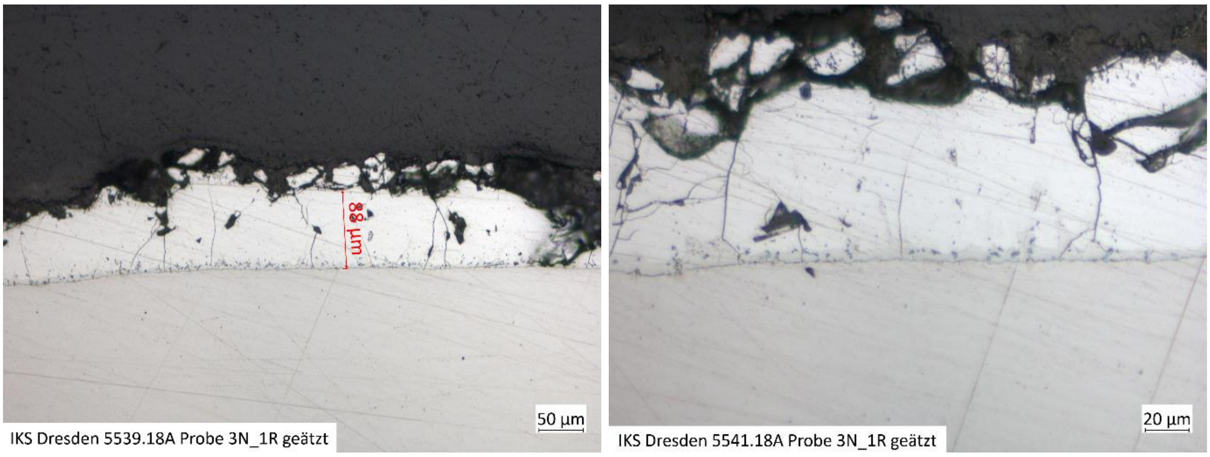

Figure 107: Microsection after the thermal impact specimen ‘3N_1’

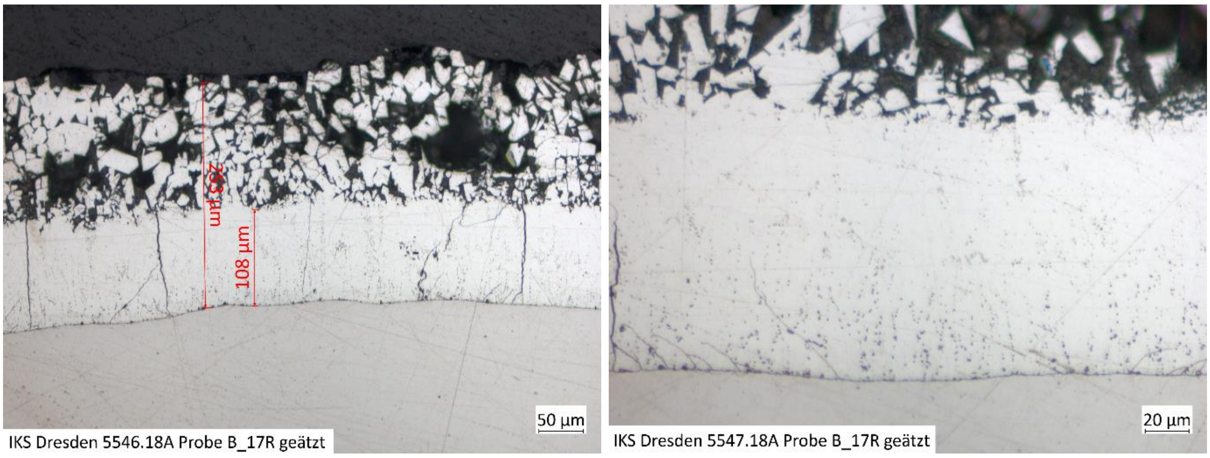

Figure 108: Microsection after the thermal impact specimen ‘B_17’

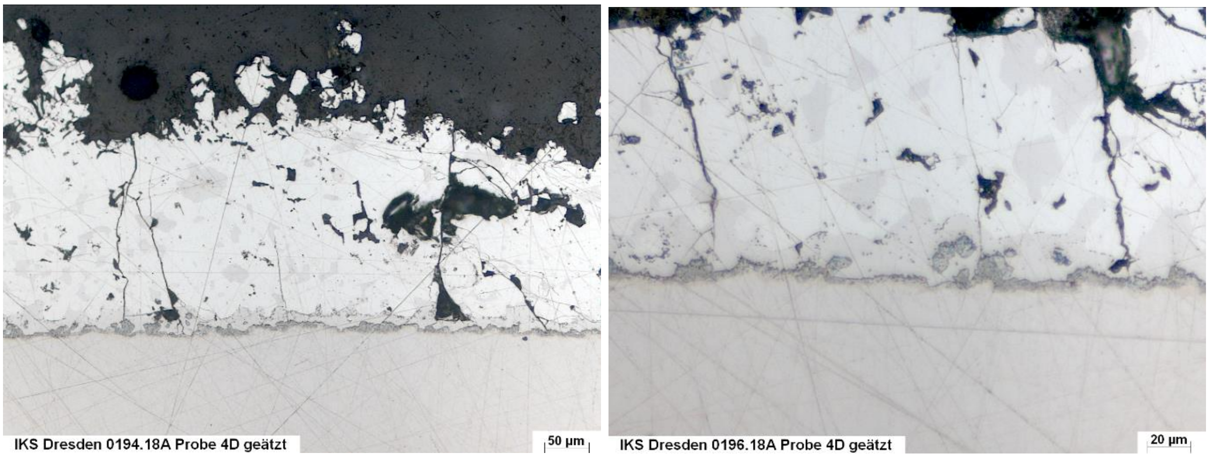

Figure 109: Microsection after the thermal impact specimen ‘4D’

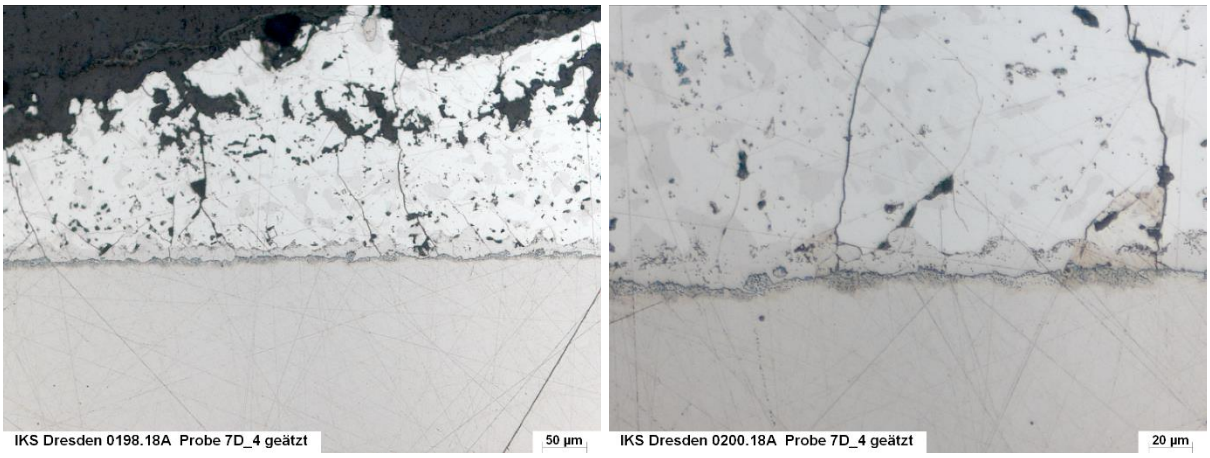

Figure 110: Microsection after the thermal impact specimen ‘7D’

Appendix ‘Nomograms’

Modified section factors

Table 38: Modified section factor for structural steel profiles (IPE & HEA)

	$k_{sh}A_m/V$	
Profile	**4-sided flamed**	**3-sided flamed**
IPE 80	296.9	242.7
IPE 100	270.9	222.8
IPE 120	250.9	207.3
IPE 140	233.8	193.7
IPE 160	216.7	180.0
IPE 180	204.1	169.8
IPE 200	189.5	157.9
IPE 220	177.8	148.2
IPE 240	165.7	138.1
IPE 270	158.8	132.4
IPE 300	150.6	125.5
IPE 330	140.9	117.9
IPE 360	131.2	110.2
IPE 400	123.6	104.4
IPE 450	116.6	99.3
IPE 500	108.6	93.1
IPE 550	102.1	88.0
IPE 600	94.6	81.9

	$k_{sh}A_m/V$	
Profile	**4-sided flamed**	**3-sided flamed**
HEA 100	166.4	124.0
HEA 120	166.5	123.8
HEA 140	156.5	116.4
HEA 160	144.7	107.6
HEA 180	139.5	103.7
HEA 200	130.5	97.0
HEA 220	120.4	89.6
HEA 240	110.2	82.0
HEA 260	105.8	78.8
HEA 280	101.7	75.8
HEA 300	94.0	70.1
HEA 320	88.5	66.8
HEA 340	85.3	65.0
HEA 360	81.8	62.9
HEA 400	78.1	61.1
HEA 450	74.8	59.7
HEA 500	71.8	58.2
HEA 550	71.3	58.6
HEA 600	70.9	58.9
HEA 650	69.9	58.8
HEA 700	68.5	58.2
HEA 800	68.6	59.2
HEA 900	66.7	58.3
HEA 1000	66.9	59.1

Table 39: Modified section factor for structural steel profiles (HEB & HEM)

Profile	$k_{sh}A_m/V$	
	4-sided flamed	**3-sided flamed**
HEB 100	138.5	103.8
HEB 120	127.1	95.3
HEB 140	117.2	87.9
HEB 160	106.1	79.6
HEB 180	99.2	74.4
HEB 200	92.2	69.1
HEB 220	87.0	65.3
HEB 240	81.5	61.1
HEB 260	79.3	59.5
HEB 280	76.9	57.7
HEB 300	72.5	54.4
HEB 320	69.3	52.5
HEB 340	67.4	51.6
HEB 360	65.6	50.7
HEB 400	63.6	50.0
HEB 450	61.9	49.5
HEB 500	60.3	49.0
HEB 550	60.2	49.6
HEB 600	60.0	50.0
HEB 650	59.8	50.3
HEB 700	58.8	50.0
HEB 800	59.3	51.2
HEB 900	58.2	50.9
HEB 1000	58.5	51.8

Profile	$k_{sh}A_m/V$	
	4-sided flamed	**3-sided flamed**
HEM 100	76.5	58.5
HEM 120	72.1	55.0
HEM 140	68.3	52.0
HEM 160	64.1	48.8
HEM 180	61.5	46.7
HEM 200	58.5	44.4
HEM 220	56.3	42.6
HEM 240	46.6	35.5
HEM 260	45.7	34.7
HEM 280	44.9	34.1
HEM 300	38.6	29.4
HEM 320	38.5	29.6
HEM 340	39.1	30.3
HEM 360	39.7	31.0
HEM 400	40.8	32.3
HEM 450	42.2	33.9
HEM 500	43.4	35.4
HEM 550	44.6	36.9
HEM 600	45.7	38.2
HEM 650	46.8	39.5
HEM 700	47.9	40.8
HEM 800	49.8	43.0
HEM 900	51.5	45.0
HEM 1000	53.1	47.0

Nomograms

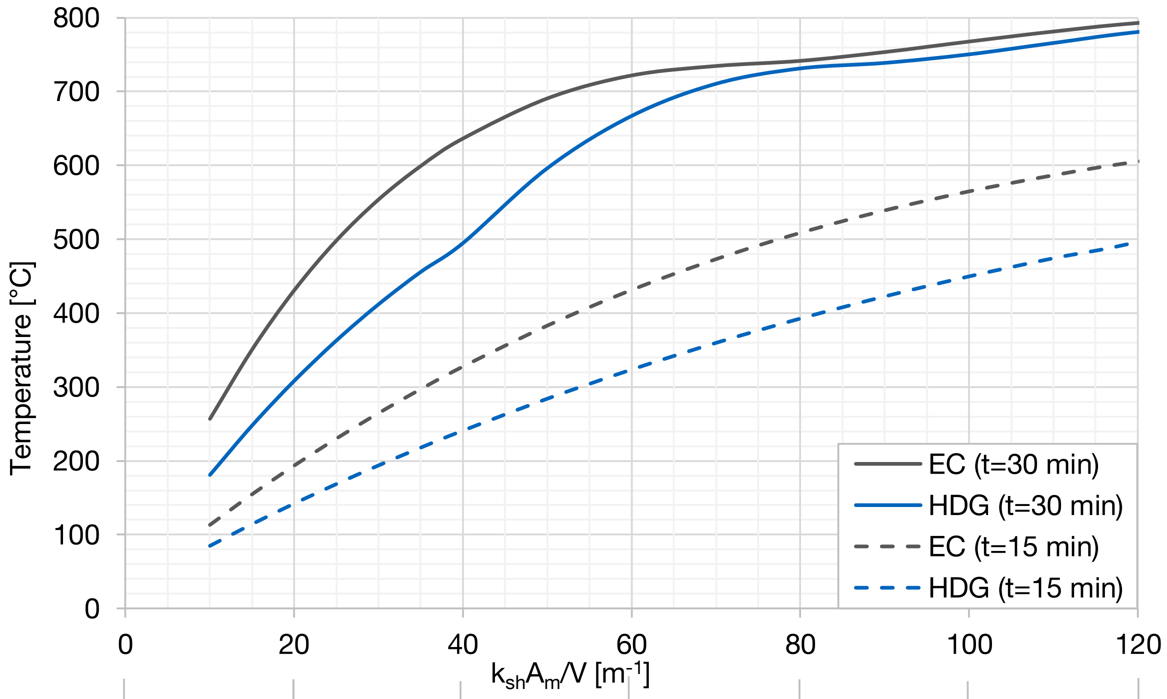

Profiles						
IPE				600		
						450
						330
HEA			400	260	200	140
			450		220	
			500	300	240	
HEB			280	200		100
			360	240	140	
			450	260	160	
HEM		300	220			
		240	140	100		
			700			

Figure 111: Nomogram for 3-sided flamed steel profiles in dependence of the modified section factor $k_{sh}A_m/V$ for an ISO 834 fire up to 15 and 30 minutes

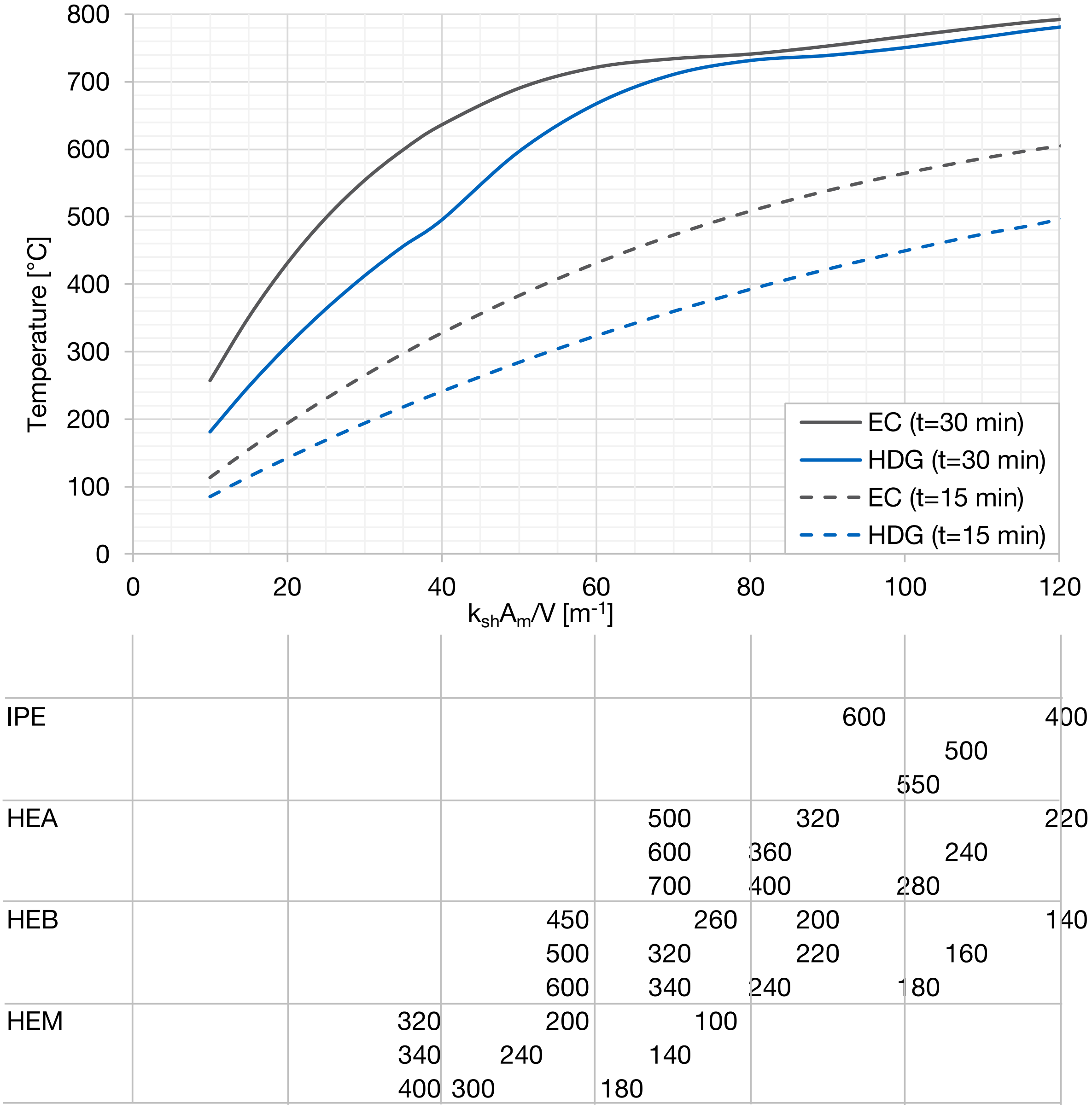

Figure 112: Nomogram for 4-sided flamed steel profiles in dependence of the modified section factor $k_{sh}A_m/V$ *for an ISO 834 fire up to 15 and 30 minutes*

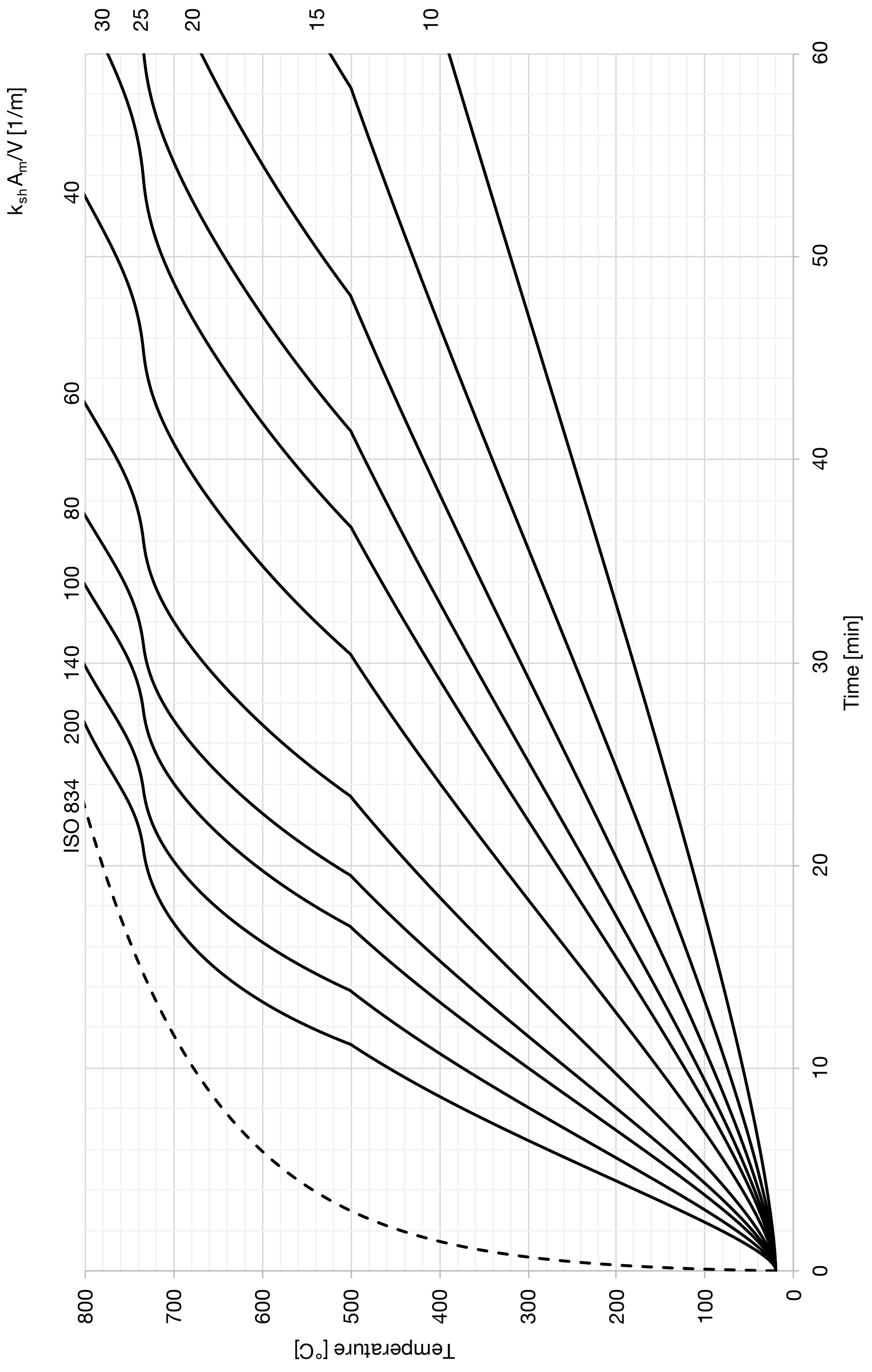

Figure 113: Nomogram for hot-dip galvanized steel members in fire

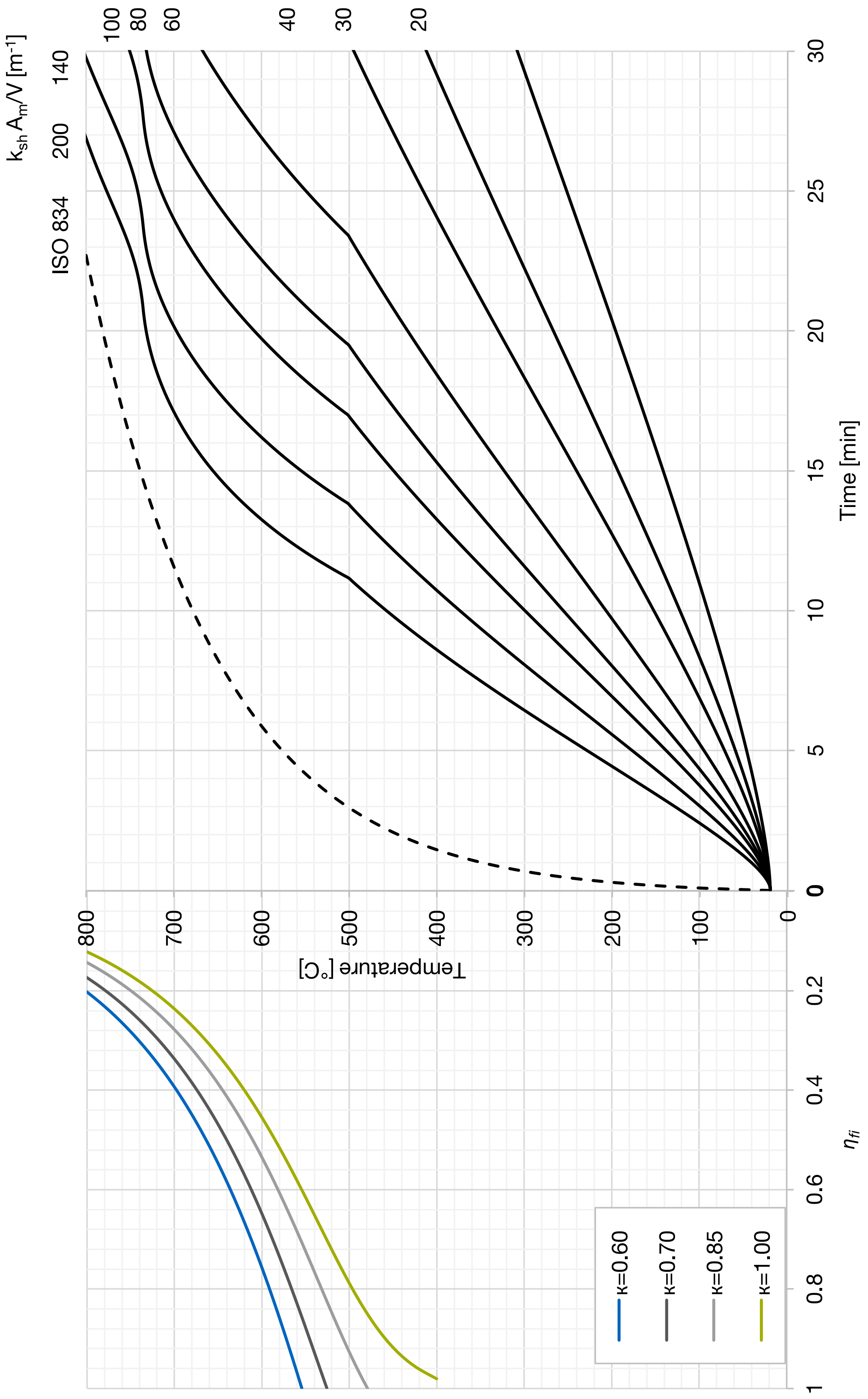

Figure 114: Nomogram in cooperation with the reduction factor η_{fi}

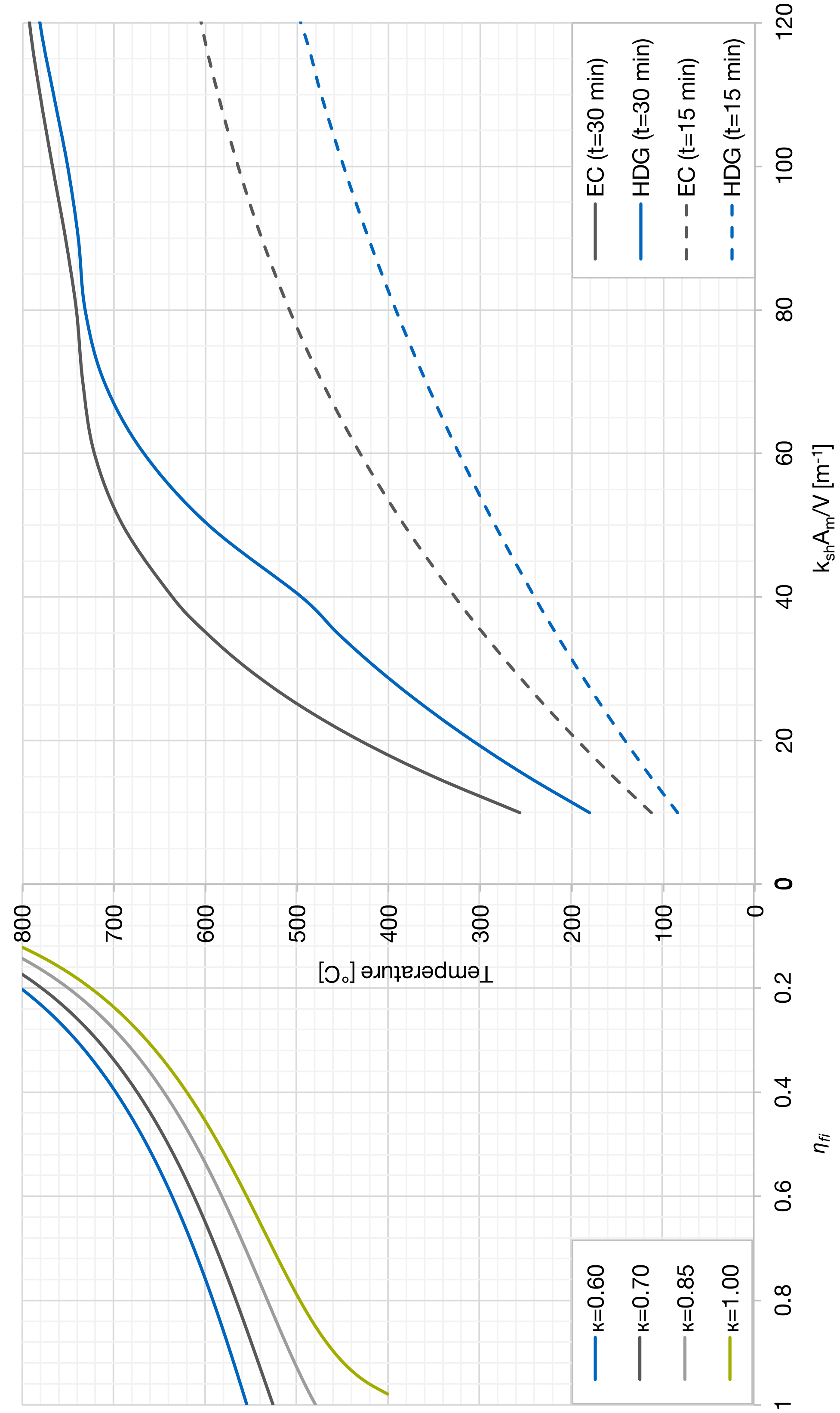

Figure 115: Nomogram in dependence of the modified section factor $k_{sh}A_m/V$ for an and in cooperation with the reduction factor η_{fi}

List of Tables

List of Figures

References

[1] DIN Deutsches Institut für Normung e. V., *DIN EN ISO 1461:2009-10, Durch Feuerverzinken auf Stahl aufgebrachte Zinküberzüge (Stückverzinken) - Anforderungen und Prüfungen*.

[2] Deutscher Ausschuss für Stahlbau, *DASt-Richtlinie 022*.

[3] Schulz, W.-D. and Thiele, M., *Feuerverzinken von Stückgut*: *Werkstoffe - Technologien - Schichtbildung - Eigenschaften - Fehler*, Leuze, Bad Saulgau, 2012.

[4] DIN Deutsches Institut für Normung e. V., *DIN EN 10020:2000-07; Begriffsbestimmung für die Einteilung der Stähle*.

[5] Läpple, V., *Wärmebehandlung des Stahls*: *Grundlagen, Verfahren und Werkstoffe*, Verl. Europa-Lehrmittel Nourney, Vollmer, Haan-Gruiten, 2003.

[6] Graef, M. de and McHenry, M. E., *Structure of materials*: *An introduction to crystallography, diffraction, and symmetry*, Cambridge University Press, Cambridge, 2008.

[7] Horstmann, D., Zum Ablauf der der Eisen-Zink-Reaktionen, 1991.

[8] Schubert, P., Schulz, W.-D. et al., Struktur und Eigenschaften von Feuerzinküberzügen in *Metall 53 (1999)*.

[9] Katzung, W. and Rittig, R., Zum Einfluß von Si und P auf das Verzinkungsverhalten Von Baustählen: The influence of Si and P contents in steels on the galvanizing behavior in *Mat.-wiss. u. Werkstofftech. (Materialwissenschaft und Werkstofftechnik)*, vol. 28, pp. 575–587.

[10] DIN Deutsches Institut für Normung e. V., *DIN EN ISO 14713-2:2009-05, Zinküberzüge – Leitfäden und Empfehlungen zum Schutz von Eisen- und Stahlkonstruktionen vor Korrosion – Teil 2: Feuerverzinken*.

[11] Seré, P. R., Culcasi, J. D. et al., Relationship between texture and corrosion resistance in hot-dip galvanized steel sheets in *Surface and Coatings Technology*, vol. 122, pp. 143–149.

[12] Waitlevertch, M. E. and Hurwitz, J. K., Emission Spectrographic Analysis of Surfaces with an Ion-Sputtering Source in *Applied Spectroscopy*, vol. 30, pp. 510–515.

[13] Chang, S. and Shin, J. C., The effect of antimony additions on hot dip galvanized coatings in *Corrosion Science*, vol. 36, pp. 1425–1436.

[14] DIN Deutsches Institut für Normung e. V., *DIN EN 1991-1-2:2010-12, Eurocode 1: Einwirkungen auf Tragwerke - Teil 1-2: Allgemeine Einwirkungen - Brandeinwirkungen auf Tragwerke*.

[15] DIN Deutsches Institut für Normung e. V., *DIN EN 1363-1:2012-10, Feuerwiderstandsprüfungen - Teil 1: Allgemeine Anforderungen*.

[16] International Organization for Standardization, *ISO 834-1:1999-09; Fire-resistance tests - Elements of building construction - Part 1: General requirements*.

[17] DIN Deutsches Institut für Normung e. V., *DIN EN 1993-1-2:2010-12, Eurocode 3: Bemessung und Konstruktion von Stahlbauten – Teil 1-2: Allgemeine Regeln – Tragwerksbemessung für den Brandfall*.

[18] DIN Deutsches Institut für Normung e. V., *DIN EN 1994-1-2:2010-12, Eurocode 4: Bemessung und Konstruktion von Verbundtragwerken aus Stahl und Beton – Teil 1-2: Allgemeine Regeln – Tragwerksbemessung für den Brandfall*.

[19] DIN Deutsches Institut für Normung e. V., *DIN EN 13501-2:2016-12, Klassifizierung von Bauprodukten und Bauarten zu ihrem Brandverhalten – Teil 2: Klassifizierung mit den Ergebnissen aus den Feuerwiderstandsprüfungen, mit Ausnahme von Lüftungsanlagen; Deutsche Fassung EN 13501-2: 2016*.

[20] DIN Deutsches Institut für Normung e. V., *DIN EN 1990:2010-12; Eurocode: Grundlagen der Tragwerksplanung*.

[21] Siegel, R. Howell, J. R. and Lohrengel, J., *Wärmeübertragung durch Strahlung*: *Teil 1 Grundlagen und Materialeigenschaften*, Springer, Berlin, 1988.

[22] Baehr, H. D. and Stephan, K., *Wärme- und Stoffübertragung*, Springer Berlin Heidelberg, Berlin, Heidelberg, 2013.

[23] Bramson, M. A. and Wolfe, W. L., *Infrared radiation*: *A handbook for applications; with a collection of reference tables*, Springer Science+Business Media, New York, 1968.

[24] Howell, J. R., Siegel, R., and Mengüç, M. P., *Thermal radiation heat transfer*, CRC Press, Boca Raton, 2010.

[25] Optris GmbH, Grundlagen der berührungslosen Temperaturmessung, 2016.

[26] VDI - Verein Deutscher Ingenieure, *VDI/VDE 3511 Blatt 4.5:2015-06; Technische Temperaturmessung - Strahlungsthermometrie - Praktische Anwendung von Strahlungsthermometern*.

[27] VDI - Verein Deutscher Ingenieure, *VDI/VDE 3511 Blatt 4:2011-12; Technische Temperaturmessung - Strahlungsthermometrie*.

[28] Sala, A., *Radiant properties of materials*: *Tables of radiant values for black bodies and real materials*, Elsevier; PWN Polish Scientific Publishers; distribution for the U.S.A. and Canada, Elsevier Science Pub. Co, Amsterdam, New York, Warsaw, New York, N.Y., 1986.

[29] Elich, J. and Hamerlinck, A., Thermal Radiation of Galvanized Steel and its Importance in Enclosure Fire Scenarios in *Fire Safety Journal*, vol. 16, pp. 469–482.

[30] Jirků, J. and Wald, F., Influence of zinc coating to a temperature of steel members in fire in *Applications of structural fire engineering*: *Proceedings of International Conference : Prague, 19-20 April 2013 ; COST Action TU0904,* F. Wald, I. Burgess, K. Horová et al., Eds., CTU Publishing House Czech Technical University, Prague, April 2013.

[31] Huckshold, M. and Thiele, M., *Korrosionsschutz - Feuerverzinken*, Beuth, Berlin, 2011.

[32] Institut Feuerverzinken, ed., *Arbeitsblätter Feuerverzinken*.

[33] Gaigl, C. and Mensinger, M., Thermal impact on HDG construction, TU München - Lehrstuhl für Metallbau, 2018.

[34] DIN Deutsches Institut für Normung e. V., *DIN EN 60584-1:2014-07; Thermoelemente - Teil 1: Thermospannungen und Grenzabweichungen (IEC 60584-1:2013); Deutsche Fassung EN 60584-1:2013*.

[35] VDI-Gesellschaft Verfahrenstechnik und Chemieingenieurwesen, *VDI-Wärmeatlas*: *Mit 320 Tabellen*, Springer Vieweg, Berlin, 2013.

[36] DIN Deutsches Institut für Normung e. V., *DIN 4760:1987-06, Gestaltsabweichungen*.

[37] Liu, Y., Su, X. P. et al., Experimental Determination and Atomistic Simulation on the Structure of FeZn13, vol. 29, pp. 488–492.

[38] Pokorny, P., Kolisko, J. et al., Description of structure of Fe-Zn intermetalic compounds present in hot-dip galvanized coatings on steel in *Metalurgija, Vol.54*.

[39] Peissker, P., *Handbuch Feuerverzinken*, Wiley Vch, 2016.

[40] Maaß, P., *Handbuch Feuerverzinken*, Dt. Verl. für Grundstoffindustrie; Wiley-VCH, Leipzig, Stuttgart, [Weinheim], 2001.

[41] DIN Deutsches Institut für Normung e. V., *DIN EN 1993-1-2/NA:2010-12, Nationaler Anhang – National festgelegte Parameter – Eurocode 3: Bemessung und Konstruktion von Stahlbauten – Teil 1-2: Allgemeine Regeln – Tragwerksbemessung für den Brandfall*.